JYU DISSERTATIONS 362

Vesa-Matti Hiltunen

Modification of Graphene Properties by Optical Forging

UNIVERSITY OF JYVÄSKYLÄ
FACULTY OF MATHEMATICS
AND SCIENCE

JYU DISSERTATIONS 362

Vesa-Matti Hiltunen

Modification of Graphene Properties by Optical Forging

sitetään Jyväskylän yliopiston matemaattis-luonnontieteellisen tiedekunnan suostumuksella
julkisesti tarkastettavaksi maaliskuun 26. päivänä 2021 kello 12.

Academic dissertation to be publicly discussed, by permission of
the Faculty of Mathematics and Science of the University of Jyväskylä,
on March 26, 2021, at 12 o'clock noon.

JYVÄSKYLÄN YLIOPISTO
UNIVERSITY OF JYVÄSKYLÄ

JYVÄSKYLÄ 2021

Editors
Ilari Maasilta
Department of Physics, University of Jyväskylä
Päivi Vuorio
Open Science Centre, University of Jyväskylä

Permanent link to this publication: http://urn.fi/URN:ISBN:978-951-39-8560-8

ISBN 978-951-39-8560-8 (PDF)
URN:ISBN:978-951-39-8560-8
ISSN 2489-9003

ABSTRACT

Hiltunen, Vesa-Matti
Modification of graphene properties by optical forging
Jyväskylä: University of Jyväskylä, 2021, 93 p. (+included articles)
JYU Dissertations
ISSN 2489-9003; 362
ISBN 978-951-39-8560-8 (PDF)

Graphene is one atom layer thin carbon material that has gained plenty of attention due to its numerous excellent properties. In this thesis a novel method to modify the structure and properties of graphene, called optical forging, is presented. In this method graphene is irradiated using femtosecond pulsed laser light and as a result of it graphene forms three-dimensional structures. Detailed characterizations have revealed that the process of optical forging causes defects to the graphene lattice, which in turn causes lattice expansion and bulging of graphene into the 3D shapes. In addition to this, some amorphous carbon is deposited onto graphene as a side effect, and the formation of the entire 3D shape is a combination of both bulging and deposition. Using nanoindentation measurements, optically forged graphene was determined to have high bending stiffness, which is very different from pristine graphene, which is very flexible. Optically forged patterns are also and more reflective than pristine graphene and they exhibit photoluminescence. As for applications, optical forging can be used to make ultralight scaffold structures from graphene, and potentially to increase the resonance frequencies of graphene resonator devices.

Keywords: graphene, nanoindentation, graphene quantum dot, chemical vapor deposition, Raman spectroscopy, atomic force microscopy, elastic modulus, defect engineering, optical forging

TIIVISTELMÄ (ABSTRACT IN FINNISH)

Hiltunen, Vesa-Matti
Grafeenin ominaisuuksien muokkaus optisella taonnalla
Jyväskylä: University of Jyväskylä, 2021, 93 s. (+artikkelit)
JYU Dissertations
ISSN 2489-9003; 362
ISBN 978-951-39-8560-8 (PDF)

Grafeeni on hiilestä koostuva yhden atomikerroksen paksuinen materiaali, joka on saanut runsaasti huomiota monien erinomaisten ominaisuuksiensa vuoksi. Tämä työ keskittyy grafeenin optiseen taontaan, joka on uusi menetelmä grafeenin rakenteeen ja ominaisuuksien muokkaamiseksi. Optisessa taonnassa grafeenia valotetaan femtosekunttiskaalassa olevilla laserpulsseilla, jolloin grafeenista muodostuu kolmiuloitteisia rakenteita. Rakenteiden yksityiskohtainen karakterisointi osoitti, että optinen taonta aiheuttaa rakennevirheiden syntymisen grafeenin kidehilaan, joka puolestaan aiheuttaa rakenteen paisumisen ja pullistumisen kolmiuloitteisiksi muodoiksi. Lisäksi optinen taonta aiheuttaa amorfisen hiilen kerrostumista grafeenin pinnalle, jolloin kokonaisrakenne on pullistuneen grafeenin ja amorfisen hiilen yhdistelmä. Nanomittakaavan painelukokeiden perusteella optisesti taotun grafeenin havaittiin omaavan korkean taivutusjäykkyyden, joka poikkeaa suuresti käsittelemättömästä grafeenista, joka on taivutettaessa hyvin joustavaa. Lisäksi optisesti taotut grafeenirakenteet heijastavat enemmän valoa kuin käsittelemätön grafeeni ja niissä esiintyy fotoluminesenssia. Optisesti taottua grafeenia voidaan käyttää sovelluksissa, kuten ultrakevyiden nanokokoisten tukirakenteiden valmistukseen ja mahdollisesti grafeeniresonaattoreiden ominaistaajuuden kasvattamiseen.

Avainsanat: grafeeni, nanopainelu, grafeenikvanttipiste, kemiallinen kaasufaasikasvatus, ramanspektroskopia, atomivoimamikroskopia, elastinen kerroin, virhevalmistus, optinen taonta

Author

Vesa-Matti Hiltunen
Department of Physics
Nanoscience Center
University of Jyväskylä
Finland

Supervisor

Senior Researcher Doc. Andreas Johansson
Department of Physics
Department of Chemistry
Nanoscience Center
University of Jyväskylä
Finland

Co-supervisor

Professor Mika Pettersson
Department of Chemistry
Nanoscience Center
University of Jyväskylä
Finland

Reviewers

Senior Scientist Dr. Hua Jiang
Department of Applied Physics
Nanomicroscopy Center
Aalto University
Finland

Scientific Researcher Dr. Ermelinda Maçôas
Instituto Superior Técnico
Department of Chemistry
University of Lisbon
Centro de Química Estrutural
Portugal

Opponent

Senior Researcher Dr. Ivan Bobrinetskiy
BioSense Institute
University of Novi Sad
Serbia
National Research University of Electronic Technology
Russia

PREFACE

The work reviewed in this thesis has been carried out during the years 2016-2021 at the Department of Physics and Nanoscience Center in the University of Jyväskylä.

First and foremost, I would like to thank my supervisor Dr. Andreas Johansson for his guidance during my Ph.D. and M.Sc. studies. I will always be grateful for his insightful and enthusiastic support that has been invaluable help for me on my road towards becoming a professional scientist. I would also like to thank my second supervisor Prof. Mika Pettersson. His abilities to see the big picture and focus on the essentials have been truly helpful.

Other people deserving my gratitude for their irreplaceable help are Prof. Pekka Koskinen for providing theoretical understanding to optical forging, Dr. Pasi Myllyperkiö for all the help with optical spectroscopy, and Dr. Kamila Mentel and Mr. Jyrki Manninen, who have helped me greatly with sample processing. Without these people, my thesis work would not have been possible.

I also want to thank the following former and current people in our broad research group who I have had a pleasure to work with: Dr. Eero Hulkko, Dr. Juha Koivistoinen, Dr. Ján Borovský, Dr. Efstratios Sitsanidis, Ms. Johanna Schirmer, Mr. Olli Rissanen, Dr. Erich See and Mr. Aku Lampinen. Additionally, I would like to thank the NSC cleanroom technical staff, Dr. Kimmo Kinnunen and Mr. Tarmo Suppula, for their excellent work keeping things running in the laboratory.

Nanoscience Center has been an awesome place to work and I want to thank in general all of the people working there for a great working atmosphere. Especially, I would like to mention Dr. Sami Kaappa and Mr. Sami Kinnunen for our numerous coffee break discussions.

Additionally, I wish to extend my warmest thanks to my family, friends and relatives outside Academia who have supported me during and before my doctoral studies.

Finally, I would like to gratefully acknowledge the Finnish Cultural Foundation for funding my work for three years.

Jyväskylä, February 2021

Vesa-Matti Hiltunen

CONTENTS

LIST OF INCLUDED ARTICLES

AI Andreas Johansson, Pasi Myllyperkiö, Pekka Koskinen, Jukka Aumanen, Juha Koivistoinen, Hung-Chieh Tsai, Chia-Hao Chen, Lo-Yueh Chang, **Vesa-Matti Hiltunen**, Jyrki J. Manninen, Wei Yen Woon, Mika Pettersson. Optical Forging of Graphene into Three-Dimensional Shapes. *Nano Letters*, **17**, 10, 6469-6474 (2017).

AII Pekka Koskinen, Karoliina Karppinen, Pasi Myllyperkiö, **Vesa-Matti Hiltunen**, Andreas Johansson, Mika Pettersson. Optically Forged Diffraction-Unlimited Ripples in Graphene. *The Journal of Physical Chemistry Letters*, **9**, 21, 6179-6184 (2018).

AIII Kamila Mentel, Jyrki Manninen, **Vesa-Matti Hiltunen**, Pasi Myllyperkiö, Andreas Johansson, Mika Pettersson. Shaping graphene with optical forging: from single blister to complex 3D structures. *Nanoscale Advances*, accepted for publication (2021).

AIV **Vesa-Matti Hiltunen**, Pekka Koskinen, Kamila Mentel, Jyrki Manninen, Pasi Myllyperkiö, Andreas Johansson, Mika Pettersson. Making Graphene Luminescent by Direct Laser Writing. *The Journal of Physical Chemistry C*, **124**, 15, 8371-8377 (2020).

AV **Vesa-Matti Hiltunen**, Pekka Koskinen, Kamila Mentel, Jyrki Manninen, Pasi Myllyperkiö, Mika Pettersson, Andreas Johansson. Ultrastiff Graphene. *npj 2D Materials and Applications*, submitted for publication (2021).

Author's contribution

In article [AI], the author made some of the sample fabrication, did the indentation measurements and analysis and participated manuscript writing. In article [AII], the author fabricated the graphene sample and participated in writing of the article. In article [AIII], the author fabricated the graphene sample, helped with data analysis and contributed in writing of the article. In articles [AIV] and [AV], the author was part of planning the studies, did all the experimental work, except for the laser exposure, performed data analyses and wrote most of the articles.

List of other articles to which the author has contributed

i Juha Koivistoinen, Jukka Aumanen, **Vesa-Matti Hiltunen**, Pasi Myllyperkiö, Andreas Johansson, and Mika Pettersson. Real-time monitoring of graphene patterning with wide-field four-wave mixing microscopy. *Applied Physics Letters*, **108**, 153112 (2016)

ii Efstratios D. Sitsanidis, Johanna Schirmer, Aku Lampinen, Kamila K. Mentel, **Vesa-Matti Hiltunen**, Visa Ruokolainen, Andreas Johansson, Pasi Myllyperkiö, Maija Nissinen and Mika Pettersson. Tuning protein adsorption on graphene surfaces via laser-induced oxidation. *Nanoscale Advances* (2021), accepted for publication

1 INTRODUCTION

Graphite is a carbon material that can be found, for example, in normal pencils. It is formed from numerous stacked layers of two-dimensional (2D) single atom layer thin sheets of carbon. These single sheets are called graphene. A graphene sheet can be thought to be the building block for other carbon allotropes, fullerene being graphene wrapped into a 0D sphere, carbon nanotube is graphene rolled into a 1D tube and graphite being graphene stacked into a 3D structure. If one of these graphene sheets is isolated, it exhibits many excellent properties. [1–3] Andre Geim and Konstantin Novoselov were the first to isolate and measure some of graphene's exotic electronic properties, which include extremely high charge carrier mobilities and quantum Hall effect at room temperature. [4–7] These discoveries resulted into a Nobel Prize in physics being awarded to them in 2010.

Other notable properties of graphene are high thermal conductivity, [8–12] high mechanical strength [13–15] and almost complete transparency. [16] Because of its properties, graphene has been suggested to be used in a plethora of applications, some of these including high frequency field effect transistors [17], nanoelectromechanical systems, [18, 19] supercapacitors [20–22], nanoscale optoelectronics and photonics devices, [23–25]. The list could go on.

Properties of graphene originate from its atomic structure. Each carbon atom has four valence electrons: one s orbital and three p orbitals. In graphene two p orbitals with the s orbital form a sp^2 hybridized orbital, which forms a covalent σ bond between the neighbouring carbon atoms. As a very strong bond, the σ bond is the reason for good mechanical strength of graphene. The hybridization results into the carbon atoms forming a planar hexagonal structure, a honeycomb lattice as presented in Figure 1(a). The remaining p orbital is perpendicular to the honeycomb lattice and it forms π bond, which is hybridized with other atoms to a π and π^* bands. The extraordinary electronic properties of graphene are due to these orbitals. [26] Figure 1(b) shows the Brillouin zone (BZ) of graphene with high symmetry points. Most interesting points are at the corners of the BZ, K and K' points or Dirac points, where the valence and conduction bands touch. At low energies around these points the dispersion is linear, and the charge carriers can be described with the Dirac equation rather than the

Schrödinger equation. [1, 27] Graphene exhibits ballistic transport resulting into extremely high mobilities, even about 200000 $cm^2V^{-1}s^{-1}$ in optimal conditions (suspended graphene, low carrier density and low temperature). [28, 29]

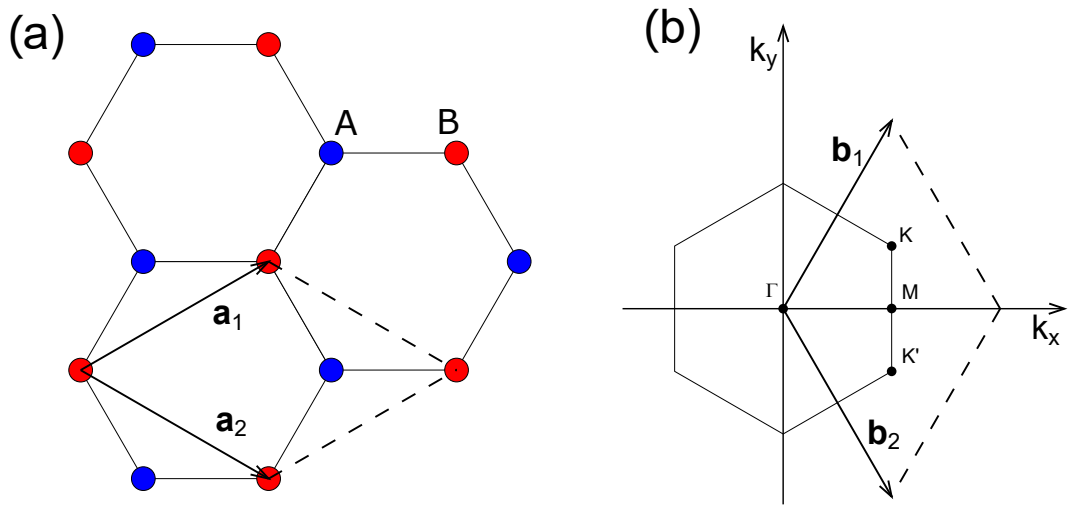

FIGURE 1 (a) Honeycomb lattice structure of graphene with lattice vectors $\mathbf{a}_1$ and $\mathbf{a}_2$. Two sublattices are marked A and B. (b) Corresponding Brillouin zone, showing reciprocal lattice vectors $\mathbf{b}_1$ and $\mathbf{b}_2$, and high symmetry points Γ, M and K.

In the context of this study, mechanical and optical properties are the most relevant graphene properties. As mentioned above, graphene has gained plenty of attention due to its mechanical properties. Utilizing nanoindentation, Lee et al. were the first to measure graphene's intrinsic strength to be 130 GPa. [13] Popularized works often cite this value and the fact that it is over 200 times larger than with the strongest steel. [30] Graphene is very stiff in the in-plane direction, but as an atomically thin material, it is also very bendable out-of-plane. In the same study by Lee et al. two-dimensional elastic modulus was measured to be 340 N/m. If the thickness of graphene is assumed to be 0.335 nm, which is the interlayer separation in graphite, [31] one receives 1 TPa for Young's modulus, which is about five times larger than with steel. [32] As a very stiff and strong material but also bendable material, it is no wonder that graphene has been thought to be used for example in bendable and stretchable electrodes. [33–36] These electrodes would also be transparent, since graphene is 97.7 % transparent trough the entire visible range. [16] Also, its reflectivity is very low ($< 0.1\%$). [37] Pristine graphene is not luminescent, though luminescence can be measured for example from graphene quantum dots [38] or from graphene under heavy electrostatic doping. [39] As for plasmonics, a direct light absorption by plasmons is not possible because of large momentum mismatch, [40] but it becomes possible for example by using grating structures or nanoribbons.

Structural defects of semiconductor materials strongly affect their proper-

ties. [41] Graphene is no exception to this. For example, while defect-free graphene is chemically quite inert, defects increase its reactivity, amount of increase being different depending on type of the defects. [42] Even though the most impressive properties of graphene are found from pristine graphene, for some applications graphene has to be defected. [43] Defects can be created by chemical treatments, plasma treatment and different beam irradiation methods, [44, 45] all of these having their own pros and cons. In order to effectively control the properties, a good defect creation method should be able to control the defect creation, both in defect amount and in position of the sample.

This study is centered on patterning of graphene using a laser patterning method called optical forging. In this method femtosecond pulsed laser irradiation causes lattice defects to the graphene, which results into graphene bulging from the surface into three-dimensional structures in a way that is reminiscent to shaping a sheet of metal with a hammer, hence the name optical forging. Patterns that form using optical forging method can be drawn in various shapes and their heights can be controlled by exposure parameters. Optical forging causes defect formation in the graphene lattice. A proposed explanation of the patterns is local lattice expansion caused by the changed defect density. Optically forging alters optical properties of graphene, making it more reflective and also photoluminescent. This also changes mechanical properties of graphene, increasing its bending stiffness up to five orders of magnitude relative to pristine graphene, and decreasing its 2D elastic modulus.

My part of studying graphene and optical forging has been experimental work. For the work presented here, I have been responsible of graphene synthesis development and fabrication of a vast majority of the graphene samples used in studies presented here. I have made most of the microscopic and spectroscopic characterizations and data analysis thereof, while relying other peoples work on operation of femtosecond laser setup as well as computational and theoretical work. This thesis is constructed as follows. In chapter 2, I describe the most important methods that were used to fabricate the graphene samples. In chapter 3, characterization methods and tools essential to the sample analysis are presented. Chapter 4 presents the laser modification technique of optical forging and describes how this modifies the structure of graphene a bit more deeply than in published articles. Details of how optical forging alters the optical and mechanical properties of graphene is presented in chapter 5. Chapter 6 summarizes the work and presents conclusions and future perspectives to optically forged graphene. Published articles are reprinted at the very end of this book.

2 FABRICATION OF GRAPHENE

Single layer graphene can be fabricated in many ways. In its simplest form, graphene can be fabricated just with adhesive tape and a piece of graphite. In this method, graphite is first peeled with the tape, which leaves quite thick layers of graphite to the tape. Then the sheared graphite layers are thinned by consecutively peeling the previous layer and finally the tape is pressed to the substrate and slowly peeled off, hopefully leaving some single layer regions on the substrate. The sample has to be then inspected with a microscope to find the sparse single layer regions and confirm the number of layers by Raman spectroscopy, making it quite labor intensive. Mechanical exfoliation, or in other words "the Scotch tape method", was the original method to make graphene and is still used to make the cleanest samples with least amount of both lattice defects and residues of any kind. [46, 47]

While mechanical exfoliation is still a good method to fabricate pure and defect free graphene, the drawbacks are that it normally yields only small regions of single layer crystals and is difficult to scale up. Graphene can be manufactured in bulk amounts by liquid exfoliation [48, 49] or graphene oxide reduction, [50] though the quality of the resulting graphene might not be very good. A method for lower quantity but higher quality (and expensive) graphene is high temperature graphitization of SiC. [51] However, the most common fabrication method is chemical vapor deposition (CVD).

In this chapter the most important methods in graphene fabrication are presented. Detailed sample fabrication details are in appendix 1.

2.1 Chemical Vapor Deposition

Chemical vapor deposition has become one of the most used methods to synthesize graphene, since it can provide large crystalline size and low amount of defects. [52–55] In CVD gaseous or vaporized precursors are used to synthesize solid product usually at elevated temperatures. [56] Methane is an often-used

precursor when synthesizing graphene, but almost any carbon containing material could be used. Alternative gaseous precursors include ethylene [57,58] and acetylene. [59] Graphene has also been produced using liquid precursors, such as methanol, ethanol, propanol [60] and benzene [61] and solid precursors like PMMA [62] and polystyrene [61,63] and even some more bizarre precursors such as cockroach leg. [64] However, at least in research purposes, most often the most important considerations in the precursor material are purity and possibility to control the carbon concentration, both of which are easily achieved with gaseous precursors. Additionally, as the most simple hydrocarbon, methane has already been used in many computational studies about CVD of graphene, making it an attractive choice as the precursor.

Catalyst material is another important consideration in graphene CVD. Copper is by far the most common catalyst, since it is cheap and it usually self-limits the graphene growth to only one layer. [65–67] Many other transition metals, such as gold, [68] ruthenium, [69,70] iridium, [71–73] rhodium, [74] rhenium, [75] cobalt, [76–78] palladium, [79, 80] platinum [81–84] and others [85] have been used for graphene synthesis. In addition, nickel can be used, though it results in mostly double-layer graphene because of high carbon solubility to nickel at elevated temperatures, causing the carbon to precipitate onto the surface once the sample is cooled. [86–89] Additionally, in some studies alloys, like Cu-Ni [90,91] and Ni-Mo, [92] have also been used successfully as the catalyst surface.

The mechanism of graphene growth is shown in Figure 2(a). The chamber is usually heated near 1000 °C, as the CH_4 dissociation requires plenty of energy, though additionally it requires a catalyst. The adsorbed and at least partially dehydrogenated carbon species can migrate around the surface, coalesce and grow into graphene crystals. According to computational studies, the methane precursor does not completely dehydrogenate into atomic carbon, but partially dehydrogenated carbon species migrate on the surface, though more likely they form dimers, trimers and even larger clusters, which can also migrate around the surface and find larger domains. [93,94] Especially on Cu(111) the larger clusters are important intermediates. [95] The growth is often promoted by impurities on the copper surface, which act as nucleation sites, where the carbon atoms can attach and the graphene domain grows. The growth is not always strictly self-limiting even on copper, as Figures 2(b) and 2(c) show. These are scanning electron microscope (SEM) images of graphene on copper after the CVD synthesis. The dark lines in Figures 2(b) and 2(c) are graphene wrinkles that form during cooling of the sample, caused by different thermal expansion coefficients between graphene and copper. [65,96] In Figure 2(b) double layer domains (darker grey hexagon-like structures) have grown on single layer graphene, which spans the entire sample. Note that there are impurity particles (white dots) present inside each of the double layer domains. Figure 2(c) shows another, much larger domain, where even a third layer has grown and multiple particles are located near the center. By using isotope labeling, studies have clearly showed that the domains grow outwards from nucleation sites. [88,97,98] Additionally, most of the studies conclude that under normal conditions any double or multilayer domains actually grow

between the copper surface and the much larger single layer domain, [97–99] although some have argued the opposite. [100] The growth of additional layers is largely suppressed by the single layer domain, which prevents the breaking of the CH_4 by blocking access to the catalytic copper. However, it is possible to grow bilayers deliberately on graphene with a multi-zone furnace system, where carbon species are catalytically activated on a different Cu surface and let to flow downstream onto a fully grown graphene surface. [101] Hydrogen has also an important role in the graphene synthesis, although it is possible to grow graphene without it. [102] Hydrogen etches the growing graphene domains, especially the defected edges, which improves the quality of resulting graphene, but it also acts as a cocatalyst for active carbon species. [103–105]

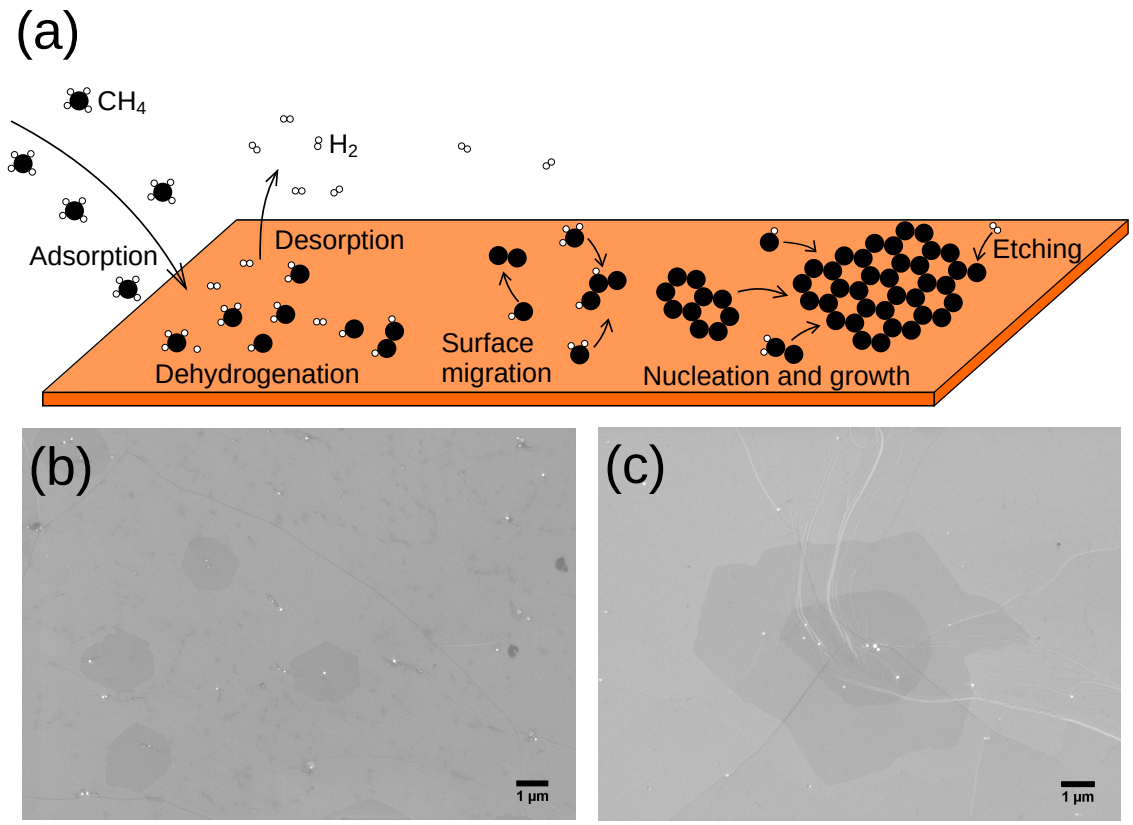

FIGURE 2 a) Schematic of graphene CVD growth mechanism. b,c) SEM images of graphene synthesized onto copper thin films using CVD with visible double layer and multilayer domains.

The self-limiting quality of copper can also be broken if carbon concentration in the gas flow is too high, especially with atmospheric pressure chemical vapor deposition (APCVD). [106] Therefore the growth is done in quite low concentrations and in APCVD the majority of the gas is usually argon. [107–110] With too low carbon concentration the hydrogen etching rate is comparable to grain growth rate and graphene grain sizes remain small and unconnected. Additionally, if the growth time increases too much, copper evaporation and copper film dewetting start to become problematic. Naturally, this is an issue only with

thin film catalyst, not with copper foil.

While CVD grown graphene domains are often large compared to exfoliated graphene domains, the graphene layers grown with CVD are oftentimes polycrystalline. [111] Grain boundaries have been shown to deteriorate graphene's electronic, [112–115] thermal [116–118] and mechanical [119, 120] properties, so fabricating graphene with large grain size is preferable. The best way to increase the grain size of CVD graphene is to decrease nucleation density, and, since impurities often cause nucleation, reducing the impurity amount is one of the best ways to achieve this. Obviously, using high purity copper is helpful, but beyond this, one of the most used methods for suppressing nucleation is long time annealing of the catalyst at high temperatures, which removes residues and increases the crystallinity of copper. [121, 122]

Crystal orientation of the catalyst surface is also a contributing factor. The most used catalyst material in publications is foil, where the copper is polycrystalline and often the grain sizes are quite small, typically in tens of microns. However, there is evidence that using Cu(111) improves the quality of CVD grown graphene due to small lattice mismatch between graphene and copper. [123–127] This also helps good quality large area graphene crystal growth, since the crystals that are grown on Cu(111) are much more likely to be aligned, making a grain boundary free fusion of separate crystals possible. [128] Also, the growth dynamics differ a bit on different crystal orientations, meaning that if the catalyst has only single orientation, variations within the sample are smaller. Copper (and nickel) surfaces with (111) orientation can be routinely prepared by annealing the metal thin films on α-Al_2O_3 (0001) (also known as c-plane sapphire) substrates. [125–127] Cu(111) can be achieved already during the deposition of the copper, [125] but it is also possible to increase copper crystal size during annealing after the deposition through a process called secondary grain growth. [129] Recently large scale Cu(111) crystals were prepared from commercial polycrystalline copper foils by contact-free annealing, [130] which enabled adlayer-free graphene synthesis. [131]

Another method to decrease the amount of nucleation sites is to oxidize the copper surface. At high temperatures, oxygen can efficiently clean impurities and excess carbon from the copper, leading to lower nucleation density. [132–135] When the foils are oxidized in high temperature the oxygen can dissolve into the copper and stay in the foil in small quantities, affecting the growth even if the growth is done at high temperatures and relatively high hydrogen concentration. [136] With some systems it is not even necessary to really oxidize the copper or add oxygen into the gas flow, but residual oxygen can be used to decrease the nucleation density by shutting down the hydrogen flow during annealing. [137,138] Additionally, oxygen lowers the energy barrier for CH_4 decomposition [139, 140] and carbon attachment to the graphene domain, [141] which leads to faster graphene growth. [141, 142] Even small amounts of oxygen (down to the ppb regime) can affect the growth, [141,143–146] however, at high enough oxygen concentration the domain growth rate decreases due to oxygen's contribution to etching the graphene. [145,146] Interestingly, when oxygen residues are removed,

more multilayer domains are grown, even with LPCVD under hydrogen containing gas mixture, indicating that in normal growth oxygen promoted etching is very important. [145] Some studies conclude that hydrogen does not even etch graphene on its own without small amounts of oxygen. [145, 147] Additionally, water as has a similar oxidizing effect during the growth. [142] These residual oxygen and water impurities in gas flow or in the copper catalyst are likely to be the reason for some discrepancies and inconsistencies in CVD synthesis results that are reported from different laboratories.

Pressure is another important CVD parameter to consider. Initially graphene was synthesized with low pressure CVD (LPCVD), though as mentioned earlier, it is possible to synthesize good quality single layer graphene with APCVD as well. [125,126,131,148] Changing the pressure does change the growth dynamics, which can be seen from different shapes in graphene domains grown under different pressures. [149] For this reason the gas concentrations have to be adjusted correctly for the pressure that is being used. With APCVD a suitable carbon concentration for single layer graphene synthesis is in the order of tens to hundreds of parts per million of the total gas flow volume. [103, 106, 148] The exact amount seems to vary a bit, likely due to the oxidizing residues mentioned above.

Temperature is also an important parameter in CVD. With APCVD, higher temperature has been reported to improve the quality of graphene. [126] Additionally, higher temperatures both decrease the amount of nucleation sites and increase the graphene crystal size (under same growth time), [150, 151] leading to lower amount and size of multilayer domains. [152] The melting temperature of copper is 1084 °C, which oftentimes sets the maximum temperature. That said, CVD of graphene is also possible using liquid copper catalyst, [153, 154] as well as some other liquid materials. [155, 156] Naturally, the sample holder has to be able to hold liquid copper, making this a bit more complicated method compared to CVD with solid copper. While in general higher temperatures result into better graphene, there are also some low-temperature CVD methods to synthesize graphene, such as using toluene with Cu catalyst at 600 °C [157] or methane with gallium catalyst even as low as 50 °C, [158] but the quality of graphene is not the best with these low temperature methods.

Another approach to decrease carbon concentration and thus to have a better control of the growth is to use a copper enclosure (or a pocket). With this method, the copper foil is folded and crimped around the edges, so that carbon concentration is greatly diminished inside the enclosure. [66, 159] With this approach, results of the process are completely different on the inside and outside surfaces of the foil with inside surface being covered mostly by single layer graphene and outside surface growing multilayers. [160, 161] The mechanism behind this is explained by carbon being able to diffuse through the copper, despite of the low carbon solubility, forming predominantly single layers on the inside and multilayers on the outside. [162] This method is actually more often targeted to fabricate large double layer domains, [160–162] but effective single layer growths have been reported with some tweaks to the basic idea. For example, Phan et al. fabricated large single layer graphene crystals by making holes in

the copper foil. [163] In a different study, the copper foil was oxidized leading to a single layer growth that was fast with low nucleation density. [164] Another modification to the method is to add a piece of tungsten inside the enclosure, which acts as a carbon sink and helps to limit the growth to just one layer. [165] In a different study the outer side of the foil was coated with tungsten or molybdenum, which act both as a diffusion barrier and a carbon sink, leading to growth of millimeter scale single layer graphene crystals. [166] Recently a tungsten coating on the other side of a normal unfolded copper foil was used effectively to limit the growth to a single layer. [167] Additional metal coating has also been used in an opposite way: by depositing nickel to one side, uniform multilayer domains were grown. [168] Yet another slightly different approach to decrease graphene nucleation is to treat the copper surface with melamine. [169] An important note when working with foils is that, in addition to chemical cleaning of the surfaces, the roughness of the foils needs to be decreased by electropolishing, which also improves the quality and uniformity of the graphene. [108, 170, 171]

As it can be gathered from everything written here so far, there are a plethora of alterations to the graphene CVD synthesis recipe on copper that was originally published by Li et al. [65] The important thing to keep in mind here is to think what the requirements for the graphene are going to be. For industrial applications, many of the methods mentioned above will not be feasible, for example, low-pressure methods are not very easy to integrate to an assembly line. If the need is for one device with "perfect" graphene for electronic measurements, CVD might still not be the best method at the moment, since CVD graphene has usually more defects than mechanically exfoliated graphene. Additionally, transferring the graphene from growth substrate to the final substrate introduces almost always residues, which will be talked about below. However, if there is a need for a large amount of samples, and the graphene quality does not have to be "perfect", many current CVD methods offer an attractive approach to achieve this goal.

2.2 Transfer

Transfer of graphene after the CVD synthesis from the catalyst surface onto a target substrate is one of the most important parts of graphene fabrication. Ideally, transfer should keep the graphene from crumpling or rolling into itself while not leaving residual material that would degrade the excellent properties of graphene. An often-used transfer method involves depositing polymer onto the graphene, etching the catalyst material and placing the released polymer/graphene stack onto the target substrate. However, as in CVD, there are many variations how the graphene transfer is done depending on sample requirements.

Using a polymer support layer on top of graphene during transfer is a very common technique. [86, 172–177] The purpose of the layer is to keep the graphene from crumpling or folding over itself, when the graphene is released from the catalyst surface. Figure 3 presents a schematic of a "normal" transfer

process. First the sample is spin-coated with a support polymer, poly(methyl methacrylate) (PMMA) being the most common support material. [178] Then the PMMA/graphene/Cu sample stack is placed to etchant bath, where the copper layer is etched leaving the PMMA/graphene stack floating on the liquid. The graphene surface is then washed from etchant residues with deionized water and placed onto the target substrate. The sample is let to dry on its own, or by baking it for a few minutes on a hot plate. Finally the PMMA layer is dissolved in acetone to leave graphene layer onto the target substrate.

While this process does enable the transfer of large graphene films onto different substrates, its main drawback is that PMMA residues are left behind, which degrade the properties of the resulting graphene. [176, 179] There are plenty of variations to each step of the "normal" transfer process in purpose of improving either purity of the final graphene or some other detail. One approach is to modify the transfer polymer so that it leaves less residues behind. These include adjusting the PMMA itself, for example by using smaller molecular size, [180] or depositing a second layer of PMMA onto the sample after transferring the graphene/PMMA stack onto the target substrate. [181] The PMMA can also be removed without using any solvents by annealing. [177] It is also possible to use a different transfer material altogether. Alternative polymers include poly(bisphenol A carbonate) (PC), [182–184] polyethylene terephthalate (PET), [174] poly(lactic acid) (PLA), [182] poly(phthalaldehyde) (PPA), [182] and polydimethylsiloxane (PDMS). [65, 185, 186] However, some of these materials are more difficult to use than PMMA, and while they can provide a cleaner transfer in some instances, they do not solve the residue issue completely.

Another approach is not to use polymers, but small molecule films as the support layer. Usually the goal of using these materials is lower adhesion and lower reactivity with graphene, which make the removal of the support film easier. For example, paraffin has been used as transfer material leading to lower doping than with standard PMMA transfer. [187, 188] Additionally, paraffin can be used make wrinkle-free graphene by relaxing the CVD induced strain when the transfer is made in warm water. [187, 188] Another small molecule material is rosin, which has the benefit of having small adhesion energy to graphene, which can yield clean and defect-free graphene. [189–191] A notable issue with small molecule films is that they are often mechanically weaker than polymer supports, which can be countered by depositing a polymer layer on top of the molecule film and using these double layer films as the support. [190] A slightly different approach when using non-polymer materials is to use a support material that is volatile and will sublimate at room temperature or when heated. With these materials, the resulting graphene is supposed to be free of residues, even without any chemical cleaning, however extra cleaning steps can still help. Examples of this type of sublimating materials that have been used in graphene transfer are cyclododecane, [192, 193] camphor, [194] pentacene, [195] naphthalene [196] and anthracene. [197]

Since polymer residues from transfer process are so hard to avoid, one approach is to not use a support polymer at all. This can be achieved using a special

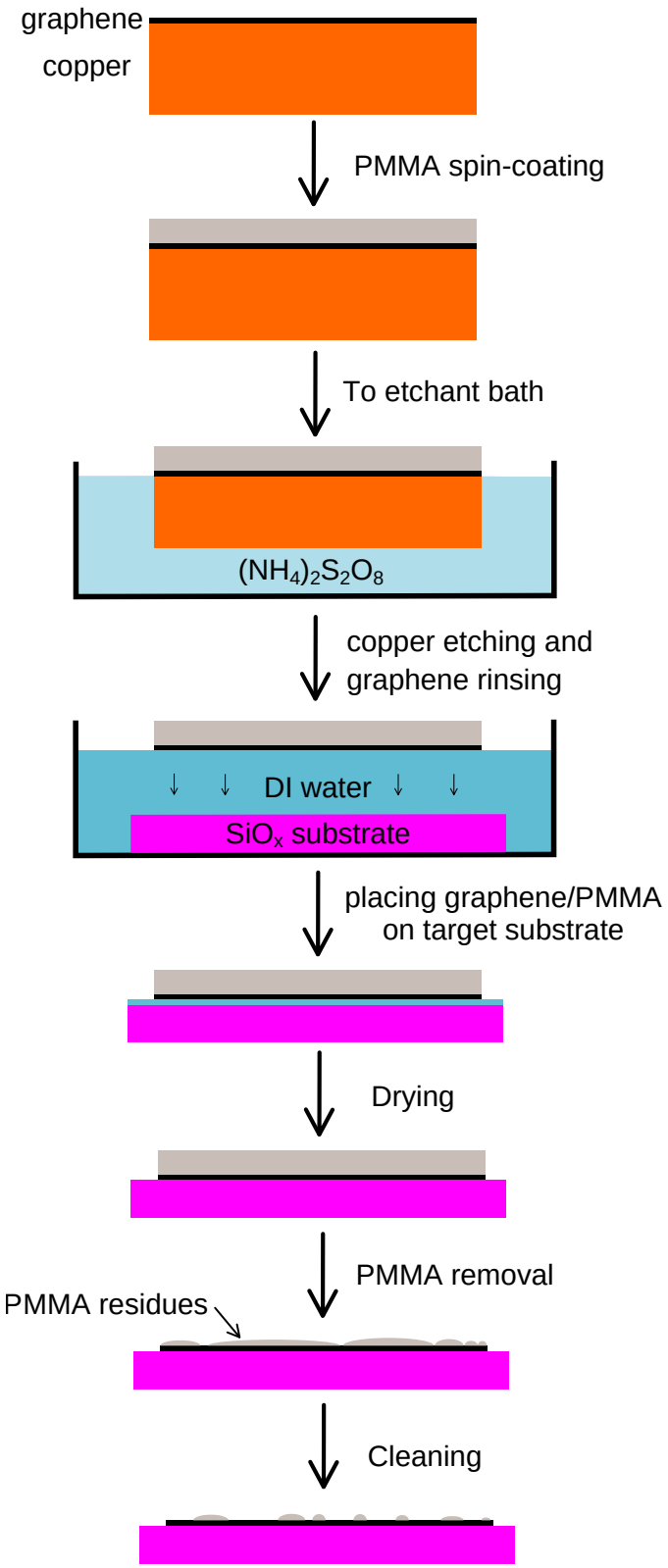

FIGURE 3 Schematic of the common graphene transfer process.

sample holder, which helps to prevent the crumpling and tearing of the graphene without the support layer. [198] Other support-free method reported is to bond graphene to the target by electrostatic charging before etching the catalyst. [199] While graphene transferred with these methods can be clean, it is difficult to do them without tearing the graphene.

Graphene can also be transferred using a so-called "bubble transfer" method. In this method, hydrogen bubbles are generated between graphene and the catalyst surface, which detaches the graphene. [81, 200–202] The bubbles are formed electrolytically between the graphene and the catalyst metal. Benefits in bubble transfer are that it is fast, and since the metal layer is not etched, it can potentially be reused as a CVD catalyst. This was originally reported with platinum, [81] but using copper is also possible, though in this case the copper is oxidized and partially dissolved. [200–202] Bubble transfer can yield graphene with less metal residues, but it does not solve the problem with support layer residues. It is possible to do the bubble transfer without the support layer, but then it is quite difficult to prevent the graphene layer from crumpling. However, even with the support layer, the H_2 bubbles can cause defects and cracks in graphene. In a modified version of the bubble transfer, called "bubble-free transfer", the copper is oxidized after the CVD. Then, during electrolysis the potential is kept lower than in bubble transfer in order not to create the H_2 bubbles, but high enough to cause a reduction of the copper oxides between graphene and the copper surface, which in turn causes the delamination of graphene. [203] In a similar study, the copper surface is oxidized during the transfer by oxygen dissolved in the electrolyte solution, which is then then reduced, releasing graphene. [204] Yet another transfer method is "soaking transfer", where after CVD the graphene is coated with PMMA and the copper is peeled from the graphene in 90 °C water, however graphene seems to tear easily with this method. [205]

Another transfer approach is dry transfer. This term means doing either the graphene release from the metal surface or support layer removal from the graphene without wet etching, usually by peeling. In some cases, when both of these are done without etching, the method is called "all-dry" or "completely-dry" transfer to draw distinction to the case when only one of them is, which is sometimes called "semi-dry" transfer. With dry transfer, the residue amounts can be lower than in typical wet transfer, especially when talking about residual water between graphene and the substrate, which can be an issue with the wet transfer. However, a difficulty in this process is that the graphene can tear or transfer only partially if the adhesion energies are not well adjusted. Additionally, especially if the adhesion energies are similar, graphene is not necessarily residue-free. Graphene has a somewhat high adhesion to copper. [206] This means that it is difficult to design the materials so that detachment and consequent attachement to the target substrate work with high yield. Therefore, dry transfer is easier when the target material is for example a polymer or boron nitride film, which have good adhesion to graphene when they are pressed together and heated. [207–209] Semi-dry transfers to silicon have been reported with SiO_2/Si substrates by etching the copper [186] and by oxidizing the copper after CVD using water vapor,

which makes it easier to delaminate the graphene. [210] All-dry transfer has been successful by synthesizing graphene on germanium (110). Ge(110) has lower adhesion to graphene than most other growth substrates making it easier to design adhesions so that the graphene detaches both from germanium and the support layer. [206]

Another notable matter in graphene transfer is that fabricating suspended graphene samples brings additional complications. Even though graphene is an extraordinarily strong material relative to its thickness, it can be easily broken if macroscopic forces are exerted to it, e.g. surface tension of a drying water droplet. Therefore, it can be beneficial to use the critical point drying (CPD) technique when removing the PMMA layer. [28, 211, 212] This means drying the sample by transforming the liquid first into supercritical fluid before turning it to gas. Practically this means that after dissolving the PMMA the fluid is changed into a suitable drying fluid, such as carbon dioxide, which is then heated in a pressurized chamber to make the fluid supercritical. Pressure is then released by slowly venting the chamber. This way the system does not cross any phase boundaries and the sample is safe from forces caused by surface tension. Although this is not a necessary method for making suspended graphene, it is a gentler method than just rinsing the sample in acetone.

2.3 Cleaning

Since the purity of graphene is often an issue and normal synthesis and transfer methods unavoidably leave residues, many methods have been proposed to clean the graphene afterwards. One of the reported wet cleaning methods is to use a modified RCA cleaning after releasing the graphene/PMMA stack from copper. [176] This method is designed to clean the underside of the graphene from residues, such as copper particles, and does not help with the residues caused by the support layer. As for the polymer residues, as mentioned above, most often the solvent to strip the PMMA layer is acetone, but other solvents, such as chloroform [182, 213] and acetic acid, [214] have also been used. These have been reported to perhaps provide cleaner graphene, but they cannot clean all the PMMA residues, and chloroform has been reported to intercalate between graphene and the substrate and cause large doping. [215] With acetone, a different PMMA removal is to do UV exposure of the PMMA during transfer, which increases its solubility and leads to cleaner graphene. [216] Another method is to use acetone vapor by suspending the PMMA/graphene/substrate over a hot acetone bath and letting acetone vapor to condense on the sample. Acetone dissolves the PMMA and droplets drop down while fresh solvent condenses on the sample, which has been reported to provide clean graphene, although the process is slow. [92]

However, wet methods alone are not enough to clean graphene from the transfer residues. Therefore many other cleaning methods have been tried, one

of the most popular methods being thermal annealing. This has been studied in various different environments, including vacuum, [213,217,218] Ar/H_2 mixture [219] and carbon dioxide. [220] In another study, the graphene sample was embedded into active carbon, which absorbs the evaporated PMMA residues improving the cleaning. [197, 221] Removal of the PMMA residues can also be enhanced catalytically by using platinum or palladium metals as catalyst during the annealing. [197,222] All of these annealing methods do some cleaning of the residual PMMA, however, none of them provide completely clean graphene. In fact, thermal annealing can cause PMMA residues to bond covalently with the graphene, making their total removal virtually impossible, [223] though at least some of these post-annealing residues can be cleaned electrolytically. [224] A drawback in thermal annealing is that it also introduces p-type doping when graphene is transferred onto Si/SiO_2 substrates. [213,219,225]

As for other dry cleaning methods, there have been various different approaches for cleaning graphene using plasma treatments. [226–228] While plasmas can clean the residues, the processes need to be very well optimized in order to preserve the graphene itself from any defects. As for a bit more specialized techniques, there are also several beam based methods for cleaning, for example by using argon cluster ion beam [229] and helium ion beam. [230] There also exists several laser cleaning methods capable of removing most of the transfer residues. [231,232] As for simple cleaning methods, it can be done with a rubbing cloth, where electrostatic forces draw the residues from the graphene surface into the cloth. [233]

Another cleaning approach is to do it mechanically, for example by sweeping the residues with AFM probe [234–236] or with nanomanipulators inside a SEM system. [237] These methods have been shown to work quite well in cleaning graphene devices, but they require specific equipment and are capable of cleaning only limited areas.

Despite the availability of many different cleaning methods, it is still difficult to achieve clean graphene. Therefore electronic devices made from graphene are cleaned with current annealing. [238,239] This means driving a large current density through the sample, which heats the sample until removing the residues. Current annealing is often done for all samples whether they are made using CVD, mechanical exfoliation or other methods, since it removes also molecules adsorbed from air, which can deteriorate the transport properties. This is a convenient method when the device is complete, as it can be done, for example, in a cryostat.

A quite recent development in making cleaner graphene is to tackle the residue issue already before the transfer. With normal graphene CVD synthesis, some amounts of amorphous carbon are unavoidably deposited on the sample. Perhaps the most important aspect in considering the reduction of deposited amorphous carbon is the amount of copper vapor in the gas flow. When only the flat copper surface is used as the catalyst, the amount of copper vapor decreases as the graphene area grows during synthesis. As mentioned above, copper catalyses the dehydrogenation of the hydrocarbon precursors, but the catalytic activity

is diminished as the amount of copper vapor in the gas stream decreases. This on the other hand promotes the formation of amorphous carbon. The copper vapor amount has been successfully increased by using copper foam on top of the copper catalyst surface [240] and by using copper(II) acetate as the precursor material. [241] The amorphous carbon can be also removed after the synthesis by using CO_2 annealing. [242] All of these methods have been reported to work well in achieving clean graphene. Interestingly, graphene samples produced with these methods are very clean also after a normal PMMA transfer without any extra cleaning steps. This has been explained by amorphous carbon acting as an "anchor" which helps the PMMA residues to stick on the graphene. Thus, when the amorphous carbon is removed, also the PMMA detaches from the graphene surface easily.

Similarly to various CVD methods, there is also a wide variety of different transfer and cleaning methods, and one should carefully pick which method to use according to the scale of the sample throughput and the requirements of the final graphene product. For example, mechanical cleaning of graphene with AFM equipment is not going to be used in large scale cleaning. Also, dissolving the copper layer is not feasible in industrial scale, since using huge amounts of copper is expensive, and additionally, it would create large quantities of hazardous chemical waste. Therefore any transfer method that enable reusable catalyst surfaces are highly beneficial.

3 CHARACTERIZATION METHODS

Having a combination of good characterization methods is crucial, whether checking the quality of graphene after synthesis or analyzing the effects of processing methods to graphene. Since graphene is only surface, it is important that the technique is surface sensitive, while being gentle enough not to create defects to the surface layer. Additionally, the ability to assess the number of graphene layers, defect amounts, doping and strain is important. The main characterization methods used in this study were Atomic Force Microscopy, Raman spectroscopy and, in the case of mechanical properties, nanoindentation. Other methods, such as Scanning Electron Microscopy (SEM), can provide high resolution, but does not offer much additional information to AFM and Raman. Additionally, electron microscopy techniques are likely to deposit amorphous carbon contaminants onto samples, [243,244] and therefore they were not used for characterizations.

3.1 Atomic Force Microscopy

Atomic Force Microscopy (AFM) is a high-resolution microscopy technique. [245] In AFM a very sharp tip is used to probe interatomic forces between the tip and sample in order to record topography of the sample. AFM can be used in different modes that slightly vary in how they function. Contact mode, where the tip is constantly "touching" the sample surface was one of the first modes. It offers good resolution, but causes large lateral forces, which can cause damages to the sample and increase tip wear. [246] A more gentle imaging mode is tapping mode, in which the cantilever of the probe is set to oscillate near its resonance frequency and the topography information is deduced (usually) from the amplitude change of oscillation. While the oscillating tip taps the sample, the contact is softer and shorter in duration and therefore imaging is gentler than in the contact mode, leading to longer tip lifetimes and less damage to the sample. [247–249]

The imaging mode used in this study was PeakForce Tapping (PFT) mode, [250] which is trademarked by Bruker. Instead of driving the probe near the reso-

nance frequency of the cantilever, in PFT the cantilever is not driven to oscillate at all. Instead, the tapping motion comes from the z-piezo. During each tapping cycle, the system records the deflection curve of the cantilever, which can be transformed to force curve when the cantilever spring constant is known. Therefore, PeakForce Tapping mode is much closer to force volume mapping than tapping mode. The difference between force volume mapping and PFT is that in force volume the drive signal is a triangle wave, while in PFT it is sinusoidal. This allows a better force control, since with sinusoidal signal the the z motion of the tip decreases already when approaching the sample surface, while with triangle wave the directional changes are ideally instantaneous. PFT is gentle enough to image biological samples, such as living cells [251] and DNA [252], without damaging them while still having good resolution.

3.2 Nanoindentation

Nanoindentation is a method used to measure mechanical properties of a sample. This can be done with a specialized nanoindentation equipment, but oftentimes AFM systems are capable of doing these measurements. The method involves pressing of very hard indenter tip into the material being measured and recording force vs. displacement curve. [253–255] Analyzing the force curve allows to determine for example Young's modulus of the sample material. The mechanical properties of graphene can also be measured with nanoindentation, although the technique is slightly different if graphene is suspended over an opening. In this case the probe does not have to be as hard nor stiff and the model to calculate the mechanical parameters is different. Lee et al. were the first to measure single layer graphene using this method. [13] To calculate the mechanical parameters from the force-displacement data they modelled the graphene membrane as a linear isotropic elastic material that is circularly clamped. When the loading happens at the center of a circular membrane the force-displacement behaviour is characterized by equation [256, 257]

$$F = \left(\sigma_0^{2\mathrm{D}}\pi\right)\delta + \left(\frac{E^{2\mathrm{D}}q^3}{R^2}\right)\delta^3, \tag{1}$$

where F is the indentation force, R is the radius of the membrane, $\sigma_0^{2\mathrm{D}}$ is the film pretension, δ is the indentation depth, $E^{2\mathrm{D}}$ is the two-dimensional elastic modulus, and $q = 1/\left(1.05 - 0.15\nu - 0.16\nu^2\right)$ is a dimensionless constant, where ν is the Poisson's ratio. Young's modulus ($E^{3\mathrm{D}}$) can be calculated from $E^{2\mathrm{D}}$ using relation $E^{3\mathrm{D}} = E^{2\mathrm{D}}/t$, where t is the thickness of the material. Because of this relation $E^{2\mathrm{D}}$ is sometimes called 2D Young's modulus but here it is called 2D elastic modulus to draw a distinction from more commonly used 3D Young's modulus. With graphene and other 2D materials $E^{2\mathrm{D}}$ is more a valid value to report. This is largely because talking about 3D Young's modulus, i.e. a bulk material property, of a 2D material is a bit problematic. Another reason is that determination

of exact thicknesses of these materials is not straightforward. For example, direct measurements of single layer graphene thicknesses often yield values between $0.4 - 1.7$ nm, [258] and this can vary depending on the measurement technique. Therefore, instead of measuring the thickness from each sample, it is often taken to be 0.335 nm, which is the layer separation in graphite. It can be questioned how meaningful it is to define graphene thickness to be graphite layer separation, since their environments are very different. However, in this thesis the focus is on E^{2D}, but the E^{3D} values are also mentioned, since it is comparable with other materials and also since many people as accustomed to think Young's modulus in units of Pa.

It is assumed in equation 1 that the bending stiffness of graphene is negligible. Since graphene is an atomically thin material, this is a valid assumption for the vast majority of cases. Originally bending stiffness of graphene was determined from phonon spectrum of pyrolytic graphite to be 1.2 eV. [259] Later, several studies have determined the bending stiffness to be in the range of 1-2 eV using various computational methods. [260–268] Lindahl et. al measured bending stiffness of 7.1 eV from single layer graphene with an electrostatic actuator device, although their error margin was large. [269] However, thermal fluctuations and static rippling of the films can increase bending stiffness of graphene and other thin films. [270–273] Highest bending stiffness value measured for rippled graphene outside of our work has been in the keV range. [274]

The bending stiffness might not be negligibly small when the material has more thickness, or when for example when the sample morphology increases the stiffness. When the bending stiffness is non-negligible, the force-displacement behaviour is [275]

$$F = \left(\frac{16\pi D}{R^2} + \sigma_0^{2D}\pi\right)\delta + \left(\frac{E^{2D}q^3}{R^2}\right)\delta^3, \tag{2}$$

where D is the bending stiffness.

A difficulty in the analysis of these force-displacement curves is the determination of zero point of indentation, i.e. the point where the tip is touching the sample but not yet exerting any force to it. To overcome this issue, by writing $F = f - f_0$ and $\delta = Z - \delta_0$, equation 2 can be modified to:

$$f - f_0 = k_1 (Z - \delta_0) + k_2 (Z - \delta_0)^3, \tag{3}$$

where f is the measured force, Z the absolute piezo movement in z direction, f_0 and δ_0 are zero points for force and indentation respectively. $k_1 = 16\pi D/R^2 + \sigma_0^{2D}\pi$ and $k_2 = E^{2D}q^3/R^2$ are linear and cubic coefficients. For fitting, this can be written as

$$f = \left(f_0 - k_1\delta_0 - k_2{\delta_0}^3\right) + \left(k_1 + 3k_2{\delta_0}^2\right) Z - (3k_2\delta_0) Z^2 + k_2 Z^3. \tag{4}$$

By using this fitting function human input is not required, but the zero point values become fitting parameters f_0 and δ_0. This approach has been used also in previous studies. [276, 277]

A schematic of the cantilever flexing and its relation to the force curve is presented in Figure 4. When the tip is far away from the sample (i) the cantilever is not flexing at all and thus the detected force is zero. Once the tip gets near the sample (ii), attractive van der Waals interactions pull the tip into contact with the sample, flexing the cantilever downwards and causing the negative force regime. This phenomenon where the force dips below zero is sometimes called "snap-in" or "snap-to-contact". When the probe is pressed further down, repulsive forces increase until the cantilever is again straight and the force is zero (iii). This point is sometimes called the zero point of indentation. After this the force keeps increasing as the tip is pressed to the sample (iv). After the zero point the force curve is following equation 2, however the indentation force has to be high enough to cause enough deformation for the calculations to be accurate. In article [AV] the force was limited to 500 nN, which is less than the force expected to break the membranes, but large enough to cause enough deformation.

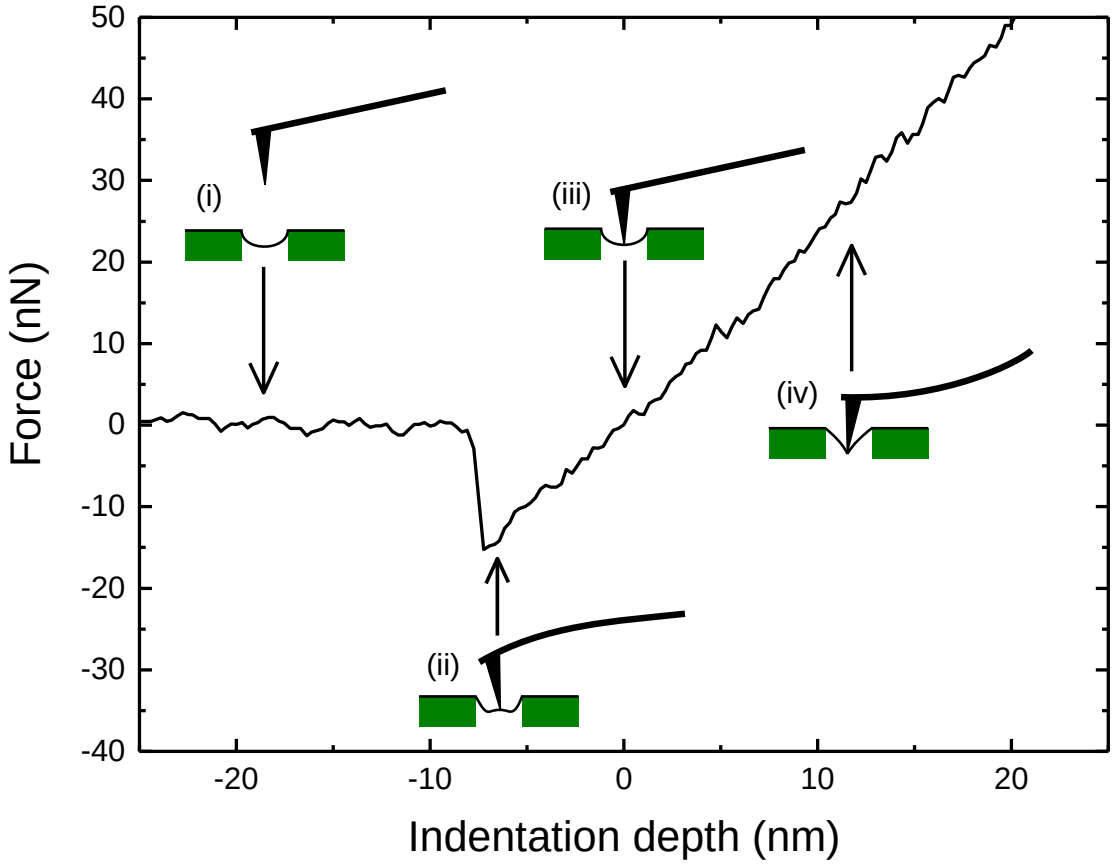

FIGURE 4 Indentation curve of optically forged graphene sample. Pictures in the graph show cantilever flexing at the specific point.

3.3 Raman spectroscopy

Raman scattering is inelastic scattering of light, where the photons are scattered by phonons. [278] In Stokes Raman scattering an incident photon excites an electron hole pair, which then scatters with a phonon before relaxation of the electron hole pair and emission of another photon. The energy of the scattered photon is lowered by the energy of the phonon, which can be detected spectroscopically if the light source is monochromatic. By convention, Raman spectrum is most often presented in units of cm^{-1} and relative to the Rayleigh peak (elastically scattered light). Oftentimes the electron is not excited to any real electronic or vibrational state, but to a very short-lived virtual state. However, when the transition is to a stationary state, the process is resonant and the intensity is strongly enhanced.

3.3.1 Raman spectrum of graphene

Raman spectroscopy is one of the most important graphene characterization methods. By analyzing the peak positions, widths and intensities, it is possible to extract information about number of layers, doping, strain and defects in graphene. Additionally, it is nondestructive and does not require vacuum conditions, like, for example, electron microscopes do.

Figure 5 shows a Raman spectrum of single layer graphene with the main Raman bands labeled and schematics of main Raman processes. [279, 280] The G band at about 1580 cm^{-1} originates from sp^2 C-C bond stretching. Mechanism is presented in Figure 5(b). It comes from E_{2g} mode iTO and iLO phonons in the center of the Brillouin zone, or the Γ point of the Brillouin zone shown in Figure 1(b). The G band is present in all sp^2 carbon materials, including carbon nanotubes, graphite and amorphous carbon, although the band shapes vary between these. [281] The D band at about 1350 cm^{-1} originates from the breathing mode of the carbon rings, corresponding to iTO phonons at the Brillouin zone corner, the K point. The mechanism is shown if Figure 5(c). The excited electron is scattered to K' and requires an elastic backscattering with a defect to fulfill momentum conservation and therefore to be active. Two of the transitions are to stationary electronic states, making the process double resonant. [282] Since the process connects two points at nonequivalent K, it is called intervalley process. The D' band at about 1620 cm^{-1} (Figure 5(d) has very similar mechanism to the D band, also being double resonant and requiring defect backscattering. It is associated to iLO phonon mode and the process is intra-valley, since it connects the points in the same K point. The 2D band at about 2700 cm^{-1} (Figure 5(e) shares similar pathway as D. It is also double resonant, but instead of satisfying the momentum conservation by defect backscattering, its mechanism involves two iTO phonons with opposite momentum. The shape of the 2D band is defined by a single Lorentzian when graphene is single layered, but with extra layers the 2D band splits into four sub-bands, which enables the determination of whether the graphene is single layered. [283] In single layer graphene the 2D band is of-

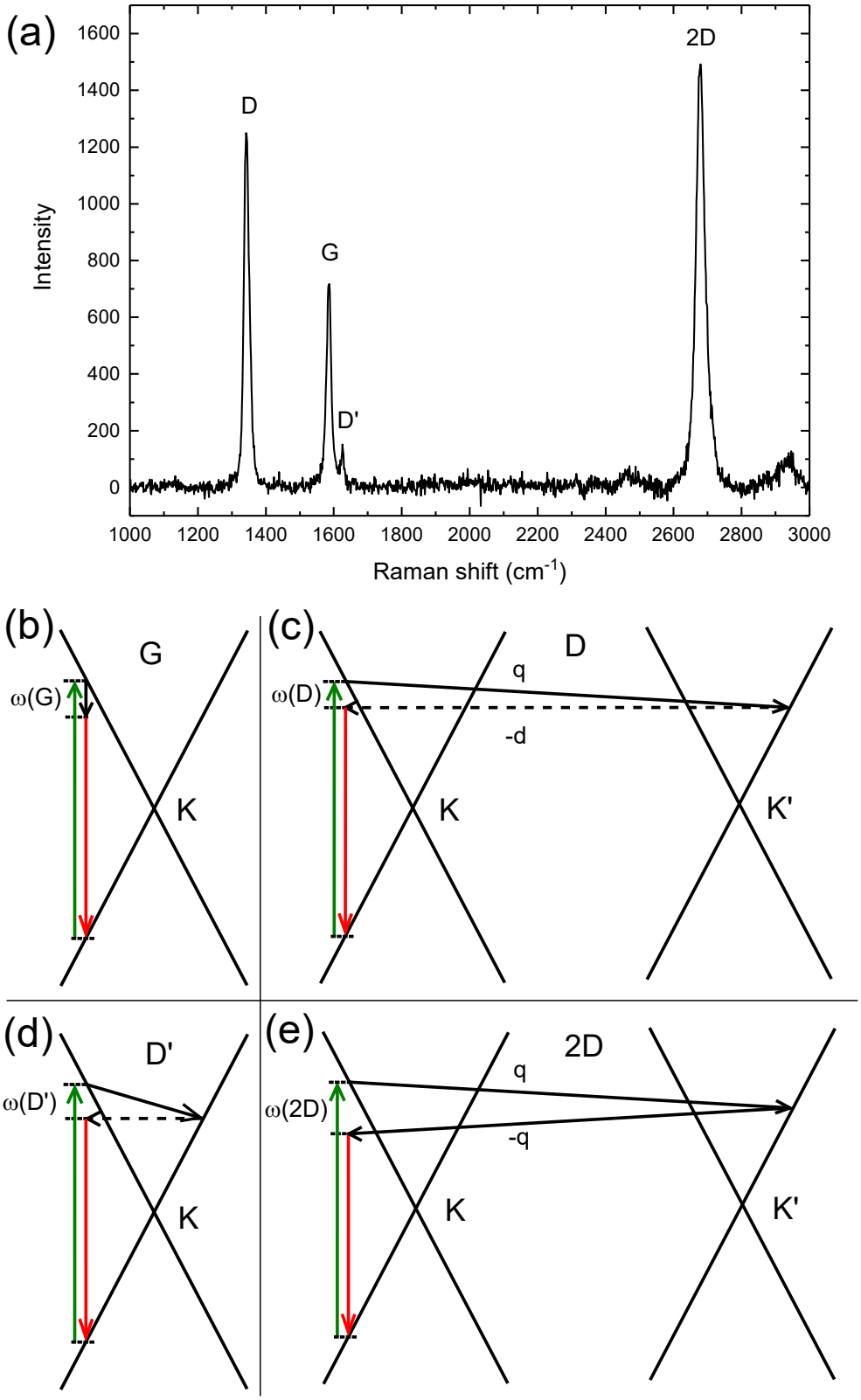

FIGURE 5 a) Raman spectrum of defected graphene. b-e) Schemes of Raman scattering mechanisms of the graphene's four main bands.

ten more intense than the G band, which is another indication of single layer graphene. However, the 2D band intensity is sensitive to doping and defects, which makes it much less reliable than the band shape. In addition to the bands mentioned here, graphene has several other modes as well, but as they are not very intense, they are not often used in analyses.

3.3.2 Strain and doping

The effect of doping on the Raman spectrum of graphene has been studied and interpreted quite extensively. [279, 284–290] The effects are visible in all of the main bands, however the G and 2D bands are the most useful since they are intensive even in defect-free graphene. For the G band, the effects of doping are upshifting of the peak position and narrowing of the FWHM, both of which happen with both hole and electron doping. [286, 291, 292] Narrowing of the G band is due to Pauli blocking of the electron-hole pair decay, when E_F gets higher than half the phonon energy. [284] While the G band FWHM could be used to estimate the doping levels, this works only for low doping since it saturates quickly as doping increases. [287, 293] Additionally, this does not work when defect amount is high, since the FWHM is increased by defects as well. [294–296] In pristine graphene strong electron-phonon coupling causes Kohn anomalies, or lowering of the phonon energy, near K and Γ points. [297–300] Doping causes a nonadiabatic removal of the Kohn anomaly at K, which in turn increases the phonon energy and thus is causing the doping dependency of the G position. [280, 293] Since the G position upshifts with both hole and electron doping, it cannot be used alone to estimate doping without knowing the type. Intensity of G band can increase under high p-type doping due to blocking of destructively interfering scattering pathways. [39,301] Additionally the G position is sensitive to strain, which will be talked about later.

The 2D band undergoes changes as well when doping changes. The intensity of the 2D band decreases with both electron and hole doping due to increased e-e collisions. [302] The 2D position increases with hole doping, while with electron doping it stays roughly constant until starting to decrease when the E_F gets high enough. [287, 293] This behaviour is caused by doping changing the lattice parameter. [293] Since the G position always increases as doping increases, using both the G and 2D positions allows to determine the doping levels.

The effect of strain to Raman bands is relatively straightforward. Strain causes change of atomic separations, which changes the energy landscape. Compressive strain causes an increase of the phonon energy while tensile strain decreases it. [303–309] If the strain is in one direction, i.e. if it is uniaxial, the separations are different depending of the lattice direction, which in turn causes splitting of the Raman peaks, if the strain is high enough. [307, 310–313] All the bands shift linearly to the same direction, which is a deviation from the effect of doping on the graphene Raman spectrum, which allows one to determine the levels of both doping and strain when both are present. Strain could be determined from the other Raman bands, for example the 2D' band, [314] though it is not that usual

since they have lower intensities.

To merge the information above, doping and strain from the Raman spectrum can be estimated most accurately from G and 2D band positions. This method was published by Lee et. al, [315] although a similar analysis procedure was published also by Mueller et. al [316]. In order to calculate these values, sensitivity factors of both of them to the Raman band positions have to be determined. The effect of biaxial strain on the G band frequency can be estimated with a sensitivity factor of $-69.1\ \mathrm{cm}^{-1}/\%$ [315], which is an average value from previous studies [305, 306, 310]. Doping can be estimated simply by $n = \left(E_F/\left(\hbar v_F\right)\right)/\pi$, where n is carrier concentration, E_F Fermi energy and v_F Fermi velocity. Shift of the G band frequency is given by $\Delta\omega_G = E_F \times 42\ \mathrm{cm}^{-1}/\mathrm{eV}$ [39]. Figure 6 shows a plot of G and 2D band positions with annotations showing directions of increasing doping and strain, values for both of them and rough examples of the band positions under different conditions. Pristine graphene is at about $1581\ \mathrm{cm}^{-1}$ G and $2671\ \mathrm{cm}^{-1}$. The red region presents a situation where graphene is fabricated using CVD and transferred with PMMA support layer, which leads to graphene which is p-type doped due to residues, and also compressively strained due to mismatch of thermal expansion coefficients between graphene and copper and transfer caused straining. [317, 318] The cyan region is graphene after annealing at about 300 °C, which does remove some of the residues, but also increases the graphene-substrate conformity. This leads to graphene having stronger coupling to the substrate and therefore also higher doping level. [315, 319]

3.3.3 Defect analysis

Raman spectroscopy is often used to characterize defects in graphene. [280, 281, 294, 320–323] As a two-dimensional material, the defects in graphene can be zero-dimensional point defects or one-dimensional line defects. Point defects can be for example additional functional groups, dopants, vacancies or just a bond rotation in the case of a Stone-Wales defect. [324] Line defects are most often grain boundaries between graphene crystals originating from graphene synthesis. [325] The relation between crytallite size and the area intensity ratio of the D and G bands was presented originally by Tuinstra and Koenig as $A_D/A_G \propto 1/L_a$, where L_a is the crystallite size. [326] The area intensities are marked here as A_D and A_G to clearly differentiate them from maximum intensity values I_D and I_G, although both notations are used in literature for area intensities. Ferrari and Robertson noted that for very small crystallite sizes (≤ 2 nm) the D band is more affected by disorder than G, since the D band originates from the breathing mode of six carbon atoms and G band only involves a vibration of two atoms. This changes the relation to $A_D/A_G \propto L_a^2$ for small crystallite sizes. [327] This relation was further studied by Cançado et al. [320]

More recently, there has been several studies about the effect of defects on the graphene Raman spectrum. Some notable studies include investigations on how point defects affect the A_D/A_G and the full width at half maximum

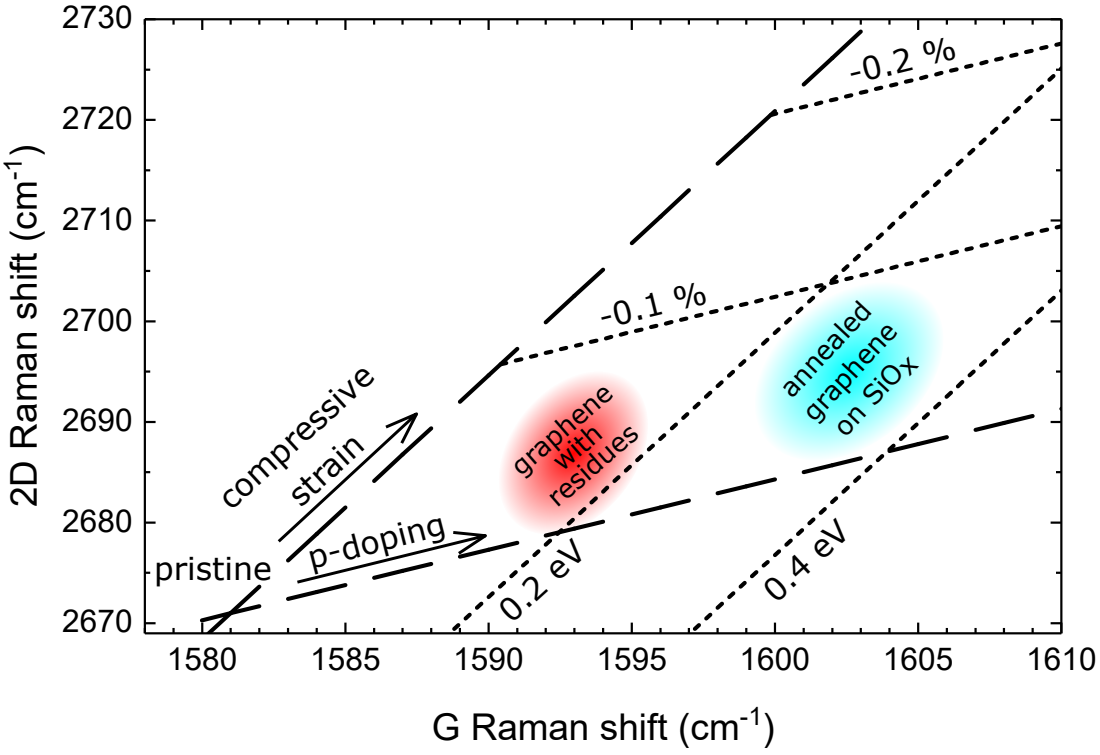

FIGURE 6 G and 2D graphene Raman peak position plot. Arrows show the directions of increasing strain and doping. Different colored regions show how the positions under different conditions.

(FWHM) of the G band. [296, 328] In ref [328] authors created a model to explain the changes in the spectrum, where two regions surround a defect. At about 2 nm radius from the defect is a structurally damaged region and between 2 nm and 4 nm is an activated region. The activated region is non-damaged graphene within electron coherence length from a defect, meaning that it contributes to D band intensity. As defect separation decreases (i.e. defect density increases) the activated regions increase leading to increase in sharp D band, but when the separation gets below 4 nm the damaged regions start to dominate. This leads to broadening of the peaks and ultimately lowering the A_D/A_G, since the D band is related to the breathing mode of the six member ring and is affected more than the G band, which requires only two atoms. A similar model was later made for line defects as well, though naturally the defected regions were defined as structurally damaged and activated ribbons instead of circles. [295] In ref [323] authors determined how excitation laser wavelength affects the A_D/A_G ratio.

Cançado et al. combined these approaches into a single model capable of estimating the amounts of point and line defects from a sample containing both defect types. [329] The model is based on the integrated intensity ratio of the D and G bands (A_D/A_G) and the G band full width at half maximum (Γ_G) having different behaviors for line and point defects. The equation used to calculate

A_D/A_G is [329]:

$$\left(\frac{A_D}{A_G}\right)E_L^4\left(L_a,L_D\right)=C_S^{0D}\left(1-e^{-\frac{\pi r_S^2}{L_D^2}}\right)+4C_S^{1D}l_S\frac{(L_a-l_S)}{L_a^2}e^{-\frac{\pi r_S^2}{L_D^2}}$$
$$+2\pi C_A^{0D}l_e\frac{(l_e+r_S)}{L_D^2}\left(1-4l_S\frac{(L_a-l_S)}{L_a^2}\right)e^{-\frac{\pi r_S^2}{L_D^2}} \quad (5)$$
$$+2C_A^{1D}l_e\frac{(L_a-2l_S)}{L_a^2}\left(1-e^{-\frac{L_a-2l_S}{l_e}}\right)e^{-\frac{\pi r_S^2}{L_D^2}},$$

where E_L is the energy of the Raman laser, L_a is the graphene average crystallite size, L_D the average distance between nearest defects, C_S^{0D}, C_S^{1D}, C_A^{0D}, and C_A^{1D} differential Raman cross-section coefficients for either point (0D) or line (1D) defects, r_S the radius of the structurally damaged area of point defects, l_S the width of the structurally damaged lines and l_e the electron coherence length. Letters S and A in Raman coefficients refer respectively to structurally damaged areas or areas activated by the defects. Equation 5 is scaled with E_L^4 in order to make measurements with different laser wavelengths comparable. [323] The full-width at half maximum of the G band was [295]:

$$\Gamma_G\left(L_a,L_D\right)=\Gamma(\infty)+C_\Gamma e^{-\xi/l_{ph}}, \quad (6)$$

where $\Gamma(\infty)$ is the FWHM of the G band with infinitely large L_a, C_Γ is a parameter related to the phonon dispersion relation, ξ the phonon localization length and l_{ph} the phonon coherence length. ξ is the minimum value between L_a and $10\cdot L_D$. Values for all the parameters are presented in Table 1.

TABLE 1 Parameter values for defect analysis.

Parameter	Value (unit)
C_Γ	87 cm^{-1}
$\Gamma(\infty)$	15 cm^{-1}
l_{ph}	16 nm
C_S^{1D}	30.3 eV^4
C_A^{1D}	30.4 eV^4
l_e	4.1 nm
l_S	2 nm
C_S^{0D}	51 eV^4
C_A^{0D}	26.5 eV^4
r_S	2.2 nm

Figure 7 shows a plot of $(A_D/A_G)\cdot E_L^4$ versus Γ_G calculated from equations 5 and 6. Pristine graphene without any defects would be at zero $(A_D/A_G)\cdot E_L^4$ and 15 cm^{-1} Γ_G. Different colored regions are meant to help the understanding of the plot. Orange strip highlights the case where there are no line defects and point defect concentration increases (dashed black line). Dark blue region shows the

opposite case, where there are no point defects and the size of graphene crystallites decrease (solid black line). The red area shows a region where both increasing point defect density and decreasing crystallite size cause roughly the same effect of decreasing A_D/A_G and increasing Γ_G, meaning that the model does not give unambiguous solutions to the defect amounts. Cyan region is where both defect types exist and their amounts can be estimated. The figure has additional lines calculated with constant defect densities of $n_D = 1 \cdot 10^{12}$ cm^{-2} (red dash-dot line) and $n_D = 5 \cdot 10^{11}$ cm^{-2} (blue dash-dot line) with decreasing L_a. These lines also demonstrate how the decrease of L_a primarily widens the G band, and the increase of point defects increase A_D/A_G ratio.

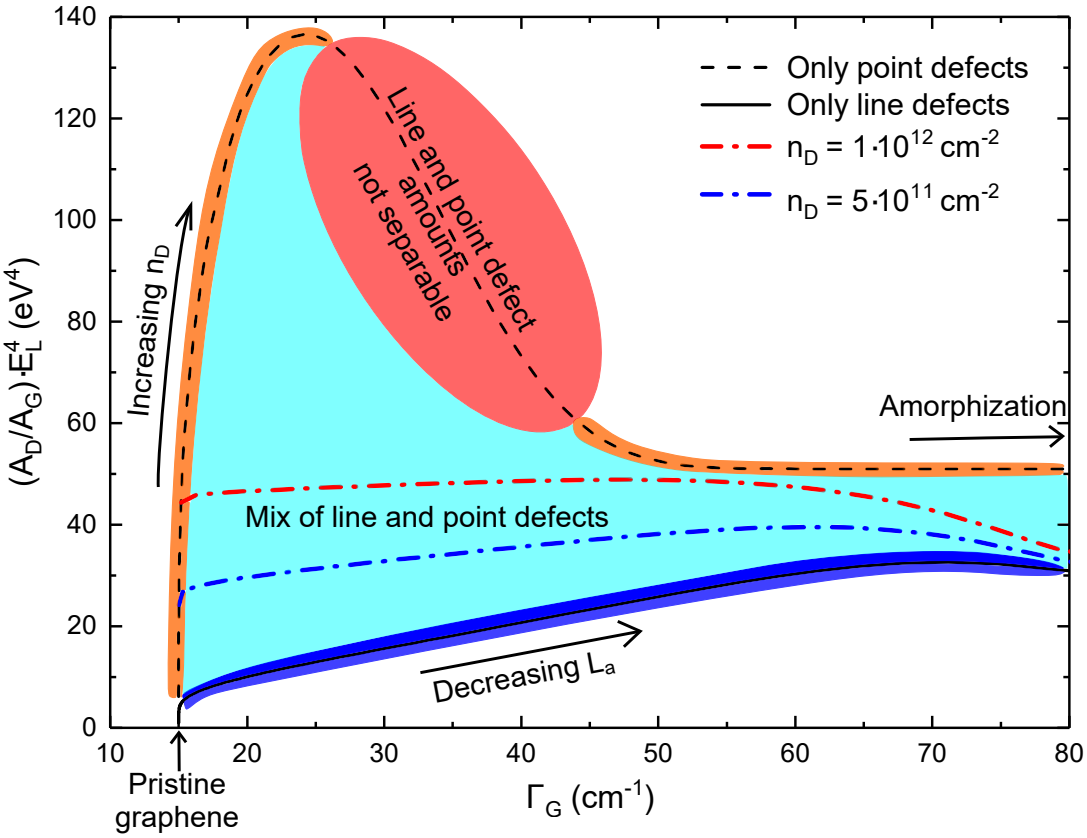

FIGURE 7 Defect plot showing $(A_D/A_G) \cdot E_L^4$ as a function of Γ_G. Orange region following the dashed black line shows region where the defects are predominantly point defects and dark blue region following the solid black line shows the region where the defects are predominantly line defects. The cyan area shows a region where the graphene has a mix of both types and densities can be calculated. Red colored area shows a region where the point and line defect concentrations cannot be determined reliably. The regions are not definitive, but only there to help to understand the plot.

A notable issue is that an underlying assumption for the entire defect analysis described here is that other things that affect the Raman spectrum, mainly number of layers and doping, are known. As pointed out by authors in ref. [329],

Γ_G is sensitive to these, especially on the left hand side of the plot. In fact, oftentimes the Γ_G falls between $10 - 15$ cm^{-1} just because of the silicon oxide substrate or residues from transfer. Additionally, and arguably even more consequentially, doping decreases the A_D/A_G ratio, [287] meaning that the analysis can easily give wrong results if doping is not taken into account, and this affects the results in the entire plot, not just at an extreme.

4 PULSED LASER MODIFICATION OF GRAPHENE

Laser based methods suit very well for modifying graphene and other 2D materials, since the effect can often be limited to the surface layer of the sample. Additionally, laser modifications can often be done directly to the sample without multi-step processes, chemical treatments or masks. There have been several studies on modification of graphene or other 2D materials by pulsed laser irradiation from micropatterning [330,331] and layer thinning [332,333] to general ablation. [334,335] In addition to simple physical removal of material, laser treatments can also induce chemical reactions, for example, graphene oxide reduction. [336]

This work centers on modification of structure and properties of graphene using a femtosecond pulsed laser writing method called optical forging. This method causes neither removal of material through ablation nor chemical reactions with oxygen or other non-carbon atoms, but generates lattice defects.

4.1 Description of the femtosecond laser setup

All the laser patterning work in this thesis was done with a home-built femtosecond laser setup. For all processing in this work the same laser (Pharos-10, 600 kHz, Light Conversion Ltd.) was used. Laser pulse processing was done with non-collinear optical parametric amplifiers (NOPA, Orpheus-N, Light Conversion Ltd.). In majority of cases 250 fs pulses centered at 515 nm were used. For some patterns in [AI] shorter 30-40 fs pulses centered at 560 nm were used. The beam was focused into a single Gaussian spot with a microscope objective (Nikon LU Plan ELWD 100x/0.80).

Writing of the patterns is done by scanning the sample using a piezo stage (Nanomax 300, Thorlabs Inc.). The laser writing processes can be controlled with pulse energy and time that each spot is being irradiated. Typical values for pulse energies range from a few to a few hundred pJ, and irradiation time between $0.1 - 10$ s. For larger than single-spot structures an additional parameter is spot separation, which is 100 nm unless otherwise specified. In order to do optical

forging, i.e. prevent oxidation, the samples were placed inside a closed chamber that was purged with N_2.

4.2 History

Laser patterning studies in Jyväskylä originated from four-wave mixing (FWM) imaging studies of carbon nanotubes. The FWM signal was stable when the nanotubes were exposed to the pulsed femtosecond laser irradiation under argon atmosphere. However, once the argon purge was turned off, the signal decayed. This was contributed to laser induced oxidation of the nanotubes via a multiphoton process. [337]

The same loss of signal happened also with graphene. The cause of this was confirmed to also be laser irradiation induced oxidation by a two-photon process, [338] which makes sense since carbon nanotubes and graphene are chemically very similar. Growth dynamics of the oxidation were studied by using single spot exposures. The oxidation patterns were determined to originate from small spots, which grow into a uniformly oxidized pattern with higher doses. [339] Chemical composition of two-photon oxidized graphene was identified to mainly contain hydroxyl groups and epoxy groups, indicating that water has an important role in the oxidation process. [340]

Large oxidized patterns can be manufactured by exposing several single-spot exposures right next to each other so that they partially overlap. By scanning the sample this way, continuous patterns up to tens of microns have been made with the setup described above. Upper limit of the pattern size that can be written is essentially the scan range of the sample stage. However, if large patterns are required, it is more convenient to use an objective with lower magnification to speed-up the process. Lower limit of the pattern size is diffraction limited, smallest linewidth being roughly 500 nm.

4.3 Optical forging

4.3.1 Effect of optical forging

Seeing that under oxygen containing atmosphere the pulsed laser irradiation causes oxidation, this naturally raises a question of what happens if the same process is performed in an oxygen-free atmosphere. Interestingly, patterns were still formed, when similar square patterns were written without oxygen. These structures were not ablated, since they still exhibited the Raman peaks characteristic to graphene after the laser irradiation. Additionally the patterns were clearly visible under optical microscope and AFM imaging showed that they had grown in height considerably. Since the irradiation causes the exposed graphene

regions to bulge outwards, analogously to metal sheet being dented by a hammer, this processing is called optical forging. Figure 8 shows a variety of different structures that can be fabricated using the optical forging method. Unlike with two-photon oxidation, where the height of the patterns maxes out at about 2 nm, patterns made without oxygen are rising consistently as irradiation dose increases. Heights of the patterns exceeded 100 nm with high irradiation doses (see Figure 8c). [AI] The images in Figure 8 clearly show that with this method formation of the patterns is well controlled both in xy direction and in z direction. It is important to note that the optically forged patterns are stable. Even after months of storing, either no change or only a slight decrease in the height of the patterns is seen.

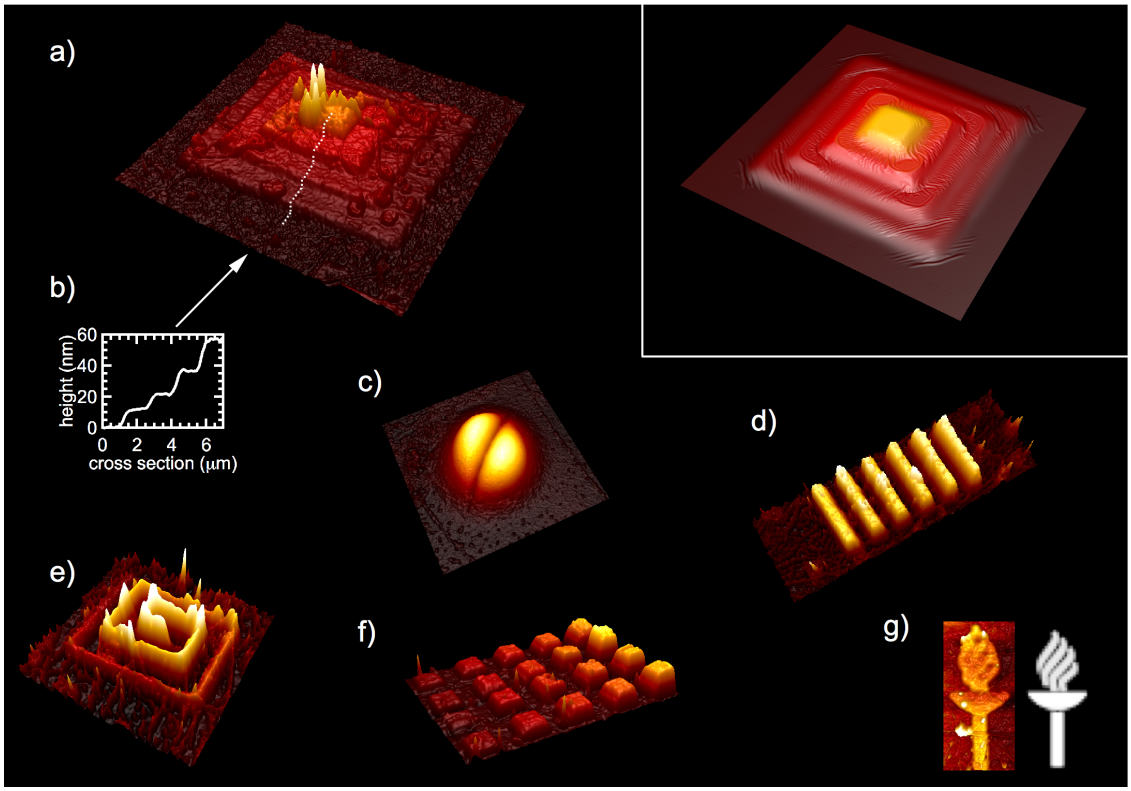

FIGURE 8 AFM images of optically forged graphene patterns. a) Step pyramid structure made by irradiating square patterns on top of each others. The field of view (FOV) is 17×17 μm^2 b) Line profile along the dashed line in a). c) Dome-like structure with a height of 115 nm. FOV is 1.8×1.8 μm^2. d) Grating structure. FOV is 20×6.7 μm^2. e) Chiral structure where the pattern height increases towards the middle. Maximum height is 31 nm. FOV is 8×8 μm^2. f) Matrix of square patterns. Maximum height is 20 nm. FOV is 19.8×14.7 μm^2. g) Torch with a bitmap image (on the right) used to write the pattern. Maximum height is 6 nm. FOV is 3.5×7.4 μm^2. Inset: Simulated pyramid with the same dimensions as in a). In all the images z-axis is exaggerated enhance visualization of the structures. Reprinted with permission from [AI]. Copyright © 2017 American Chemical Society.

Square patterns fabricated with the optical forging method are presented in Figure 9, showing typical characterization results with different imaging techniques. The optical microscope image in Figure 9(b) shows that the forging process causes a color change at the patterned areas, and that the color becomes more intense with higher irradiation times. The change of color coincides with the increase of the height of the patterns, seen in the AFM image in Figure 9(c). In Figure 9(d) is a Raman D band map, i.e. an image showing integrated intensity of the Raman D band gathered from each spot. This shows yet again the same trend: the D band intensity increases consistently with exposure time. This result shows that optical forging causes lattice defect formation. Still, it is important to underline that characteristic carbon Raman bands are still present after forging, which can be seen from Figure 21 and also from Raman spectra shown in all of the included articles.

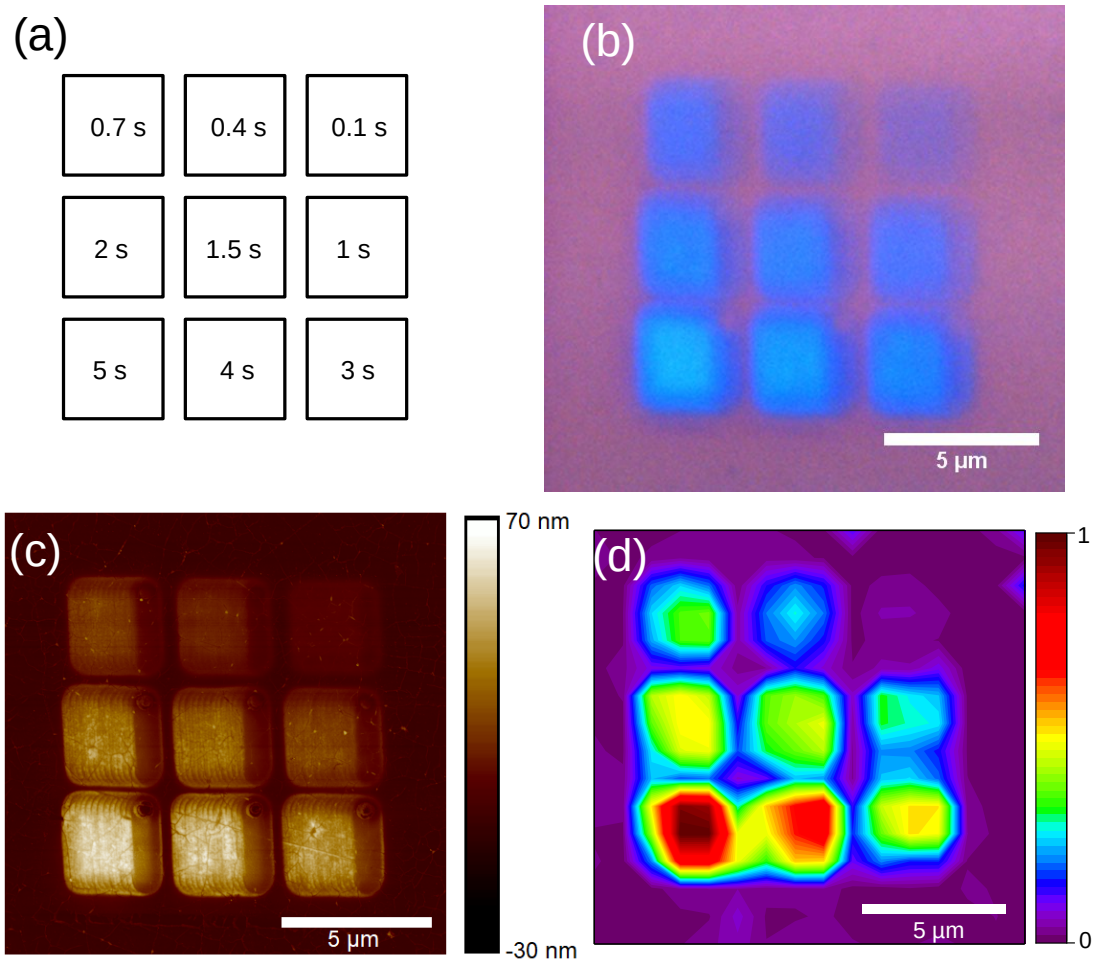

FIGURE 9 Set of patterns fabricated using optical forging of graphene on SiO_x with 160 pJ pulse energy. (a) Forging pattern showing irradiation times per single spot in each square. (b) An optical microscope image of the optically forged patterns. (c) An AFM image of the patterns. (d) A Raman map of the patterns constructed by integrating the spectra over the D band (between Raman shift of $1326 - 1373\ \mathrm{cm}^{-1}$).

The results highlighted in Figures 8 and 9 raise multiple questions about the exact content of the patterns and the formation mechanism. In article [AI] optically forged patterns were characterized using X-ray photoelectron spectroscopy (XPS). These results show that there is no significant change in chemical composition of the graphene sample. This means that no oxygen or other elements were observed to bond with the graphene. However, the C 1s spectrum does widen slightly due to optical forging, indicating that more of the carbon becomes sp^3 hybridized. This is essentially the same result as we can see from the Raman spectra. In article [AI] the proposed reason for the formation of the 3D structures is local lattice expansion caused by the defect creation. This proposal was also tested with simulations based on thin sheet elasticity theory. Results from the simulations show that the forged patterns can be reconstructed by locally straining the graphene, showing that the proposed mechanism is at least possible. A Stone-Wales defect could be the type of defect that optical forging causes, since its formation energy is quite low and it does not require any addition of removal of atoms, but just a 90° bond rotation. Additionally, it causes suitable amount of lattice expansion.

4.3.2 From single spots to complex structures

Before going into details about how optical forging alters the crystalline structure of graphene, I am first presenting how the structures form on a larger scale. The most simple structures are made by exposing graphene only at a single spot. Since single spot exposures causes small bulged structures with circular symmetry, these structures are called blisters. Larger and more complex structures are made the same way as larger oxidized patterns, by overlapping several single spot exposures partially on top of each others. Since single blisters are essentially building blocks for larger structures, studying their formation can give important insight as to how and why larger structures form into the shape that they do.

AFM images of several single blisters with varying growth conditions are presented in Figure 10. Figure 10a shows well how the shape of the blister can be drastically different when patterning parameters (pulse energy and irradiation time) are changed. This is highlighted in Figures 10(b-e). First shape that develops with the lowest doses is a single dome (Fig. 10(b)). When graphene is irradiated with higher pulse energy the center of the blister bends down, while the edges keep growing, forming a ring structure (Fig. 10(c)). If the pulse energy is still increased, a new smaller central dome appears in addition to the ring walls (Fig. 10(d)). Finally, with the highest doses the second central dome disappears, leaving a structure with two rings (Fig. 10(e)). Other examples of blisters with varying shapes, such as more fringes, are shown in articles [AII] and [AIII]. Blisters shown in Figures 10(b-e) are made by increasing the pulse energy while keeping the irradiation time constant, but similar development of the blister shape is noticeable also with changing irradiation time. The effect is not exactly the same, though. Usually longer irradiation time causes higher structures than if the structures have been made with higher pulse energy, even if dose is equal.

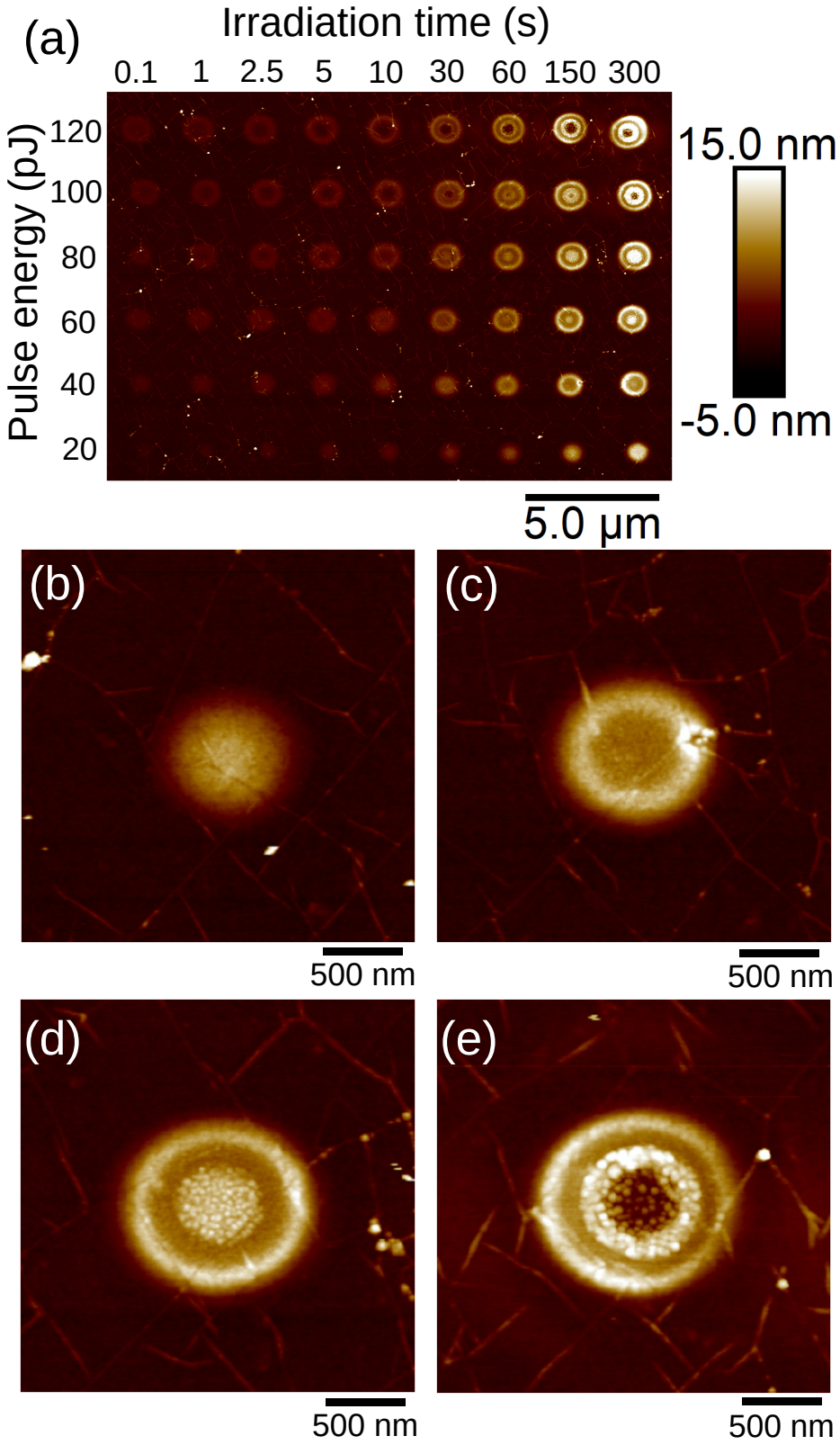

FIGURE 10 AFM images of single spot optically forged graphene, i.e. blisters. a) Matrix of blisters made with different irradiation times and pulse energies. (b)-(e) Zoomed in images with 150 s irradiation time and pulse energies of (b) 20 pJ, (c) 40 pJ, (d) 80 pJ and (e) 120 pJ. All the images have the same color scale.

The initial formation of a single dome is reasonable, since the laser beam line shape is single Gaussian. However, the latter formation of the various different shapes is not obvious. Ring structures in Figure 10 are as thin as 100 nm at FWHM, well below the diffraction limit. Additionally, sizes of the entire blisters are wider than the laser spot size when the dose is high enough. These types of observations are very difficult to explain with straightforward ablation or deposition of some unknown material. In the final step, laser energy is high enough that it might be possible that the hole in the middle can be caused by ablation, however, this does not help to explain the other shapes. It is important to also note that the typical fluencies used during optical forging are much lower than the ablation threshold, see article [AIII] for details.

As explained above and in article [AI], the process of optical forging causes formation of lattice defects in graphene, which in turn causes expansion of the lattice. In article [AII] formation of these various shapes was explained with interplay of the lattice expansion and graphene adhesion to SiO_x. In article [AIII] it was noted that if a new blister is made close to existing blisters, the shape of the

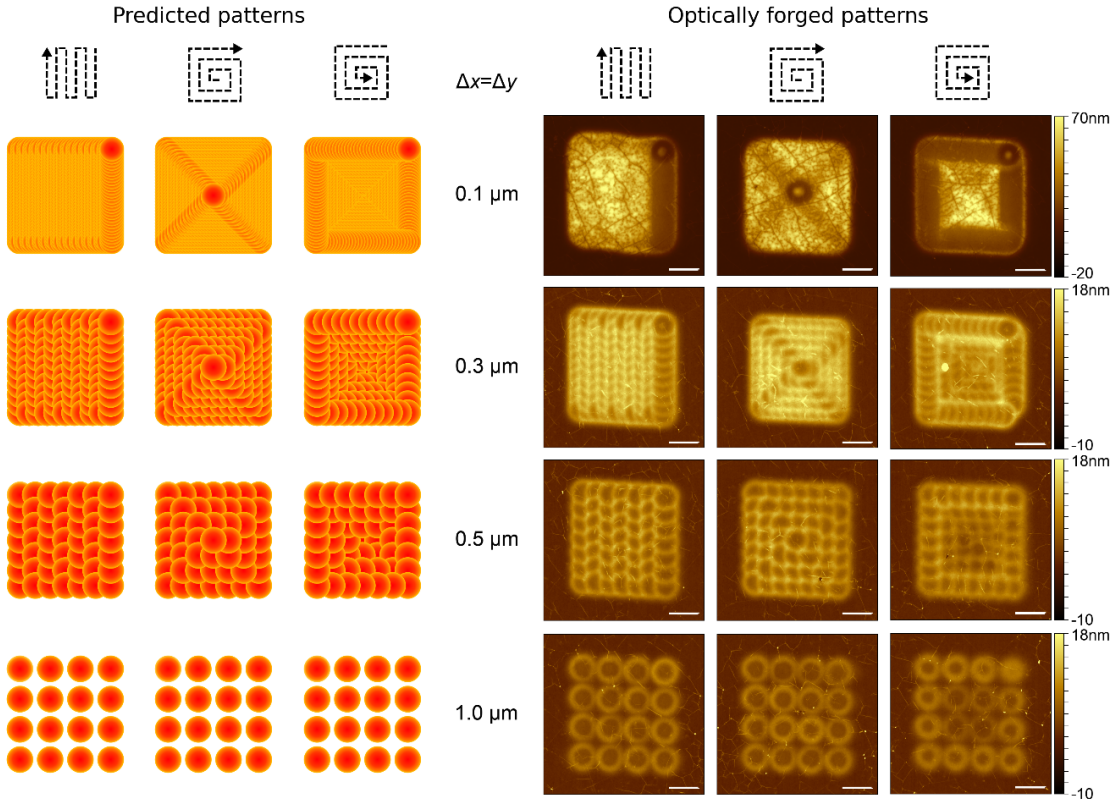

FIGURE 11 Predicted shapes (left) and AFM images of patterns (right) made using optical forging using bidirectional, inside-out and outside-in patterning pathways. All the patterns have been made with 100 pJ pulse energy and 10 s exposure time per spot. Separations between spots were $\Delta x = \Delta y =$ 0.1; 0.3; 0.5 and 1 μm. All scale bars are 1 μm. Reprinted with permission from [AIII]. Copyright © the Royal Society of Chemistry.

new blister is affected by the existing ones. This can also be seen from lower right corner of Figure 11, where the outer blisters have been made before the inner four blisters, and the inner ones have lower height. This does not prove the proposed explanation of blister formation by lattice expansion, but it does add credibility to it, since altered inplain strain can explain how the effect extends beyond the blister area, while this cannot be explained with material deposition.

The above-mentioned order of blister formation can be used to explain or predict shapes of larger patterns, since larger patterns are formed from many single blisters close each other. In Figure 11 the shape of the resulting pattern (on the right) is explained by constructing square patterns from single blisters using three different patterning pathways (on the left) and using four different separation distances between neighboring blisters. In Figure 11, when studying images in the middle rows (with 0.3 μm and 0.5 μm separation), it can be seen that a new spot irradiation and blister formation does not change the shape of the old blister, but the new blister forms only in the area that has not been exposed before. The real patterns made with optical forging are clearly following the predicted pattern. While the images with smaller overlap clearly show that a new blister structure forms only at unirradiated areas, with the highest overlap (0.1 μm spot separation) the individual blisters are so close to each other that the final structures appear to have a smooth top surface. The height of the large square structure can be seen to increase when blister separation decreases, which is due to increased dose.

4.3.3 Defect formation

As it has already been alluded, the process of optical forging causes lattice defects in graphene. Defect development was studied in article [AIV]. This was based on defect analysis using the intensity ratio of D and G Raman bands and the G band FWHM, as explained in section 3.3.3.

However, with higher irradiation dose the point defect concentration starts to decrease. In fact, according to this analysis, with pulse energies of 120 pJ, 140 pJ and 160 pJ the point defect concentration decreases so much that they disappear completely. This can be seen from Figure 12(b), where data points with these pulse energies overlap or even fall below the solid black line, which is a theoretical line for the case where the graphene sample has only line defects. Since some of these measurement points would result into negative point defect densities they are not shown in Figure 12(c). The graphene crystallite size decreases (i.e. the line defect amount increases) the entire time with all pulse energies, except for the lowest (30 pJ). The decreasing crystallite size in Figure 12(d) coincides also with increasing photoluminescence intensity that was measured from the square patterns in Figure 12(a), and this will be discussed in chapter 5.

The formation of line defects during optical forging was also investigated with computer simulations in article [AIV]. As in [AI], an attractive defect type to use to explain these results is the Stone-Wales defect. This is because the SW defect causes an asymmetric strain field. Due to this, the formation energy of a

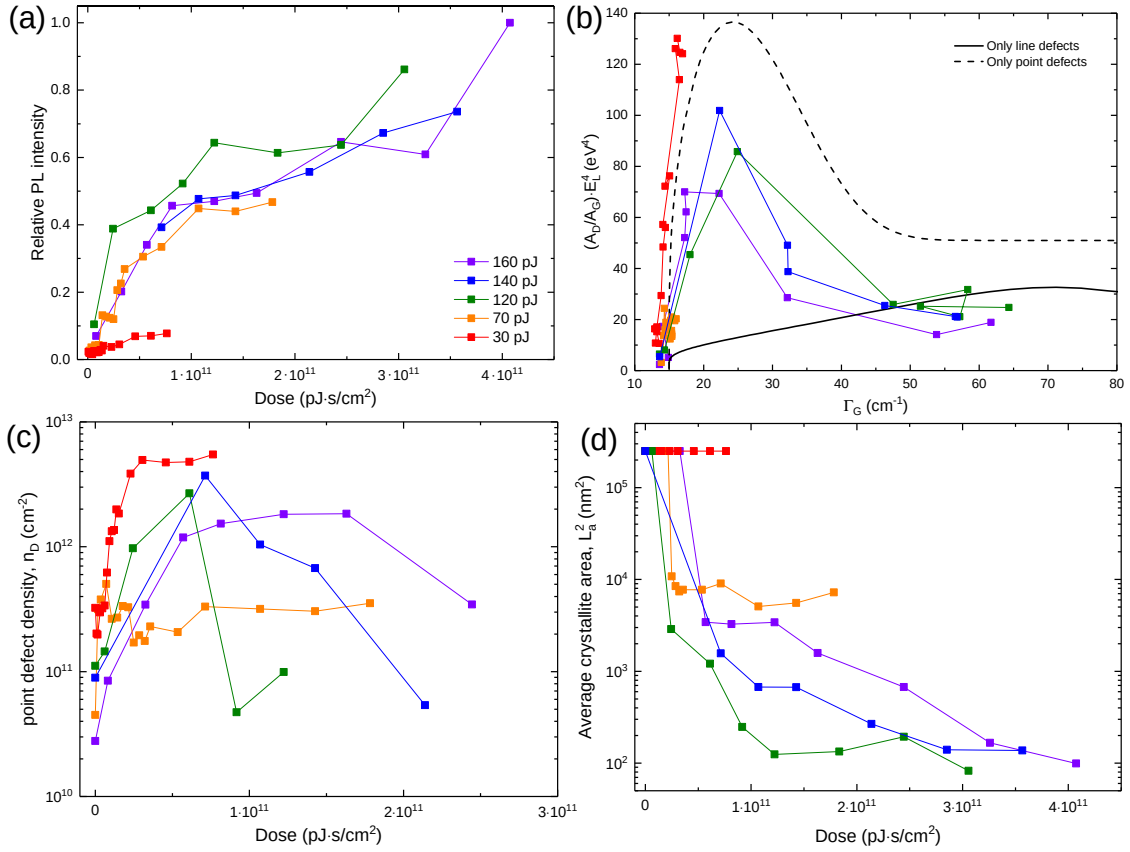

FIGURE 12 Defect development during pulsed laser irradiation. (a) Integrated photoluminescence intensity between $1800 - 2400$ cm^{-1} divided by integrated intensity of the G band versus pulsed irradiation dose. (b) Experimental $(A_D/A_G)\,E_L^4$ as a function of Γ_G (lines with markers). The solid black line represents the case where graphene has only line defects and no point defects, and the dashed black line represents the opposite. (c) Point defect density versus irradiation dose. (d) Average crystallite area versus irradiation dose. Reprinted with permission from [AIV]. Copyright © 2020 American Chemical Society.

new SW defect right next to an existing one varies depending on which side of the defect it is formed. At a suitable point the formation energy of a new SW defect is lower next to an existing defect than for a new isolated defect. These results suggest that SW defects can explain how the defects develop from point defects to line defects that cut the graphene into small domains. This is an interesting point since grain boundaries and line defects can cause bulged shapes in graphene, [341, 342] possibly playing a role in formation of the optically forged structures. This development has some similarities to two-photon oxidation, where the oxidized area starts to form from very small spots and these islands grow and connect at higher irradiation doses. [339] However, with optical forging the growth of additional defects does not appear to be isotropic.

4.3.4 Lattice expansion versus deposition

Naturally three-dimensional patterns such as these could form as a result of expansion of the underlying substrate due to the high intensity pulses. [343] AFM images of a mechanically exfoliated graphene flake in Figure 13 show that even though the bare SiO_x area around the flake was patterned, it cannot be seen in the AFM images. Instead, only areas with graphene have a height difference. The patterned area in Figure 13 is much larger than the flake (about 3×3 μm^2), and the effect can also be seen from thicker graphene flakes in the upper left and lower right corners of Figure 13(b), but nowhere on the substrate or even the residue particles around the flake. A similar point was made in [AI] with CVD grown graphene. Also, in [AIII] some forged graphene patterns were etched using oxygen plasma, leading to bare SiO_x surface where the pattern was. However, it should be noted that in Figure 13 the forging process does not grow the size of graphene flake in lateral direction. The edge shape of the forged flake is very sharp, indicating that the shape is not completely caused by expansion of the graphene, but deposition of material may play a role as well.

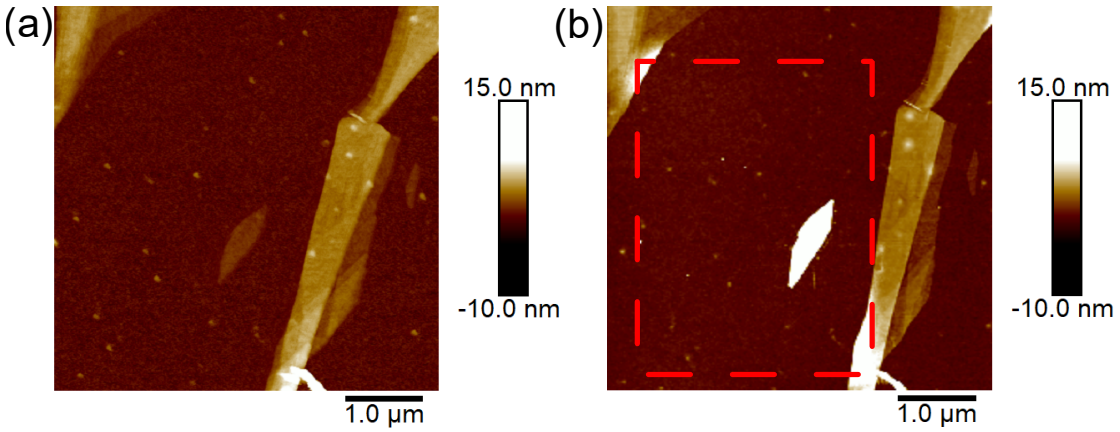

FIGURE 13 AFM images of an individual graphene flake before (a) and after (b) optical forging process. Region that was irradiated was approximately 3×4 μm^2, which is outlined in (b).

It is important to note that optical forging does work with graphene suspended over a hole, however there are differences compared to substrate supported graphene. All the fabrication details for suspended graphene samples are described in appendix 1. Figure 14 shows AFM images and Raman spectra of a freestanding graphene membrane before and after the optical forging process. The difference in their shape is huge. Before the forging process the graphene membrane is bending downwards. This is to be expected, since the graphene fabrication and transfer process leads to compressively strained graphene. The membrane is bending downwards since graphene's adhesion energy to silicon nitride (Si_3N_4) is quite high. [344] After optical forging the membrane is bulging upwards from the substrate with clear corrugations. Maximum height of the mem-

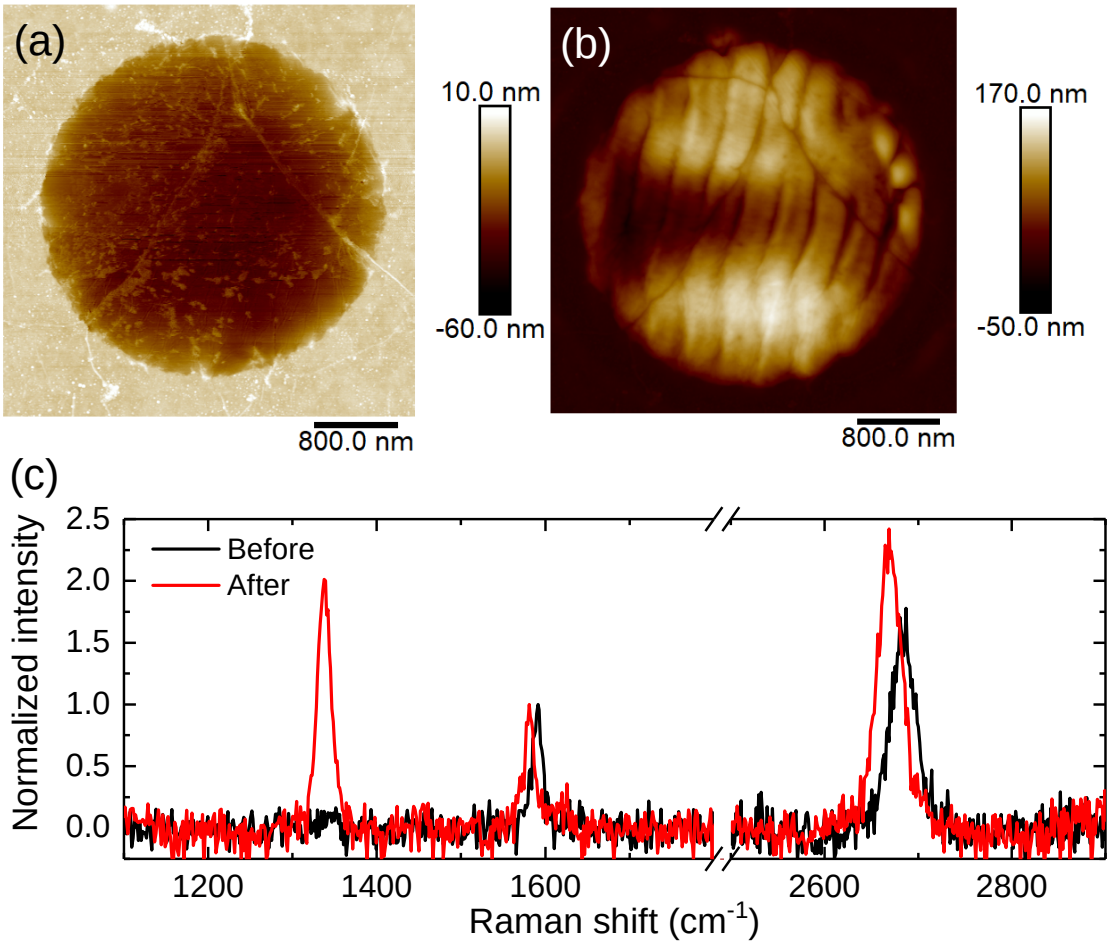

FIGURE 14 AFM images of a freestanding graphene membranes (a) before and (b) after optical forging. (c) Raman spectra of membranes shown in (a) and (b). The membrane was processed using 60 pJ pulse energy and 10 s exposure time per spot and the separation between each spot was 0.1 μm.

brane is about 160 nm from the substrate surface, much higher than the depth of the membrane before forging, which was 40 nm. Corrugations to the vertical direction in Figure 14(b) might seem similar to corrugations caused by writing, seen for example in Figures 9(c) and 11. However, the distance between corrugations in Figure 14(b) is 350 − 400 nm, which is much larger than the 100 nm that was used as the spot separation to forge this structure. Also, graphene on Si_3N_4 does not bulge as on SiO_x, which will be discussed later.

Raman spectra before and after the optical forging process in Figure 14(c) show that the membrane still consists of graphene, despite of the drastic change in shape. The most drastic change is the appearance of a sharp and high intensity D band, indicating a large increase of defects, which is in line with previous results from optically forged graphene. The G band is not widening, which indicates that the generated defects are point defects. With similar doses in Figure 12 the graphene crystallite size is already getting smaller. A possible explanation to this discrepancy can be found from having different substrates. In Fig-

ure 12 graphene was resting on $\sim$ 300 nm SiO_x thin film on silicon wafer. The pulsed laser light can backreflect from the silicon interface and cause extra dose compared to suspended graphene, which in turn explains why the crystallite size does not decrease yet in Figure 14. Additional observations from the Raman spectra are that the 2D band intensity increases and the band position downshifts, as well as G band position. As explained in section 3.3.2, these changes suggest that doping decreases during the optical forging process. The small initial doping can be explained with polymer residues, as was described in chapter 2. These residues can be seen in Figure 14(a), but they are absent in Figure 14(b). Therefore it is safe to say that optical forging removes residues, which in turn neutralizes the doping. Decrease of doping was seen in every measured membrane in article [AV].

This is an important observation related to the idea that the structures formed during optical forging are caused by deposition of some material. This material would most likely be amorphous carbon, since XPS results indicate that there is no significant change in chemical composition of optically forged patterns compared to pristine graphene. Additionally, in Raman spectra there are no other peaks than carbon and silicon peaks. However, there is evidence that some amount of amorphous carbon is deposited on graphene on SiO_x. This can be seen from Raman spectra in article [AIV], where wide G and D bands appear in the spectra in addition to the sharp graphene peaks. Optical forging has been tested with ^{13}C labeled graphene and in this case only ^{12}C related amorphous signal appears (not shown here). This indicates that the amorphous carbon originates either from polymer residues or carbon traces in the N_2 gas flow during the process. The thickness of the residual polymer layer is maximally a few nanometers and therefore does not contain enough material to explain the 3D shapes. The patterns can be successfully formed under both nitrogen and argon gas purging, which contain only trace amounts of carbon. Carbon could in principle be deposited onto the sample from the gas stream in a similar way as carbon contamination builds up during electron microscopy. [243, 244] It is worth to note that, despite attempts, amorphous carbon has not been successfully deposited onto a SiO_x substrate without graphene. This elusive nature makes it difficult to exactly asses how much of carbon gets deposited and how it affects the measurements. Additionally, amorphous carbon cannot be the sole reason for all of the patterns, since in some cases patterns with height of tens of nanometers do not show any sign of amorphous carbon in their Raman spectra (i.e. widening of the peaks) in article [AIV]. This is also the case in Figure 14, where the height difference before and after optical forging is about 200 nm. If this much amorphous carbon would be deposited onto the graphene membrane, there is no doubt that this would show up in the Raman spectrum. Also, when graphene is irradiated with low dose, the graphene membrane does not necessarily bulge out from the surface. This is shown in Figure 15, where AFM images before and after optical forging and profiles extracted from them clearly present how the membrane partially slumps down because of the forging process. This behavior cannot be explained by build-up of material, but defect-induced lattice expansion leading

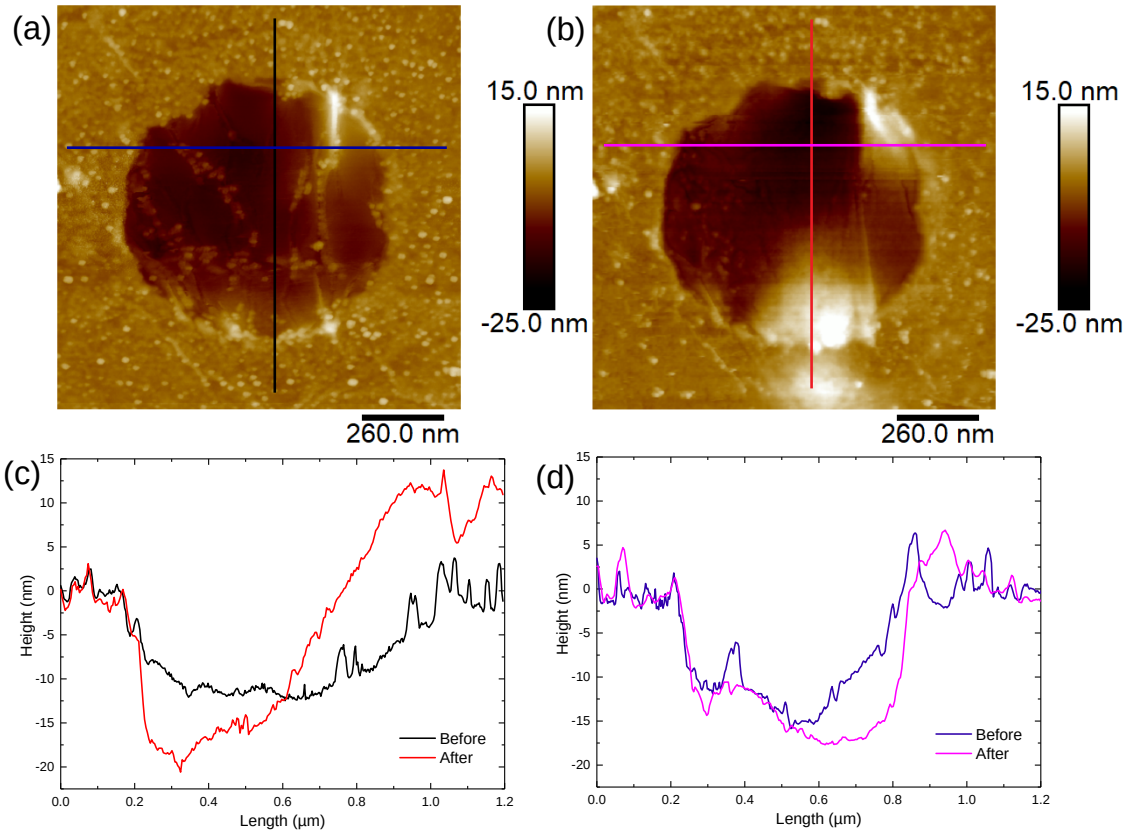

FIGURE 15 Effect of low dose optical forging on suspended graphene membranes. Panels (a) and (b) show before and after images respectively. The membrane was exposed using 60 pJ pulse energy, 2 s exposure time and 100 nm spot separation. Panels (c) and (d) show line profiles from the lines in (a) and (b). The directions of the lines are from up to down and from left to right.

to relaxation of the shape can.

Optically forged patterns can have different Raman spectra even though they have the same height. This is presented in Figure 16. Square patterns shown here are made on same graphene sample with different exposure parameters. The square heights, measured from the AFM images, are almost identical. Shapes of the squares are slightly different with square in 16(b) having rippled structure, while square in 16(a) is smoother. This is a result of blister shape being different by using different irradiation parameters. In 16(a) the blister is shaped as a dome and in 16(b) as a ring, akin to Figures 10(b) and 10(c) respectively. The square pattern in 16(a) made with 30 pJ has sharp Raman bands with the D band being the most intense of all the bands, indicating high point defect density. The square pattern in 16(b) made with 160 pJ has much more intensive background luminescence, wide D band and a wide shoulder right next to the sharp G band, indicating presence of amorphous carbon. These spectra suggest that there is almost no amorphous carbon deposited onto the graphene during optical forging when the pulse energy low, but the 3D shape is formed nevertheless. This is a clear indication that either graphene causes the 3D shape or deposited material

is different. However, there is no evidence of any other material than graphene and amorphous carbon either in Raman spectra or anywhere else. Therefore it can be suggested that most of the bulging seen in 16(a) is from graphene bulging, however more studies are needed to confirm this.

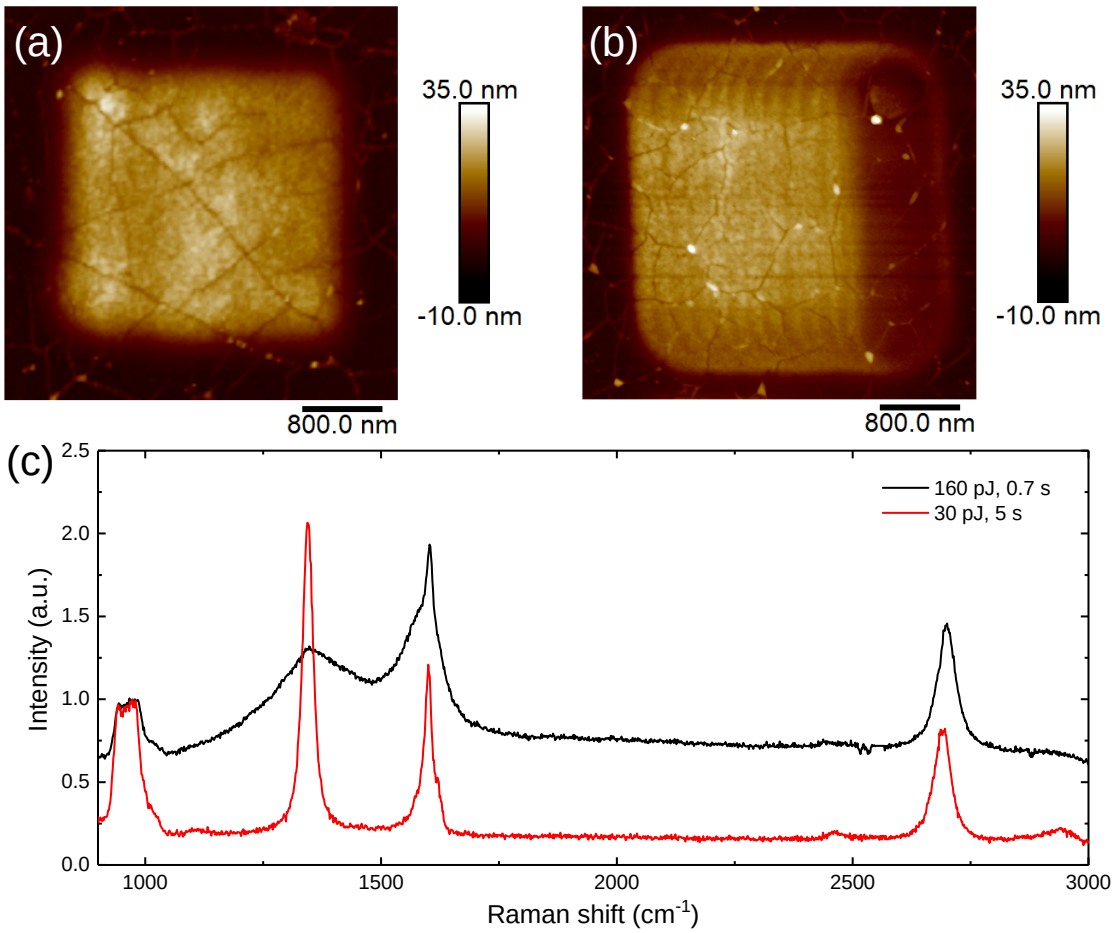

FIGURE 16 Comparison between two optically forged squares with average heights of 21.8 nm in (a) and 21.7 nm in (b). Square in (a) was patterned using 30 pJ pulse energy and 5 s irradiation time per spot and square in (b) 160 pJ and 0.7 s. (c) Raman spectra from the middle of the squares in (a) (red spectrum) and (b) (black spectrum). The squares are on the same graphene sample.

Deposition of material on suspended membrane is presented in Figure 17. AFM images before and after the optical forging show that during the process the membrane height increases up to 25 nm, but the increase is not uniform everywhere on the membrane. Raman spectra in Figure 17(c) show yet again that defects are formed during the process, but there is no sign of amorphous carbon or any other deposition. However, height differences in 17(b) are also visible in TEM image in Figure 17(d). This can be seen even more clearly from Figures 17(e) and 17(f), which are from a different membrane. Note that on the highest features in 17(e) on the lower left part of the membrane, which are the darkest features in 17(f), are residues and not a result of optical forging. However, the four ridges

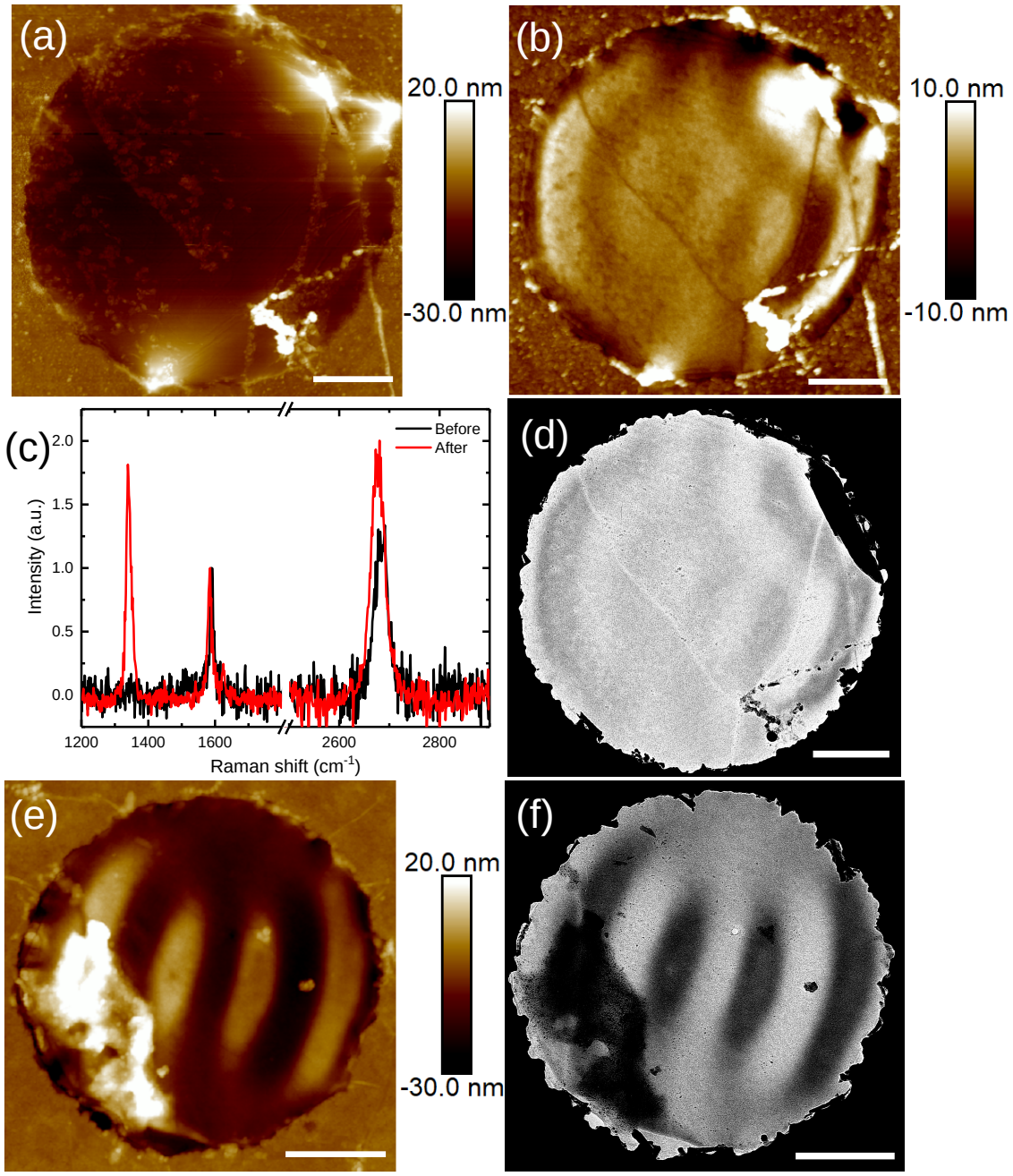

FIGURE 17 AFM images of a graphene membrane (a) before and (b) after optical forging process. The membrane was irradiated using 60 pJ pulse energy, 0.5 s exposure time per spot and 100 nm separation between spots. (c) Raman spectra measured from membrane in (a) (black) and (b) (red). (d) TEM image after the process. (e) and (f) show AFM and TEM images of another membrane, irradiated using 60 pJ pulse energy, 2 s exposure time per spot and 100 nm separation between spots. All scale bars are 500 nm.

in the images are caused by optical forging. They are clearly visible in both images and the taller the structure is in the AFM image, the darker that structure is in the TEM image. This indicates that there is a thickness difference between

different regions, however this material does not show up in Raman spectra. It is not clear what this material exactly is, but the situation is very similar to Figure 16, although when the graphene is suspended the height modulation is not even and does not follow the patterning, as it does when graphene is on SiO_x. The lack of any Raman signals suggests that the deposition is quite thin, however more studies are needed to determine the exact content of it.

There is an additional interesting observation when a suspended graphene membrane is forged. Figure 18 shows AFM images of two suspended graphene membranes before (a,c) and after (b,d) optical forging. In the after images in Figures 18(b) and 18(d) clear ring structures can be seen surrounding the openings. Black squares around the openings show the region that was forged. Image sizes in the panels (a) and (c) are smaller than in (b) and (d) since the the formation of the rings was not foreseen. However, it is clear that the structure was not present

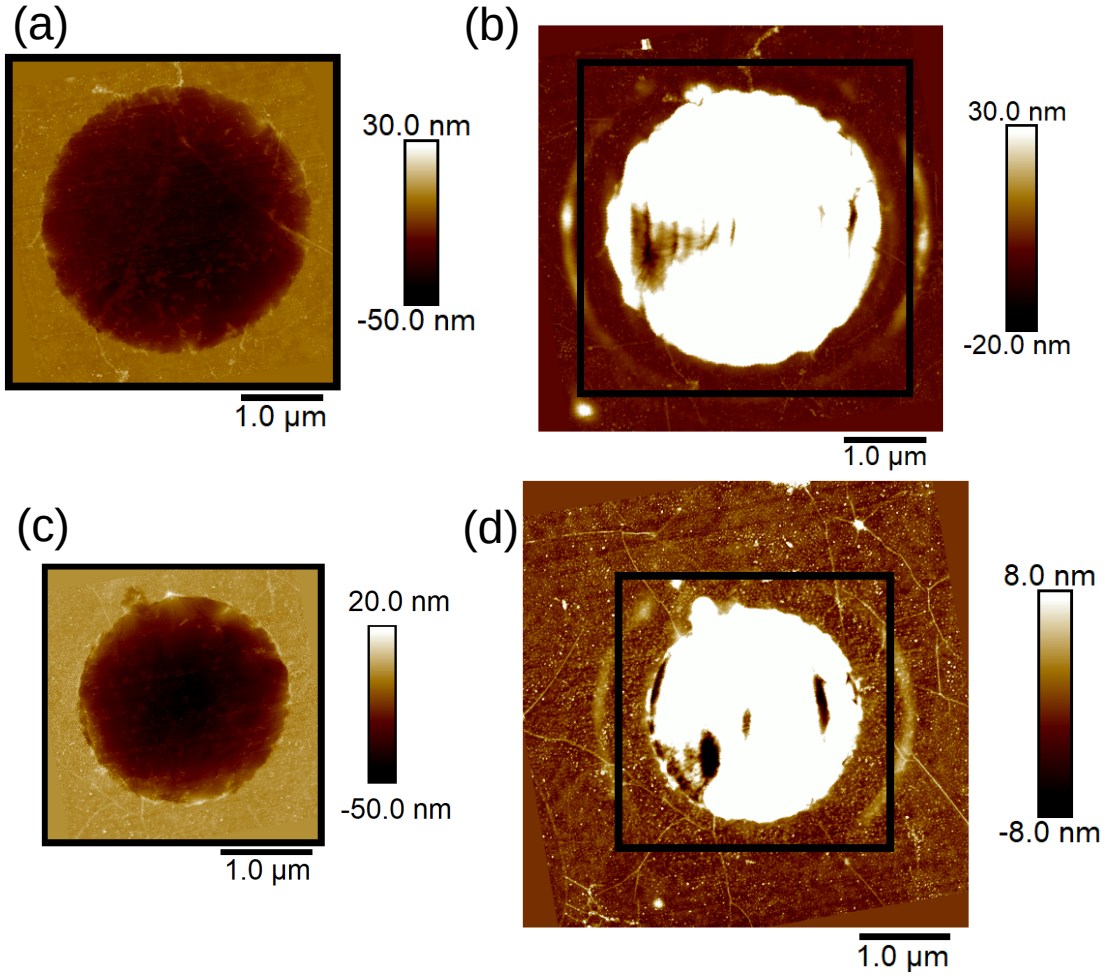

FIGURE 18 AFM images before (a,c) and after (b,d) optical forging of suspended graphene. Graphene in (b) was irradiated with 60 pJ pulse energy and with 10 s irradiation time per point. In (d) pulse energy was also 60 pJ and 3 s irradiation time per point. Black squares in each image shows the exposed area.

before the forging process. The rings can be seen to clearly follow the shape of the opening instead of the written square shape. This structure can be observed only when the membranes are forged with a high dose. The structure formation is similar to the effect seen with blisters, where the ring structure forms outside of the maximum intensity of the laser beam. However, the scale of the effect seen in Figure 18 is much larger. In fact, at some regions of the rings the graphene was not exposed to the pulsed laser light at all, but the structures are formed nevertheless. This is another example how there are long-range effects related to optically forged graphene that are best explained by strain relaxation.

A closer look at what happens to graphene that is optically forged on Si_3N_4 substrate is presented in Figure 19. Figures 19(a) and 19(b) are zoomed in to the top right corner of the images in Figures 14(a) and 14(b) respectively. Figure 19(b) shows that after optical forging process there is more roughness on the surface due to particle-like features. The features resemble more two-photon oxidized graphene than optically forged graphene on SiO_x. [339] These could be redeposition of particles that are removed from the membrane during forging. Removal of the particles can be seen from Figures 14(a) and 14(b), as well as from Figure 15(a) and 15(b), which was forged using a lower dose. Even though the residues are removed in Figure 15(b), there does not appear to be a similar change in roughness as in Figure 19. In fact, the substrate in Figure 15(b) appears to be slightly cleaner than in 15(a), indicating that the change is not due to redeposition. Another solution could be that this could be the result of optical forging of graphene on silicon nitride surface, similar to lifting from the substrate as seen with graphene on SiO_x. In article [AIV] the patterns made with similar doses are about 40 nm high. However, adhesion energy of graphene is almost six times

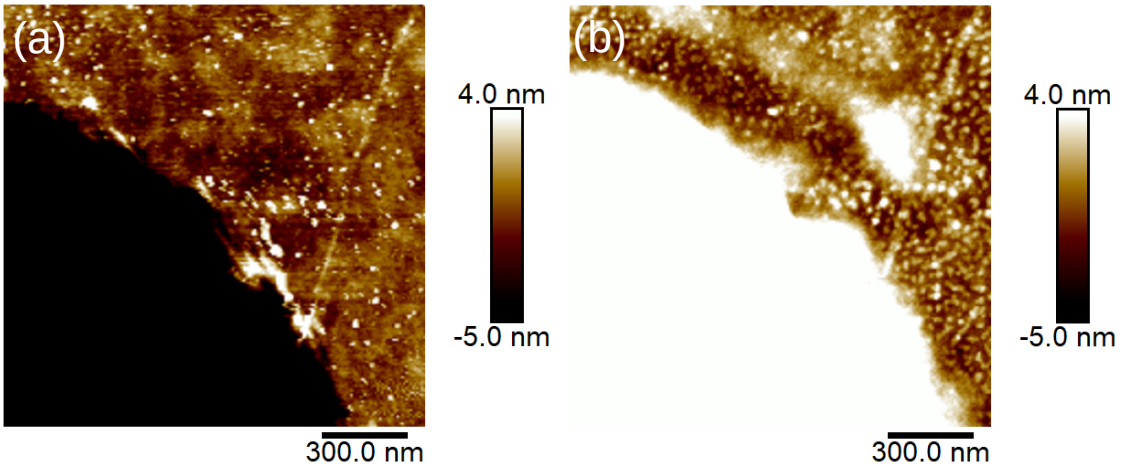

FIGURE 19 Effect of optical forging of graphene on silicon nitride substrate (a) before and (b) after the process. The graphene membrane was irradiated with 60 pJ pulse energy, 10 s exposure time per spot and 100 nm spot separation. The panels (a) and (b) are images zoomed into the top right corners of Figures 14(a) and 14(b) respectively.

larger on silicon nitride than on silicon oxide, [344] and therefore, if the structures resulted from optical forging process are caused by detachment and bulging of graphene, the pulsed laser dose should also be larger in order to cause the same effect. It is worth to note that the roughening is more clear near openings where forging causes the ring structure presented in Figure 18, as they should if they are caused by the assumed mechanism of lattice expansion.

5 PROPERTIES OF OPTICALLY FORGED GRAPHENE

While being able to pattern three-dimensional shapes out of graphene is in itself interesting, it is important to take a look at some of the properties of optically forged graphene. While optical forging likely alters most of the properties, in here those are narrowed into optical and mechanical properties. Additionally, the emphasis is on those properties that differ most from pristine graphene.

5.1 Optical properties

Oftentimes the fastest way to see the effect of optical forging is by simply using an optical microscope. This can be seen for example from Figure 9(b), which shows an optical microscope image of a pattern set made using optical forging. In Figure 9(b) the forged patterns turn brighter as the height of the patterns increase. The color change has been investigated by reflection spectroscopy, and it was concluded that this was caused simply by the changed interference due to height change. [345] That is, instead of graphene forming a cavity with the silicon surface, with SiO_x layer acting as a spacer, in the forged case the spacer thickness is defined as a sum of the SiO_x and the pattern height.

The situation is slightly different when graphene is suspended. Figure 20 shows optical microscope images of suspended graphene membranes before and after the optical forging. Figure 20(a) shows the sample before the optical forging process. This shows a typical behaviour of graphene, which does not reflect light almost at all. [16] In Figure 20(b) the membrane in the middle of the image has been optically forged and it shows up very clearly in the image. Naturally, this change cannot be due to interference. Reflectivity of the membrane was measured to be about 10 % (not shown here), which is of course a huge increase. Reflectivity is also larger in membranes that have been forged with higher dose. The reason for this increase is not yet clear. More detailed measurements as well as theoretical explanation of the behavior is still ongoing work.

In addition to the change in reflectivity, optical forging causes significant

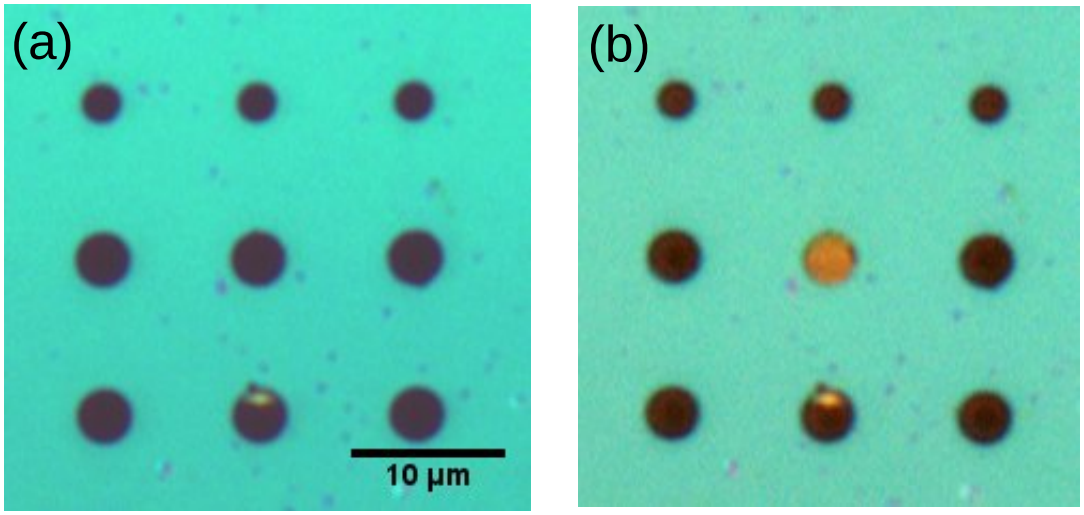

FIGURE 20 Optical microscope images of suspended graphene (a) before and (b) after optical forging with 60 pJ pulse energy, 10 s irradiation time per spot and 100 nm spot separation. Note that only the membrane in the center of the images was patterned.

changes in Raman spectrum, as presented in [AIV]. Spectra measured from optically forged patterns are presented in Figure 21(a). As was mentioned in section 4.3.3, these changes can be used to determine that optical forging causes a decrease in graphene crystallite size. However, there is also a very clear increase of the background photoluminescence signal that is very wide, spanning the entire spectrum's range. The signal is also quite intensive. Integrated intensity of this luminescence signal from a pattern made with the highest dose is more than 400 times more intense than integrated intensity of pristine graphene G band.

Normalized photoluminescence spectra gained from the Raman spectra are presented in Figure 21(b). These show clearly how the signal is very wide. Note that the entire spectra in Figure 21(b) were gathered using two excitation lasers, 532 nm for the short wavelength part and 633 nm for the high wavelength tail, and the stitching of these two sections is not perfect. Peaks of the spectra are in the range of $580 - 600$ nm. As was discussed earlier, optical forging causes defects to graphene lattice, and with high irradiation doses graphene crystallite size decreases. This coincides with increasing photoluminescence intensity, as can be seen from Figures 12(a) and 12(d). In article [AIV] it was proposed that the photoluminescence could be the result of graphene crystallite size becoming so small that they become similar to quantum dots. There are several studies about graphene quantum dots (GQDs), which do show that the photoluminescence from the GQDs is similar to optically forged graphene shown in Figure 21(b). [346–348] However, there are no atomic resolution images to confirm this. Bandgap of the GQDs, and therefore the emission wavelength, is defined by quantum confinement effect, and therefore the size of the QCDs strongly affects the luminescence. [349–351] In literature GQDs with similar photoluminescence spectra are just a few nanometers in size, while smallest crystallite size inferred

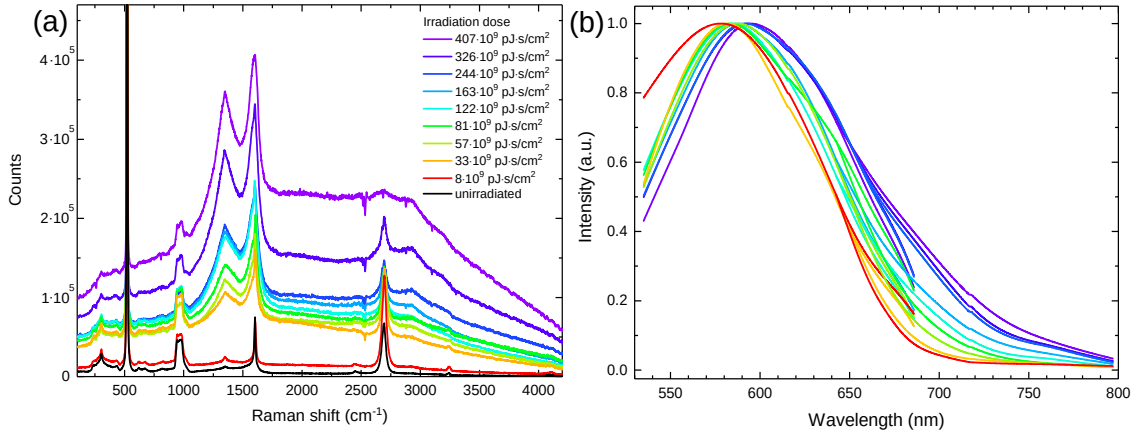

FIGURE 21 (a) Raman spectra from graphene patterns processed using optical forging with various irradiation doses. (b) Luminescence spectra extracted from the Raman spectra. Intensities of the spectra are normalized to better visualize the shape and shift of peak positions. Reprinted with permission from [AIV]. Copyright © 2020 American Chemical Society.

from optically forged graphene is about 10 nm. This value is estimated from the Raman spectra and therefore it is an averaged value from the laser spot area and it is likely that there is a wide crystallite size distribution in this area. Therefore it is feasible that there are graphene crystallites in the $1-2$ nm range. The luminescence peak shifts towards red with increasing irradiation dose in Figure 21(b), which might at first glance seem contradictory to the GQD explanation. However, if the crystallite size distribution is shifting towards smaller sizes, the amount of large luminescent domains will increase faster, resulting in a shift towards red. However, it should be stated that quantum confinement is not the only underlying luminescence mechanism. Besides the core of the GQDs, various different aspects, such as defects, heteroatom doping and chemical environment, affect their properties. [352–355] Since at the moment there is no detailed atomic information about optically forged graphene, making comparisons to GQDs in literature is difficult.

Additionally, it is not clear what is the impact of amorphous carbon residues that appear on forged graphene. There are similarities in photoluminescence spectra of optically forged graphene and those measured from amorphous carbon films. [356,357] In a more recent study monolayer amorphous carbon was synthesized and characterized. [358] Since both Raman and photoluminescence spectra from this material resemble graphene that has been optically forged with high dose, they are likely very similar. This does not indicate whether the 3D shape of the structures is caused by deposition, since in reference [358] the monolayer films exhibited high Raman and photoluminescence intensities. It is possible that forged patterns could have a luminescent amorphous carbon crust, but this does not explain all the features that appear, for example on suspended graphene, as discussed in 4.3.4. Additionally, there is no direct correlation between heights of the patterns and their photoluminescence intensity, but patterns with the same

height can have quite different looking spectra, some exhibiting photoluminescence and some not.

Interestingly, atomic resolution images in reference [358] showed that the monolayer amorphous carbon has some amount of small $1-2$ nm graphene-like crystalline domains, which does not actually differ much from the earlier GQD explanation. The difference between these two explanations is whether graphene or the amorphous carbon deposits cause the luminescence. Unfortunately, differentiation between these has not been successful yet. The main reason for this is that, despite of several attempts, amorphous carbon has not been deposited onto SiOx without graphene, but graphene is seemingly needed as a catalyst. However, graphene alone is not enough either, since amorphous carbon is not deposited when graphene is on Si_3N_4 substrate. More insight to this can be gained by doing atomic resolution imaging on the optically forged graphene membranes.

5.2 Mechanical properties

Mechanical properties of a suspended graphene membrane can be probed using nanoindentation. Figure 22 shows typical force curves for pristine graphene, optically forged graphene and Si_3N_4 substrate. The curve from pristine graphene shows the normal situation with suspended graphene membranes, where the initial increase in force is very small, even though the membrane is pressed down several tens of nanometers, because bending stiffness of graphene is very low. The completely opposite case is measured from substrate, where the force increases very rapidly. Here it can be assumed that the sample does not bend at all, and that the force curve behaviour comes purely from cantilever bending. The middle curve is from graphene after laser treatment showing behaviour that is different from the others. This membrane has a higher bending stiffness than the pristine graphene, however the membrane still bends to some extent unlike the substrate. [AV]

First of all, looking at the adhesive regime of the force curves can give some interesting qualitative information. Figure 22(b) shows the same curves as in Figure 22(a), but zoomed into near zero force and indentation depth. The point where both force and indentation depth are zero is the zero point of indentation, and the region where both of them are negative is the adhesive regime. The curves show that the materials behave differently already at the adhesion regime. Pristine graphene does not cause almost any cantilever deflection in this scale. When graphene is optically forged using a high dose, the force drop is quite sudden. The shape is different compared to behavior of the silicon nitride substrate in Figure 22, where the force drops gradually as the tip moves closer to the surface. All of these different behaviors can be explained with bending of the sample. With the silicon nitride substrate, as the cantilever approaches the surface, the nitride is too stiff to flex upwards. Therefore the cantilever bends

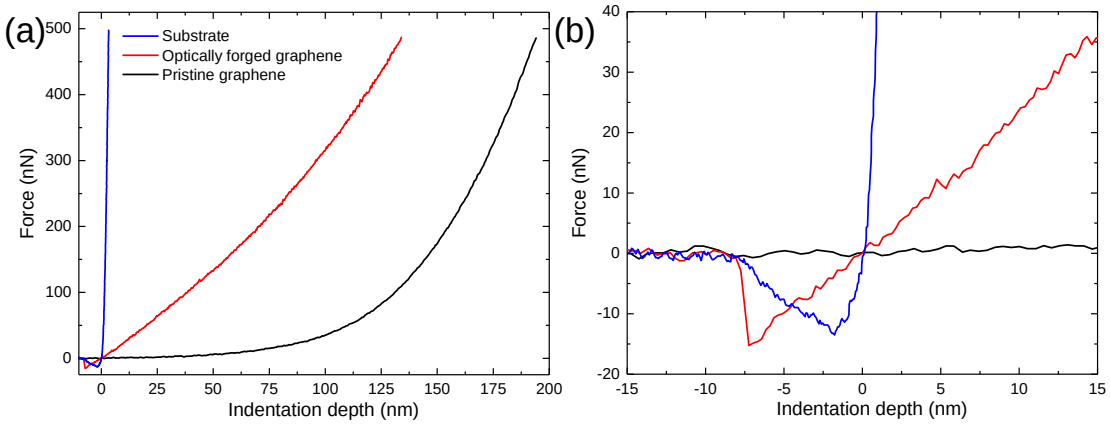

FIGURE 22 Force-displacement curves for Si_3N_4 substrate (blue), pristine graphene (black), and same graphene membrane after optical forging (red). Optical forging was done using 60 pJ pulse energy, 10 s irradiation time per spot and 100 nm separation between spots. This membrane is the same as in Figure 14.

more and more downwards gradually as the tip approaches the surface and the attractive interactions are felt more strongly, until the tip gets so close that the repulsive interactions start to take over. In the case of optically forged graphene the sample is dynamic. As the tip approaches the membrane and they start to feel the attractive forces, both of them bend towards each other, which further increases the attractive forces causing them to snap-in quickly, leading to the sudden drop in force. At this point the membrane is tensed and as the tip moves further down the tension is released causing the force to become less negative. With pristine graphene the bending stiffness of the membrane is too low to cause any significant bending of the cantilever, because when the tip gets close enough of the surface to feel the attractive forces, it is too close to tense the membrane enough to cause any cantilever bending. The force curve of optically forged graphene is much more linear compared to pristine graphene, which also indicates increased bending stiffness, as discussed in section 3.2.

More indentation data is presented in Figure 23. The shape of the membranes in AFM images is different, even though membranes in 23(b) and 23(d) were processed using the same optical forging parameters. It is possible that the laser was at a different focus when they were processed. In any case, the force curves seems to be affected more by how much the graphene membrane is corrugated rather than the optical forging dose, though in every case linearity of the force curve increases when the membrane is forged. The membrane in Figure 23(a) is only slightly corrugated at the lower part of the membrane (as can be seen from Figure 15 as well). The membrane in 23(c) has a ring-like feature near the edge and 23(e) has clearly a wavy structure. Changes in force curves after forging follow this trend with curve in 23(b) being almost the same as before forging, curve in 23(d) being a bit more linear and 23(f) being clearly more linear. The red curve in Figure 22(a) shows the force curve of a membrane that was forged with even higher dose, showing even more clear change.

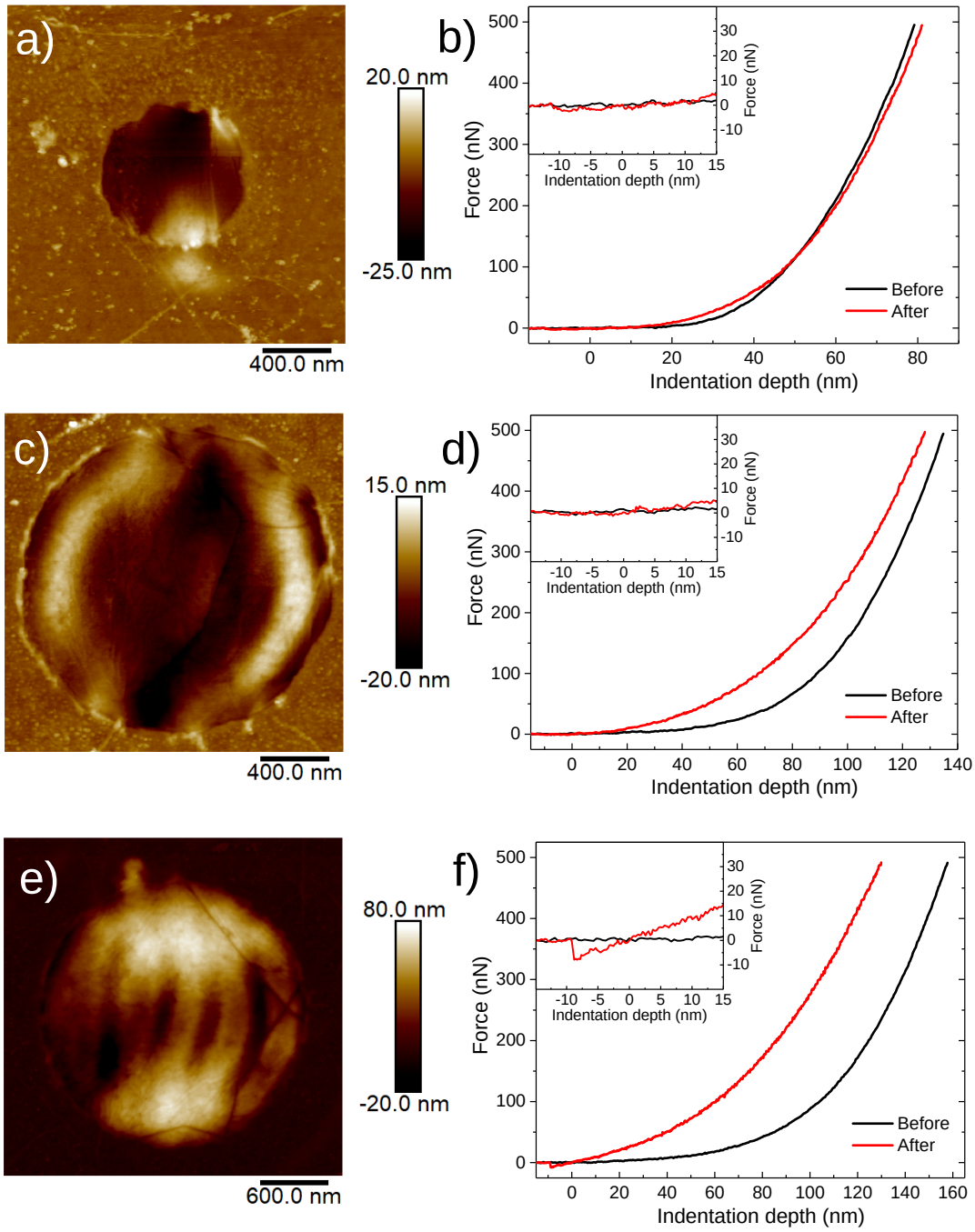

FIGURE 23 AFM images and corresponding force curves from optically forged graphene membranes. With every membrane pulse energy was 60 pJ and spot separation 100 nm. Irradiation time per spot in (a,b) and (c,d) was 2 s and in (e,f) 3 s. Reprinted with permission from [AV]. Copyright © 2021, The Authors.

In article [AV] mechanical properties of graphene membranes were calculated by fitting equation 4 to the force curves. Elastic stiffness results calculated from the fits are presented in Figure 24. Before forging, two-dimensional elastic

constant (E^{2D}) determined from the center of normal distribution fit to the data is 315 N/m. This corresponds to Young's modulus of 0.94 TPa, assuming graphene thickness of 0.335 nm. There are two openings, which have elastic constant values of about 250 N/m, and if these are excluded the center of the distribution shifts to 350 N/m (1.05 TPa), which is very close to 2D elastic stiffness values reported before. [13] After forging, the distribution is centered to 143 N/m (0.42 TPa), less than half of pristine graphene. In previous studies Young's modulus has been found to either decrease or increase when defect density increases, important aspect here being type of the defect with monovacancies increasing the stiffness and others types decreasing it. [277, 359–361]

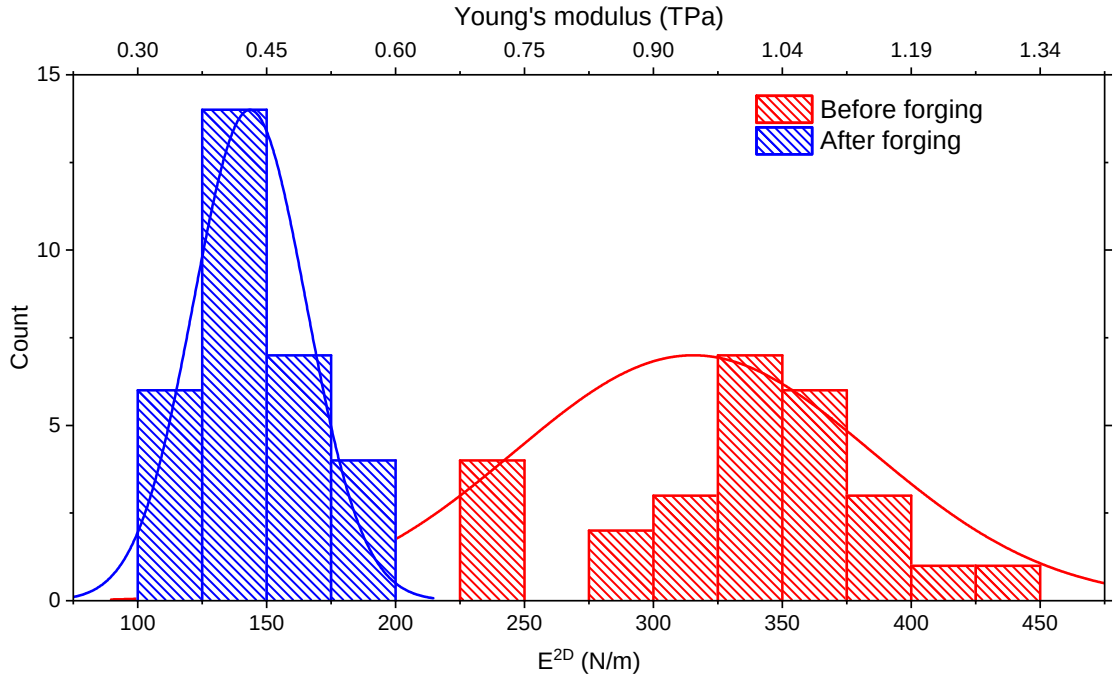

FIGURE 24 Histogram of E^{2D} calculated from indentation curves of graphene membranes before (red) and after (blue) optical forging. Data is gathered from eight different membranes. Solid lines are normal distributions fitted to the two data sets.

However, the most interesting finding of article [AV] is the increase of bending stiffness of graphene. In order to calculate the bending stiffness, pre-stresses of the membranes were first determined from the Raman spectra using the procedure detailed in section 3.3.2. Bending stiffnesses were then estimated from the linear term of equation 2. Bending stiffnesses for membranes in Figure 23 were calculated to be 3 keV (a,b), 19 keV (c,d) and 93 keV (e,f), and for a membrane shown in Figures 14 and 22 it is 790 keV. It needs to be noted that the smallest bending stiffness values that can be reliably measured are about 20 keV, estimated from noise level of the system. Therefore all that can be said from the low bending stiffness membranes (Figures 23(a-d)) is that their stiffnesses are somewhere under 20 keV. However, bending stiffnesses of the two other membranes

are well above this. They are very high compared to pristine graphene bending stiffness, which is $1 - 2$ eV. Already 93 keV is very high compared to this, but the 790 keV value is extremely high, five orders of magnitude larger. This is also two orders of magnitude larger than highest previously reported from rippled graphene. [274] The indentation experiments were studied further by using computer simulations in article [AV]. These simulations show that the stiffness comes from the corrugated shape of the membranes. Interestingly, the simulations also indicate that optical forging increases the stiffness in nanoscale as well. For the future work, in order to gain more detailed understanding of the underlying mechanisms behind the stiffening, atomic resolution imaging of the optically forged membranes is necessary.

6 CONCLUSIONS

In this thesis, I have studied a novel graphene modification technique called optical forging. This is an all optical method, where graphene is irradiated using femtosecond laser pulses in an inert atmosphere. It is presented how optical forging causes graphene to bulge into three-dimensional shapes and structures. The most simple structure that can be fabricated with this is a blister, which is made by irradiating a single spot. The shape of the blister can be controlled by adjusting process parameters, most important of which are pulse energy and irradiation time per spot. Blisters made with different parameters exhibit various different shapes, such as domes, ring structures and mixes of these. Some of the features in the blisters are below the diffraction limit. Large three-dimensional patterns can be made by doing multiple single spot irradiations close to each others, which introduces another patterning parameter: separation between the spots. Various different structures, such as step-pyramid, gratings and spirals, can be fabricated with the optical forging method.

It was determined that optical forging causes formation of defects in the graphene lattice. Detailed analysis of Raman spectra of patterns fabricated using the optical forging method revealed that with lower doses mainly point defects are formed, which then develop into line defects when higher doses are used. This causes a significant decrease in size of the graphene crystals within the irradiated area. With the help of computer simulations, formation of the three-dimensional structures were explained by defect induced lattice expansion, which causes local straining of graphene and eventually bulging from the substrate surface. However, it is clear that this is not the only reason for the height of the patterns, but there is also some amount of amorphous carbon deposition. It is not yet clear how much either of these contribute to the entire three-dimensional structure and more studies are needed to determine it.

Optically forged patterns in graphene are measured to be photoluminescent. The luminescence tends to become more intensive as the patterns are more heavily forged, however this is not true in every case. There are two feasible explanations for the luminescence. First of these is that graphene is being cut into nanometer-scale crystals and thus becomes luminescent in a similar way as

graphene quantum dots. The other possible explanation is that a thin amorphous carbon layer is deposited onto the graphene during the pulsed laser irradiation. From luminescence point of view these are very similar with the same atomic structure and bandgap.

Optical forging also makes graphene much more stiffer to bend. The highest bending stiffness measured from an optically forged membrane was 790 keV, which is five orders of magnitude higher than pristine graphene. This is due to the structure of the graphene membrane, which becomes highly corrugated with high irradiation doses. At the same time the elastic modulus decreases, but not more than half of the original value.

From fundamental research point of view, there is more to be learnt from the mechanism of how the structures are formed and their properties. More suspended membranes should be studied by processing them with wider range of patterning parameters. This would help to better understand how these structures form and how the mechanical properties develop as a result of this. For example, one interesting experiment would be to test the breaking strength of optically forged graphene membranes. This was not studied here because there was a need to do other characterizations of the membranes after the indentations, and breaking them would obviously prevent any additional measurements afterwards. Since the forming of optically forged patterns behaves differently when graphene is on Si_3N_4 compared to SiO_x, testing the processing with graphene that is on other substrates can give revealing information about the process. Additionally, since there is some evidence that amorphous carbon is deposited by a chemical process where graphene is a catalyst, it would be interesting to test the optical forging process at different temperatures, pressures and sample bias voltages. A different research avenue is to study optical forging of other two-dimensional materials. This has been already tested to a small extent and preliminary results indicate that optical forging is universal to two-dimensional materials. However, the most important step forwards in terms of understanding the mechanism at work in optical forging is atomic resolution imaging. While a lot of information can be gained from Raman spectroscopy and simulating the structure formation, direct imaging will give information of how graphene lattice structure is altered and what defect types are involved, and if they develop into lines. This will be a difficult experiment, since ideally there should be thorough characterization of the membranes before as well as after the optical forging process. The forging dose has to be correct for imaging, so that the defect density is not too low or too high, i.e. the sample should not be fully amorphous, but there should be sufficient amount of defects so that there is a good chance of finding them. In addition, the samples need to be relatively clean from residues, which might not be the case after heavy irradiation doses, though suspended samples shown in this work seem to be sufficiently clean.

Optically forged graphene can potentially be used in various applications. First of all, even though the optical forging process decreases the elastic modulus of graphene, the optically forged structures are still strong and very thin. Since the bending stiffness is dramatically increased they can be used as strong but ul-

tralight scaffold structures. As a different approach, since the smallest structures that can be made with optical forging are in range of 100 nm, it could be to used to create structures that can act as plasmonic devices. Stiffening of a graphene membrane can also be used to increase the resonance frequency of graphene resonator devices. Since the resonance frequency is related to bending stiffness by $f \propto \sqrt{D}$, [362] the membranes with large bending stiffness can be expected to have much higher resonance frequencies, perhaps even up to GHz range. Additionally, similarly as graphene kirigami structures were used by Blees et al., [274] optically forged graphene could be used to make ultralight nanoscale springs and other NEMS devices, or to combine these by adjusting the stiffness of kirigami devices with forging or using forging to enable new types of kirigami structures.

As the final note, since the optical forging method bulges the material due to lattice expansion, is not exclusive only to graphene, but other 2D materials can be modified in similar fashion, and in preliminary studies this has been successful. Additional research avenues for further research would be to study how optical forging works on bi- and multilayer materials, 2D heterostructures and nanotubes.

REFERENCES

[1] A. K. Geim and K. S. Novoselov. The rise of graphene. *Nat. Mater.*, 6:183 – 191, 2007.

[2] A. K. Geim. Graphene: Status and prospects. *Science*, 324(5934):1530–1534, 2009.

[3] Edward P. Randviir, Dale A.C. Brownson, and Craig E. Banks. A decade of graphene research: production, applications and outlook. *Mater. Today*, 17(9):426 – 432, 2014.

[4] K. S. Novoselov, A. K. Geim, S. V. Morozov, D. Jiang, Y. Zhang, S. V. Dubonos, I. V. Grigorieva, and A. A. Firsov. Electric field effect in atomically thin carbon films. *Science*, 306(5696):666–669, 2004.

[5] K. S. Novoselov, A. K. Geim, S. V. Morozov, D. Jiang, M. I. Katsnelson, I. V. Grigorieva, S. V. Dubonos, and A. A. Firsov. Two-dimensional gas of massless dirac fermions in graphene. *Nature*, 438:197–200, 2005.

[6] K. S. Novoselov, D. Jiang, F. Schedin, T. J. Booth, V. V. Khotkevich, S. V. Morozov, and A. K. Geim. Two-dimensional atomic crystals. *Proc. Natl. Acad. Sci.*, 102(30):10451–10453, 2005.

[7] Yuanbo Zhang, Yan-Wen Tan, Horst L. Stormer, and Philip Kim. Experimental observation of the quantum hall effect and berry's phase in graphene. *Nature*, 438:201–204, 2005.

[8] Alexander A. Balandin, Suchismita Ghosh, Wenzhong Bao, Irene Calizo, Desalegne Teweldebrhan, Feng Miao, and Chun Ning Lau. Superior thermal conductivity of single-layer graphene. *Nano Lett.*, 8(3):902–907, 2008.

[9] Weiwei Cai, Arden L. Moore, Yanwu Zhu, Xuesong Li, Shanshan Chen, Li Shi, and Rodney S. Ruoff. Thermal transport in suspended and supported monolayer graphene grown by chemical vapor deposition. *Nano Lett.*, 10(5):1645–1651, 2010.

[10] Shanshan Chen, Arden L. Moore, Weiwei Cai, Ji Won Suk, Jinho An, Columbia Mishra, Charles Amos, Carl W. Magnuson, Junyong Kang, Li Shi, and Rodney S. Ruoff. Raman measurements of thermal transport in suspended monolayer graphene of variable sizes in vacuum and gaseous environments. *ACS Nano*, 5(1):321–328, 2011.

[11] Alexander A. Balandin. Thermal properties of graphene and nanostructured carbon materials. *Nat. Mater.*, 10:569 – 581, 2011.

[12] Shanshan Chen, Qingzhi Wu, Columbia Mishra, Junyong Kang, Hengji Zhang, Kyeongjae Cho, Weiwei Cai, Alexander A. Balandin, and Rodney S.

Ruoff. Thermal conductivity of isotopically modified graphene. *Nat. Mater.*, 11:203 – 207, 2012.

[13] Changgu Lee, Xiaoding Wei, Jeffrey W. Kysar, and James Hone. Measurement of the elastic properties and intrinsic strength of monolayer graphene. *Science*, 321(5887):385–388, 2008.

[14] Hamzeh Kashani, Yoshikazu Ito, Jiuhui Han, Pan Liu, and Mingwei Chen. Extraordinary tensile strength and ductility of scalable nanoporous graphene. *Sci. Adv.*, 5(2), 2019.

[15] Dimitrios G. Papageorgiou, Ian A. Kinloch, and Robert J. Young. Mechanical properties of graphene and graphene-based nanocomposites. *Prog. Mater. Sci.*, 90:75 – 127, 2017.

[16] R. R. Nair, P. Blake, A. N. Grigorenko, K. S. Novoselov, T. J. Booth, T. Stauber, N. M. R. Peres, and A. K. Geim. Fine structure constant defines visual transparency of graphene. *Science*, 320(5881):1308–1308, 2008.

[17] Y.-M. Lin, C. Dimitrakopoulos, K. A. Jenkins, D. B. Farmer, H.-Y. Chiu, A. Grill, and Ph. Avouris. 100-GHz transistors from wafer-scale epitaxial graphene. *Science*, 327(5966):662–662, 2010.

[18] Changyao Chen, Sami Rosenblatt, Kirill I. Bolotin, William Kalb, Philip Kim, Ioannis Kymissis, Horst L. Stormer, Tony F. Heinz, and James Hone. Performance of monolayer graphene nanomechanical resonators with electrical readout. *Nat. Nanotechnol.*, 4:861 – 867, 2009.

[19] Minkyung Jung, Peter Rickhaus, Simon Zihlmann, Alexander Eichler, Peter Makk, and Christian Schönenberger. GHz nanomechanical resonator in an ultraclean suspended graphene p-n junction. *Nanoscale*, 11:4355–4361, 2019.

[20] Meryl D. Stoller, Sungjin Park, Yanwu Zhu, Jinho An, and Rodney S. Ruoff. Graphene-based ultracapacitors. *Nano Lett.*, 8(10):3498–3502, 2008.

[21] Wen Yang, Mei Ni, Xin Ren, Yafen Tian, Ning Li, Yuefeng Su, and Xiaoling Zhang. Graphene in supercapacitor applications. *Curr. Opin. Colloid Interface Sci.*, 20(5):416 – 428, 2015.

[22] Qingqing Ke and John Wang. Graphene-based materials for supercapacitor electrodes - A review. *Journal of Materiomics*, 2(1):37 – 54, 2016.

[23] Feng Wang, Yuanbo Zhang, Chuanshan Tian, Caglar Girit, Alex Zettl, Michael Crommie, and Y. Ron Shen. Gate-variable optical transitions in graphene. *Science*, 320(5873):206–209, 2008.

[24] Fengnian Xia, Thomas Mueller, Roksana Golizadeh-Mojarad, Marcus Freitag, Yu-ming Lin, James Tsang, Vasili Perebeinos, and Phaedon Avouris. Photocurrent imaging and efficient photon detection in a graphene transistor. *Nano Lett.*, 9(3):1039–1044, 2009.

[25] F. Bonaccorso, Z. Sun, T. Hasan, and A. C. Ferrari. Graphene photonics and optoelectronics. *Nat. Photonics*, 4:611 – 622, 2010.

[26] A. H. Castro Neto, F. Guinea, N. M. R. Peres, K. S. Novoselov, and A. K. Geim. The electronic properties of graphene. *Rev. Mod. Phys.*, 81:109–162, 2009.

[27] M. I. Katsnelson, K. S. Novoselov, and A. K. Geim. Chiral tunnelling and the Klein paradox in graphene. *Nat. Phys.*, 2:620 – 625, 2006.

[28] K.I. Bolotin, K.J. Sikes, Z. Jiang, M. Klima, G. Fudenberg, J. Hone, P. Kim, and H.L. Stormer. Ultrahigh electron mobility in suspended graphene. *Solid State Commun.*, 146(9):351 – 355, 2008.

[29] Xu Du, Ivan Skachko, Anthony Barker, and Eva Y. Andrei. Approaching ballistic transport in suspended graphene. *Nat. Nanotechnol.*, 3:491 – 495, 2008.

[30] Graphene Flagship. How strong is graphene? https://graphene-flagship.eu/how-strong-is-graphene, 2016. (accessed: 18.08.2020).

[31] R. Al-Jishi and G. Dresselhaus. Lattice-dynamical model for graphite. *Phys. Rev. B*, 26:4514–4522, 1982.

[32] Engineering ToolBox. Young's modulus - tensile and yield strength for common materials. https://www.engineeringtoolbox.com/young-modulus-d_417.html, 2003. (accessed: 29.09.2020).

[33] Seoung-Ki Lee, Beom Joon Kim, Houk Jang, Sung Cheol Yoon, Changjin Lee, Byung Hee Hong, John A. Rogers, Jeong Ho Cho, and Jong-Hyun Ahn. Stretchable graphene transistors with printed dielectrics and gate electrodes. *Nano Lett.*, 11(11):4642–4646, 2011.

[34] Juhua Liu, Yaohua Yi, Yihua Zhou, and Huafei Cai. Highly stretchable and flexible graphene/ITO hybrid transparent electrode. *Nanoscale Res. Lett.*, 11:108, 2016.

[35] Nan Liu, Alex Chortos, Ting Lei, Lihua Jin, Taeho Roy Kim, Won-Gyu Bae, Chenxin Zhu, Sihong Wang, Raphael Pfattner, Xiyuan Chen, Robert Sinclair, and Zhenan Bao. Ultratransparent and stretchable graphene electrodes. *Sci. Adv.*, 3(9), 2017.

[36] Russell Kai Liang Tan, Sean P. Reeves, Niloofar Hashemi, Deepak George Thomas, Emrah Kavak, Reza Montazami, and Nicole N. Hashemi. Graphene as a flexible electrode: review of fabrication approaches. *J. Mater. Chem. A*, 5:17777–17803, 2017.

[37] Long Ju, Baisong Geng, Jason Horng, Caglar Girit, Michael Martin, Zhao Hao, Hans A. Bechtel, Xiaogan Liang, Alex Zettl, Y. Ron Shen, and Feng

Wang. Graphene plasmonics for tunable terahertz metamaterials. *Nat. Nanotechnol.*, 6:630 – 634, 2011.

[38] Yibo Yan, Jun Gong, Jie Chen, Zhiping Zeng, Wei Huang, Kanyi Pu, Jiyang Liu, and Peng Chen. Recent advances on graphene quantum dots: From chemistry and physics to applications. *Adv. Mater.*, 31(21):1808283, 2019.

[39] Chi-Fan Chen, Cheol-Hwan Park, Bryan W. Boudouris, Jason Horng, Baisong Geng, Caglar Girit, Alex Zettl, Michael F. Crommie, Rachel A. Segalman, Steven G. Louie, and Feng Wang. Controlling inelastic light scattering quantum pathways in graphene. *Nature*, 471:617–620, 2011.

[40] Kin Fai Mak, Long Ju, Feng Wang, and Tony F. Heinz. Optical spectroscopy of graphene: From the far infrared to the ultraviolet. *Solid State Commun.*, 152(15):1341 – 1349, 2012.

[41] Charles Kittel. *Introduction to Solid State Physics*. John Wiley & Sons, Ltd, 8th edition, 2004.

[42] Pablo A. Denis and Federico Iribarne. Comparative study of defect reactivity in graphene. *J. Phys. Chem. C*, 117(37):19048–19055, 2013.

[43] Ali Eftekhari and Hermenegildo Garcia. The necessity of structural irregularities for the chemical applications of graphene. *Mater. Today Chem.*, 4:1 – 16, 2017.

[44] Shwetank Yadav, Zhihui Zhu, and Chandra Veer Singh. Defect engineering of graphene for effective hydrogen storage. *Int. J. Hydrogen Energy*, 39(10):4981 – 4995, 2014.

[45] Jie Jiang, Tao Xu, Junpeng Lu, Litao Sun, and Zhenhua Ni. Defect engineering in 2D materials: Precise manipulation and improved functionalities. *Research*, 2019. 4641739.

[46] Y. Kopelevich, S. Bud'ko, Daniel R. Cooper, Benjamin D'Anjou, Nageswara Ghattamaneni, Benjamin Harack, Michael Hilke, Alexandre Horth, Norberto Majlis, Mathieu Massicotte, Leron Vandsburger, Eric Whiteway, and Victor Yu. Experimental review of graphene. *Int. Scholarly Res. Not.*, 3, 2012. 501686.

[47] Min Yi and Zhigang Shen. A review on mechanical exfoliation for the scalable production of graphene. *J. Mater. Chem. A*, 3:11700–11715, 2015.

[48] Sungjin Park and Rodney S. Ruoff. Chemical methods for the production of graphenes. *Nat. Nanotechnol.*, 4:217 – 224, 2009.

[49] Longxiu Zhu, Xin Zhao, Yingzhi Li, Xinyi Yu, Chen Li, and Qinghua Zhang. High-quality production of graphene by liquid-phase exfoliation of expanded graphite. *Mater. Chem. Phys.*, 137(3):984 – 990, 2013.

[50] Goki Eda, Giovanni Fanchini, and Manish Chhowalla. Large-area ultrathin films of reduced graphene oxide as a transparent and flexible electronic material. *Nat. Nanotechnol.*, 3:270 – 274, 2008.

[51] Konstantin V. Emtsev, Aaron Bostwick, Karsten Horn, Johannes Jobst, Gary L. Kellogg, Lothar Ley, Jessica L. McChesney, Taisuke Ohta, Sergey A. Reshanov, Jonas Röhrl, Eli Rotenberg, Andreas K. Schmid, Daniel Waldmann, Heiko B. Weber, and Thomas Seyller. Towards wafer-size graphene layers by atmospheric pressure graphitization of silicon carbide. *Nat. Mater.*, 8:203 – 207, 2009.

[52] Roberto Muñoz and Cristina Gómez-Aleixandre. Review of CVD synthesis of graphene. *Chem. Vap. Deposition*, 19(10-11-12):297–322, 2013.

[53] H. Cheun Lee, Wei-Wen Liu, Siang-Piao Chai, Abdul Rahman Mohamed, Azizan Aziz, Cheng-Seong Khe, N. M. S. Hidayah, and U. Hashim. Review of the synthesis, transfer, characterization and growth mechanisms of single and multilayer graphene. *RSC Adv.*, 7:15644–15693, 2017.

[54] Sukang Bae, Hyeongkeun Kim, Youngbin Lee, Xiangfan Xu, Jae-Sung Park, Yi Zheng, Jayakumar Balakrishnan, Tian Lei, Hye Ri Kim, Young Il Song, Young-Jin Kim, Kwang S. Kim, Barbaros Özyilmaz, Jong-Hyun Ahn, Byung Hee Hong, and Sumio Iijima. Roll-to-roll production of 30-inch graphene films for transparent electrodes. *Nat. Nanotechnol.*, 5:574 – 578, 2010.

[55] Xuesong Li, Luigi Colombo, and Rodney S. Ruoff. Synthesis of graphene films on copper foils by chemical vapor deposition. *Adv. Mater.*, 28(29):6247–6252, 2016.

[56] Sami Franssila. *Introduction to Microfabrication*. John Wiley & Sons, Ltd, 2nd edition, 2010.

[57] Li Gao, Jeffrey R. Guest, and Nathan P. Guisinger. Epitaxial graphene on Cu(111). *Nano Lett.*, 10(9):3512–3516, 2010.

[58] Rafik Addou, Arjun Dahal, Peter Sutter, and Matthias Batzill. Monolayer graphene growth on Ni(111) by low temperature chemical vapor deposition. *Appl. Phys. Lett.*, 100(2):021601, 2012.

[59] G Nandamuri, S Roumimov, and R Solanki. Chemical vapor deposition of graphene films. *Nanotechnology*, 21(14):145604, 2010.

[60] Abdeladim Guermoune, Tarun Chari, Filip Popescu, Shadi S. Sabri, Jonathan Guillemette, Helgi S. Skulason, Thomas Szkopek, and Mohamed Siaj. Chemical vapor deposition synthesis of graphene on copper with methanol, ethanol, and propanol precursors. *Carbon*, 49(13):4204 – 4210, 2011.

[61] Zhancheng Li, Ping Wu, Chenxi Wang, Xiaodong Fan, Wenhua Zhang, Xiaofang Zhai, Changgan Zeng, Zhenyu Li, Jinlong Yang, and Jianguo Hou. Low-temperature growth of graphene by chemical vapor deposition using solid and liquid carbon sources. *ACS Nano*, 5(4):3385–3390, 2011.

[62] Zhengzong Sun, Zheng Yan, Jun Yao, Elvira Beitler, Yu Zhu, and James M. Tour. Growth of graphene from solid carbon sources. *Nature*, 468:549 – 552, 2010.

[63] Satoru Suzuki, Yusuke Takei, Kazuaki Furukawa, Gregory Webber, Shinichi Tanabe, and Hiroki Hibino. Graphene growth from spin-coated polymers without a gas. *Jpn. J. Appl. Phys.*, 51:06FD01, 2012.

[64] Gedeng Ruan, Zhengzong Sun, Zhiwei Peng, and James M. Tour. Growth of graphene from food, insects, and waste. *ACS Nano*, 5(9):7601–7607, 2011.

[65] Xuesong Li, Weiwei Cai, Jinho An, Seyoung Kim, Junghyo Nah, Dongxing Yang, Richard Piner, Aruna Velamakanni, Inhwa Jung, Emanuel Tutuc, Sanjay K. Banerjee, Luigi Colombo, and Rodney S. Ruoff. Large-area synthesis of high-quality and uniform graphene films on copper foils. *Science*, 324(5932):1312–1314, 2009.

[66] Xuesong Li, Carl W. Magnuson, Archana Venugopal, Rudolf M. Tromp, James B. Hannon, Eric M. Vogel, Luigi Colombo, and Rodney S. Ruoff. Large-area graphene single crystals grown by low-pressure chemical vapor deposition of methane on copper. *J. Am. Chem. Soc.*, 133(9):2816–2819, 2011.

[67] Libo Gao, Wencai Ren, Jinping Zhao, Lai-Peng Ma, Zongping Chen, and Hui-Ming Cheng. Efficient growth of high-quality graphene films on Cu foils by ambient pressure chemical vapor deposition. *Appl. Phys. Lett.*, 97(18):183109, 2010.

[68] Tuba Oznuluer, Ercag Pince, Emre O. Polat, Osman Balci, Omer Salihoglu, and Coskun Kocabas. Synthesis of graphene on gold. *Appl. Phys. Lett.*, 98(18):183101, 2011.

[69] Peter W. Sutter, Jan-Ingo Flege, and Eli A. Sutter. Epitaxial graphene on ruthenium. *Nat. Mater.*, 7:406–411, 2008.

[70] Junfeng Gao and Feng Ding. The study on the medium-sized carbon islands on Ru(0001) surface. *J. Cluster Sci.*, 26:347–360, 2015.

[71] Johann Coraux, Alpha T N'Diaye, Martin Engler, Carsten Busse, Dirk Wall, Niemma Buckanie, Frank-J Meyer zu Heringdorf, Raoul van Gastel, Bene Poelsema, and Thomas Michely. Growth of graphene on Ir(111). *New J. Phys.*, 11(2):023006, 2009.

[72] H. Hattab, A. T. N'Diaye, D. Wall, G. Jnawali, J. Coraux, C. Busse, R. van Gastel, B Poelsema, T. Michely, F.-J. Meyer zu Heringdorf, and M. Horn-von Hoegen. Growth temperature dependent graphene alignment on Ir(111). *Appl. Phys. Lett.*, 98(14):141903, 2011.

[73] Shu Nie, Andrew L. Walter, Norman C. Bartelt, Elena Starodub, Aaron Bostwick, Eli Rotenberg, and Kevin F. McCarty. Growth from below: Graphene bilayers on Ir(111). *ACS Nano*, 5(3):2298–2306, 2011.

[74] Apostolis Kordatos, Nikolaos Kelaidis, Sigiava Aminalragia Giamini, Jose Marquez-Velasco, Evangelia Xenogiannopoulou, Polychronis Tsipas, George Kordas, and Athanasios Dimoulas. Ab stacked few layer graphene growth by chemical vapor deposition on single crystal Rh(111) and electronic structure characterization. *Appl. Surf. Sci.*, 369:251 – 256, 2016.

[75] E. Miniussi, M. Pozzo, T.O. Menteş, M.A. Niño, A. Locatelli, E. Vesselli, G. Comelli, S. Lizzit, D. Alfé, and A. Baraldi. The competition for graphene formation on Re(0001): A complex interplay between carbon segregation, dissolution and carburisation. *Carbon*, 73:389–402, 2014.

[76] Xianbao Wang, Haijun You, Fangming Liu, Mingjian Li, Li Wan, Shaoqing Li, Qin Li, Yang Xu, Rong Tian, Ziyong Yu, Dong Xiang, and Jing Cheng. Large-scale synthesis of few-layered graphene using CVD. *Chem. Vap. Deposition*, 15(1-3):53–56, 2009.

[77] Hiroki Ago, Yoshito Ito, Noriaki Mizuta, Kazuma Yoshida, Baoshan Hu, Carlo M. Orofeo, Masaharu Tsuji, Ken-ichi Ikeda, and Seigi Mizuno. Epitaxial chemical vapor deposition growth of single-layer graphene over cobalt film crystallized on sapphire. *ACS Nano*, 4(12):7407–7414, 2010.

[78] H.-A. Mehedi, B. Baudrillart, D. Alloyeau, O. Mouhoub, C. Ricolleau, V. D. Pham, C. Chacon, A. Gicquel, J. Lagoute, and S. Farhat. Synthesis of graphene by cobalt-catalyzed decomposition of methane in plasma-enhanced CVD: Optimization of experimental parameters with Taguchi method. *J. Appl. Phys.*, 120(6):065304, 2016.

[79] Xiaohong An, Fangze Liu, Yung Joon Jung, and Swastik Kar. Large-area synthesis of graphene on palladium and their Raman spectroscopy. *J. Phys. Chem. C*, 116(31):16412–16420, 2012.

[80] Soon-Yong Kwon, Cristian V. Ciobanu, Vania Petrova, Vivek B. Shenoy, Javier Bareño, Vincent Gambin, Ivan Petrov, and Suneel Kodambaka. Growth of semiconducting graphene on palladium. *Nano Lett.*, 9(12):3985–3990, 2009.

[81] Libo Gao, Wencai Ren, Huilong Xu, Li Jin, Zhenxing Wang, Teng Ma, Lai-Peng Ma, Zhiyong Zhang, Qiang Fu, Lian-Mao Peng, Xinhe Bao, and Hui-Ming Cheng. Repeated growth and bubbling transfer of graphene with

millimetre-size single-crystal grains using platinum. *Nat. Commun.*, 3:699, 2012.

[82] Byeong-Joo Lee and Goo-Hwan Jeong. Comparative study on graphene growth mechanism using Ni films, Ni/Mo sheets, and Pt substrates. *Appl. Phys. A*, 116:15–24, 2014.

[83] L. Golanski, D. Rouchon, H. Okuno, and P. Fugier. Graphene monolayer produced on Pt reusable substrates for transparent conductive electrodes applications. *Int. J. Nanotechnol.*, 13(8-9):678–684, 2016.

[84] Robert S. Weatherup, Ashwin J. Shahani, Zhu-Jun Wang, Ken Mingard, Andrew J. Pollard, Marc-Georg Willinger, Robert Schloegl, Peter W. Voorhees, and Stephan Hofmann. In situ graphene growth dynamics on polycrystalline catalyst foils. *Nano Lett.*, 16(10):6196–6206, 2016.

[85] Zhiyu Zou, Lei Fu, Xiuju Song, Yanfeng Zhang, and Zhongfan Liu. Carbide-forming groups IVB-VIB metals: A new territory in the periodic table for CVD growth of graphene. *Nano Lett.*, 14(7):3832–3839, 2014.

[86] Alfonso Reina, Stefan Thiele, Xiaoting Jia, Sreekar Bhaviripudi, Mildred S. Dresselhaus, Juergen A. Schaefer, and Jing Kong. Growth of large-area single- and bi-layer graphene by controlled carbon precipitation on polycrystalline Ni surfaces. *Nano Res.*, 2:509–516, 2009.

[87] Alfonso Reina, Xiaoting Jia, John Ho, Daniel Nezich, Hyungbin Son, Vladimir Bulovic, Mildred S. Dresselhaus, and Jing Kong. Large area, few-layer graphene films on arbitrary substrates by chemical vapor deposition. *Nano Lett.*, 9(1):30–35, 2009.

[88] Xuesong Li, Weiwei Cai, Luigi Colombo, and Rodney S. Ruoff. Evolution of graphene growth on Ni and Cu by carbon isotope labeling. *Nano Lett.*, 9(12):4268–4272, 2009.

[89] J.C. Shelton, H.R. Patil, and J.M. Blakely. Equilibrium segregation of carbon to a nickel (111) surface: A surface phase transition. *Surf. Sci.*, 43(2):493 – 520, 1974.

[90] Shanshan Chen, Weiwei Cai, Richard D. Piner, Ji Won Suk, Yaping Wu, Yujie Ren, Junyong Kang, and Rodney S. Ruoff. Synthesis and characterization of large-area graphene and graphite films on commercial Cu-Ni alloy foils. *Nano Lett.*, 11(9):3519–3525, 2011.

[91] Xun Liu, Lei Fu, Nan Liu, Teng Gao, Yanfeng Zhang, Lei Liao, and Zhongfan Liu. Segregation growth of graphene on Cu-Ni alloy for precise layer control. *J. Phys. Chem. C*, 115(24):11976–11982, 2011.

[92] Boya Dai, Lei Fu, Zhiyu Zou, Min Wang, Haitao Xu, Sheng Wang, and Zhongfan Liu. Rational design of a binary metal alloy for chemical vapour

deposition growth of uniform single-layer graphene. *Nat. Commun.*, 2:522, 2011.

[93] Hua Chen, Wenguang Zhu, and Zhenyu Zhang. Contrasting behavior of carbon nucleation in the initial stages of graphene epitaxial growth on stepped metal surfaces. *Phys. Rev. Lett.*, 104:186101, 2010.

[94] Wenhua Zhang, Ping Wu, Zhenyu Li, and Jinlong Yang. First-principles thermodynamics of graphene growth on Cu surfaces. *J. Phys. Chem. C*, 115(36):17782–17787, 2011.

[95] Tianchao Niu, Miao Zhou, Jialin Zhang, Yuanping Feng, and Wei Chen. Growth intermediates for CVD graphene on Cu(111): Carbon clusters and defective graphene. *J. Am. Chem. Soc.*, 135(22):8409–8414, 2013.

[96] A.N. Obraztsov, E.A. Obraztsova, A.V. Tyurnina, and A.A. Zolotukhin. Chemical vapor deposition of thin graphite films of nanometer thickness. *Carbon*, 45(10):2017 – 2021, 2007.

[97] Qiongyu Li, Harry Chou, Jin-Hui Zhong, Jun-Yang Liu, Andrei Dolocan, Junyan Zhang, Yinghui Zhou, Rodney S. Ruoff, Shanshan Chen, and Weiwei Cai. Growth of adlayer graphene on Cu studied by carbon isotope labeling. *Nano Lett.*, 13(2):486–490, 2013.

[98] O. Frank, L. Kavan, and M. Kalbac. Carbon isotope labelling in graphene research. *Nanoscale*, 6:6363–6370, 2014.

[99] Johan Ek Weis, Sara D. Costa, Otakar Frank, and Martin Kalbac. Growth of adlayers studied by fluorination of isotopically engineered graphene. *Phys. Status Solidi (b)*, 251(12):2505–2508, 2014.

[100] Martin Kalbac, Otakar Frank, and Ladislav Kavan. The control of graphene double-layer formation in copper-catalyzed chemical vapor deposition. *Carbon*, 50(10):3682 – 3687, 2012.

[101] Kai Yan, Hailin Peng, Yu Zhou, Hui Li, and Zhongfan Liu. Formation of bilayer bernal graphene: Layer-by-layer epitaxy via chemical vapor deposition. *Nano Lett.*, 11(3):1106–1110, 2011.

[102] Yong Cheol Shin and Jing Kong. Hydrogen-excluded graphene synthesis via atmospheric pressure chemical vapor deposition. *Carbon*, 59:439 – 447, 2013.

[103] Ivan Vlassiouk, Murari Regmi, Pasquale Fulvio, Sheng Dai, Panos Datskos, Gyula Eres, and Sergei Smirnov. Role of hydrogen in chemical vapor deposition growth of large single-crystal graphene. *ACS Nano*, 5(7):6069–6076, 2011.

[104] Maria Losurdo, Maria Michela Giangregorio, Pio Capezzuto, and Giovanni Bruno. Graphene CVD growth on copper and nickel: role of hydrogen in kinetics and structure. *Phys. Chem. Chem. Phys.*, 13:20836–20843, 2011.

[105] Zewdu M. Gebeyehu, Aloïs Arrighi, Marius V. Costache, Clivia M. Sotomayor-Torres, Maria J. Esplandiu, and Sergio O. Valenzuela. Impact of the in situ rise in hydrogen partial pressure on graphene shape evolution during CVD growth of graphene. *RSC Adv.*, 8:8234–8239, 2018.

[106] Sreekar Bhaviripudi, Xiaoting Jia, Mildred S. Dresselhaus, and Jing Kong. Role of kinetic factors in chemical vapor deposition synthesis of uniform large area graphene using copper catalyst. *Nano Lett.*, 10(10):4128–4133, 2010.

[107] Lili Fan, Zhen Li, Xiao Li, Kunlin Wang, Minlin Zhong, Jinquan Wei, Dehai Wu, and Hongwei Zhu. Controllable growth of shaped graphene domains by atmospheric pressure chemical vapour deposition. *Nanoscale*, 3:4946–4950, 2011.

[108] Ivan Vlassiouk, Pasquale Fulvio, Harry Meyer, Nick Lavrik, Sheng Dai, Panos Datskos, and Sergei Smirnov. Large scale atmospheric pressure chemical vapor deposition of graphene. *Carbon*, 54:58 – 67, 2013.

[109] Pierre Trinsoutrot, Caroline Rabot, Hugues Vergnes, Alexandru Delamoreanu, Aziz Zenasni, and Brigitte Caussat. High quality graphene synthesized by atmospheric pressure CVD on copper foil. *Surf. Coat. Technol.*, 230:87 – 92, 2013. 19th European Conference on Chemical Vapor Deposition (EuroCVD19), Varna, Bulgaria, 1st - 6th September 2013.

[110] Shengnan Wang, Hiroki Hibino, Satoru Suzuki, and Hideki Yamamoto. Atmospheric pressure chemical vapor deposition growth of millimeter-scale single-crystalline graphene on the copper surface with a native oxide layer. *Chem. Mater.*, 28(14):4893–4900, 2016.

[111] Pinshane Y. Huang, Carlos S. Ruiz-Vargas, Arend M. van der Zande, William S. Whitney, Mark P. Levendorf, Joshua W. Kevek, Shivank Garg, Jonathan S. Alden, Caleb J. Hustedt, Ye Zhu, Jiwoong Park, Paul L. McEuen, and David A. Muller. Grains and grain boundaries in single-layer graphene atomic patchwork quilts. *Nature*, 469:389 – 392, 2011.

[112] Oleg V. Yazyev and Steven G. Louie. Electronic transport in polycrystalline graphene. *Nat. Mater.*, 9:806 – 809, 2010.

[113] Adam W. Tsen, Lola Brown, Mark P. Levendorf, Fereshte Ghahari, Pinshane Y. Huang, Robin W. Havener, Carlos S. Ruiz-Vargas, David A. Muller, Philip Kim, and Jiwoong Park. Tailoring electrical transport across grain boundaries in polycrystalline graphene. *Science*, 336(6085):1143–1146, 2012.

[114] Hengji Zhang, Geunsik Lee, Cheng Gong, Luigi Colombo, and Kyeongjae Cho. Grain boundary effect on electrical transport properties of graphene. *J. Phys. Chem. C*, 118(5):2338–2343, 2014.

[115] Vidya Kochat, Chandra Sekhar Tiwary, Tathagata Biswas, Gopalakrishnan Ramalingam, Kimberly Hsieh, Kamanio Chattopadhyay, Srinivasan Raghavan, Manish Jain, and Arindam Ghosh. Magnitude and origin of electrical noise at individual grain boundaries in graphene. *Nano Lett.*, 16(1):562–567, 2016.

[116] Akbar Bagri, Sang-Pil Kim, Rodney S. Ruoff, and Vivek B. Shenoy. Thermal transport across twin grain boundaries in polycrystalline graphene from nonequilibrium molecular dynamics simulations. *Nano Lett.*, 11(9):3917–3921, 2011.

[117] Andrey Y. Serov, Zhun-Yong Ong, and Eric Pop. Effect of grain boundaries on thermal transport in graphene. *Appl. Phys. Lett.*, 102(3):033104, 2013.

[118] H. K. Liu, Y. Lin, and S. N. Luo. Grain boundary energy and grain size dependences of thermal conductivity of polycrystalline graphene. *J. Phys. Chem. C*, 118(42):24797–24802, 2014.

[119] Rassin Grantab, Vivek B. Shenoy, and Rodney S. Ruoff. Anomalous strength characteristics of tilt grain boundaries in graphene. *Science*, 330(6006):946–948, 2010.

[120] Ji Won Suk, Yufeng Hao, Kenneth M. Liechti, and Rodney S. Ruoff. Impact of grain boundaries on the elastic behavior of transferred polycrystalline graphene. *Chem. Mater.*, 32(14):6078–6084, 2020.

[121] Hong Wang, Guanzhong Wang, Pengfei Bao, Shaolin Yang, Wei Zhu, Xing Xie, and Wen-Jun Zhang. Controllable synthesis of submillimeter single-crystal monolayer graphene domains on copper foils by suppressing nucleation. *J. Am. Chem. Soc.*, 134(8):3627–3630, 2012.

[122] Zheng Yan, Jian Lin, Zhiwei Peng, Zhengzong Sun, Yu Zhu, Lei Li, Changsheng Xiang, E. Loïc Samuel, Carter Kittrell, and James M. Tour. Toward the synthesis of wafer-scale single-crystal graphene on copper foils. *ACS Nano*, 6(10):9110–9117, 2012.

[123] Masatou Ishihara, Yoshinori Koga, Jaeho Kim, Kazuo Tsugawa, and Masataka Hasegawa. Direct evidence of advantage of Cu(111) for graphene synthesis by using Raman mapping and electron backscatter diffraction. *Mater. Lett.*, 65(19):2864 – 2867, 2011.

[124] L. Zhao, K.T. Rim, H. Zhou, R. He, T.F. Heinz, A. Pinczuk, G.W. Flynn, and A.N. Pasupathy. Influence of copper crystal surface on the CVD growth of large area monolayer graphene. *Solid State Commun.*, 151(7):509 – 513, 2011.

[125] Kongara M. Reddy, Andrew D. Gledhill, Chun-Hu Chen, Julie M. Drexler, and Nitin P. Padture. High quality, transferrable graphene grown on single crystal Cu(111) thin films on basal-plane sapphire. *Appl. Phys. Lett.*, 98(11):113117, 2011.

[126] Baoshan Hu, Hiroki Ago, Yoshito Ito, Kenji Kawahara, Masaharu Tsuji, Eisuke Magome, Kazushi Sumitani, Noriaki Mizuta, Ken ichi Ikeda, and Seigi Mizuno. Epitaxial growth of large-area single-layer graphene over Cu(111)/sapphire by atmospheric pressure CVD. *Carbon*, 50(1):57 – 65, 2012.

[127] David L. Miller, Mark W. Keller, Justin M. Shaw, Ann N. Chiaramonti, and Robert R. Keller. Epitaxial (111) films of Cu, Ni, and Cu_xNi_y on α-Al_2O_3 (0001) for graphene growth by chemical vapor deposition. *J. Appl. Phys.*, 112(6):064317, 2012.

[128] Van Luan Nguyen, Bong Gyu Shin, Dinh Loc Duong, Sung Tae Kim, David Perello, Young Jin Lim, Qing Hong Yuan, Feng Ding, Hu Young Jeong, Hyeon Suk Shin, Seung Mi Lee, Sang Hoon Chae, Quoc An Vu, Seung Hee Lee, and Young Hee Lee. Seamless stitching of graphene domains on polished copper (111) foil. *Adv. Mater.*, 27(8):1376–1382, 2015.

[129] David L. Miller, Mark W Keller, Justin M. Shaw, Katherine P. Rice, Robert R. Keller, and Kyle M. Diederichsen. Giant secondary grain growth in Cu films on sapphire. *AIP Adv.*, 3(8):082105, 2013.

[130] Sunghwan Jin, Ming Huang, Youngwoo Kwon, Leining Zhang, Bao-Wen Li, Sangjun Oh, Jichen Dong, Da Luo, Mandakini Biswal, Benjamin V. Cunning, Pavel V. Bakharev, Inyong Moon, Won Jong Yoo, Dulce C. Camacho-Mojica, Yong-Jin Kim, Sun Hwa Lee, Bin Wang, Won Kyung Seong, Manav Saxena, Feng Ding, Hyung-Joon Shin, and Rodney S. Ruoff. Colossal grain growth yields single-crystal metal foils by contact-free annealing. *Science*, 362(6418):1021–1025, 2018.

[131] Da Luo, Meihui Wang, Yunqing Li, Changsik Kim, Ka Man Yu, Yohan Kim, Huijun Han, Mandakini Biswal, Ming Huang, Youngwoo Kwon, Min Goo, Dulce C. Camacho-Mojica, Haofei Shi, Won Jong Yoo, Michael S. Altman, Hyung-Joon Shin, and Rodney S. Ruoff. Adlayer-free large-area single crystal graphene grown on a Cu(111) foil. *Adv. Mater.*, 31(35):1903615, 2019.

[132] Hailong Zhou, Woo Jong Yu, Lixin Liu, Rui Cheng, Yu Chen, Xiaoqing Huang, Yuan Liu, Yang Wang, Yu Huang, and Xiangfeng Duan. Chemical vapour deposition growth of large single crystals of monolayer and bilayer graphene. *Nat. Commun.*, 4:2096, 2013.

[133] Jinbo Pang, Alicja Bachmatiuk, Lei Fu, Chenglin Yan, Mengqi Zeng, Jiao Wang, Barbara Trzebicka, Thomas Gemming, Juergen Eckert, and Mark H. Rummeli. Oxidation as a means to remove surface contaminants on Cu foil

prior to graphene growth by chemical vapor deposition. *J. Phys. Chem. C*, 119(23):13363–13368, 2015.

[134] Philipp Braeuninger-Weimer, Barry Brennan, Andrew J. Pollard, and Stephan Hofmann. Understanding and controlling Cu-catalyzed graphene nucleation: The role of impurities, roughness, and oxygen scavenging. *Chem. Mater.*, 28(24):8905–8915, 2016.

[135] Min-Chiang Chuang and Wei-Yen Woon. Nucleation and growth dynamics of graphene on oxygen exposed copper substrate. *Carbon*, 103:384 – 390, 2016.

[136] Dong Ding, Pablo Solís-Fernández, Rozan Mohamad Yunus, Hiroki Hibino, and Hiroki Ago. Behavior and role of superficial oxygen in Cu for the growth of large single-crystalline graphene. *Appl. Surf. Sci.*, 408:142 – 149, 2017.

[137] Lin Gan and Zhengtang Luo. Turning off hydrogen to realize seeded growth of subcentimeter single-crystal graphene grains on copper. *ACS Nano*, 7(10):9480–9488, 2013.

[138] Seiya Suzuki, Yoshifumi Terada, and Masamichi Yoshimura. Suppression of graphene nucleation by turning off hydrogen supply just before atmospheric pressure chemical vapor deposition growth. *Coatings*, 7(11), 2017.

[139] I. Alstrup, I. Chorkendorff, and S. Ullmann. The interaction of CH_4 at high temperatures with clean and oxygen precovered Cu(100). *Surf. Sci.*, 264(1):95 – 102, 1992.

[140] Bin Xing, Xian-Yong Pang, and Gui-Chang Wang. C-H bond activation of methane on clean and oxygen pre-covered metals: A systematic theoretical study. *J. Catal.*, 282(1):74 – 82, 2011.

[141] Yufeng Hao, M. S. Bharathi, Lei Wang, Yuanyue Liu, Hua Chen, Shu Nie, Xiaohan Wang, Harry Chou, Cheng Tan, Babak Fallahazad, H. Ramanarayan, Carl W. Magnuson, Emanuel Tutuc, Boris I. Yakobson, Kevin F. McCarty, Yong-Wei Zhang, Philip Kim, James Hone, Luigi Colombo, and Rodney S. Ruoff. The role of surface oxygen in the growth of large single-crystal graphene on copper. *Science*, 342(6159):720–723, 2013.

[142] Wei Guo, Bin Wu, Shuai Wang, and Yunqi Liu. Controlling fundamental fluctuations for reproducible growth of large single-crystal graphene. *ACS Nano*, 12(2):1778–1784, 2018.

[143] Piran R. Kidambi, Caterina Ducati, Bruno Dlubak, Damian Gardiner, Robert S. Weatherup, Marie-Blandine Martin, Pierre Seneor, Harry Coles, and Stephan Hofmann. The parameter space of graphene chemical vapor deposition on polycrystalline Cu. *J. Phys. Chem. C*, 116(42):22492–22501, 2012.

[144] Nicolas Reckinger, Alexandre Felten, Cristiane N. Santos, Benoît Hackens, and Jean-François Colomer. The influence of residual oxidizing impurities on the synthesis of graphene by atmospheric pressure chemical vapor deposition. *Carbon*, 63:84 – 91, 2013.

[145] Saman Choubak, Pierre L. Levesque, Etienne Gaufres, Maxime Biron, Patrick Desjardins, and Richard Martel. Graphene CVD: Interplay between growth and etching on morphology and stacking by hydrogen and oxidizing impurities. *J. Phys. Chem. C*, 118(37):21532–21540, 2014.

[146] Siyu Wu, Wei Zhao, Xinliang Yang, Yijun Chen, Wenjie Wu, Yenan Song, and Qinghong Yuan. Suitable surface oxygen concentration on copper contributes to the growth of large graphene single crystals. *J. Phys. Chem. Lett.*, 10(17):4868–4874, 2019.

[147] Saman Choubak, Maxime Biron, Pierre L. Levesque, Richard Martel, and Patrick Desjardins. No graphene etching in purified hydrogen. *J. Phys. Chem. Lett.*, 4(7):1100–1103, 2013.

[148] Nathaniel S. Safron and Michael S. Arnold. Experimentally determined model of atmospheric pressure CVD of graphene on Cu. *J. Mater. Chem. C*, 2:744–755, 2014.

[149] Amanda M. Lewis, Brian Derby, and Ian A. Kinloch. Influence of gas phase equilibria on the chemical vapor deposition of graphene. *ACS Nano*, 7(4):3104–3117, 2013.

[150] Lixin Liu, Hailong Zhou, Rui Cheng, Yu Chen, Yung-Chen Lin, Yongquan Qu, Jingwei Bai, Ivan A. Ivanov, Gang Liu, Yu Huang, and Xiangfeng Duan. A systematic study of atmospheric pressure chemical vapor deposition growth of large-area monolayer graphene. *J. Mater. Chem.*, 22:1498–1503, 2012.

[151] Rujing Zhang, Limin He, Zhen Zhen, Zhenhua Xu, Na Li, and Hongwei Zhu. Controlled nucleation of graphene domains on copper with an oxide layer by atmospheric pressure chemical vapor deposition. *Front. Mater.*, 6:186, 2019.

[152] Sirui Xing, Wei Wu, Yanan Wang, Jiming Bao, and Shin-Shem Pei. Kinetic study of graphene growth: Temperature perspective on growth rate and film thickness by chemical vapor deposition. *Chem. Phys. Lett.*, 580:62 – 66, 2013.

[153] Dechao Geng, Bin Wu, Yunlong Guo, Liping Huang, Yunzhou Xue, Jianyi Chen, Gui Yu, Lang Jiang, Wenping Hu, and Yunqi Liu. Uniform hexagonal graphene flakes and films grown on liquid copper surface. *Proc. Natl. Acad. Sci.*, 109(21):7992–7996, 2012.

[154] Dechao Geng, Birong Luo, Jie Xu, Yunlong Guo, Bin Wu, Wenping Hu, Yunqi Liu, and Gui Yu. Self-aligned single-crystal graphene grains. *Adv. Funct. Mater.*, 24(12):1664–1670, 2014.

[155] Guqiao Ding, Yun Zhu, Shumin Wang, Qian Gong, Lei Sun, Tianru Wu, Xiaoming Xie, and Mianheng Jiang. Chemical vapor deposition of graphene on liquid metal catalysts. *Carbon*, 53:321 – 326, 2013.

[156] Dechao Geng and Gui Yu. Liquid catalysts: an innovative solution to 2D materials in CVD processes. *Mater. Horiz.*, 5:1021–1034, 2018.

[157] Bin Zhang, Wi Hyoung Lee, Richard Piner, Iskandar Kholmanov, Yaping Wu, Huifeng Li, Hengxing Ji, and Rodney S Ruoff. Low-temperature chemical vapor deposition growth of graphene from toluene on electropolished copper foils. *ACS Nano*, 6(3):2471–2476, 2012.

[158] Jun-ichi Fujita, Takaki Hiyama, Ayaka Hirukawa, Takahiro Kondo, Junji Nakamura, Shin-ichi Ito, Ryosuke Araki, Yoshikazu Ito, Masaki Takeguchi, and Woei Wu Pai. Near room temperature chemical vapor deposition of graphene with diluted methane and molten gallium catalyst. *Sci. Rep.*, 7:12371, 2017.

[159] Shanshan Chen, Hengxing Ji, Harry Chou, Qiongyu Li, Hongyang Li, Ji Won Suk, Richard Piner, Lei Liao, Weiwei Cai, and Rodney S. Ruoff. Millimeter-size single-crystal graphene by suppressing evaporative loss of Cu during low pressure chemical vapor deposition. *Adv. Mater.*, 25(14):2062–2065, 2013.

[160] Wenjing Fang, Allen L. Hsu, Roman Caudillo, Yi Song, A. Glen Birdwell, Eugene Zakar, Martin Kalbac, Madan Dubey, Tomás Palacios, Millie S. Dresselhaus, Paulo T. Araujo, and Jing Kong. Rapid identification of stacking orientation in isotopically labeled chemical-vapor grown bilayer graphene by Raman spectroscopy. *Nano Lett.*, 13(4):1541–1548, 2013.

[161] Wenjing Fang, Allen L. Hsu, Yi Song, Anthony G. Birdwell, Matin Amani, Madan Dubey, Mildred S. Dresselhaus, Tomás Palacios, and Jing Kong. Asymmetric growth of bilayer graphene on copper enclosures using low-pressure chemical vapor deposition. *ACS Nano*, 8(6):6491–6499, 2014.

[162] Zhijuan Zhao, Zhifa Shan, Cankun Zhang, Qiongyu Li, Bo Tian, Zhiyi Huang, Weiyi Lin, Xiangping Chen, Hengxing Ji, Weifeng Zhang, and Weiwei Cai. Study on the diffusion mechanism of graphene grown on copper pockets. *Small*, 11(12):1418–1422, 2015.

[163] Hoang Danh Phan, Jaehyuck Jung, Youngchan Kim, Van Ngoc Huynh, and Changgu Lee. Large-area single-crystal graphene grown on a recrystallized Cu(111) surface by using a hole-pocket method. *Nanoscale*, 8:13781–13789, 2016.

[164] Phi H.Q. Pham, Weiwei Zhou, Nhi V. Quach, Jinfeng Li, Jian-Guo Zheng, and Peter J. Burke. Controlling nucleation density while simultaneously promoting edge growth using oxygen-assisted fast synthesis of isolated large-domain graphene. *Chem. Mater.*, 28(18):6511–6519, 2016.

[165] Wenjing Fang, Allen Hsu, Yong Cheol Shin, Albert Liao, Shengxi Huang, Yi Song, Xi Ling, Mildred S. Dresselhaus, Tomas Palacios, and Jing Kong. Application of tungsten as a carbon sink for synthesis of large-domain uniform monolayer graphene free of bilayers/multilayers. *Nanoscale*, 7:4929–4934, 2015.

[166] Birong Luo, José M Caridad, Patrick R Whelan, Joachim Dahl Thomsen, David M A Mackenzie, Antonija Grubišić Čabo, Sanjoy K Mahatha, Marco Bianchi, Philip Hofmann, Peter Uhd Jepsen, Peter Bøggild, and Timothy J Booth. Sputtering an exterior metal coating on copper enclosure for large-scale growth of single-crystalline graphene. *2D Mater.*, 4(4):045017, 2017.

[167] Nicolas Reckinger, Marcello Casa, Jeroen E. Scheerder, Wout Keijers, Matthieu Paillet, Jean-Roch Huntzinger, Emile Haye, Alexandre Felten, Joris Van de Vondel, Maria Sarno, Luc Henrard, and Jean-François Colomer. Restoring self-limited growth of single-layer graphene on copper foil via backside coating. *Nanoscale*, 11:5094–5101, 2019.

[168] Min Seok Yoo, Hyo Chan Lee, Siyoung Lee, Seon Baek Lee, Nam-Suk Lee, and Kilwon Cho. Chemical vapor deposition of Bernal-stacked graphene on a Cu surface by breaking the carbon solubility symmetry in Cu foils. *Adv. Mater.*, 29(32):1700753, 2017.

[169] Li Lin, Jiayu Li, Huaying Ren, Ai Leen Koh, Ning Kang, Hailin Peng, H. Q. Xu, and Zhongfan Liu. Surface engineering of copper foils for growing centimeter-sized single-crystalline graphene. *ACS Nano*, 10(2):2922–2929, 2016.

[170] Zhengtang Luo, Ye Lu, Daniel W. Singer, Matthew E. Berck, Luke A. Somers, Brett R. Goldsmith, and A. T. Charlie Johnson. Effect of substrate roughness and feedstock concentration on growth of wafer-scale graphene at atmospheric pressure. *Chem. Mater.*, 23(6):1441–1447, 2011.

[171] Nadya Mason, Ya-Ping Hsieh, Yi-Wen Wang, Chu-Chi Ting, Hsiang-Chen Wang, Kuang-Yao Chen, and Chang-Chung Yang. Effect of catalyst morphology on the quality of CVD grown graphene. *J. Nanomater.*, 2013:393724, 2013.

[172] Xuesong Li, Yanwu Zhu, Weiwei Cai, Mark Borysiak, Boyang Han, David Chen, Richard D. Piner, Luigi Colombo, and Rodney S. Ruoff. Transfer of large-area graphene films for high-performance transparent conductive electrodes. *Nano Lett.*, 9(12):4359–4363, 2009.

[173] Alfonso Reina, Hyungbin Son, Liying Jiao, Ben Fan, Mildred S. Dresselhaus, ZhongFan Liu, and Jing Kong. Transferring and identification of single- and few-layer graphene on arbitrary substrates. *J. Phys. Chem. C*, 112(46):17741–17744, 2008.

[174] Ved Prakash Verma, Santanu Das, Indranil Lahiri, and Wonbong Choi. Large-area graphene on polymer film for flexible and transparent anode in field emission device. *Appl. Phys. Lett.*, 96(20):203108, 2010.

[175] Helin Cao, Qingkai Yu, L. A. Jauregui, J. Tian, W. Wu, Z. Liu, R. Jalilian, D. K. Benjamin, Z. Jiang, J. Bao, S. S. Pei, and Yong P. Chen. Electronic transport in chemical vapor deposited graphene synthesized on Cu: Quantum hall effect and weak localization. *Appl. Phys. Lett.*, 96(12):122106, 2010.

[176] Xuelei Liang, Brent A. Sperling, Irene Calizo, Guangjun Cheng, Christina Ann Hacker, Qin Zhang, Yaw Obeng, Kai Yan, Hailin Peng, Qiliang Li, Xiaoxiao Zhu, Hui Yuan, Angela R. Hight Walker, Zhongfan Liu, Lian-mao Peng, and Curt A. Richter. Toward clean and crackless transfer of graphene. *ACS Nano*, 5(11):9144–9153, 2011.

[177] Ji Won Suk, Alexander Kitt, Carl W. Magnuson, Yufeng Hao, Samir Ahmed, Jinho An, Anna K. Swan, Bennett B. Goldberg, and Rodney S. Ruoff. Transfer of CVD-grown monolayer graphene onto arbitrary substrates. *ACS Nano*, 5(9):6916–6924, 2011.

[178] Lai-Peng Ma, Wencai Ren, and Hui-Ming Cheng. Transfer methods of graphene from metal substrates: A review. *Small Methods*, 3(7):1900049, 2019.

[179] A. Pirkle, J. Chan, A. Venugopal, D. Hinojos, C. W. Magnuson, S. McDonnell, L. Colombo, E. M. Vogel, R. S. Ruoff, and R. M. Wallace. The effect of chemical residues on the physical and electrical properties of chemical vapor deposited graphene transferred to SiO_2. *Appl. Phys. Lett.*, 99(12):122108, 2011.

[180] Seonyeong Kim, Somyeong Shin, Taekwang Kim, Hyewon Du, Minho Song, ChangWon Lee, Kisoo Kim, Seungmin Cho, David H. Seo, and Sunae Seo. Robust graphene wet transfer process through low molecular weight polymethylmethacrylate. *Carbon*, 98:352 – 357, 2016.

[181] Gabriela Borin Barin, Yi Song, Iara de Fátima Gimenez, Antonio Gomes Souza Filho, Ledjane Silva Barreto, and Jing Kong. Optimized graphene transfer: Influence of polymethylmethacrylate (PMMA) layer concentration and baking time on graphene final performance. *Carbon*, 84:82 – 90, 2015.

[182] Joshua D Wood, Gregory P Doidge, Enrique A Carrion, Justin C Koepke, Joshua A Kaitz, Isha Datye, Ashkan Behnam, Jayan Hewaparakrama, Basil

Aruin, Yaofeng Chen, Hefei Dong, Richard T Haasch, Joseph W Lyding, and Eric Pop. Annealing free, clean graphene transfer using alternative polymer scaffolds. *Nanotechnology*, 26(5):055302, 2015.

[183] Hye Jin Park, Jannik Meyer, Siegmar Roth, and Viera Skákalová. Growth and properties of few-layer graphene prepared by chemical vapor deposition. *Carbon*, 48(4):1088 – 1094, 2010.

[184] Yung-Chang Lin, Chuanhong Jin, Jung-Chi Lee, Shou-Feng Jen, Kazu Suenaga, and Po-Wen Chiu. Clean transfer of graphene for isolation and suspension. *ACS Nano*, 5(3):2362–2368, 2011.

[185] Keun Soo Kim, Yue Zhao, Houk Jang, Sang Yoon Lee, Jong Min Kim, Kwang S. Kim, Jong-Hyun Ahn, Philip Kim, Jae-Young Choi, and Byung Hee Hong. Large-scale pattern growth of graphene films for stretchable transparent electrodes. *Nature*, 457:706 – 710, 2009.

[186] Jie Song, Fong-Yu Kam, Rui-Qi Png, Wei-Ling Seah, Jing-Mei Zhuo, Geok-Kieng Lim, Peter K. H. Ho, and Lay-Lay Chua. A general method for transferring graphene onto soft surfaces. *Nat. Nanotechnol.*, 8:356 – 362, 2013.

[187] Wei Sun Leong, Haozhe Wang, Jingjie Yeo, Francisco J. Martin-Martinez, Ahmad Zubair, Pin-Chun Shen, Yunwei Mao, Tomas Palacios, Markus J. Buehler, Jin-Yong Hong, and Jing Kong. Paraffin-enabled graphene transfer. *Nat. Commun.*, 10(867), 2019.

[188] Pengwei Qi, Yinan Huang, Yuanzhou Yao, Qin Li, Yuebin Lian, Ling Lin, Xuebin Wang, Yindong Gu, Liqiang Li, Zhao Deng, Yang Peng, and Zhongfan Liu. Wax-assisted crack-free transfer of monolayer CVD graphene: Extending from standalone to supported copper substrates. *Appl. Surf. Sci.*, 493:81 – 86, 2019.

[189] Zhikun Zhang, Jinhong Du, Dingdong Zhang, Hengda Sun, Lichang Yin, Laipeng Ma, Jiangshan Chen, Dongge Ma, Hui-Ming Cheng, and Wencai Ren. Rosin-enabled ultraclean and damage-free transfer of graphene for large-area flexible organic light-emitting diodes. *Nat. Commun.*, 8:14560, 2017.

[190] Dingdong Zhang, Jinhong Du, Yi-Lun Hong, Weimin Zhang, Xiao Wang, Hui Jin, Paul L. Burn, Junsheng Yu, Maolin Chen, Dong-Ming Sun, Meng Li, Lianqing Liu, Lai-Peng Ma, Hui-Ming Cheng, and Wencai Ren. A double support layer for facile clean transfer of two-dimensional materials for high-performance electronic and optoelectronic devices. *ACS Nano*, 13(5):5513–5522, 2019.

[191] Kashif Shahzad, Kunpeng Jia, Chao Zhao, Xiangyu Yan, Zhang Yadong, Muhammad Usman, and Jun Luo. An improved rosin transfer process for the reduction of residue particles for graphene. *Nanoscale Res. Lett.*, 15:85, 2020.

[192] A. Capasso, M. De Francesco, E. Leoni, T. Dikonimos, F. Buonocore, L. Lancellotti, E. Bobeico, M. S. Sarto, A. Tamburrano, G. De Bellis, and N. Lisi. Cyclododecane as support material for clean and facile transfer of large-area few-layer graphene. *Appl. Phys. Lett.*, 105(11):113101, 2014.

[193] Nicola Lisi, Theodoros Dikonimos, Francesco Buonocore, Martina Pittori, Raffaello Mazzaro, Rita Rizzoli, Sergio Marras, and Andrea Capasso. Contamination-free graphene by chemical vapor deposition in quartz furnaces. *Sci. Rep.*, 7:9927, 2017.

[194] Bananakere Nanjegowda Chandrashekar, Nianduo Cai, Louis W.Y. Liu, Ankanahalli Shankaregowda Smitha, Zefei Wu, Pengcheng Chen, Run Shi, Weijun Wang, Jingwei Wang, Chunmei Tang, and Chun Cheng. Oil boundary approach for sublimation enabled camphor mediated graphene transfer. *J. Colloid Interface Sci.*, 546:11 – 19, 2019.

[195] Hyun Ho Kim, Boseok Kang, Ji Won Suk, Nannan Li, Kwang S. Kim, Rodney S. Ruoff, Wi Hyoung Lee, and Kilwon Cho. Clean transfer of wafer-scale graphene via liquid phase removal of polycyclic aromatic hydrocarbons. *ACS Nano*, 9(5):4726–4733, 2015.

[196] Mingguang Chen, Dejan Stekovic, Wangxiang Li, Bassim Arkook, Robert C Haddon, and Elena Bekyarova. Sublimation-assisted graphene transfer technique based on small polyaromatic hydrocarbons. *Nanotechnology*, 28(25):255701, 2017.

[197] Alexander Yulaev, Guangjun Cheng, Angela R. Hight Walker, Ivan V. Vlassiouk, Alline Myers, Marina S. Leite, and Andrei Kolmakov. Toward clean suspended CVD graphene. *RSC Adv.*, 6:83954–83962, 2016.

[198] Wei-Hsiang Lin, Ting-Hui Chen, Jan-Kai Chang, Jieh-I Taur, Yuan-Yen Lo, Wei-Li Lee, Chia-Seng Chang, Wei-Bin Su, and Chih-I Wu. A direct and polymer-free method for transferring graphene grown by chemical vapor deposition to any substrate. *ACS Nano*, 8(2):1784–1791, 2014.

[199] Di-Yan Wang, I-Sheng Huang, Po-Hsun Ho, Shao-Sian Li, Yun-Chieh Yeh, Duan-Wei Wang, Wei-Liang Chen, Yu-Yang Lee, Yu-Ming Chang, Chia-Chun Chen, Chi-Te Liang, and Chun-Wei Chen. Clean-lifting transfer of large-area residual-free graphene films. *Adv. Mater.*, 25(32):4521–4526, 2013.

[200] Yu Wang, Yi Zheng, Xiangfan Xu, Emilie Dubuisson, Qiaoliang Bao, Jiong Lu, and Kian Ping Loh. Electrochemical delamination of CVD-grown graphene film: Toward the recyclable use of copper catalyst. *ACS Nano*, 5(12):9927–9933, 2011.

[201] César J. Lockhart de la Rosa, Jie Sun, Niclas Lindvall, Matthew T. Cole, Youngwoo Nam, Markus Löffler, Eva Olsson, Kenneth B. K. Teo, and August Yurgens. Frame assisted H_2O electrolysis induced H_2 bubbling trans-

fer of large area graphene grown by chemical vapor deposition on Cu. *Appl. Phys. Lett.*, 102(2):022101, 2013.

[202] Jaeyeong Lee, Shinyoung Lee, and Hak Ki Yu. Contamination-free graphene transfer from Cu-foil and Cu-thin-film/sapphire. *Coatings*, 7(12), 2017.

[203] Christie Thomas Cherian, Francesco Giustiniano, Iñigo Martin-Fernandez, Henrik Andersen, Jayakumar Balakrishnan, and Barbaros Özyilmaz. 'Bubble-free' electrochemical delamination of CVD graphene films. *Small*, 11(2):189–194, 2015.

[204] Filippo Pizzocchero, Bjarke S. Jessen, Patrick R. Whelan, Natalie Kostesha, Sunwoo Lee, Jonas D. Buron, Irina Petrushina, Martin B. Larsen, Paul Greenwood, Wu Joon Cha, Ken Teo, Peter U. Jepsen, James Hone, Peter Bøggild, and Timothy J. Booth. Non-destructive electrochemical graphene transfer from reusable thin-film catalysts. *Carbon*, 85:397 – 405, 2015.

[205] Priti Gupta, Pratiksha D. Dongare, Sameer Grover, Sudipta Dubey, Hitesh Mamgain, Arnab Bhattacharya, and Mandar M. Deshmukh. A facile process for soak-and-peel delamination of CVD graphene from substrates using water. *Sci. Rep.*, 4:3882, 2014.

[206] Seong-Jun Yang, Shinyoung Choi, Francis Okello Odongo Ngome, Ki-Jeong Kim, Si-Young Choi, and Cheol-Joo Kim. All-dry transfer of graphene film by van der Waals interactions. *Nano Lett.*, 19(6):3590–3596, 2019.

[207] Luca Banszerus, Michael Schmitz, Stephan Engels, Jan Dauber, Martin Oellers, Federica Haupt, Kenji Watanabe, Takashi Taniguchi, Bernd Beschoten, and Christoph Stampfer. Ultrahigh-mobility graphene devices from chemical vapor deposition on reusable copper. *Sci. Adv.*, 1(6), 2015.

[208] Guilhermino J.M. Fechine, Iñigo Martin-Fernandez, George Yiapanis, Ricardo Bentini, Eeshan Sandeep Kulkarni, Ricardo V. Bof de Oliveira, Xiao Hu, Irene Yarovsky, Antônio H. Castro Neto, and Barbaros Özyilmaz. Direct dry transfer of chemical vapor deposition graphene to polymeric substrates. *Carbon*, 83:224 – 231, 2015.

[209] Runlai Li, Qinghua Zhang, Eric Zhao, Jin Li, Qiao Gu, and Ping Gao. Etching- and intermediate-free graphene dry transfer onto polymeric thin films with high piezoresistive gauge factors. *J. Mater. Chem. C*, 7:13032–13039, 2019.

[210] Da Luo, Xueqiu You, Bao-Wen Li, Xianjue Chen, Hyo Ju Park, Minbok Jung, Taeg Yeoung Ko, Kester Wong, Masood Yousaf, Xiong Chen, Ming Huang, Sun Hwa Lee, Zonghoon Lee, Hyung-Joon Shin, Sunmin Ryu, Sang Kyu Kwak, Noejung Park, Revathi R. Bacsa, Wolfgang Bacsa, and Rodney S.

Ruoff. Role of graphene in water-assisted oxidation of copper in relation to dry transfer of graphene. *Chem. Mater.*, 29(10):4546–4556, 2017.

[211] Tim J. Booth, Peter Blake, Rahul R. Nair, Da Jiang, Ernie W. Hill, Ursel Bangert, Andrew Bleloch, Mhairi Gass, Kostya S. Novoselov, M. I. Katsnelson, and A. K. Geim. Macroscopic graphene membranes and their extraordinary stiffness. *Nano Lett.*, 8(8):2442–2446, 2008.

[212] Arend M. van der Zande, Robert A. Barton, Jonathan S. Alden, Carlos S. Ruiz-Vargas, William S. Whitney, Phi H. Q. Pham, Jiwoong Park, Jeevak M. Parpia, Harold G. Craighead, and Paul L. McEuen. Large-scale arrays of single-layer graphene resonators. *Nano Lett.*, 10(12):4869–4873, 2010.

[213] Zengguang Cheng, Qiaoyu Zhou, Chenxuan Wang, Qiang Li, Chen Wang, and Ying Fang. Toward intrinsic graphene surfaces: A systematic study on thermal annealing and wet-chemical treatment of SiO_2-supported graphene devices. *Nano Lett.*, 11(2):767–771, 2011.

[214] Michael Her, Ryan Beams, and Lukas Novotny. Graphene transfer with reduced residue. *Phys. Lett. A*, 377(21):1455 – 1458, 2013.

[215] Hyun Ho Kim, Jae Won Yang, Sae Byeok Jo, Boseok Kang, Seong Kyu Lee, Hyojin Bong, Geunsik Lee, Kwang S. Kim, and Kilwon Cho. Substrate-induced solvent intercalation for stable graphene doping. *ACS Nano*, 7(2):1155–1162, 2013.

[216] A. Suhail, K. Islam, B. Li, D. Jenkins, and G. Pan. Reduction of polymer residue on wet-transferred CVD graphene surface by deep UV exposure. *Appl. Phys. Lett.*, 110(18):183103, 2017.

[217] Zhen Hua Ni, Hao Min Wang, Zhi Qiang Luo, Ying Ying Wang, Ting Yu, Yi Hong Wu, and Ze Xiang Shen. The effect of vacuum annealing on graphene. *J. Raman Spectrosc.*, 41(5):479–483, 2010.

[218] Jack Chan, Archana Venugopal, Adam Pirkle, Stephen McDonnell, David Hinojos, Carl W. Magnuson, Rodney S. Ruoff, Luigi Colombo, Robert M. Wallace, and Eric M. Vogel. Reducing extrinsic performance-limiting factors in graphene grown by chemical vapor deposition. *ACS Nano*, 6(4):3224–3229, 2012.

[219] Kitu Kumar, Youn-Su Kim, and Eui-Hyeok Yang. The influence of thermal annealing to remove polymeric residue on the electronic doping and morphological characteristics of graphene. *Carbon*, 65:35 – 45, 2013.

[220] Cheng Gong, Herman Carlo Floresca, David Hinojos, Stephen McDonnell, Xiaoye Qin, Yufeng Hao, Srikar Jandhyala, Greg Mordi, Jiyoung Kim, Luigi Colombo, Rodney S. Ruoff, Moon J. Kim, Kyeongjae Cho, Robert M. Wallace, and Yves J. Chabal. Rapid selective etching of PMMA residues from

transferred graphene by carbon dioxide. *J. Phys. Chem. C*, 117(44):23000–23008, 2013.

[221] Gerardo Algara-Siller, Ossi Lehtinen, Andrey Turchanin, and Ute Kaiser. Dry-cleaning of graphene. *Appl. Phys. Lett.*, 104(15):153115, 2014.

[222] Jean-Nicolas Longchamp, Conrad Escher, and Hans-Werner Fink. Ultraclean freestanding graphene by platinum-metal catalysis. *J. Vac. Sci. Technol. B*, 31(2):020605, 2013.

[223] Yung-Chang Lin, Chun-Chieh Lu, Chao-Huei Yeh, Chuanhong Jin, Kazu Suenaga, and Po-Wen Chiu. Graphene annealing: How clean can it be? *Nano Lett.*, 12(1):414–419, 2012.

[224] Jianbo Sun, Harry O Finklea, and Yuxin Liu. Characterization and electrolytic cleaning of poly(methyl methacrylate) residues on transferred chemical vapor deposited graphene. *Nanotechnology*, 28(12):125703, 2017.

[225] Youngkun Ahn, Hyein Kim, Young-Hwan Kim, Yeonjin Yi, and Seong-Il Kim. Procedure of removing polymer residues and its influences on electronic and structural characteristics of graphene. *Appl. Phys. Lett.*, 102(9):091602, 2013.

[226] Yeong-Dae Lim, Dae-Yeong Lee, Tian-Zi Shen, Chang-Ho Ra, Jae-Young Choi, and Won Jong Yoo. Si-compatible cleaning process for graphene using low-density inductively coupled plasma. *ACS Nano*, 6(5):4410–4417, 2012.

[227] G. Cunge, D. Ferrah, C. Petit-Etienne, A. Davydova, H. Okuno, D. Kalita, V. Bouchiat, and O. Renault. Dry efficient cleaning of poly-methyl-methacrylate residues from graphene with high-density H_2 and H_2-N_2 plasmas. *J. Appl. Phys.*, 118(12):123302, 2015.

[228] Djawhar Ferrah, Olivier Renault, Daniil Marinov, Javier Arias-Zapata, Nicolas Chevalier, Denis Mariolle, Denis Rouchon, Hanako Okuno, Vincent Bouchiat, and Gilles Cunge. CF_4/H_2 plasma cleaning of graphene regenerates electronic properties of the pristine material. *ACS Appl. Nano Mater.*, 2(3):1356–1366, 2019.

[229] Bonnie J. Tyler, Barry Brennan, Helena Stec, Trupti Patel, Ling Hao, Ian S. Gilmore, and Andrew J. Pollard. Removal of organic contamination from graphene with a controllable mass-selected argon gas cluster ion beam. *J. Phys. Chem. C*, 119(31):17836–17841, 2015.

[230] Chenxing Deng, Weiwei Lin, Guillaume Agnus, Diana Dragoe, Debora Pierucci, Abdelkarim Ouerghi, Sylvain Eimer, Ivanka Barisic, Dafiné Ravelosona, Claude Chappert, and Weisheng Zhao. Reversible charge-transfer doping in graphene due to reaction with polymer residues. *J. Phys. Chem. C*, 118(25):13890–13897, 2014.

[231] Yuehui Jia, Xin Gong, Pei Peng, Zidong Wang, Zhongzheng Tian, Liming Ren, Yunyi Fu, and Han Zhang. Toward high carrier mobility and low contact resistance: Laser cleaning of PMMA residues on graphene surfaces. *Nano-Micro Lett.*, 8:336 – 346, 2016.

[232] Hyeon Jun Hwang, Yongsu Lee, Chunhum Cho, and Byoung Hun Lee. Facile process to clean PMMA residue on graphene using KrF laser annealing. *AIP Adv.*, 8(10):105326, 2018.

[233] Won Jin Choi, Yoon Jang Chung, Serin Park, Cheol-Soo Yang, Young Kuk Lee, Ki-Seok An, You-Seop Lee, and Jeong-O Lee. A simple method for cleaning graphene surfaces with an electrostatic force. *Adv. Mater.*, 26(4):637–644, 2014.

[234] Niclas Lindvall, Alexey Kalabukhov, and August Yurgens. Cleaning graphene using atomic force microscope. *J. Appl. Phys.*, 111(6):064904, 2012.

[235] A. M. Goossens, V. E. Calado, A. Barreiro, K. Watanabe, T. Taniguchi, and L. M. K. Vandersypen. Mechanical cleaning of graphene. *Appl. Phys. Lett.*, 100(7):073110, 2012.

[236] Woosuk Choi, Muhammad Arslan Shehzad, Sanghoon Park, and Yongho Seo. Influence of removing PMMA residues on surface of CVD graphene using a contact-mode atomic force microscope. *RSC Adv.*, 7:6943–6949, 2017.

[237] Peter Schweizer, Christian Dolle, Daniela Dasler, Gonzalo Abellán, Frank Hauke, Andreas Hirsch, and Erdmann Spiecker. Mechanical cleaning of graphene using in situ electron microscopy. *Nat. Nanotechnol.*, 11:1743, 2020.

[238] J. Moser, A. Barreiro, and A. Bachtold. Current-induced cleaning of graphene. *Appl. Phys. Lett.*, 91(16):163513, 2007.

[239] Haidong Wang, Xing Zhang, and Hiroshi Takamatsu. Ultraclean suspended monolayer graphene achieved by in situ current annealing. *Nanotechnology*, 28(4):045706, 2016.

[240] Li Lin, Jincan Zhang, Haisheng Su, Jiayu Li, Luzhao Sun, Zihao Wang, Fan Xu, Chang Liu, Sergei Lopatin, Yihan Zhu, Kaicheng Jia, Shulin Chen, Dingran Rui, Jingyu Sun, Ruiwen Xue, Peng Gao, Ning Kang, Yu Han, H. Q. Xu, Yang Cao, K. S. Novoselov, Zhongqun Tian, Bin Ren, Hailin Peng, and Zhongfan Liu. Towards super-clean graphene. *Nat. Commun.*, 10:1912, 2019.

[241] Kaicheng Jia, Jincan Zhang, Li Lin, Zhenzhu Li, Jing Gao, Luzhao Sun, Ruiwen Xue, Jiayu Li, Ning Kang, Zhengtang Luo, Mark H. Rummeli, Hailin Peng, and Zhongfan Liu. Copper-containing carbon feedstock for growing superclean graphene. *J. Am. Chem. Soc.*, 141(19):7670–7674, 2019.

[242] Jincan Zhang, Kaicheng Jia, Li Lin, Wei Zhao, Huy Ta Quang, Luzhao Sun, Tianran Li, Zhenzhu Li, Xiaoting Liu, Liming Zheng, Ruiwen Xue, Jing Gao, Zhengtang Luo, Mark H. Rummeli, Qinghong Yuan, Hailin Peng, and Zhongfan Liu. Large-area synthesis of superclean graphene via selective etching of amorphous carbon with carbon dioxide. *Angew. Chem. Int. Ed.*, 58(41):14446–14451, 2019.

[243] A E Ennos. The origin of specimen contamination in the electron microscope. *Br. J. Appl. Phys.*, 4(4):101–106, 1953.

[244] A E Ennos. The sources of electron-induced contamination in kinetic vacuum systems. *Br. J. Appl. Phys.*, 5(1):27–31, 1954.

[245] G. Binnig, C. F. Quate, and Ch. Gerber. Atomic force microscope. *Phys. Rev. Lett.*, 56:930–933, 1986.

[246] M.L. Bloo, H. Haitjema, and W.O. Pril. Deformation and wear of pyramidal, silicon-nitride AFM tips scanning micrometre-size features in contact mode. *Measurement*, 25(3):203 – 211, 1999.

[247] Q. Zhong, D. Inniss, K. Kjoller, and V.B. Elings. Fractured polymer/silica fiber surface studied by tapping mode atomic force microscopy. *Surf. Sci.*, 290(1):L688 – L692, 1993.

[248] C.A. Putman, K.O. van der Werf, B.G. de Grooth, N.F. van Hulst, and J. Greve. Viscoelasticity of living cells allows high resolution imaging by tapping mode atomic force microscopy. *Biophys. J.*, 67(4):1749 – 1753, 1994.

[249] S.N. Magonov, V. Elings, and M.-H. Whangbo. Phase imaging and stiffness in tapping-mode atomic force microscopy. *Surf. Sci.*, 375(2):L385 – L391, 1997.

[250] Ke Xu, Weihang Sun, Yongjian Shao, Fanan Wei, Xiaoxian Zhang, Wei Wang, and Peng Li. Recent development of PeakForce tapping mode atomic force microscopy and its applications on nanoscience. *Nanotechnol. Rev.*, 7(6):605 – 621, 2018.

[251] H Schillers, I Medalsy, S Hu, AL Slade, and JE Shaw. PeakForce tapping resolves individual microvilli on living cells. *J. Mol. Recognit.*, 29(2):95 – 101, 2016.

[252] Alice Pyne, Ruth Thompson, Carl Leung, Debdulal Roy, and Bart W. Hoogenboom. Single-molecule reconstruction of oligonucleotide secondary structure by atomic force microscopy. *Small*, 10(16):3257–3261, 2014.

[253] Upadrasta Ramamurty and Jae-il Jang. Nanoindentation for probing the mechanical behavior of molecular crystals - a review of the technique and how to use it. *CrystEngComm*, 16:12–23, 2014.

[254] Nikolaos Michailidis, Konstantinos-Dionysios Bouzakis, Ludger Koenders, and Konrad Herrmann. *Nanoindentation*, pages 1–9. Springer Berlin Heidelberg, Berlin, Heidelberg, 2014.

[255] Christopher A. Schuh. Nanoindentation studies of materials. *Mater. Today*, 9(5):32 – 40, 2006.

[256] Kai-Tak Wan, Shu Guo, and David A. Dillard. A theoretical and numerical study of a thin clamped circular film under an external load in the presence of a tensile residual stress. *Thin Solid Films*, 425(1):150 – 162, 2003.

[257] U. Komaragiri, M. R. Begley, and J. G. Simmonds. The mechanical response of freestanding circular elastic films under point and pressure loads. *J. Appl. Mech.*, 72(2):203–212, 2005.

[258] Cameron J Shearer, Ashley D Slattery, Andrew J Stapleton, Joseph G Shapter, and Christopher T Gibson. Accurate thickness measurement of graphene. *Nanotechnology*, 27(12):125704, 2016.

[259] R. Nicklow, N. Wakabayashi, and H. G. Smith. Lattice dynamics of pyrolytic graphite. *Phys. Rev. B*, 5:4951–4962, 1972.

[260] J. Tersoff. Energies of fullerenes. *Phys. Rev. B*, 46:15546–15549, 1992.

[261] Daniel Sánchez-Portal, Emilio Artacho, José M. Soler, Angel Rubio, and Pablo Ordejón. Ab initio structural, elastic, and vibrational properties of carbon nanotubes. *Phys. Rev. B*, 59:12678–12688, 1999.

[262] Konstantin N. Kudin, Gustavo E. Scuseria, and Boris I. Yakobson. C_2F, BN, and C nanoshell elasticity from ab initio computations. *Phys. Rev. B*, 64:235406, 2001.

[263] Zhan-chun Tu and Zhong-can Ou-Yang. Single-walled and multiwalled carbon nanotubes viewed as elastic tubes with the effective Young's moduli dependent on layer number. *Phys. Rev. B*, 65:233407, 2002.

[264] M. Arroyo and T. Belytschko. Finite crystal elasticity of carbon nanotubes based on the exponential Cauchy-Born rule. *Phys. Rev. B*, 69:115415, 2004.

[265] Qiang Lu, Marino Arroyo, and Rui Huang. Elastic bending modulus of monolayer graphene. *J. Phys. D Appl. Phys.*, 42(10):102002, 2009.

[266] Pekka Koskinen and Oleg O. Kit. Approximate modeling of spherical membranes. *Phys. Rev. B*, 82:235420, 2010.

[267] Enrique Muñoz, Abhishek K. Singh, Morgana A. Ribas, Evgeni S. Penev, and Boris I. Yakobson. The ultimate diamond slab: Graphane versus graphene. *Diamond Relat. Mater.*, 19(5):368 – 373, 2010. Proceedings of Diamond 2009, The 20th European Conference on Diamond, Diamond-Like Materials, Carbon Nanotubes and Nitrides, Part 1.

[268] Yujie Wei, Baoling Wang, Jiangtao Wu, Ronggui Yang, and Martin L. Dunn. Bending rigidity and gaussian bending stiffness of single-layered graphene. *Nano Lett.*, 13(1):26–30, 2013.

[269] Niklas Lindahl, Daniel Midtvedt, Johannes Svensson, Oleg A. Nerushev, Niclas Lindvall, Andreas Isacsson, and Eleanor E. B. Campbell. Determination of the bending rigidity of graphene via electrostatic actuation of buckled membranes. *Nano Lett.*, 12(7):3526–3531, 2012.

[270] J. H. Los, M. I. Katsnelson, O. V. Yazyev, K. V. Zakharchenko, and A. Fasolino. Scaling properties of flexible membranes from atomistic simulations: Application to graphene. *Phys. Rev. B*, 80:121405, 2009.

[271] F. L. Braghin and N. Hasselmann. Thermal fluctuations of free-standing graphene. *Phys. Rev. B*, 82:035407, 2010.

[272] Rafael Roldán, Annalisa Fasolino, Kostyantyn V. Zakharchenko, and Mikhail I. Katsnelson. Suppression of anharmonicities in crystalline membranes by external strain. *Phys. Rev. B*, 83:174104, 2011.

[273] Andrej Košmrlj and David R. Nelson. Mechanical properties of warped membranes. *Phys. Rev. E*, 88:012136, 2013.

[274] Melina K. Blees, Arthur W. Barnard, Peter A. Rose, Samantha P. Roberts, Kathryn L. McGill, Pinshane Y. Huang, Alexander R. Ruyack, Joshua W. Kevek, Bryce Kobrin, David A. Muller, and Paul L. McEuen. Graphene kirigami. *Nature*, 524:204–207, 2015.

[275] Andres Castellanos-Gomez, Menno Poot, Gary A. Steele, Herre S. J. van der Zant, Nicolás Agraït, and Gabino Rubio-Bollinger. Elastic properties of freely suspended MoS_2 nanosheets. *Adv. Mater.*, 24(6):772–775, 2012.

[276] Qing-Yuan Lin, Guangyin Jing, Yang-Bo Zhou, Yi-Fan Wang, Jie Meng, Ya-Qing Bie, Da-Peng Yu, and Zhi-Min Liao. Stretch-induced stiffness enhancement of graphene grown by chemical vapor deposition. *ACS Nano*, 7(2):1171–1177, 2013.

[277] Guillermo López-Polín, Cristina Gómez-Navarro, Vincenzo Parente, Francisco Guinea, Mikhail I. Katsnelson, Francesc Pérez-Murano, and Julio Gómez-Herrero. Increasing the elastic modulus of graphene by controlled defect creation. *Nat. Phys.*, 11:26–31, 2015.

[278] C. V. Raman and K. S. Krishnan. A new type of secondary radiation. *Nature*, 121:501–502, 1928.

[279] A. C. Ferrari, J. C. Meyer, V. Scardaci, C. Casiraghi, M. Lazzeri, F. Mauri, S. Piscanec, D. Jiang, K. S. Novoselov, S. Roth, and A. K. Geim. Raman spectrum of graphene and graphene layers. *Phys. Rev. Lett.*, 97:187401, 2006.

[280] A. Ferrari and D. Basko. Raman spectroscopy as a versatile tool for studying the properties of graphene. *Nature Nanotech*, 8:235–246, 2013.

[281] Andrea C. Ferrari. Raman spectroscopy of graphene and graphite: Disorder, electron-phonon coupling, doping and nonadiabatic effects. *Solid State Commun.*, 143(1):47 – 57, 2007.

[282] C. Thomsen and S. Reich. Double resonant Raman scattering in graphite. *Phys. Rev. Lett.*, 85:5214–5217, 2000.

[283] A. C. Ferrari, J. C. Meyer, V. Scardaci, C. Casiraghi, M. Lazzeri, F. Mauri, S. Piscanec, D. Jiang, K. S. Novoselov, S. Roth, and A. K. Geim. Raman spectrum of graphene and graphene layers. *Phys. Rev. Lett.*, 97:187401, 2006.

[284] Simone Pisana, Michele Lazzeri, Cinzia Casiraghi, Kostya S. Novoselov, A. K. Geim, Andrea C. Ferrari, and Francesco Mauri. Breakdown of the adiabatic Born-Oppenheimer approximation in graphene. *Nat. Mater.*, 6:198–201, 2007.

[285] Junku Liu, Qunqing Li, Yuan Zou, Qingkai Qian, Yuanhao Jin, Guanhong Li, Kaili Jiang, and Shoushan Fan. The dependence of graphene Raman D-band on carrier density. *Nano Lett.*, 13(12):6170–6175, 2013.

[286] C. Casiraghi, S. Pisana, K. S. Novoselov, A. K. Geim, and A. C. Ferrari. Raman fingerprint of charged impurities in graphene. *Appl. Phys. Lett.*, 91(23):233108, 2007.

[287] Matteo Bruna, Anna K. Ott, Mari Ijäs, Duhee Yoon, Ugo Sassi, and Andrea C. Ferrari. Doping dependence of the raman spectrum of defected graphene. *ACS Nano*, 8(7):7432–7441, 2014.

[288] C. Casiraghi. Doping dependence of the Raman peaks intensity of graphene close to the Dirac point. *Phys. Rev. B*, 80:233407, 2009.

[289] Martin Kalbáč, Alfonso Reina-Cecco, Hootan Farhat, Jing Kong, Ladislav Kavan, and Mildred S. Dresselhaus. The influence of strong electron and hole doping on the Raman intensity of chemical vapor-deposition graphene. *ACS Nano*, 4(10):6055–6063, 2010.

[290] Ryan Beams, Luiz Gustavo Cançado, and Lukas Novotny. Raman characterization of defects and dopants in graphene. *J. Phys.: Condens. Matter*, 27(8):083002, 2015.

[291] Jun Yan, Yuanbo Zhang, Philip Kim, and Aron Pinczuk. Electric field effect tuning of electron-phonon coupling in graphene. *Phys. Rev. Lett.*, 98:166802, 2007.

[292] A. Das, B. Chakraborty, S. Piscanec, S. Pisana, A. K. Sood, and A. C. Ferrari. Phonon renormalization in doped bilayer graphene. *Phys. Rev. B*, 79:155417, 2009.

[293] A Das, S Pisana, Biswanath Chakraborty, S Piscanec, S K Saha, Umesh Waghmare, K S Novoselov, H Krishnamurthy, A.K. Geim, A.C. Ferrari, and A. K. Sood. Monitoring dopants by Raman scattering in an electrochemically top-gated graphene transistor. *Nat. Nanotechnol.*, 3:210–215, 2008.

[294] M. A. Pimenta, G. Dresselhaus, M. S. Dresselhaus, L. G. Cançado, A. Jorio, and R. Saito. Studying disorder in graphite-based systems by Raman spectroscopy. *Phys. Chem. Chem. Phys.*, 9:1276–1290, 2007.

[295] J. Ribeiro-Soares, M.E. Oliveros, C. Garin, M.V. David, L.G.P. Martins, C.A. Almeida, E.H. Martins-Ferreira, K. Takai, T. Enoki, R. Magalhães-Paniago, A. Malachias, A. Jorio, B.S. Archanjo, C.A. Achete, and L.G. Cançado. Structural analysis of polycrystalline graphene systems by Raman spectroscopy. *Carbon*, 95:646–652, 2015.

[296] E. H. Martins Ferreira, Marcus V. O. Moutinho, F. Stavale, M. M. Lucchese, Rodrigo B. Capaz, C. A. Achete, and A. Jorio. Evolution of the Raman spectra from single-, few-, and many-layer graphene with increasing disorder. *Phys. Rev. B*, 82:125429, 2010.

[297] W. Kohn. Image of the Fermi surface in the vibration spectrum of a metal. *Phys. Rev. Lett.*, 2:393–394, 1959.

[298] S. Piscanec, M. Lazzeri, Francesco Mauri, A. C. Ferrari, and J. Robertson. Kohn anomalies and electron-phonon interactions in graphite. *Phys. Rev. Lett.*, 93:185503, 2004.

[299] Michele Lazzeri and Francesco Mauri. Nonadiabatic Kohn anomaly in a doped graphene monolayer. *Phys. Rev. Lett.*, 97:266407, 2006.

[300] Stefano Piscanec, Michele Lazzeri, J. Robertson, Andrea C. Ferrari, and Francesco Mauri. Optical phonons in carbon nanotubes: Kohn anomalies, Peierls distortions, and dynamic effects. *Phys. Rev. B*, 75:035427, 2007.

[301] D M Basko. Calculation of the Raman G peak intensity in monolayer graphene: role of Ward identities. *New J. Phys.*, 11(9):095011, 2009.

[302] D. M. Basko, S. Piscanec, and A. C. Ferrari. Electron-electron interactions and doping dependence of the two-phonon Raman intensity in graphene. *Phys. Rev. B*, 80:165413, 2009.

[303] Ting Yu, Zhenhua Ni, Chaoling Du, Yumeng You, Yingying Wang, and Zexiang Shen. Raman mapping investigation of graphene on transparent flexible substrate: The strain effect. *J. Phys. Chem. C*, 112(33):12602–12605, 2008.

[304] Georgia Tsoukleri, John Parthenios, Konstantinos Papagelis, Rashid Jalil, Andrea C. Ferrari, Andre K. Geim, Kostya S. Novoselov, and Costas Galiotis. Subjecting a graphene monolayer to tension and compression. *Small*, 5(21):2397–2402, 2009.

[305] Fei Ding, Hengxing Ji, Yonghai Chen, Andreas Herklotz, Kathrin Dörr, Yongfeng Mei, Armando Rastelli, and Oliver G. Schmidt. Stretchable graphene: A close look at fundamental parameters through biaxial straining. *Nano Lett.*, 10(9):3453–3458, 2010.

[306] Jakob Zabel, Rahul R. Nair, Anna Ott, Thanasis Georgiou, Andre K. Geim, Kostya S. Novoselov, and Cinzia Casiraghi. Raman spectroscopy of graphene and bilayer under biaxial strain: Bubbles and balloons. *Nano Lett.*, 12(2):617–621, 2012.

[307] Nicola Ferralis. Probing mechanical properties of graphene with Raman spectroscopy. *J. Mater. Sci.*, 45:5135–5149, 2010.

[308] Dominik Metten, François Federspiel, Michelangelo Romeo, and Stéphane Berciaud. Probing built-in strain in freestanding graphene monolayers by Raman spectroscopy. *Phys. Status Solidi (b)*, 250(12):2681–2686, 2013.

[309] Ch. Androulidakis, G. Tsoukleri, N. Koutroumanis, G. Gkikas, P. Pappas, J. Parthenios, K. Papagelis, and C. Galiotis. Experimentally derived axial stress-strain relations for two-dimensional materials such as monolayer graphene. *Carbon*, 81:322–328, 2015.

[310] T. M. G. Mohiuddin, A. Lombardo, R. R. Nair, A. Bonetti, G. Savini, R. Jalil, N. Bonini, D. M. Basko, C. Galiotis, N. Marzari, K. S. Novoselov, A. K. Geim, and A. C. Ferrari. Uniaxial strain in graphene by Raman spectroscopy: G peak splitting, Grüneisen parameters, and sample orientation. *Phys. Rev. B*, 79:205433, 2009.

[311] Mingyuan Huang, Hugen Yan, Changyao Chen, Daohua Song, Tony F. Heinz, and James Hone. Phonon softening and crystallographic orientation of strained graphene studied by Raman spectroscopy. *Proc. Natl. Acad. Sci.*, 106(18):7304–7308, 2009.

[312] M. Mohr, J. Maultzsch, and C. Thomsen. Splitting of the Raman 2D band of graphene subjected to strain. *Phys. Rev. B*, 82:201409, 2010.

[313] Y. C. Cheng, Z. Y. Zhu, G. S. Huang, and U. Schwingenschlögl. Grüneisen parameter of the G mode of strained monolayer graphene. *Phys. Rev. B*, 83:115449, 2011.

[314] Elena del Corro, Ladislav Kavan, Martin Kalbac, and Otakar Frank. Strain assessment in graphene through the Raman 2D' mode. *J. Phys. Chem. C*, 119(45):25651–25656, 2015.

[315] Ji Eun Lee, Gwanghyun Ahn, Jihye Shim, Young Sik Lee, and Sunmin Ryu. Optical separation of mechanical strain from charge doping in graphene. *Nat. Commun.*, 3:1024, 2012.

[316] Niclas S Mueller, Sebastian Heeg, Miriam Peña Alvarez, Patryk Kusch, Sören Wasserroth, Nick Clark, Fredrik Schedin, John Parthenios, Konstantinos Papagelis, Costas Galiotis, Martin Kalbáč, Aravind Vijayaraghavan, Uwe Huebner, Roman Gorbachev, Otakar Frank, and Stephanie Reich. Evaluating arbitrary strain configurations and doping in graphene with Raman spectroscopy. *2D Mater.*, 5(1):015016, 2017.

[317] Martin Benjamin B.S. Larsen, David M.A. Mackenzie, José M. Caridad, Peter Bøggild, and Timothy J. Booth. Transfer induced compressive strain in graphene: Evidence from raman spectroscopic mapping. *Microelectron. Eng.*, 121:113 – 117, 2014.

[318] Zehao Wu, Xuewei Zhang, Atanu Das, Jinglan Liu, Zhenxing Zou, Zilong Zhang, Yang Xia, Pei Zhao, and Hongtao Wang. Step-by-step monitoring of cvd-graphene during wet transfer by raman spectroscopy. *RSC Adv.*, 9:41447–41452, 2019.

[319] Hong Goo Kim, Kenneth D. Kihm, Woomin Lee, Gyumin Lim, Sosan Cheon, Woorim Lee, Kyung Rok Pyun, Seung Hwan Ko, and Seungha Shin. Effect of graphene-substrate conformity on the in-plane thermal conductivity of supported graphene. *Carbon*, 125:39 – 48, 2017.

[320] L. G. Cançado, K. Takai, T. Enoki, M. Endo, Y. A. Kim, H. Mizusaki, A. Jorio, L. N. Coelho, R. Magalhães-Paniago, and M. A. Pimenta. General equation for the determination of the crystallite size L_a of nanographite by Raman spectroscopy. *Appl. Phys. Lett.*, 88(16):163106, 2006.

[321] Cinzia Casiraghi. Probing disorder and charged impurities in graphene by Raman spectroscopy. *Phys. Status Solidi RRL*, 3(6):175–177, 2009.

[322] L.M. Malard, M.A. Pimenta, G. Dresselhaus, and M.S. Dresselhaus. Raman spectroscopy in graphene. *Phys. Rep.*, 473(5):51 – 87, 2009.

[323] L. G. Cançado, A. Jorio, E. H. Martins Ferreira, F. Stavale, C. A. Achete, R. B. Capaz, M. V. O. Moutinho, A. Lombardo, T. S. Kulmala, and A. C. Ferrari. Quantifying defects in graphene via Raman spectroscopy at different excitation energies. *Nano Lett.*, 11(8):3190–3196, 2011.

[324] Florian Banhart, Jani Kotakoski, and Arkady V. Krasheninnikov. Structural defects in graphene. *ACS Nano*, 5(1):26–41, 2011. PMID: 21090760.

[325] Oleg V. Yazyev and Yong P. Chen. Polycrystalline graphene and other two-dimensional materials. *Nat. Nanotechnol.*, 9(755), 2014.

[326] F. Tuinstra and J. L. Koenig. Raman spectrum of graphite. *J. Chem. Phys.*, 53(3):1126–1130, 1970.

[327] A. C. Ferrari and J. Robertson. Interpretation of Raman spectra of disordered and amorphous carbon. *Phys. Rev. B*, 61:14095–14107, 2000.

[328] M.M. Lucchese, F. Stavale, E.H. Martins Ferreira, C. Vilani, M.V.O. Moutinho, Rodrigo B. Capaz, C.A. Achete, and A. Jorio. Quantifying ion-induced defects and Raman relaxation length in graphene. *Carbon*, 48(5):1592 – 1597, 2010.

[329] Luiz Gustavo Cançado, Mateus Gomes da Silva, Erlon H Martins Ferreira, Ferdinand Hof, Katerina Kampioti, Kai Huang, Alain Pénicaud, Carlos Alberto Achete, Rodrigo B Capaz, and Ado Jorio. Disentangling contributions of point and line defects in the Raman spectra of graphene-related materials. *2D Mater.*, 4(2):025039, 2017.

[330] Golap Kalita, Litao Qi, Yoshiharu Namba, Koichi Wakita, and Masayoshi Umeno. Femtosecond laser induced micropatterning of graphene film. *Mater. Lett.*, 65(11):1569 – 1572, 2011.

[331] W. Zhang, L. Li, Z. B. Wang, A. A. Pena, D. J. Whitehead, M. L. Zhong, Z. Lin, and H. W. Zhu. Ti:sapphire femtosecond laser direct micro-cutting and profiling of graphene. *Appl. Phys. A*, 109:291 – 297, 2012.

[332] Zhe Lin, Xiaohui Ye, Jinpeng Han, Qiao Chen, Peixun Fan, Hongjun Zhang, Dan Xie, Hongwei Zhu, and Minlin Zhong. Precise control of the number of layers of graphene by picosecond laser thinning. *Sci. Rep.*, 5:11662, 2015.

[333] Mengmeng Wang, Dawei Li, Kun Liu, Qitong Guo, Sumei Wang, and Xin Li. Nonlinear optical imaging, precise layer thinning, and phase engineering in $MoTe_2$ with femtosecond laser. *ACS Nano*, 14(9):11169–11177, 2020.

[334] Ramazan Sahin, Selcuk Akturk, and Ergun Simsek. Quantifying the quality of femtosecond laser ablation of graphene. *Appl. Phys. A*, 116:555 – 560, 2014.

[335] Tianqi Dong, Martin Sparkes, Colm Durkan, and William O'Neill. Evaluating femtosecond laser ablation of graphene on SiO_2/Si substrate. *J. Laser Appl.*, 28(2):022202, 2016.

[336] Yonglai Zhang, Li Guo, Shu Wei, Yinyan He, Hong Xia, Qidai Chen, Hong-Bo Sun, and Feng-Shou Xiao. Direct imprinting of microcircuits on graphene oxides film by femtosecond laser reduction. *Nano Today*, 5(1):15 – 20, 2010.

[337] Jukka Aumanen, Andreas Johansson, Olli Herranen, Pasi Myllyperkiö, and Mika Pettersson. Local photo-oxidation of individual single walled carbon nanotubes probed by femtosecond four wave mixing imaging. *Phys. Chem. Chem. Phys.*, 17:209–216, 2015.

[338] Jukka Aumanen, Andreas Johansson, Juha Koivistoinen, Pasi Myllyperkiö, and Mika Pettersson. Patterning and tuning of electrical and optical properties of graphene by laser induced two-photon oxidation. *Nanoscale*, 7:2851–2855, 2015.

[339] Juha Koivistoinen, Lucia Sládková, Jukka Aumanen, Pekka Koskinen, Kevin Roberts, Andreas Johansson, Pasi Myllyperkiö, and Mika Pettersson. From seeds to islands: Growth of oxidized graphene by two-photon oxidation. *J. Phys. Chem. C*, 120(39):22330–22341, 2016.

[340] Andreas Johansson, Hung-Chieh Tsai, Jukka Aumanen, Juha Koivistoinen, Pasi Myllyperkiö, Yi-Zhe Hung, Min-Chiang Chuang, Chia-Hao Chen, Wei Yen Woon, and Mika Pettersson. Chemical composition of two-photon oxidized graphene. *Carbon*, 115:77 – 82, 2017.

[341] Yuanyue Liu and Boris I. Yakobson. Cones, pringles, and grain boundary landscapes in graphene topology. *Nano Lett.*, 10(6):2178–2183, 2010.

[342] Topi Kähärä and Pekka Koskinen. Rippling of two-dimensional materials by line defects. *Phys. Rev. B*, 102:075433, 2020.

[343] Joel P. McDonald, Vanita R. Mistry, Katherine E. Ray, Steven M. Yalisove, John A. Nees, and Neville R. Moody. Femtosecond-laser-induced delamination and blister formation in thermal oxide films on silicon (100). *Appl. Phys. Lett.*, 88(15):153121, 2006.

[344] Jorge Torres, Yisi Zhu, Pei Liu, Seong Chu Lim, and Minhee Yun. Adhesion energies of 2D graphene and MoS_2 to silicon and metal substrates. *Phys. Status Solidi A*, 215(1):1700512, 2018.

[345] Miska Karttila. Grafeenin optiset ja spektroskopiset ominaisuudet, 2020. Master's thesis, University of Jyväskylä.

[346] Shoujun Zhu, Junhu Zhang, Chunyan Qiao, Shijia Tang, Yunfeng Li, Wenjing Yuan, Bo Li, Lu Tian, Fang Liu, Rui Hu, Hainan Gao, Haotong Wei, Hao Zhang, Hongchen Sun, and Bai Yang. Strongly green-photoluminescent graphene quantum dots for bioimaging applications. *Chem. Commun.*, 47:6858–6860, 2011.

[347] Fuchi Liu, Yuanyuan Sun, Yongping Zheng, Nujiang Tang, Ming Li, Wei Zhong, and Youwei Du. Gram-scale synthesis of high-purity graphene quantum dots with multicolor photoluminescence. *RSC Adv.*, 5:103428–103432, 2015.

[348] Tian Gao, Xi Wang, Li-Yun Yang, Huan He, Xiao-Xu Ba, Jie Zhao, Feng-Lei Jiang, and Yi Liu. Red, yellow, and blue luminescence by graphene quantum dots: Syntheses, mechanism, and cellular imaging. *ACS Appl. Mater. Interfaces*, 9(29):24846–24856, 2017.

[349] Shoujun Zhu, Yubin Song, Xiaohuan Zhao, Jieren Shao, Junhu Zhang, and Bai Yang. The photoluminescence mechanism in carbon dots (graphene quantum dots, carbon nanodots, and polymer dots): current state and future perspective. *Nano Res.*, 8:355 – 381, 2015.

[350] Shoujun Zhu, Yubin Song, Joy Wang, Hao Wan, Yuan Zhang, Yang Ning, and Bai Yang. Photoluminescence mechanism in graphene quantum dots: Quantum confinement effect and surface/edge state. *Nano Today*, 13:10–14, 2017.

[351] Carlo Maria Carbonaro, Riccardo Corpino, Marcello Salis, Francesca Mocci, Swapneel Vijay Thakkar, Chiara Olla, and Pier Carlo Ricci. On the emission properties of carbon dots: Reviewing data and discussing models. *C*, 5(4):60, 2019.

[352] Dengyu Pan, Jingchun Zhang, Zhen Li, and Minghong Wu. Hydrothermal route for cutting graphene sheets into blue-luminescent graphene quantum dots. *Adv. Mater.*, 22(6):734–738, 2010.

[353] Shoujun Zhu, Junhu Zhang, Shijia Tang, Chunyan Qiao, Lei Wang, Haiyu Wang, Xue Liu, Bo Li, Yunfeng Li, Weili Yu, Xingfeng Wang, Hongchen Sun, and Bai Yang. Surface chemistry routes to modulate the photoluminescence of graphene quantum dots: From fluorescence mechanism to upconversion bioimaging applications. *Adv. Funct. Mater.*, 22(22):4732–4740, 2012.

[354] Dan Qu, Min Zheng, Jing Li, Zhigang Xie, and Zaicheng Sun. Tailoring color emissions from N-doped graphene quantum dots for bioimaging applications. *Light: Sci. Appl.*, 4:e364, 2015.

[355] Suzuka Tachi, Hiroki Morita, Misaki Takahashi, Yusuke Okabayashi, Takuya Hosokai, Toshiki Sugai, and Shota Kuwahara. Quantum yield enhancement in graphene quantum dots via esterification with benzyl alcohol. *Sci. Rep.*, 9:14115, 2019.

[356] Francesca Demichelis, Steffen Schreiter, and Alberto Tagliaferro. Photoluminescence in a-C:H films. *Phys. Rev. B*, 51:2143–2147, 1995.

[357] Rusli, Gehan A.J. Amaratunga, and S.R.P. Silva. Photoluminescence in amorphous carbon thin films and its relation to the microscopic properties. *Thin Solid Films*, 270(1):160 – 164, 1995. 22nd International Conference on Metallurgical Coatings and Thin Films.

[358] Chee-Tat Toh, Hongji Zhang, Junhao Lin, Alexander S. Mayorov, Yun-Peng Wang, Carlo M. Orofeo, Darim Badur Ferry, Henrik Andersen, Nurbek Kakenov, Zenglong Guo, Irfan Haider Abidi, Hunter Sims, Kazu Suenaga, Sokrates T. Pantelides, and Barbaros Özyilmaz. Synthesis and properties of free-standing monolayer amorphous carbon. *Nature*, 577:199 – 203, 2020.

[359] Nuannuan Jing, Qingzhong Xue, Cuicui Ling, Meixia Shan, Teng Zhang, Xiaoyan Zhou, and Zhiyong Jiao. Effect of defects on Young's modulus of graphene sheets: A molecular dynamics simulation. *RSC Adv.*, 2:9124–9129, 2012.

[360] Ardavan Zandiatashbar, Gwan-Hyoung Lee, Sung Joo An, Sunwoo Lee, Nithin Mathew, Mauricio Terrones, Takuya Hayashi, Catalin R. Picu, James Hone, and Nikhil Koratkar. Effect of defects on the intrinsic strength and stiffness of graphene. *Nat. Commun.*, 5:3186, 2014.

[361] D.G. Kvashnin and P.B. Sorokin. Effect of ultrahigh stiffness of defective graphene from atomistic point of view. *J. Phys. Chem. Lett.*, 6(12):2384–2387, 2015.

[362] A. Lima-Rodriguez, A. Gonzalez-Herrera, and J. Garcia-Manrique. Study of the dynamic behaviour of circular membranes with low tension. *Appl. Sci.*, 9(4716):4716, 2019.

APPENDIX 1 DETAILS OF SAMPLE FABRICATION

Graphene synthesis and transfer

A vast majority of the graphene samples used in this work were synthesized using chemical vapor deposition method described in section 2.1. Details of the actual processes and equipment are presented here. The processing parameters that are mentioned are typical values and there can be slight differences in different samples.

Fabrication of graphene started by preparing sapphire substrate. Single crystal sapphire (α-Al_2O_3) wafers were cut using dicing saw to chips. Chip sizes were typically 5×5 mm^2. The chips were cleaned in hot acetone by rubbing them with cotton swabs and by using sonication, after which they were rinsed in isopropanol alcohol (IPA) and dried with N_2 gun. The chips were examined under optical microscope to verify that they do not have large particle contamination. The sapphire samples were then annealed in a furnace (Carbolite CTF 12/65/550 with an Eurotherm 3216 temperature/process controller) under oxygen atmosphere at 1100 °C for $\sim$ 12 h. After this, the sapphire substrates were ready for copper deposition.

Copper catalyst film was deposited onto the sapphire chips using an electron beam evaporator (Baltec BAE 250, modified). Typical deposition rate was 5 Å/s and film thickness 600 nm.

CVD synthesis of graphene was typically done immediately after the copper deposition. The synthesis was done in a high temperature furnace (MTI GSL-1100X). Samples were loaded onto a quartz sample stage and inserted into the preheated furnace for annealing. Typically the samples were annealed for 45 minutes at 1060 °C temperature under 30 sccm H_2 + 470 sccm Ar gas flows. All processing was done in atmospheric pressure. After annealing, the synthesis was initiated by adding 2 sccm of 1 % CH_4 in argon to the gas flow for five minutes. Samples were then pulled out of the hot zone of the furnace and let cool naturally. After synthesis the samples were examined under optical microscope. The samples were baked in air for about five minutes at $\sim$ 120 °C to oxidize the regions that graphene is not covering in order to visualize the graphene coverage.

Transfer of graphene started by depositing PMMA onto graphene. Typically PMMA A4 950 was spin coated (Laurell Technologies, WS-650MZ-23NPPB) using 3000 rpm for one minute. Edges of the PMMA layer were scraped with a scalpel to make copper etching easier. Copper was etched in 1 M ammonium persulfate bath typically overnight. Then the released PMMA/graphene layer was moved through four consecutive DI water baths to remove etchant residues. The samples were kept in 10 % hydrochloric acid bath for 5 minutes in order to clean any metallic residues, after which the samples were moved again through the water baths to rinse them. At the final water bath, the water was drained to gently lower the PMMA/graphene stack onto a target substrate. The samples were then let to dry and baked at about 100 °C for five minutes to remove as much of the water as possible. Then the PMMA layer was removed in hot acetone, after which the sample was rinsed in IPA.

Substrate fabrication for suspended graphene samples

Substrate used in this work for suspended graphene was silicon nitride membrane window. Fabrication steps for making this are presented in Figure A1. The starting substrate for this sample was a silicon chip with LPCVD grown 300 nm thick silicon nitride (Si_3N_4) coating on both sides. Sample processing started by depositing photoresist (AZ 1514H) on the sample. This was done by spin coating it in a spinner (Laurell Technologies, WS-650MZ-23NPPB) at 4000 rpm for one minute. The sample was baked for one minute at 100 °C. The other side of the chip was spin coated as well to prevent unwanted etching of the silicon nitride.

Then one side of the sample was exposed to UV light using a mask aligner (Karl Zuss) for 50 s. The sample was developed in 1:3 solution of AZ 351B developer and water for one minute. Silicon nitride was then etched using reactive ion etching (Oxford Instruments, Plasmalab 80 Plus). Before the nitride etch the resist residues were cleaned using a mild O_2 plasma treatment using 50 sccm O_2 flow for 15 s at 15 mTorr with 20 W forward power. Nitride was ethced with gas flows of 50 sccm CHF_3 and 5 sccm O_2 for 25 minutes at 55 mTorr with 100 W power. Oxygen was added into the gas flow to prevent a passivation layer from forming. Both RIE treatments were done at room temperature. The photoresist was then stripped using hot acetone. The silicon was etched through using 35 % potassium hydroxide (KOH) at approximately 98 °C water bath for 6 hours. KOH etches the silicon anisotropically, which is based on the etching rate being different depending on the silicon crystal plane, (111) plane etching rate being much slower than (100). This results into silicon being etched in pyramidical shape with 54.7° angle. This left the silicon nitride membrane window.

Next was fabrication of holes in the silicon nitride window. This started with depositing $\sim$ 20 nm of copper onto the sample using modified Baltec BAE 250 electron beam evaporator. This film serves as a conductive layer during the electron beam lithography and also as an etch mask. A PMMA layer (PMMA A2 950) was deposited onto the copper film by spin coating at 4000 rpm and baked at 160 °C for two minutes. Writing of the patterns was done using Raith eLine SEM using 300 $\mu As/cm^2$ dose. Several cirular patterns of varying diameters were drawn. Next, the PMMA was developed in 1:3 solution of methyl isobutyl ketone (MIBK) and isopropanol alcohol (IPA) for 50 seconds. Copper was etched by dipping the sample into etching solution of $H_2O + CH_3COOH + H_2O_2$ (18:1:1) for a few seconds. Then the exposed silicon nitride was etched using RIE with the same recipe as above. Finally, the entire copper layer was etched.

When the graphene was transferred onto the substrates, the PMMA layer was removed in acetone and the sample was dried using critical point drying apparatus (Leica EM CPD300).

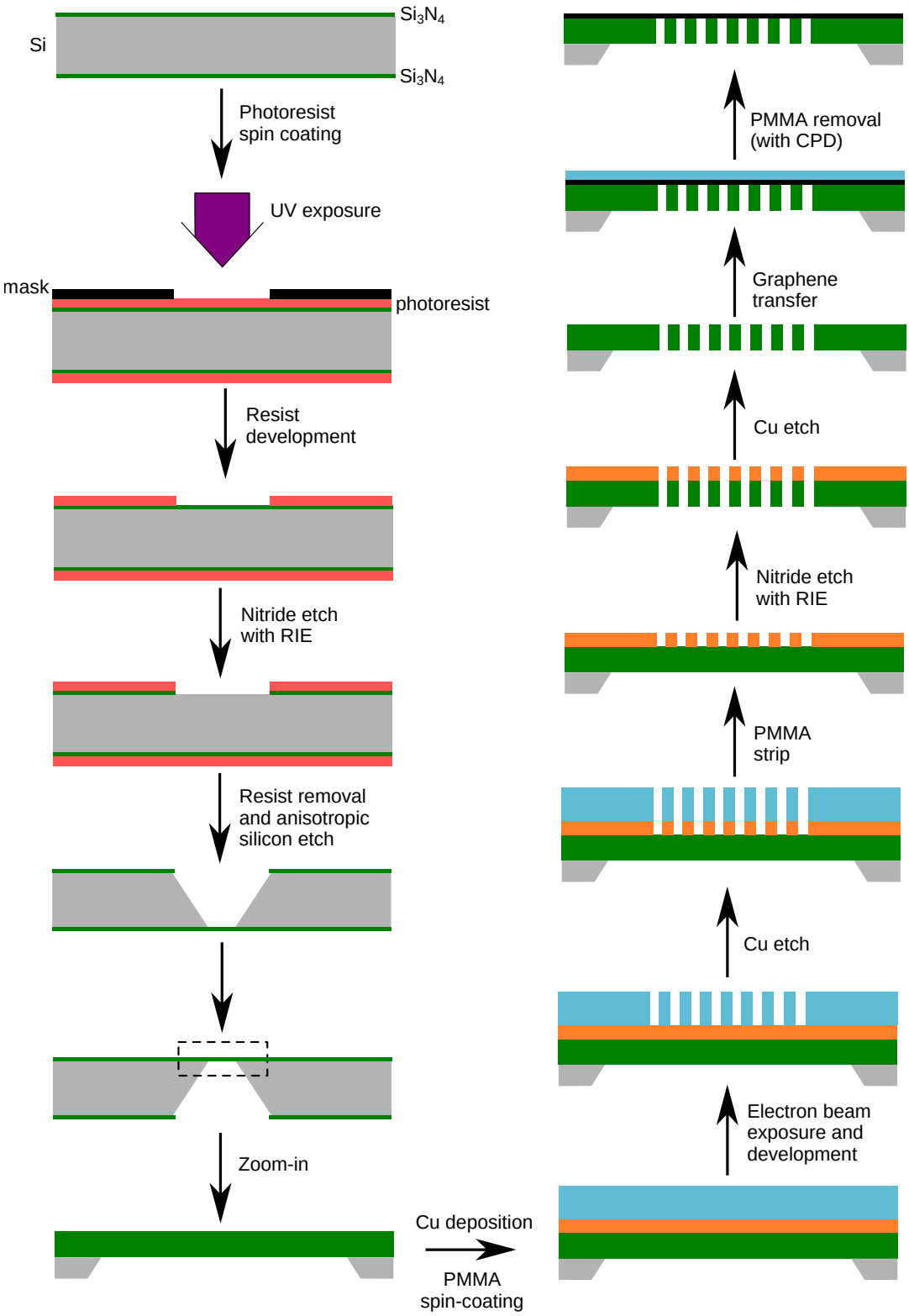

FIGURE A1 Fabrication steps for a suspended graphene sample.

ORIGINAL PAPERS

AI

OPTICAL FORGING OF GRAPHENE INTO THREE-DIMENSIONAL SHAPES

by

Andreas Johansson, Pasi Myllyperkiö, Pekka Koskinen, Jukka Aumanen, Juha Koivistoinen, Hung-Chieh Tsai, Chia-Hao Chen, Lo-Yueh Chang, Vesa-Matti Hiltunen, Jyrki J. Manninen,Wei YenWoon, Mika Pettersson 2017

Nano Letters, 17, 10, 6469-6474

DOI: 10.1021/acs.nanolett.7b03530

NANO LETTERS

Letter

pubs.acs.org/NanoLett

Optical Forging of Graphene into Three-Dimensional Shapes

Andreas Johansson,[†,‡] Pasi Myllyperkiö,[†] Pekka Koskinen,[‡] Jukka Aumanen,[†] Juha Koivistoinen,[†] Hung-Chieh Tsai,[§] Chia-Hao Chen,[∥] Lo-Yueh Chang,[∥] Vesa-Matti Hiltunen,[‡] Jyrki J. Manninen,[‡] Wei Yen Woon,[§] and Mika Pettersson*[,†]

[†]Nanoscience Center, Department of Chemistry, [‡]Nanoscience Center, Department of Physics, University of Jyväskylä, P.O. Box 35, FI-40014 Jyväskylä, Finland

[§]Department of Physics, National Central University, Jungli, 32054, Taiwan, Republic of China

[∥]National Synchrotron Radiation Research Center, Hsinchu, 30076, Taiwan, Republic of China

S *Supporting Information*

ABSTRACT: Atomically thin materials, such as graphene, are the ultimate building blocks for nanoscale devices. But although their synthesis and handling today are routine, all efforts thus far have been restricted to flat natural geometries, since the means to control their three-dimensional (3D) morphology has remained elusive. Here we show that, just as a blacksmith uses a hammer to forge a metal sheet into 3D shapes, a pulsed laser beam can forge a graphene sheet into controlled 3D shapes in the nanoscale. The forging mechanism is based on laser-induced local expansion of graphene, as confirmed by computer simulations using thin sheet elasticity theory.

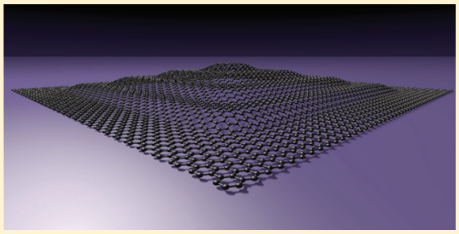

KEYWORDS: *Graphene, strain-engineering, femtosecond laser, defects, 3-dimensional, elasticity modeling*

Graphene, a single atomic layer of carbon, is the most studied 2D material and is characterized by excellent carrier mobility, strength, flexibility, transparency, and constant absorption in a broad range of the electromagnetic spectrum, making graphene an excellent material for novel applications in electronics, photonics, and optoelectronics.[1,2] Examples of reported devices include sensors, field effect transistors (FET), supercapacitors, and photodetectors.[3] Graphene is not strictly planar but contains corrugations, wrinkles, ripples, and other out-of-plane deformations.[4] These structural changes provide a way to modify the electronic properties of graphene, but controlling them is challenging.[5−8] So far, the modification of the third dimension of graphene has relied on spot-blistering, substrate molding, or strain-induced periodic modulation, as well as cutting graphene or connecting graphene flakes with functional groups, while controlled shaping of graphene itself into more complex custom-made 3D architectures has remained elusive.[9−13]

Here, we demonstrate the forging of graphene into free-standing 3D shapes by exploiting local strain induction due to irradiation with femtosecond laser pulses under inert atmosphere. While laser irradiation in air has earlier been shown to generate two-photon functionalization of the graphene surface with oxygen containing groups,[14] we argue here that the inert atmosphere allows a fundamentally different process of defect engineering to take place. Computer simulations using elasticity theory confirm experimental observations and provide the theoretical basis for the method. The optical forging opens new possibilities for fundamental studies and for the development of applications based on 3D shapes of graphene.

We patterned single-layer graphene on a Si/SiO_2 substrate by direct laser writing with tightly focused femtosecond pulses under nitrogen and argon atmospheres, which both produced qualitatively similar results. A matrix of 2×2 μm^2 squares was patterned on graphene. Each square was irradiated by 441 partially overlapping spots at 100 nm spot separation. The irradiation time per spot was varied from 0.1 to 2.0 s. Surprisingly, the irradiated squares formed elevated flat plateaus with sharp boundaries, as seen in atomic force microscope (AFM) images (Figure 1a). The height varies from ∼3 nm up to ∼20 nm (Figure 1b) and is proportional to the square root of irradiation time (Supporting Information, Figure S1). This proportionality can be theoretically justified, as shown later. We did not observe any wrinkling on the plateaus or just outside them, except for folding already present in graphene before patterning. Remarkably, the patterned matrix is well visible under an optical microscope due to enhanced reflection of the irradiated areas (Figure 1c). With increasing irradiation time, the brightness of the irradiated spots increases, and the color changes from greenish toward yellow.

The squares are visible in a Raman map of the integrated intensity of the D-band including the contribution from the overlapping broad emission, which increases with irradiation

Received: August 17, 2017
Revised: September 12, 2017
Published: September 19, 2017

DOI: 10.1021/acs.nanolett.7b03530
Nano Lett. 2017, 17, 6469−6474

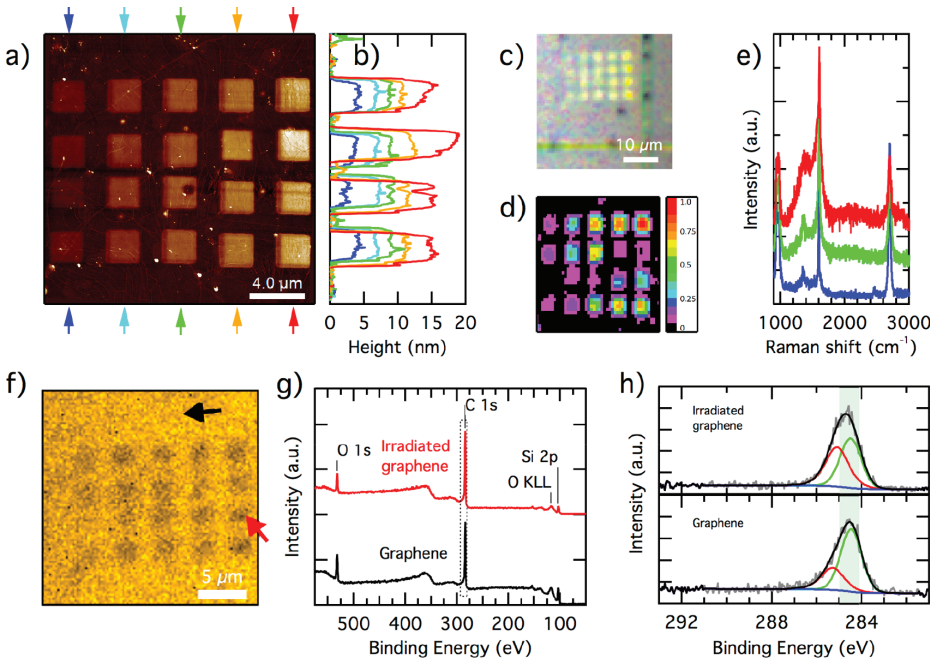

Figure 1. Characterization of irradiated graphene. (a) AFM image. (b) Line profiles of the AFM image between the arrows, shown in a. (c) Optical microscope image. The lines on the bottom and right are a part of the 30 nm thick and 1 μm wide gold reference grid. (d) Raman map showing integrated intensity in the D-band area at ~1350 cm^{-1}. (e) Raman spectra measured from graphene with no irradiation (bottom) and with 0.5 s (middle) and 2 s (top) of irradiation per spot. (f) XPS image of the C 1s signal at 285.0−284.2 eV. (g) XPS survey spectra of nonirradiated graphene (bottom) and irradiated graphene (top). (h) XPS C 1s spectra of nonirradiated area (bottom; black arrow in f) and irradiated area (top; red arrow in f). The shaded area shows the region used to construct the image in f. The gray line shows the raw spectrum; the black line is the fit that contains components of C═C (green), C−C (red), and background (blue).

(see Figures 1d and e). While local variations are observed, there is an overall trend toward increased integrated intensity with increased irradiation time. The characteristic spectrum of nonirradiated graphene (Figure 1e, bottom) is observed also in the irradiated areas (Figure 1e, middle and top). Note that the Raman spectrum of nonirradiated graphene does not show any significant presence of amorphous carbon, which excludes amorphous carbon redeposition or exfoliation[15] as the cause for the elevated plateaus. With increasing irradiation dose, broadened G- and D-bands develop, while the normal Raman spectrum of (nonirradiated) graphene remains (Figure 1e). The total spectrum is thus a sum of two components: normal and broad (additional Raman spectra are shown in Supporting Information, Figure S2). The broad spectrum resembles highly disordered graphene, but there is no growth of a sharp D-band, which is a characteristic signature of scattered point defects in graphene.[16,17] These observations suggest that irradiation transforms local regions of graphene into disordered form. In Raman spectra, also a broad emission background emerges upon irradiation (seen as a rising background in Figure 1e).

The sample was imaged by X-ray photoelectron spectroscopy (XPS) at submicrometer spatial resolution (Figure 1f). XPS did not reveal significant change in the chemical composition of graphene irradiated under nitrogen atmosphere (Figure 1g). Yet, contrast is found in scanning photoelectron microscopy due to overall lower XPS intensity for patterned areas (Figure 1f). The carbon C 1s peak becomes broader toward the higher binding energy tail, indicating a decrease in the sp^2 C═C bond and increase in the C−C bond density (Figure 1h). The XPS data are consistent with the defect generation picture as deduced from Raman spectra. The lack of oxygen containing groups again supports the notion that amorphous carbon does not contribute to the elevated plateaus. For comparison, irradiation of the same sample with analogous patterns under air reveals characteristic signals of oxidized carbon (Supporting Information, Figure S3).[14,18,19]

To further investigate the nature of the elevated plateaus we prepared a series of square patterns and compared them to square patterns made under air. In Figure 2a, two rows of squares patterned on graphene are presented. The barely visible top row was patterned under air, leading to functionalization of the surface with mainly epoxy and hydroxyl groups.[14,19] The height of the squares is about 1.3 nm. The bottom row was patterned under nitrogen, leading to elevated plateaus of about 20 nm in height. At the center of the image there is a triangular-shaped area in which the graphene has folded toward the upper right corner. In that area, no pattern is formed under either oxygen or nitrogen atmosphere, and the surface seems unaffected by the laser exposure. This observation again refutes that amorphous carbon deposition would contribute to the elevated plateaus. Additionally, it refutes the possibility of formation of elevated plateaus due to swelling of the underlying SiO_2 substrate.[20,21] Folds, cracks, and other surface features on graphene continue from the areas outside the plateaus to the inside. This is strong additional evidence that deposition of material cannot be responsible for the elevated features.

DOI: 10.1021/acs.nanolett.7b03530
Nano Lett. 2017, 17, 6469−6474

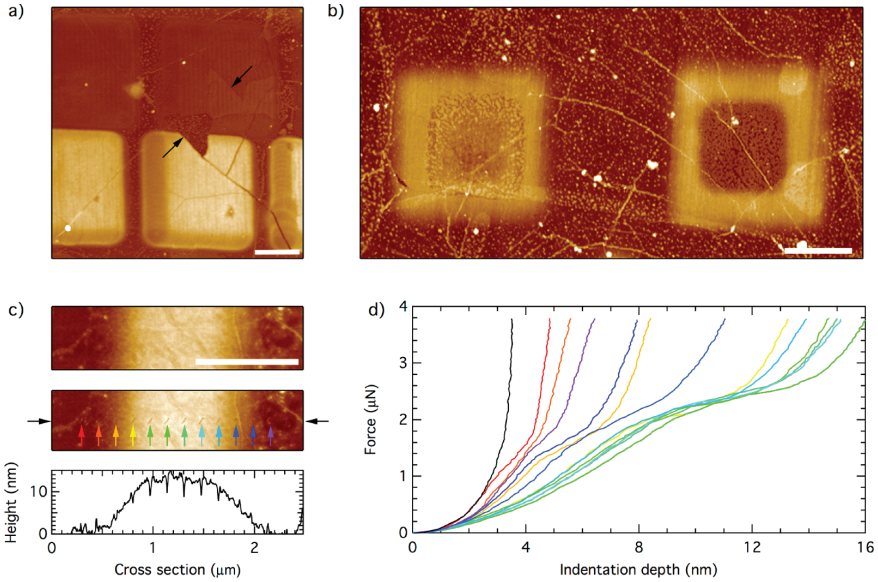

Figure 2. (a) AFM image of squares patterned under air (top) and nitrogen (bottom). The arrows point out where a triangular shaped section of graphene has folded. (b) AFM image of large squares patterned under nitrogen, with center regions in addition patterned under air. The center region was patterned after the larger square for the left pattern and before the larger square for the right pattern. (c) AFM data from nanoindentation area, showing topography before (top pane) and after (middle pane). The cross section (bottom pane) is taken between the black arrows in the middle pane. (d) Nanoindentation data showing the measured force versus indentation depth. The trace colors correspond to the arrow colors in c showing the measurement location, except for the black trace, which is measured on bare SiO_2. All scale bars are 1 um.

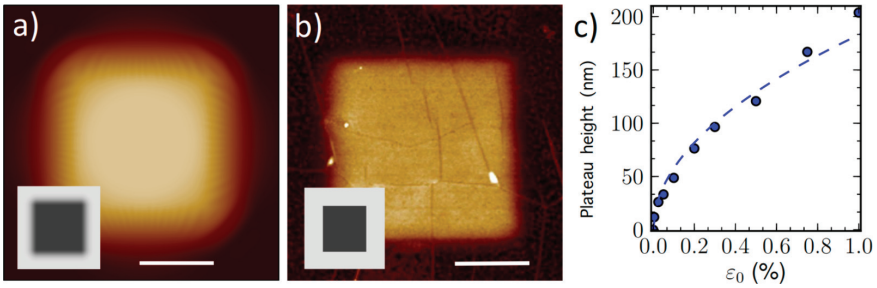

Figure 3. Elasticity modeling of plateau formation by local expansion. (a) Optimized topography of a simulated 2 × 2 μm^2 square pattern. Inset: the input strain field $\epsilon(\mathbf{r})$; maximum strain is $\varepsilon_0 = 4.5 \times 10^{-5}$. (b) AFM topography of the plateau (corresponding to 1.5 s irradiation time in Figure 1a). The plateau height is 12 nm in both simulation and experiment. Inset: bitmap image used for laser writing. Scale bars, 1 μm. (c) Simulated height of 2 × 2 μm^2 square plateaus at different ε_0; the dashed line is eq 1.

Figure 2b shows two square patterns prepared by combining laser patterning under both air and nitrogen. For the left square pattern, first the large 2 × 2 μm^2 square was patterned under nitrogen, forming a 6 nm high plateau. Then the inner 1 × 1 μm^2 square was patterned under air. The inner square is somewhat crumpled with an average height of 3.5 nm. For the right square pattern, first the inner 1 × 1 μm^2 square was patterned under air and the outer 2 × 2 μm^2 square patterned under nitrogen. Here the inner square has a height of 1.3 nm, which is similar to oxidized areas in Figure 2a. The outer frame is again 6 nm high. The data show that functionalization of the graphene surface with oxygen containing groups leads to suppression of elevated plateau formation.

We also performed AFM nanoindentation across a 12 nm high, 1 μm wide, and 6 μm long graphene plateau. The nanoindentation area is shown in Figure 2c before (top) and after indentation (middle), together with a cross section (bottom) along the indentation line. The measured force versus indentation depth curves are shown in Figure 2d, with color corresponding to the arrows in Figure 2c pointing out their measurement locations. The resulting force versus indentation depth curves show initially a nonlinear increase, with a much weaker response than indentation on bare SiO_2 surface (black trace). At around 2 μN a plateau develops, which is interpreted as the graphene feature buckling toward the surface. It is interesting to note that this force is very similar to the nanoindentation force at which suspended graphene membranes break.[22,23] The force curve then increases again with a dependence similar to that of indentation on a bare SiO_2 surface. The onset of the second increase corresponds well to the height of the graphene structure, indicating that the onset corresponds to the tip reaching the SiO_2 surface. The AFM

DOI: 10.1021/acs.nanolett.7b03530
Nano Lett. 2017, 17, 6469−6474

image taken after nanoindentation (Figure 2c, middle) shows that the graphene structure has returned to its original shape, except for piercing marks where the AFM probe was indenting the surface.

All of the evidence taken together suggests that irradiation under inert atmosphere leads to the formation of elevated graphene structures containing only carbon. The most plausible explanation for the underlying driving force is that, by analogy to the blister formation in polymers, photons modify the lattice and induce local expansion of graphene.

To investigate this hypothesis, we used thin sheet elasticity theory to model expanded and deformed graphene (see Supporting Information). We assumed that, via a mechanism discussed later, the laser-induced lattice expansion field $\varepsilon(\mathbf{r})$ is proportional to the spatial irradiation dose $I(\mathbf{r})$. The spatial dependency was adopted from experimental input in conjunction with a Gaussian beam profile (full-width at half-maximum, fwhm = 500 nm).[18] The maximum strain $\varepsilon_0 = \max[\varepsilon(\mathbf{r})]$ was chosen, and the topography was searched for by structural optimization. As a result, simulation of a 2×2 μm^2 pattern with $\varepsilon_0 \approx 4.5 \times 10^{-5}$ gave topography and dimensions in perfect agreement with the experiments (Figure 3a,b). The agreement is the first indication suggesting that local expansion indeed is the driving force behind the observed structures.

The plateau formation can be understood simply in terms of increased surface area. Geometrical considerations provide an estimate for the height of a $L_0 \times L_0$ square pattern as

$$h(\varepsilon_0) = \sqrt{0.81\varepsilon_0 w(L_0 + 1.1 \times \text{fwhm})} \quad (1)$$

where w is the edge width (see Supporting Information). We simulated the 2×2 μm^2 pattern with expansions up to $\varepsilon_0 = 1\%$ and observed that eq 1 with $w \approx 3 \times$ fwhm captures well the dependence of height on strain (Figure 3c). Especially the square root dependence indicates how modest expansions are able to trigger notable structures. By inverting eq 1 and using the experimental data for $h(t)$, we could plot $\varepsilon_0(t)$, the expansion as a function of time (Supporting Information, Figure S4). The plot shows that strain grows linearly with irradiation time, here at rates around ~0.01% per second.

The most plausible mechanism for the expansion mechanism is irradiation-induced defect formation. Raman spectra indicate that irradiation produces disordered regions (Figure 1e). It is reasonable to assume that, in the beginning of the process, isolated defects are formed. The density of isolated point defects can be estimated from the $I(D)/I(G)$ ratio.[24] Our nonirradiated CVD-grown graphene sample shows a ratio of ~0.1, corresponding to an initial defect density ~10^{11} cm^{-2} (Figure 1e).[24] Since the sharp D-band does not grow significantly in irradiation, the point defect density does not grow much beyond ~10^{11} cm^{-2}. Yet, because the lattice nevertheless expands, after the initial formation of scattered point defects, the expansion must be driven mainly by growth of isolated disordered regions. To investigate this possibility, we simulated mean lattice expansion due to repulsive point defects at various densities and strengths of influence (Figure 4a). Simulations show that $h \lesssim 20$ nm structures ($\varepsilon_0 \lesssim 0.01\%$) can be created by defect densities ~10^{11}–10^{12} cm^{-2} and $h \approx 1$ nm structures ($\varepsilon_0 \sim 3 \times 10^{-5}$ %) by defect densities ~10^{9} cm^{-2}. This explains why elevated structures can be formed already at defect densities not visible in the Raman spectra.

The situation at longer irradiation times is different. Prolonged single spot irradiation created a ~1.2-μm-diameter, 150-nm-high structure (Figure 4b). Measurement of the surface area indicated $\varepsilon_0 = 5\%$ expansion, assuming saturated expansion throughout the structure. Its stability was confirmed also in the simulation (Figure 4c). Most important, its Raman spectrum shows dominantly broad features, which is consistent with having highly disordered graphene (Figure 4d). Strains in the 5% range require defect densities above 10^{14} cm^{-2} (Figure 4a), which is in accordance with Raman spectra at high defect density.[24] At intermediate irradiations, the coexistence of normal and broad spectra can be understood by assuming that defects form preferentially in the vicinity of pre-existing defect regions that remain separated. As defect regions grow and finally coalesce at densities ~10^{14}–10^{15} cm^{-2}, the entire irradiated area becomes disordered and yields a completely broad Raman spectrum (see illustrative schematic in Supporting Information, Figure S5).

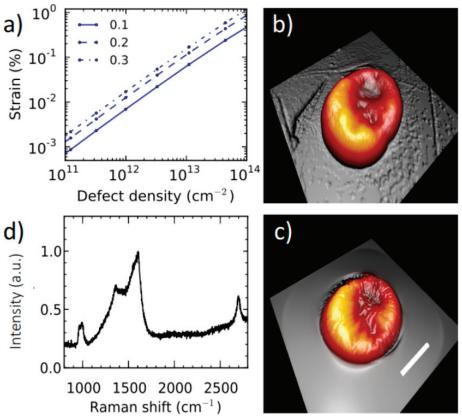

Figure 4. Point defects as the mechanism behind local expansion. (a) Averaged strain in graphene as a function of density of point defects, calculated using the elastic model with 2.5 Å grid spacing. The three different defect strengths of influence stand for the strain in the defected lattice point. (b) Experimentally observed, a 150 nm high partially collapsed structure resulting from prolonged irradiation at one spot. (c) Simulated and optimized structure corresponding to panel b ($\varepsilon_0 = 5\%$ within the structure). Vertical dimensions in b and c are scaled by a factor of 2; scale bar, 0.5 μm. (d) Raman spectrum of the collapsed structure.

We lack direct evidence for the atomic structure of the defect, but let us consider one promising candidate—the bond rotation or Stone–Wales (SW) defect.[25] It is a fitting defect type because it requires no additional atoms, its formation energy of 4.6–5.7 eV[25] is close to the two-photon energy of 4–5 eV in experiments, and it causes expansion of suitable magnitude at suitable defect densities (Figure 4a and Supporting Information, Figure S6). Moreover, the SW defects have attractive interaction and can gradually develop into extended Haeckelite structures that consist of arrangements of pentagons, hexagons, and heptagons.[26,27] For example, the most stable Haeckelite, $H_{5,6,7}$, is 3% less dense than graphene, which is in rough agreement with the experimental saturation strain of 5% (Figure 4b).[28] Haeckelites are also metallic, which matches with the increased reflectance within the structures (Figure 1c).[27] While other mechanisms such as thin film interference could as well contribute to increased optical response,[29,30] SW defects and Haeckelite structures stand out as promising candidates to explain both increased reflectance and

DOI: 10.1021/acs.nanolett.7b03530
Nano Lett. 2017, 17, 6469–6474

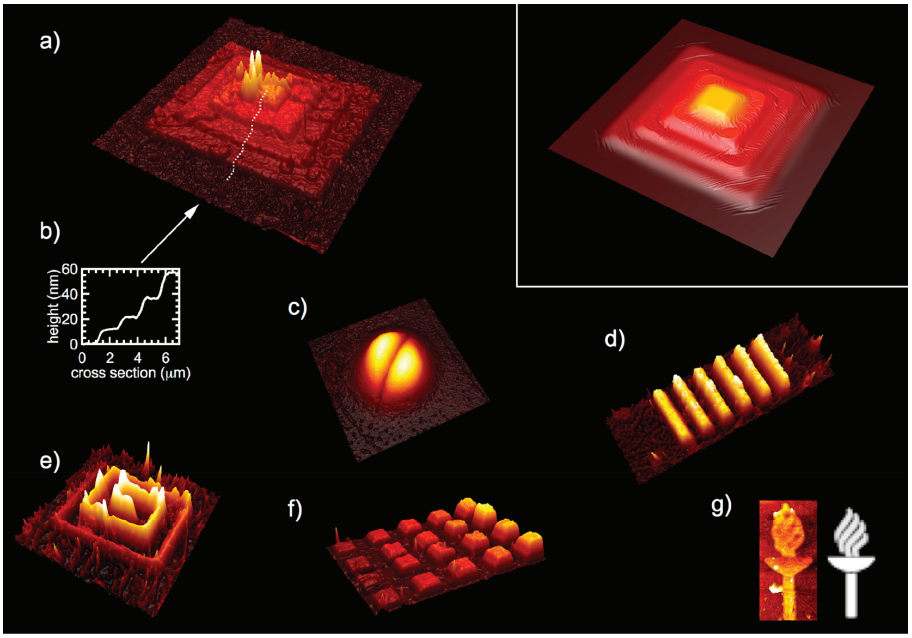

Figure 5. AFM images of 3D structures fabricated by direct laser writing. (a) Pyramid structure created by stepwise irradiation of levels. The field of view (FOV) is 17 × 17 μm^2. (b) Step profile along the dashed line in a. (c) 115 nm high semisphere which has collapsed symmetrically in the center. FOV is 1.8 × 1.8 μm^2. (d) Grating structure. FOV is 20 × 6.7 μm^2, and the maximum height is 25 nm. (e) Chiral structure with continuously increasing height. FOV is 8 × 8 μm^2, and the maximum height is 31 nm. (f) Matrix of squares. FOV is 19.8 × 14.7 μm^2, and the maximum height is 20 nm. (g) Torch with the bitmap image (on the right) used for direct laser writing. FOV is 3.5 × 7.4 μm^2, and the maximum height is 6 nm. Inset: Simulated pyramid structure with the same dimensions as in a. In the images the *z*-axis scale has been exaggerated to better visualize the structures.

lattice expansion, although confirmation requires further studies.

After establishing the method and mechanism for 3D patterning we describe fabrication of more complex 3D structures. The first example is a pyramid structure (Figure 5a). The pyramid was fabricated by first making the base level and then building the next levels stepwise (profile in Figure 5b). Such a pyramid was confirmed to be stable also in simulation (Figure 5, inset). The pyramid is a fascinating demonstration of the possibility to repeat the structure formation on a previously formed flat structure—such progressive control enables building arbitrarily complex architectures. In addition, we fabricated a 150 nm-high round semisphere, which had collapsed symmetrically, a miniature grating, a chiral structure (spiral), a matrix of squares, and a torch (Figures 5c–g).

The presented method for forging 2D graphene into 3D shapes opens exciting possibilities for further research. For example, shaping graphene into curved structures can be used to generate giant pseudomagnetic fields[5−7] or to control surface plasmon polaritons.[8] In addition, we propose that 3D structures of graphene can be used for fabricating scaffolds for layered materials, suspended device structures, and channel networks for nanofluidics, as well as optical and electronic devices. Finally, as the formation of 3D structures is simply based on lattice expansion, the presented concept is most likely generic to other 2D materials.

■ ASSOCIATED CONTENT

Supporting Information

The Supporting Information is available free of charge on the ACS Publications website at DOI: 10.1021/acs.nanolett.7b03530.

Additional materials and methods; details on elastic modeling; AFM, Raman and μm-XPS characterization data; and Figures S1−S6 (PDF)

■ AUTHOR INFORMATION

Corresponding Author

*E-mail: mika.j.pettersson@jyu.fi.

ORCID

Pasi Myllyperkiö: 0000-0003-1651-1676
Juha Koivistoinen: 0000-0002-7304-005X
Chia-Hao Chen: 0000-0003-1311-8342
Wei Yen Woon: 0000-0001-7299-9122
Mika Pettersson: 0000-0002-6880-2283

Author Contributions

A.J. and P.M. contributed equally to this work. M.P. planned the experiments, coordinated and supervised the work, and wrote the main part of the manuscript. A.J. planned the experiments and the sample fabrication and conducted AFM measurements and data analysis, as well as optical imaging. P.M. designed and developed the laser setups, performed most of the direct laser writing experiments, and did the data analysis. P. K. planned the simulations, wrote the computer codes, performed the simulations, did the data analysis, and wrote the

DOI: 10.1021/acs.nanolett.7b03530
Nano Lett. 2017, 17, 6469−6474

computational part of the manuscript. J.A. built a part of the laser writing setup and performed initial laser writing experiments. J.K. and H.C.T. performed Raman measurements. V.M.H. and J.J.M. performed sample fabrication and characterization, including nanoindentation measurements and analysis. W.Y.W. planned and supervised XPS measurements and analysis, and wrote the XPS part of the manuscript. H.C.T., L.Y.C., and C.H.C. conducted XPS measurements and analysis. All of the authors discussed the results and commented on the manuscript.

Notes

The authors declare no competing financial interest.

■ ACKNOWLEDGMENTS

We thank Gerrit Groenhof for reading and commenting the manuscript and Kevin Roberts for help in sample fabrication. P.K. acknowledges the Academy of Finland for funding. W.Y.W. acknowledges funding from Ministry of Science and Technology of the Republic of China (MOST 106-2112-M-008-003-MY3).

■ REFERENCES

(1) Ferrari, A. C.; et al. *Nanoscale* **2015**, *7* (11), 4598−4810.
(2) Franklin, A. D. *Science* **2015**, *349* (6249), aab2750.
(3) Bao, Q.; Loh, K.-P. *ACS Nano* **2012**, *6* (5), 3677−3694.
(4) Deng, S.; Berry, V. *Mater. Today* **2016**, *19* (4), 197−212.
(5) Guinea, F.; Katsnelson, M. I.; Vozmediano, M. A. H. *Phys. Rev. B: Condens. Matter Mater. Phys.* **2008**, *77* (7), 075422.
(6) Guinea, F.; Katsnelson, M. I.; Geim, A. K. *Nat. Phys.* **2010**, *6* (1), 30−33.
(7) Levy, N.; Burke, S. A.; Meaker, K. L.; Panlasigui, M.; Zettl, A.; Guinea, F.; Castro Neto, A. H.; Crommie, M. F. *Science* **2010**, *329* (5991), 544−547.
(8) Smirnova, D.; Mousavi, S. H.; Wang, Z.; Kivshar, Y. S.; Khanikaev, A. B. *ACS Photonics* **2016**, *3* (5), 875−880.
(9) Bunch, J. S.; Verbridge, S. S.; Alden, J. S.; Van Der Zande, A. M.; Parpia, J. M.; Craighead, H. G.; Mceuen, P. L. *Nano Lett.* **2008**, *8* (8), 2458−2462.
(10) Lu, J.; Castro Neto, A. H.; Loh, K.-P. *Nat. Commun.* **2012**, *3*, 823.
(11) Boddeti, N. G.; Liu, X.; Long, R.; Xiao, J.; Bunch, J. S.; Dunn, M. L. *Nano Lett.* **2013**, *13* (12), 6216−6221.
(12) Blees, M. K.; Barnard, A. W.; Rose, P. A.; Roberts, S. P.; McGill, K. L.; Huang, P. Y.; Ruyack, A. R.; Kevek, J. W.; Kobrin, B.; Muller, D. A.; Mceuen, P. L. *Nature* **2015**, *524*, 204.
(13) Mu, J.; Hou, C.; Wang, H.; Li, Y.; Zhang, Q.; Zhu, M. *Science Advances* **2015**, *1* (10), e1500533−e1500533.
(14) Aumanen, J.; Johansson, A.; Koivistoinen, J.; Myllyperkiö, P.; Pettersson, M. *Nanoscale* **2015**, *7* (7), 2851−2855.
(15) Singh, G.; Rice, P.; Hurst, K. E.; Lehman, J. H.; Mahajan, R. L. *Appl. Phys. Lett.* **2007**, *91*, 033101.
(16) Ferrari, A. C.; Basko, D. M. *Nat. Nanotechnol.* **2013**, *8* (4), 235−246.
(17) Beams, R.; Cançado, L. G.; Novotny, L. *J. Phys.: Condens. Matter* **2015**, *27* (8), 083002.
(18) Koivistoinen, J.; Sládková, L.; Aumanen, J.; Koskinen, P.; Roberts, K.; Johansson, A.; Myllyperkiö, P.; Pettersson, M. *J. Phys. Chem. C* **2016**, *120* (39), 22330−22341.
(19) Johansson, A.; Tsai, H.-C.; Aumanen, J.; Koivistoinen, J.; Myllyperkiö, P.; Hung, Y.-Z.; Chuang, M.-C.; Chen, C.-H.; Woon, W. Y.; Pettersson, M. *Carbon* **2017**, *115*, 77−82.
(20) Farrokhi, H.; Zheng, H. Y.; Zhou, W.; Li, Z. L. *Opt. Express* **2012**, *20* (21), 23180−23185.
(21) Dong, T.; Sparkes, M.; Durkan, C.; O'Neill, W. *J. Laser Appl.* **2016**, *28* (2), 022202.
(22) Lee, C.; Wei, X.; Kysar, J. W.; Hone, J. *Science* **2008**, *321* (5887), 385−388.
(23) Rasool, H. I.; Ophus, C.; Klug, W. S.; Zettl, A.; Gimzewski, J. K. *Nat. Commun.* **2013**, *4*, 2811.
(24) Lucchese, M. M.; Stavale, F.; Ferreira, E. H. M.; Vilani, C.; Moutinho, M. V. O.; Capaz, R. B.; Achete, C. A.; Jorio, A. *Carbon* **2010**, *48* (5), 1592−1597.
(25) Ma, J.; Alfè, D.; Michaelides, A.; Wang, E. *Phys. Rev. B: Condens. Matter Mater. Phys.* **2009**, *80* (3), 033407.
(26) Openov, L. A.; Podlivaev, A. I. *Phys. Solid State* **2015**, *57* (7), 1477−1481.
(27) Terrones, H.; Terrones, M.; Hernández, E.; Grobert, N.; Charlier, J.-C.; Ajayan, P. M. *Phys. Rev. Lett.* **2000**, *84* (8), 1716−1719.
(28) Lusk, M. T.; Carr, L. D. *Phys. Rev. Lett.* **2008**, *100* (17), 175503.
(29) Cartamil-Bueno, S. J.; Steeneken, P. G.; Centeno, A.; Zurutuza, A.; van der Zant, H. S. J.; Houri, S. *Nano Lett.* **2016**, *16* (11), 6792−6796.
(30) Cartamil-Bueno, S. J.; Centeno, A.; Zurutuza, A.; Steeneken, P. G.; van der Zant, H. S. J.; Houri, S. *Nanoscale* **2017**, *9* (22), 7559−7564.

DOI: 10.1021/acs.nanolett.7b03530
Nano Lett. 2017, 17, 6469−6474

Supporting information: Optical Forging of Graphene into Three-Dimensional Shapes

*Andreas Johansson[1,2]†, Pasi Myllyperkiö[1]†, Pekka Koskinen[2], Jukka Aumanen[1], Juha Koivistoinen[1], Hung-Chieh Tsai[3], Chia-Hao Chen[4], Lo-Yueh Chang[4], Vesa-Matti Hiltunen[2], Jyrki J. Manninen[2], Wei Yen Woon[3], Mika Pettersson[1]**

[1]Nanoscience Center, Department of Chemistry, P.O. Box 35, FI-40014, University of Jyväskylä, Finland.

[2]Nanoscience Center, Department of Physics, P.O. Box 35, FI-40014, University of Jyväskylä, Finland.

[3]Department of Physics, National Central University, Jungli, 32054, Taiwan, Republic of China.

[4]National Synchrotron Radiation Research Center, Hsinchu, 30076, Taiwan, Republic of China.

†These authors contributed equally to this work.

*Corresponding author. E-mail: mika.j.pettersson@jyu.fi

Additional Materials and Methods

Samples

Silicon chips (10 mm by 10 mm in size with a top-layer of 300 nm SiO_2) with a monolayer of chemical vapor deposition grown graphene on top were purchased from Graphenea Inc. A reference grid was patterned on the top surface, using electron beam lithography in PMMA. The patterned grid was made of 1 μm wide lines, defining a 10 by 10 matrix of 200 μm by 200 μm squares. Oxygen reactive ion etching was used to remove graphene from the bottom of the pattern, after which it was metallized with 2 nm Ti as adhesion layer and 30 nm Au on top. The chips were covered with an additional PMMA layer as protection, and then diced to our preferred size of 5 mm by 5 mm before finalizing the patterning with a lift-off procedure. The resulting reference grid allowed positioning of irradiated patterns at known locations so that they could be found during characterization measurements.

Direct laser writing

Direct laser writing of the patterns was performed with a setup consisting of an amplified femtosecond laser (Pharos-10, 600 kHz, Light Conversion Ltd.), two non-collinear optical parametric amplifiers (NOPA, Orpheus-N, Light Conversion Ltd.) and a home-built optical microscope with nano-positioning system (Nanomax 300, Thorlabs Inc.). The microscope was equipped with a camera, allowing precise alignment and visual inspection of the sample.

Laser beams were focused to the sample by a microscope objective (Nikon LU Plan ELWD 100x/0.80). The sample was installed to a closed chamber that was purged with argon or nitrogen to prevent oxidation of the graphene during the writing process.

Two different femtosecond laser configurations were used for the writing experiments, short 30-40 fs and longer 250 fs laser pulses. The short pulses were taken from the non-collinear optical parametric amplifier (NOPA, Orpheus-N, Light Conversion Ltd.) and were centered at 560 nm. Pulse energies for the writing were 5 - 25 pJ/pulse. The longer pulses centered at 515 nm were made using the second harmonic generation from the fundamental of the laser and the energy was ~40 pJ/pulse. The writing speed was varied for different structures from 0.1 s to 10 s per spot.

Raman spectroscopy

Raman measurements were carried out with a home-built Raman setup in a backscattering geometry using 532 nm excitation wavelength produced with continuous wave single frequency laser (Alphalas, Monolas-532-100-SM). The beam was focused on a sample and the signal was collected with a 100x microscope objective (Nikon L Plan SLWD 100x with 0.70 N.A.). The scattered light was dispersed in a 0.5 m imaging spectrograph (Acton, SpectraPro 2500i) using 600 g/mm grating (with resolution: ~ 5 - 7 cm^{-1}). The signal was detected with EMCCD camera (Andor Newton EM DU971N-BV) using 60 μm slit width. A beam splitter was placed between the objective and the spectrometer in order to observe the exact measurement point visually. The Rayleigh scattering was attenuated with an edge filter (Semrock). The approximate sample positioning was done with XYZ-piezoscanner (Attocube, ANPxyz101) with smallest step of 50

nm in each direction. A laser power of ~1 mW was utilized and measurement time per accumulation was 5 s. Mapping was conducted using 300 nm steps between measurement points and the total map consisted of 50 x 50 points.

Atomic Force Microscopy

All imaging and characterization was made on a Bruker Dimension Icon atomic force microscope, using Peak Force Tapping mode. ScanAsyst Air probes from Bruker were used during imaging with the peak force limited to 2 nN. Nanoindentation was made with RTESPA-300 probes from Bruker. The cantilever spring constant was determined to be 50.9 N/m, using the Sader method.[1] With a nominal radius of 8 nm, the RTESPA-300 probe tip was just before nanoindentation measurements characterized to have a radius of 31.5 nm. The AFM images in Figure 4 have been smoothed with a Gaussian low-pass filter to suppress noise and visually enhance the patterned 3D structures.

XPS

XPS (X-ray photoelectron spectroscopy) measurement was conducted at National Synchrotron Radiation Research Center, Taiwan (SPEM end station of beamline 09A1). The soft X-ray beam (photon energy 620 eV) was focused with Fresnel zone-plate optics to achieve spatial resolution of 100 nm. The photon energy was routinely calibrated with the core-level line of Au at binding energy 84 eV. The overall energy resolution was better than 100 meV, and the experiments were conducted at room temperature.

Simulations

The elastic modeling of graphene used thin sheet elasticity theory, known to describe deformed graphene over several length scales.[2,3] The in-plane elastic modulus was $k_s = 21$ eV/Å^2, the Poisson ratio $\upsilon = 0.2$, and the bending modulus $k_b = 1.0$ eV.[4,5] The strain tensor $e_{\alpha\beta}(\mathbf{r})$ was modified into $e'_{\alpha\beta}(\mathbf{r}) = e_{\alpha\beta}(\mathbf{r}) - \delta e_{\alpha\beta}(\mathbf{r})$ in order to account for the expansion field $\varepsilon(\mathbf{r})$. To simulate the $2x2$ μm^2 square patterns, we fixed $5x5$ μm^2 sheets at the edges, discretized them on a $200x200$ rectangular grid and optimized to stresses below 10^{-7} eV/Å^2 under the given expansion field using the FIRE method.[6] The flimsiness of sheets required multiple initial guesses to ascertain the topography of the global energy minimum. The substrate was treated as a hard surface, which was justified, because a lower threshold for ε_0, below which the graphene would have preferred to stay flat on the substrate, was not observed in the experiment. The strains in the pyramid levels were calculated from the experimental (cumulative) irradiation times 0.5 s, 1.0 s, 2.0 s, and 3.5 s by using a 3.9×10^{-5} s^{-1} strain rate. Eq. (1) was derived by first noticing that the length expansion across any line profile is $\Delta L = \int \varepsilon(\mathbf{r}) ds$, which for a square pattern of length L_0 becomes $\Delta L_\varepsilon = \varepsilon_0 (L_0 + FWHM \times \sqrt{\pi / \log 16})$. Structure of height h requires an expansion $\Delta L_h = \pi^2 h^2 / 8w$, assuming an edge height profile $h \sin^2(x\pi / 2w)$, where w is the edge width $(h \ll w)$ and x is the distance along the substrate $(0 \le x \le w)$; Eq. (1) follows by setting $\Delta L_\varepsilon = \Delta L_h$.

The atomistic simulations of Stone-Wales (SW) defects were done using the LAMMPS package with the REBO interatomic potential.[7,8] SW defects were created in periodic simulation cells of rectangular shape and varying aspect ratio; the SW defect density was the inverse of the

cell area. Structures were optimized to maximum force criterion 0.5 meV/Å under a planar constraint and the mean expansion was calculated from the stress tensor.

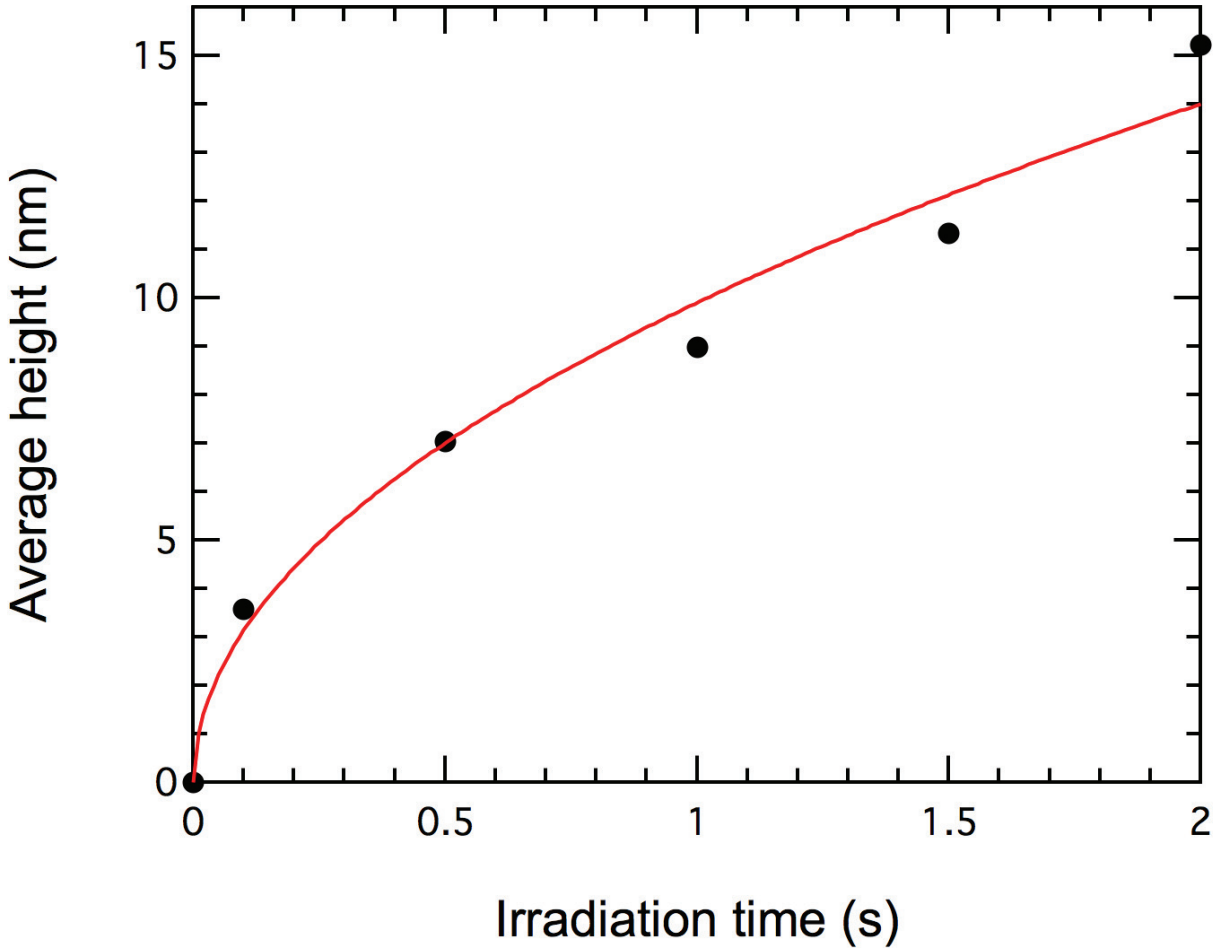

Figure S1. Height of elevated structures as a function of irradiation time per spot. The height data is extracted from the AFM data set in Figure 1a. The red curve shows a fit to square root dependence on the irradiation time.

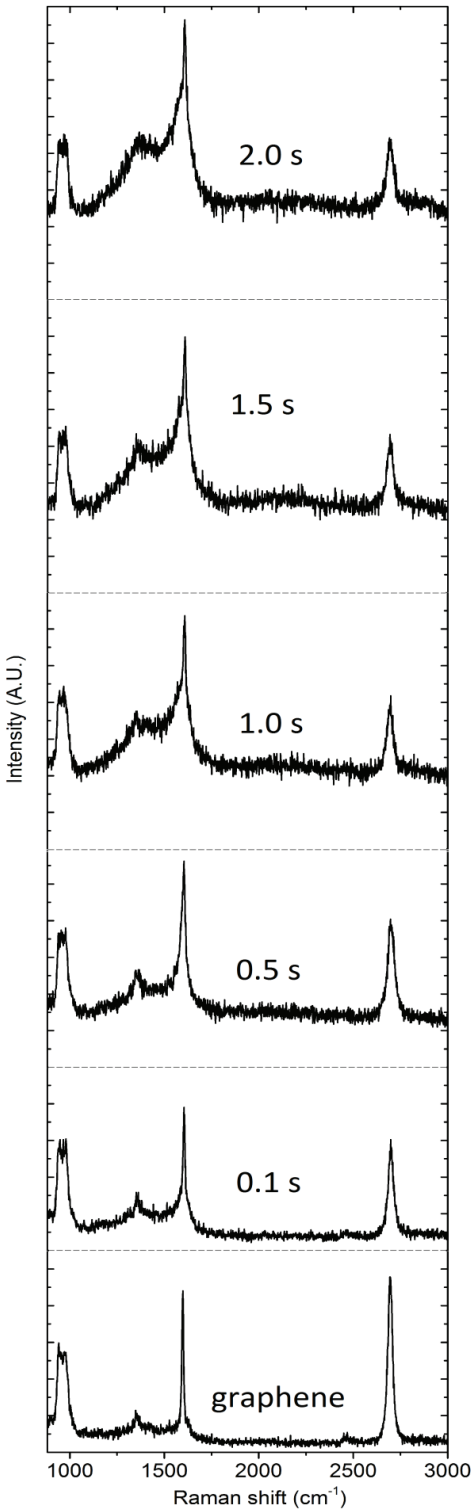

Figure S2. Raman spectra from the sample in Fig. 1. The labels show the irradiation time per spot. The dashed line indicates the 0-level of the signal.

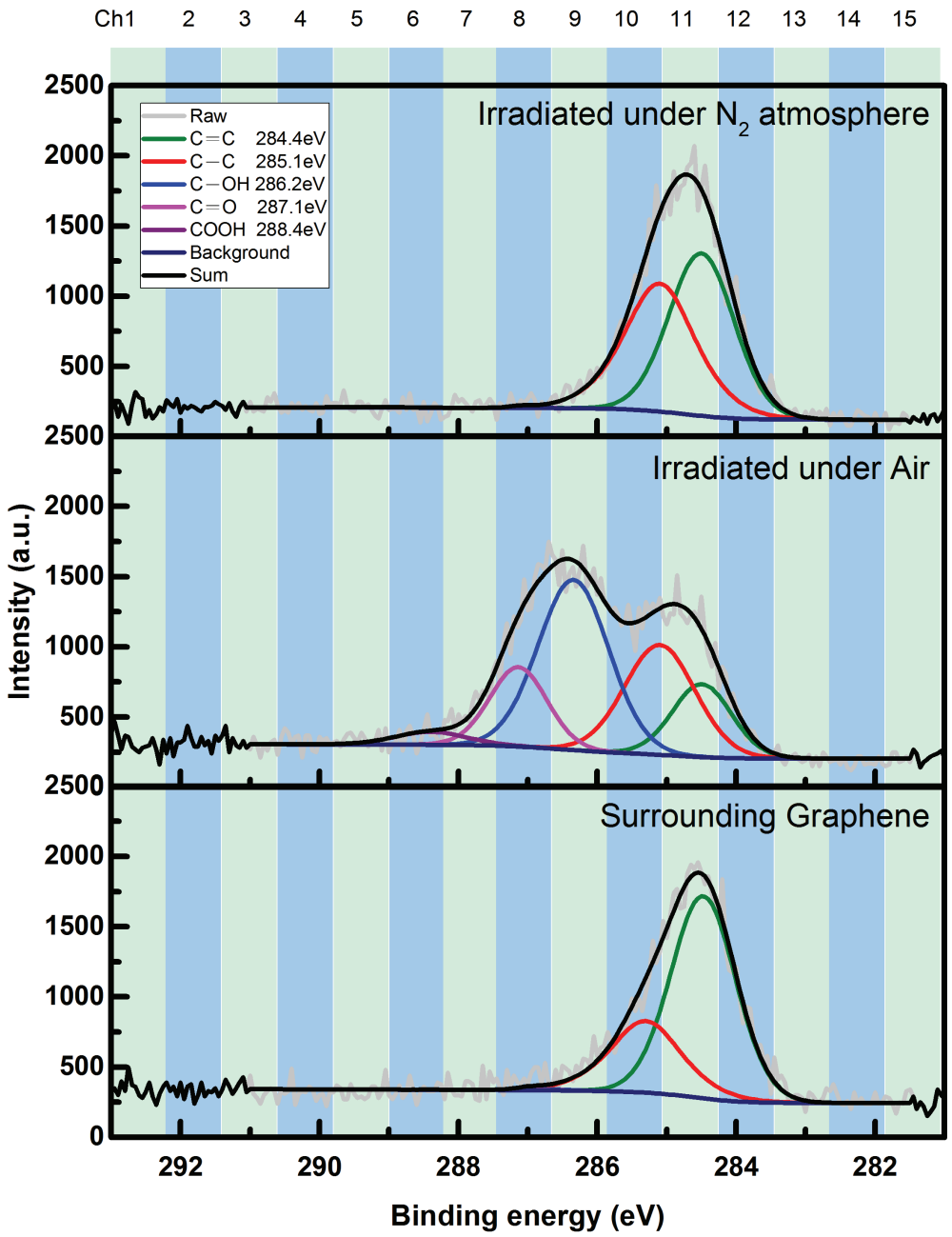

Figure S3. Comparison of XPS data for non-irradiated graphene (bottom), graphene irradiated under N_2 atmosphere (top), and graphene irradiated under air atmosphere (middle). All the areas were located on the same sample.

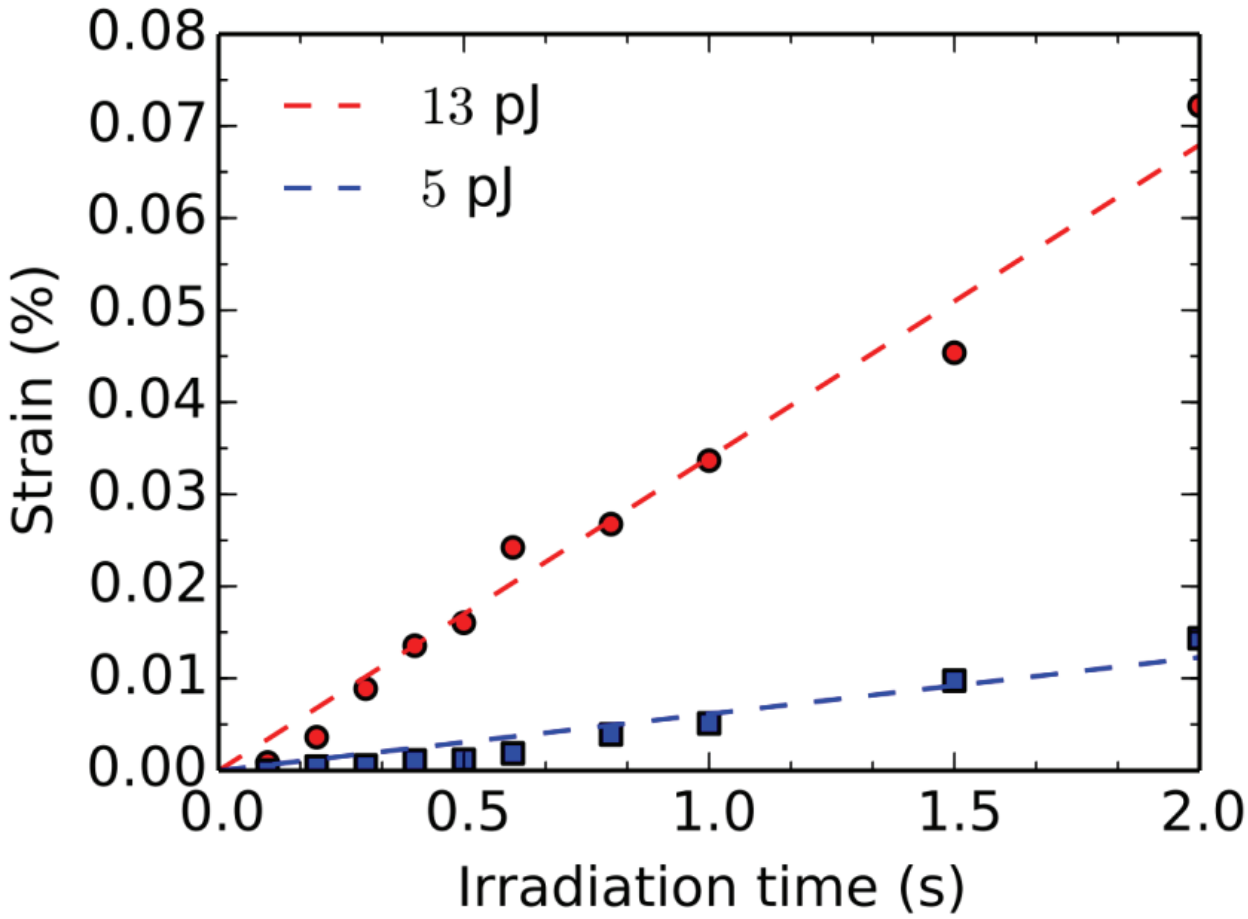

Figure S4. Strain as a function of irradiation time. The curves were obtained by inverting Eq. (1) for $\varepsilon_0(t) = \varepsilon_0(h(t))$ and using experimental data for square plateaus up to 50 nm in height. The linear fits for the growth rates are 3.5×10^{-4} (13 pJ pulses) and 6.1×10^{-5} 1/s (5 pJ pulses).

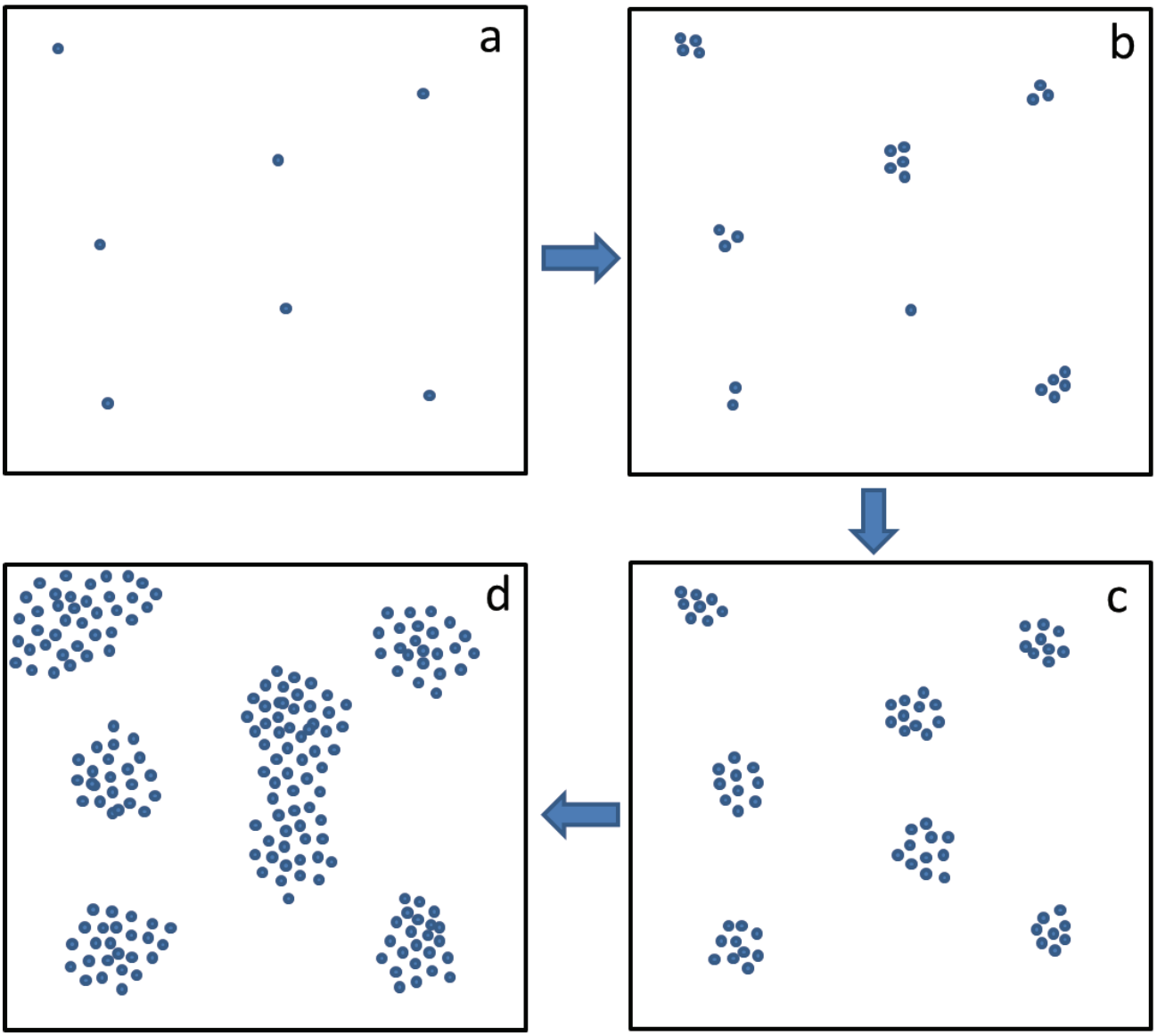

Figure S5. Cartoon showing the proposed mechanism of defect formation in graphene upon irradiation. a) Initially point defects (blue dots) are formed in graphene. b) New defects form preferentially close to existing defects. c) More defects lead to regions that are disordered. d) The area of disordered regions grows as new defects are formed, eventually leading to coalescence of the defected regions.

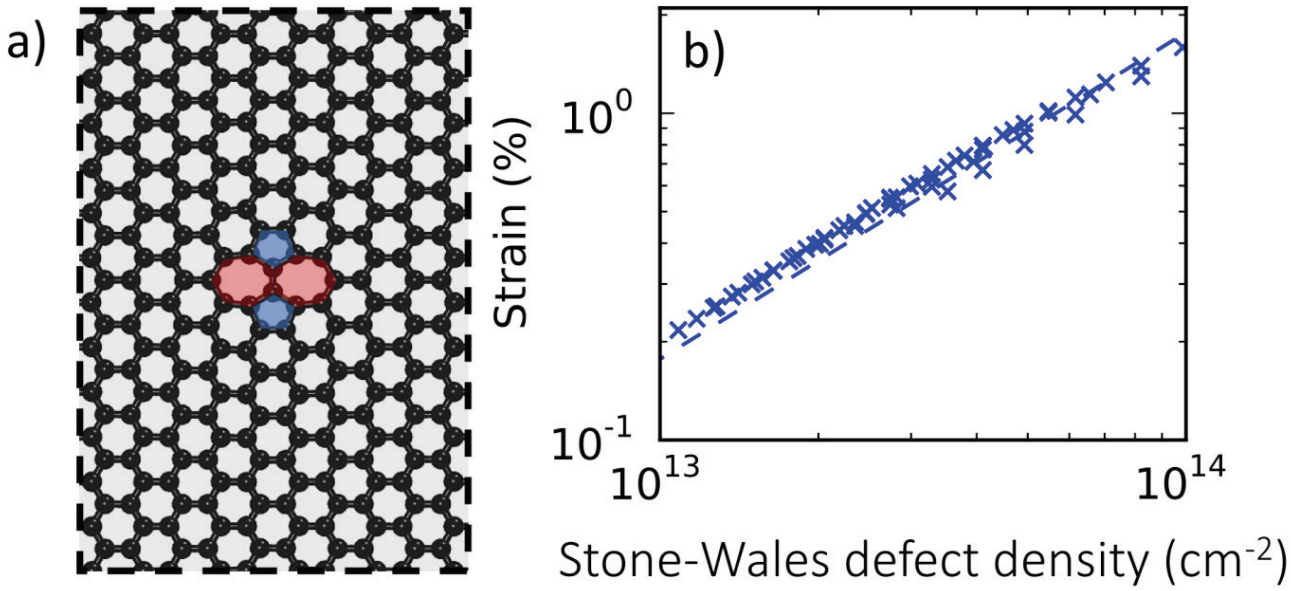

Figure S6. Lattice expansion with Stone-Wales defects. a) Stone-Wales defect in a rectangular unit cell, optimized with REBO potential under planar constraint. b) Biaxial strain in the unit cell as a function of defect density (inverse of unit cell area); defect density was changed by varying cell size and aspect ratio.

REFERENCES

(1) Sader, J. E.; Chon, J. W. M.; Mulvaney, P. *Rev. Sci. Instrum.* **1999**, *70* (10), 3967–3969.

(2) Landau, L. D.; Lifshitz, E. M. *Theory of Elasticity*, 3rd ed.; Pergamon: New York, 1986.

(3) Neto, A. C.; Guinea, F.; Peres, N.; Novoselov, K. S.; Geim, A. K. *Rev. Mod. Phys.* **2009**, *81* (1), 109–162.

(4) Do Carmo, M. P. *Differential Geometry of Curves and Surfaces*; Prentice-Hall: New Jersey, 1976.

(5) Koskinen, P.; Kit, O. O. *Phys Rev B* **2010**, *82* (23), 235420.

(6) Bitzek, E.; Koskinen, P.; Gähler, F.; Moseler, M.; Gumbsch, P. *Phys Rev Lett* **2006**, *97* (17), 170201.

(7) Plimpton, S. *J. Comp. Phys.* **1995**, *117* (1), 1–19.

(8) Brenner, D. W.; Shenderova, O. A.; Harrison, J. A.; Stuart, S. J.; Ni, B.; Sinnott, S. B. *J. Phys. Cond. Mat.* **2002**, *14* (4), 783–802.

AII

OPTICALLY FORGED DIFFRACTION-UNLIMITED RIPPLES IN GRAPHENE

by

Pekka Koskinen, Karoliina Karppinen, Pasi Myllyperkiö, Vesa-Matti Hiltunen, Andreas Johansson, Mika Pettersson 2018

The Journal of Physical Chemistry Letters, 9, 21, 6179-6184

DOI: 10.1021/acs.jpclett.8b02461

THE JOURNAL OF PHYSICAL CHEMISTRY Letters

Letter

Cite This: J. Phys. Chem. Lett. 2018, 9, 6179−6184

pubs.acs.org/JPCL

Optically Forged Diffraction-Unlimited Ripples in Graphene

Pekka Koskinen,*[,†] Karoliina Karppinen,[‡] Pasi Myllyperkiö,[‡] Vesa-Matti Hiltunen,[†] Andreas Johansson,[†,‡] and Mika Pettersson[‡]

[†]Nanoscience Center, Department of Physics, University of Jyväskylä, 40014 Jyväskylä, Finland

[‡]Nanoscience Center, Department of Chemistry, University of Jyväskylä, 40014 Jyväskylä, Finland

Supporting Information

ABSTRACT: In nanofabrication, just as in any other craft, the scale of spatial details is limited by the dimensions of the tool at hand. For example, the smallest details of direct laser writing with far-field light are set by the diffraction limit, which is approximately half of the used wavelength. In this work, we overcome this universal assertion by optically forging graphene ripples that show features with dimensions unlimited by diffraction. Thin sheet elasticity simulations suggest that the scaled-down ripples originate from the interplay between substrate adhesion, in-plane strain, and circular symmetry. The optical forging technique thus offers an accurate way to modify and shape 2D materials and facilitates the creation of controllable nanostructures for plasmonics, resonators, and nano-optics.

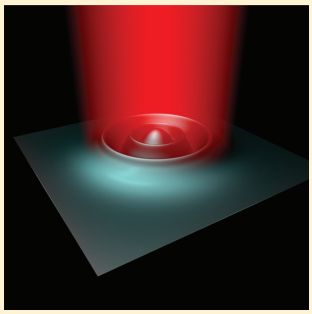

One of the central aims in nanoscience is to be able to modify nanostructures at will. Modifications are necessary because it is rarely the pristine materials but the modified and engineered materials that establish functionalities for practical applications.[1,2] Modifications are particularly necessary for 2D materials.[3,4] Graphene, for instance, gains specific functionalities once modified into ribbons,[5,6] introduced with pores or adsorbants,[7−10] or curved into 3D shapes.[11−13]

However, all modification techniques have their limitations. Direct mechanical manipulation is either slow and accurate,[14] or fast, coarse, and nonreproducible.[15,16] Thermal annealing,[17,18] electron irradiation,[19,20] chemical treatment,[21,22] and Joule heating[23] may be scalable but spatially imprecise due to their random character. It is particularly challenging to modify 2D materials into customized ripples and other 3D shapes. Such modifications frequently require dedicated experimental apparatuses[24] or specially prepared substrates.[25] The difficulty for 3D modification lies partly in substrate adhesion. Although often of weak van der Waals type, adhesion effectively prevents controlled detachment of 2D membranes from the substrate.

Limitations exist also in optical patterning. Although optical techniques may be scalable and easy to apply, the spatial details are determined by the size of the focused laser beam. Creating patterns with details finer than beam size is just as difficult as scribbling equations on a piece of paper with a spray can. Still, optical techniques have plenty of potential for exploration because irradiation provides various mechanisms to modify 2D materials, depending on laser energy and ambient atmosphere.[26,27] One particularly promising, still mostly untapped technique is the so-called optical forging, which alone enables controlled and on-the-fly 3D shaping of graphene.[28]

Given the ubiquity of various limitations, there is urgency to improve techniques to modify and engineer 2D materials scalably, accurately, and preferably in situ, without customized preparations.

In this work, we demonstrate optical forging of graphene into circular ripples with features much smaller than the size of the laser beam. By using thin sheet elasticity simulations, the rippling is shown to arise from the interplay between substrate adhesion, in-plane stress due to optical forging, and the underlying circular symmetry. Being based on direct irradiation of graphene without specially prepared experimental settings, optical forging provides a practical technique and thereby substantially broadens our abilities to modify and enhance the functionalities of graphene and maybe even other 2D materials.

To prepare the sample, we grew single-layer graphene by chemical vapor deposition (CVD) on a Cu substrate[29] and transferred it to thermally grown SiO_2. For fabrication details and graphene characterization, see the Supporting Information (SI).

Selected points in the sample were then irradiated by a 515 nm femtosecond laser focused with an objective lens (N.A. of 0.8) to a single Gaussian spot. To prevent photoinduced oxidation during the irradiation, the sample was installed inside a closed chamber purged with N_2.[27] The laser produced 250 fs pulses at 5−25 pJ/pulse energy and 600 kHz repetition rate for a tunable irradiation time τ. This process is called optical forging and results in blistering of the graphene membrane (Figure 1a and Movie 1 in the SI). Blistering occurs due to

Received: August 10, 2018
Accepted: October 11, 2018
Published: October 11, 2018

DOI: 10.1021/acs.jpclett.8b02461
J. Phys. Chem. Lett. 2018, 9, 6179−6184

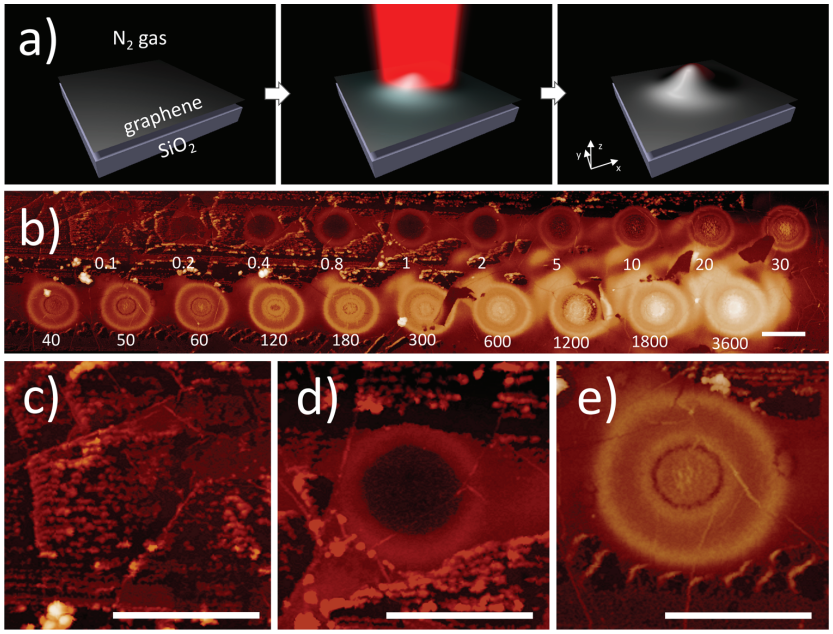

Figure 1. Monitoring the gradual formation of optically forged graphene blisters on SiO_2. (a) In optical forging, graphene is irradiated by focused femtosecond laser beam under an inert N_2 atmosphere. The laser creates defects that cause isotropic expansion of graphene membrane and trigger the formation of blisters. The blisters are hollow and not pressurized.[28] (b) Atomic force microscope image of blisters formed at progressively increasing irradiation time τ (numbers show τ in seconds; highest features are 60 nm). Blisters form at $\tau > 0.4$ s, initially with one circular ripple, later with several ripples and a dome in the center. (c) Zoom into an irradiated area with $\tau = 0.2$ s, where the graphene still remains flat. Visible are only the patchy residues from sample processing. (d) Zoom into a blister with one ripple ($\tau = 1$ s). (e) Zoom into a blister with multiple ripples ($\tau = 50$ s). Scale bars, 1 μm.

local expansion of the membrane, caused by laser-induced defects and the related compressive in-plane stress.[28] The local expansion field $\varepsilon(r)$ therefore depends on the time-integrated laser intensity profile $I(r)$, which enables accurate control over the expansion and blister height via the irradiation time τ. Consequently, we irradiated the sample at separate spots for irradiation times ranging from $\tau = 0.1$ to 3600 s. Finally, the blistered sample was characterized by Raman spectroscopy and measured by an atomic force microscope (AFM; see the SI).

The systematic increase in irradiation time produced a nontrivial but beautiful and reproducible pattern of blisters (Figure 1b and Figure S4). In particular, blisters had profiles more complex than the usual domes.[30] At short irradiation times ($\tau < 0.4$ s) the graphene remained flat on the substrate (Figure 1c). At intermediate irradiation times ($0.4 \leq \tau \leq 2$ s), the graphene developed blisters with one circular ripple (Figure 1d). At long irradiation times ($\tau \geq 5$ s) the graphene developed concentric ripples in progressively increasing numbers and a gradually developing central dome (Figure 1e and Movie 2 in the SI). Parts of the area between the blisters were detached from the substrate because the laser irradiated also during the movement from one spot to another. Note that the radial features in the ripples have dimensions down to 100 nm, nearly 10 times smaller than the laser spot and the ripple diameters themselves. Optical forging can thus reach 3D shaping of graphene that beats the diffraction limit. This is our main result.

To quantify the expansion of the graphene membrane, we used AFM height profiles to measure the increase in the surface area of the blisters. Within the projected areas of ~1 μm^2, the corrugated membrane areas increase nearly monotonously upon increasing irradiation time, reaching 10^{-2} μm^2 (~1%) area increase at $\tau = 1$ h (Figure 2a). Initially,

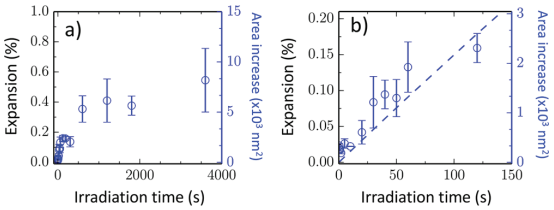

Figure 2. Effective expansion of graphene membrane during laser irradiation. (a) Area increase due to blister formation, as measured from the blister profiles of Figure 1b (right scale). Area increase transformed into maximum linear expansion in the middle of the laser spot (left scale). (b) Zoom into $\tau < 150$ s. A linear fit gives an expansion rate 1.5×10^{-3} %/s or 22 nm^2/s (dashed line). The vertical bars are uncertainties in blister areas.

the area increases linearly in irradiation time, at rate 22 nm^2/s (Figure 2b). This area increase was used to determine radius-dependent linear expansion, $\varepsilon(r)$. By assuming here a one-photon process and a Gaussian laser intensity profile $I(r)$, we obtain

$$\varepsilon(r) = \varepsilon_0 \exp(-4r^2 \log 2/\mathrm{fwhm}^2) \quad (1)$$

DOI: 10.1021/acs.jpclett.8b02461
J. Phys. Chem. Lett. 2018, 9, 6179−6184

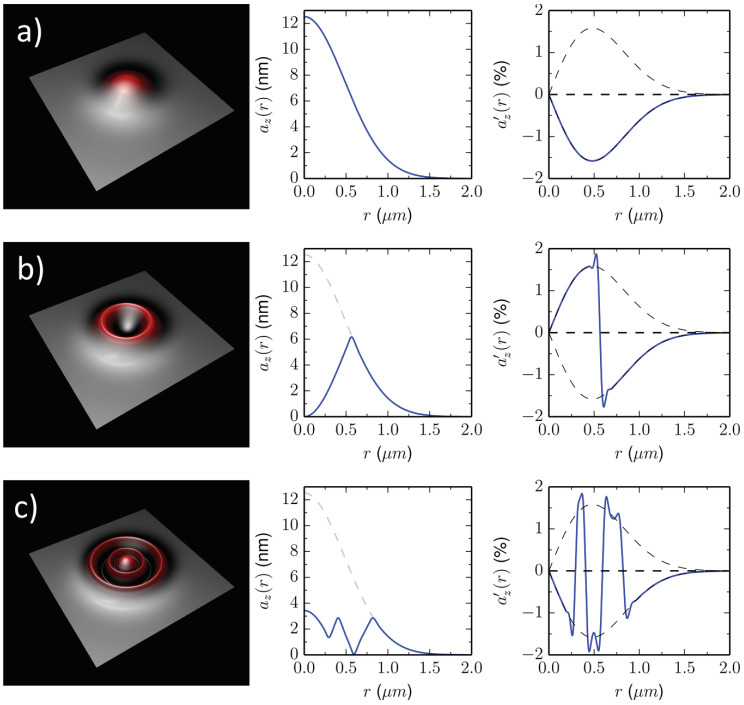

Figure 3. Thin sheet elasticity modeling of blisters with $\varepsilon_0 = 0.017\%$ and $\varepsilon_{adh} = 0$ (no substrate adhesion). (a) Blister with one central dome. (b) Blister with one circular ripple. (c) Blister with two concentric ripples and a central dome. Panels show visualizations (left; height exaggerated), radial height profiles $a_z(r)$ (middle), and the slopes of the radial height profiles $a_z'(r)$ (right). Dashed lines on the right show the analytical limits for $a_z'(r)$ from eq 3.

where $r = 0$ at the center of the spot and fwhm = 800 nm is the full width at half-maximum of the laser beam. Because the laser focal spot was difficult to maintain, fwhm had to be treated as a parameter and adjusted to give the best overall fit to the observed lateral dimensions in the experiment. The maximal expansion ε_0 increases at the rate 1.5×10^{-3} %/s at short irradiation times and saturates at almost 1% at long irradiation times (Figure 2). The initial linear rate and the saturation are in good agreement with previous experiments.[28]

The diffraction-unlimited rippling suggests a mechanism that involves competition between surface adhesion and expansion-induced stress. To investigate the mechanism in detail, we simulate blister growth by classical thin sheet elasticity model.[31] Such models have proven successful in the modeling of deformed graphene membranes.[16,32−36] The energy in the model contains in-plane strain energy, out-of-plane bending energy, and surface adhesion. The laser-induced isotropic expansion is introduced via the diagonal of the in-plane strain tensor as $e_{\alpha\beta}(\boldsymbol{r}) = e^0_{\alpha\beta}(\boldsymbol{r}) - \delta_{\alpha\beta}\varepsilon(\boldsymbol{r})$, where $\varepsilon(\boldsymbol{r})$ is the expansion field and $e^0_{\alpha\beta}(\boldsymbol{r})$ is the strain tensor of the unexpanded, pristine graphene.[28] The adhesion is modeled by the generic 12−6 Lennard-Jones potential.[37] This model was discretized, implemented in two computer codes (with and without circular symmetry), and used to optimize blister geometries for given ε_0 and adhesion energy ε_{adh}.[38] For details, see the SI.

Before analyzing the model in full, it is instructive first to ignore adhesion and calculate a few analytical results. Because of the smallness of the graphene bending modulus, on micrometer-length scales the mechanical behavior is dominated by in-plane strain energy.[39] The strain energy is minimized when $e_{\alpha\beta} \approx 0$ or $e^0_{\alpha\beta} \approx \delta_{\alpha\beta}\varepsilon(\boldsymbol{r})$. To a first approximation, eq 1 then implies an area increase of $\Delta A = [\pi/(2 \log 2)] \times \text{fwhm}^2\varepsilon_0$. (This relation was previously used to transform ΔA into ε_0.) With the displacement vector $\vec{a}(r) = a_r(r)\hat{r} + a_z(r)\hat{z}$, the diagonal components of the strain tensor become

$$\begin{cases} e_{rr}(r) = a_r'(r) + \dfrac{1}{2}[a_r'(r)^2 + a_z'(r)^2] - \varepsilon(r) \\ e_{tt}(r) = a_r(r)/r + \dfrac{1}{2}[a_r(r)/r]^2 - \varepsilon(r) \end{cases} \tag{2}$$

where r refers to radial and t refers to tangential in-plane component, and prime stands for a derivative with respect to r. Because the in-plane strain energy minimizes at $e_{\alpha\beta} \approx 0$, we obtain $a_r(r) \approx r\varepsilon(r)$ and

$$a_z'(r) \approx \pm\sqrt{16 \log 2 \times \varepsilon(r)}\,(r/\text{fwhm}) \tag{3}$$

That is, when the membrane adapts to isotropic expansion under radial symmetry, energy gets minimized by adjusting the slope into a fixed absolue value. When the slope is negative for all r, integration yields the profile $a_z(r) = \text{fwhm} \times \sqrt{\varepsilon(r)/\log 2}$. This profile corresponds to a blister with one central dome and a maximum height of $h_{max} = \text{fwhm} \times \sqrt{\varepsilon_0/\log 2}$. The numerically optimized blister profile follows this analytical estimate accurately (Figure 3a).

DOI: 10.1021/acs.jpclett.8b02461
J. Phys. Chem. Lett. 2018, 9, 6179−6184

However, positive and negative slopes in eq 3 are equally acceptable. Because the energy cost of bending is small, it is cheap to create a kink that reverses the sign of $a_z'(r)$ abruptly. This kink appears topologically as a perfectly round ripple (Figure 3b). Multiple kinks at different radii produce concentric ripples of varying heights and diameters (Figure 3c). Compared with the scale of in-plane strain energy, blisters of different ripple counts are nearly isoenergetic. When the number of ripples increases, the slopes progressively deviate from eq 3. Otherwise, the analytical description of the blister profiles without adhesion is apparent.

The role of adhesion, then, is to pull the membrane down, toward the substrate. Understanding the behavior of adhesion-free membranes is helpful, but when elastic and adhesive energies compete, we have to rely on numerical simulations. We took a closer look at the blister with $\tau = 1$ s, which is near the onset of blistering (Figure 1d). This 4 nm high blister has a 0.97 μm ripple diameter and $\varepsilon_0 = 0.017\%$ expansion, as given by the AFM profile. We simulated this blister using the experimental ε_0 and adhesion in the range $\varepsilon_{adh} = 0...1$ eV/nm^2.

When $\varepsilon_{adh} < 1$ μeV/nm^2, the ripple is broad and the middle of the blister is mostly detached from the substrate, disagreeing with the experiment (Figure 4a); adhesion remains a minor perturbation to the zero-adhesion profile (Figure 3b). When $\varepsilon_{adh} > 10$ μeV/nm^2, in turn, the ripple becomes too narrow and shallow, also disagreeing with the experiment; when $\varepsilon_{adh} \gtrsim 100$ μeV/nm^2, the membrane ultimately snaps flat on the substrate. However, around $\varepsilon_{adh} \approx 3$ μeV/nm^2, adhesion pulls the membrane down so that both the ripple width and height agree with the experiment. Using the adhesion $\varepsilon_{adh} = 3$ μeV/nm^2, one-ripple blistering occurs at $\varepsilon_0 \approx 0.005\%$, and the blister height increases linearly when ε_0 further increases (Figure 4b). This simulated trend agrees with the experimental trend in one-ripple blisters ($\tau \lesssim 2$ s). These agreements suggest that the adhesion between laser-modified graphene and SiO_2 is observable but substantially smaller than typically observed for pristine van der Waals solids and clean interfaces.[40]

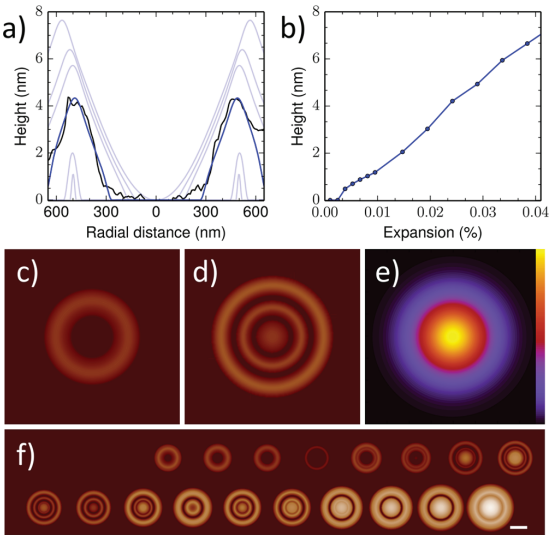

Figure 4. Thin sheet elasticity modeling of blisters with adhesion. (a) Experimental profile of $\tau = 1$ s blister (black curve) compared with simulated profiles of one-ripple blisters with different adhesions (blue curves from top to bottom: $\varepsilon_{adh} = 0$, 0.5, 1.0, 3.0, 10, and 100 μeV/nm^2). (b) Height of one-ripple blister as a function of expansion ε_0. (c) Contour plot of a one-ripple blister with $\varepsilon_0 = 0.017\%$ (corresponding to $\tau = 1$ s, Figure 1d). (d) Contour plot of a multiple-ripple blister with $\varepsilon_0 = 0.09\%$ (corresponding to $\tau = 50$ s, Figure 1e). (e) Contour plot of $\varepsilon(r)/\varepsilon_0$ for all blisters. The color scale is linear from zero to one. (f) Contour plots for all energy-optimized blisters, using the expansions from Figure 2b and the initial guesses from Figure 1b. Scale bar, 1 μm. Field of view in panels c–e is 2.2 × 2.2 μm^2. Panels b–f have $\varepsilon_{adh} = 3$ μeV/nm^2, and all blisters are optimized without imposing radial symmetry.

For completeness, we optimized all 18 blisters by using $\varepsilon_{adh} = 3$ μeV/nm^2 and by adopting the observed set of ripples as initial guesses. After optimization, the resulting pattern of blisters turned out similar to the experimental ones (Figure 4f). At small ε_0, stable blisters have only one ripple (Figure 4c), but at larger ε_0, stable blisters have multiple ripples (Figure 4d). Simulations capture the main features of the experimental blisters, even if they deviate with respect to certain details, presumably due to the asymmetric expansion field and small variations in the initial conditions of the graphene membrane, generated during the sample fabrication.

Yet a question remains: Why do blisters initially appear with one circular ripple? This question can be addressed by considering eq 3. The preferred slope has a maximum at $r_0 = \text{fwhm}/2\sqrt{\ln 2} = 0.48$ μm. In other words, around radius r_0, the energy to keep the membrane flat is the largest. When the in-plane stress in a flat membrane increases upon increasing ε_0, it becomes energetically favorable to release the stress by creating the kink right at r_0 and making a circular ripple with diameter $2r_0 = 0.96$ μm. This result agrees well with the observations. Upon continuous irradiation, after the initial ripple has appeared, the ripple height increases until it becomes energetically favorable to create more ripples. This implies a process-dependent rippling of ever-increasing complexity.

This scenario for rippling was confirmed by performing global optimizations for blisters with $\varepsilon_{adh} = 0.1–100$ μeV/nm^2, $\varepsilon_0 = 0.001...1\%$, and various types of initial guesses. First, at sufficiently small ε_0, the membrane remains flat without blistering. A critical limit for blistering is around $\varepsilon_0^c \approx 0.02 \times (\varepsilon_{adh}/\text{eV nm}^{-2})^{1/2}$. Second, when ε_0 increases just above the critical limit, the first blisters always have one ripple with diameter $D_0 \approx 1$ μm, independent of ε_{adh}. This result is in agreement with the experiments and with the maximum-slope argument given above ($D_0 \approx 2r_0$). Third, at intermediate values of ε_0, blisters show a complex pattern of ripples of varying heights and diameters. Fourth, at the limit of large ε_0, the in-plane strain energy dominates, and the minimum energy blisters always have one central dome (Figure 3a).

Compared with the typical magnitude of adhesion (1 to 2 eV/nm^2) between clean interfaces of van der Waals solids,[40–43] the adhesion in the model (~1 μeV/nm^2) is small. The smallness, however, is apparent even in a back-of-the-envelope calculation. Namely, upon blistering, the gain in elastic energy density is $k_s\varepsilon_0^2/(1-\nu)$, and the cost of adhesion energy density is ε_{adh}. At the onset of blistering, the two energies are equal, $\varepsilon_{adh} \approx k_s\varepsilon_0^2/(1-\nu)$. Because the blisters appear at $\varepsilon_0 \approx 0.02\%$, the adhesion has to be around 1–10 μeV/nm^2. The small adhesion may be due to water or functional groups,[44] topographic corrections,[45] electrostatics due to localized charge traps,[46] or other experimental details.[47,48] A detailed

DOI: 10.1021/acs.jpclett.8b02461
J. Phys. Chem. Lett. 2018, 9, 6179–6184

investigation of the laser-modified adhesion will be pursued later.

To summarize, by using the optical forging technique, we created diffraction-unlimited circular ripples in graphene on SiO_2. The rippling could be explained by the presence of circular symmetry amid the competition between substrate adhesion and in-plane compressive stress. In other words, the tiny rippling results spontaneously after creating an inhomogeneous expansion field on a much larger length scale. We can therefore straightforwardly predict that upon shrinking the size of the laser beam, the ripples will get smaller still. Once the mechanism responsible for the expansion of graphene is understood better, the technique could also be applied to other substrates and 2D materials. However, already now the technique and our observations provide many openings for novel research. A straightforward extension will be to control the rippling by engineering beam shapes. The technique produces beautiful circular blisters that probably have well-defined vibrational frequencies and can be used in resonators.[49] Via the formation of circular ripples, the technique also produced controllable curvatures that can be used to launch localized plasmons.[50] Thus, in addition to producing new physics and posing fundamental questions such as that of the laser-modified adhesion, the technique opens new avenues in the research of 2D materials.

■ ASSOCIATED CONTENT

Supporting Information

The Supporting Information is available free of charge on the ACS Publications website at DOI: 10.1021/acs.jpclett.8b02461.

Details of sample characterization and computer simulations (PDF)

Two movies illustrating the blister formation (ZIP)

■ AUTHOR INFORMATION

Corresponding Author

*E-mail: pekka.j.koskinen@jyu.fi.

ORCID

Pekka Koskinen: 0000-0001-7711-3562

Pasi Myllyperkiö: 0000-0003-1651-1676

Andreas Johansson: 0000-0003-0906-6287

Mika Pettersson: 0000-0002-6880-2283

Notes

The authors declare no competing financial interest.

■ ACKNOWLEDGMENTS

We acknowledge the Academy of Finland for funding (projects 297115 and 311330).

■ REFERENCES

(1) Stankovich, S.; Dikin, D. a.; Dommett, G. H. B.; Kohlhaas, K. M.; Zimney, E. J.; Stach, E. a.; Piner, R. D.; Nguyen, S. T.; Ruoff, R. S. Graphene-based composite materials. *Nature* **2006**, *442*, 282−286.

(2) Duong, D. L.; Yun, S. J.; Lee, Y. H. van der Waals Layered Materials: Opportunities and Challenges. *ACS Nano* **2017**, *11*, 11803.

(3) Geim, A. K.; Novoselov, K. S. The rise of graphene. *Nat. Mater.* **2007**, *6*, 183−191.

(4) Geim, A. K.; Grigorieva, I. V. Van der Waals heterostructures. *Nature* **2013**, *499*, 419−425.

(5) Son, Y.-W.; Cohen, M. L.; Louie, S. G. Half-metallic graphene nanoribbons. *Nature* **2006**, *444*, 347−349.

(6) Koskinen, P. Electromechanics of twisted graphene nanoribbons. *Appl. Phys. Lett.* **2011**, *99*, 013105.

(7) Gomes da Rocha, C.; Clayborne, P. A.; Koskinen, P.; Häkkinen, H. Optical and electronic properties of graphene nanoribbons upon adsorption of ligand-protected aluminum clusters. *Phys. Chem. Chem. Phys.* **2014**, *16*, 3558−3565.

(8) Zhao, J.; Deng, Q.; Bachmatiuk, A.; Sandeep, G.; Popov, A.; Eckert, J.; Rümmeli, M. H. Free-standing single-atom-thick iron membranes suspended in graphene pores. *Science* **2014**, *343*, 1228−1232.

(9) Koskinen, P.; Korhonen, T. Plenty of motion at the bottom: Atomically thin liquid gold membrane. *Nanoscale* **2015**, *7*, 10140.

(10) Antikainen, S.; Koskinen, P. Growth of two-dimensional Au patches in graphene pores: A density-functional study. *Comput. Mater. Sci.* **2017**, *131*, 120−125.

(11) Castro Neto, A. H.; Guinea, F.; Peres, N. M. R.; Novoselov, K. S.; Geim, A. K. The electronic properties of graphene. *Rev. Mod. Phys.* **2009**, *81*, 109−162.

(12) Levy, N.; Burke, S. a.; Meaker, K. L.; Panlasigui, M.; Zettl, A.; Guinea, F.; Neto, A. H. C.; Crommie, M. F. Strain-induced pseudo-magnetic fields greater than 300 T in graphene nanobubbles. *Science* **2010**, *329*, 544−547.

(13) Korhonen, T.; Koskinen, P. Electromechanics of graphene spirals. *AIP Adv.* **2014**, *4*, 127125.

(14) Eigler, D. M.; Schweizer, E. K. Positioning single atoms with a scanning tunneling microscope. *Nature* **1990**, *344*, 524.

(15) Kawai, T.; Okada, S.; Miyamoto, Y.; Hiura, H. Self-redirection of tearing edges in graphene: Tight-binding molecular dynamics simulations. *Phys. Rev. B: Condens. Matter Mater. Phys.* **2009**, *80*, 033401.

(16) Kit, O. O.; Tallinen, T.; Mahadevan, L.; Timonen, J.; Koskinen, P. Twisting Graphene Nanoribbons into Carbon Nanotubes. *Phys. Rev. B: Condens. Matter Mater. Phys.* **2012**, *85*, 085428.

(17) Chuvilin, A.; Kaiser, U.; Bichoutskaia, E.; Besley, N. A.; Khlobystov, A. N. Direct transformation of graphene to fullerene. *Nat. Chem.* **2010**, *2*, 450−453.

(18) Wang, D.; Chen, G.; Li, C.; Cheng, M.; Yang, W.; Wu, S.; Xie, G.; Zhang, J.; Zhao, J.; Lu, X.; et al. Thermally Induced Graphene Rotation on Hexagonal Boron Nitride. *Phys. Rev. Lett.* **2016**, *116*, 126101.

(19) Kotakoski, J.; Krasheninnikov, A. V.; Kaiser, U.; Meyer, J. C. From point defects in graphene to two-dimensional amorphous carbon. *Phys. Rev. Lett.* **2011**, *106*, 105505.

(20) Kotakoski, J.; Meyer, J. C.; Kurasch, S.; Santos-Cottin, D.; Kaiser, U.; Krasheninnikov, A. V. Stone-Wales-type transformations in carbon nanostructures driven by electron irradiation. *Phys. Rev. B: Condens. Matter Mater. Phys.* **2011**, *83*, 245420.

(21) Thompson-Flagg, R. C.; Moura, M. J. B.; Marder, M. Rippling of graphene. *EPL* **2009**, *85*, 46002.

(22) Svatek, S. A.; Scott, O. R.; Rivett, J. P. H.; Wright, K.; Baldoni, M.; Bichoutskaia, E.; Taniguchi, T.; Watanabe, K.; Marsden, A. J.; Wilson, N. R.; et al. Adsorbate-Induced Curvature and Stiffening of Graphene. *Nano Lett.* **2015**, *15*, 159−164.

(23) Jia, X.; Hofmann, M.; Meunier, V.; Sumpter, B. G.; Campos-Delgado, J.; Romo-Herrera, J. M.; Son, H.; Hsieh, Y.-P.; Reina, A.; Kong, J.; et al. Controlled formation of sharp zigzag and armchair edges in graphitic nanoribbons. *Science* **2009**, *323*, 1701−1705.

(24) Bao, W.; Miao, F.; Chen, Z.; Zhang, H.; Jang, W.; Dames, C.; Lau, C. N. Controlled ripple texturing of suspended graphene and ultrathin graphite membranes. *Nat. Nanotechnol.* **2009**, *4*, 562−566.

(25) Yamamoto, M.; Pierre-Louis, O.; Huang, J.; Fuhrer, M. S.; Einstein, T. L.; Cullen, W. G. "The Princess and the Pea" at the Nanoscale: Wrinkling and Delamination of Graphene on Nanoparticles. *Phys. Rev. X* **2012**, *2*, 041018.

(26) Aumanen, J.; Johansson, A.; Koivistoinen, J.; Myllyperkiö, P.; Pettersson, M. Patterning and tuning of electrical and optical properties of graphene by laser induced two-photon oxidation. *Nanoscale* **2015**, *7*, 2851−2855.

DOI: 10.1021/acs.jpclett.8b02461
J. Phys. Chem. Lett. 2018, 9, 6179−6184

(27) Koivistoinen, J.; Sladkova, L.; Aumanen, J.; Koskinen, P. J.; Roberts, K.; Johansson, A.; Myllyperkiö, P.; Pettersson, M. From Seeds to Islands: Growth of Oxidized Graphene by Two-Photon Oxidation. *J. Phys. Chem. C* **2016**, *120*, 22330.
(28) Johansson, A.; Myllyperkiö, P.; Koskinen, P.; Aumanen, J.; Koivistoinen, J.; Tsai, H. C.; Chen, C. H.; Chang, L. Y.; Hiltunen, V. M.; Manninen, J. J.; et al. Optical Forging of Graphene into Three-Dimensional Shapes. *Nano Lett.* **2017**, *17*, 6469−6474.
(29) Miller, D. L.; Keller, M. W.; Shaw, J. M.; Rice, K. P.; Keller, R. R.; Diederichsen, K. M. Giant secondary grain growth in Cu films on sapphire. *AIP Adv.* **2013**, *3*, 082105.
(30) Koenig, S. P.; Boddeti, N. G.; Dunn, M. L.; Bunch, J. S. Ultrastrong adhesion of graphene membranes. *Nat. Nanotechnol.* **2011**, *6*, 543−546.
(31) Landau, L. D.; Lifshitz, E. M. *Theory of Elasticity*, 3rd ed.; Pergamon: New York, 1986.
(32) Kudin, K.; Scuseria, G.; Yakobson, B. C2F, BN, and C nanoshell elasticity from ab initio computations. *Phys. Rev. B: Condens. Matter Mater. Phys.* **2001**, *64*, 235406.
(33) Shenoy, V.; Reddy, C.; Ramasubramaniam, A.; Zhang, Y. Edge-Stress-Induced Warping of Graphene Sheets and Nanoribbons. *Phys. Rev. Lett.* **2008**, *101*, 245501.
(34) Shenoy, V. B.; Reddy, C. D.; Zhang, Y.-W. Spontaneous curling of graphene sheets with reconstructed edges. *ACS Nano* **2010**, *4*, 4840−4844.
(35) Lambin, P. Elastic Properties and Stability of Physisorbed Graphene. *Appl. Sci.* **2014**, *4*, 282−304.
(36) Koskinen, P. Quantum Simulations of One-Dimensional Nanostructures under Arbitrary Deformations. *Phys. Rev. Appl.* **2016**, *6*, 034014.
(37) Koskinen, P. Graphene cardboard: From ripples to tunable metamaterial. *Appl. Phys. Lett.* **2014**, *104*, 101902.
(38) Bitzek, E.; Koskinen, P.; Gähler, F.; Moseler, M.; Gumbsch, P. Structural Relaxation Made Simple. *Phys. Rev. Lett.* **2006**, *97*, 170201.
(39) Korhonen, T.; Koskinen, P. Peeling of multilayer graphene creates complex interlayer sliding patterns. *Phys. Rev. B: Condens. Matter Mater. Phys.* **2015**, *92*, 115427.
(40) Björkman, T.; Gulans, A.; Krasheninnikov, A.; Nieminen, R. van der Waals Bonding in Layered Compounds from Advanced Density-Functional First-Principles Calculations. *Phys. Rev. Lett.* **2012**, *108*, 235502.
(41) Vanin, M.; Mortensen, J. J.; Kelkkanen, A. K.; Garcia-Lastra, J. M.; Thygesen, K. S.; Jacobsen, K. W. Graphene on metals: a Van den Waals density functional study. *Phys. Rev. B: Condens. Matter Mater. Phys.* **2010**, *81*, 081408.
(42) Hamada, I.; Otani, M. Comparative van der Waals density-functional study of graphene on metal surfaces. *Phys. Rev. B: Condens. Matter Mater. Phys.* **2010**, *82*, 153412.
(43) Tang, D.-M.; Kvashnin, D. G.; Najmaei, S.; Bando, Y.; Kimoto, K.; Koskinen, P.; Ajayan, P. M.; Yakobson, B. I.; Sorokin, P. B.; Lou, J.; et al. Nanomechanical cleavage of molybdenum disulphide atomic layers. *Nat. Commun.* **2014**, *5*, 3631.
(44) Gao, W.; Xiao, P.; Henkelman, G.; Liechti, K. M.; Huang, R. Interfacial adhesion between graphene and silicon dioxide by density functional theory with van der Waals corrections. *J. Phys. D: Appl. Phys.* **2014**, *47*, 255301.
(45) Delrio, F. W.; De Boer, M. P.; Knapp, J. A.; Reedy, E. D.; Clews, P. J.; Dunn, M. L. The role of van der Waals forces in adhesion of micromachined surfaces. *Nat. Mater.* **2005**, *4*, 629−634.
(46) Miwa, R. H.; Schmidt, T. M.; Scopel, W. L.; Fazzio, A. Doping of graphene adsorbed on the a-SiO2 surface. *Appl. Phys. Lett.* **2011**, *99*, 163108.
(47) Boddeti, N. G.; Liu, X.; Long, R.; Xiao, J.; Bunch, J. S.; Dunn, M. L. Graphene blisters with switchable shapes controlled by pressure and adhesion. *Nano Lett.* **2013**, *13*, 6216−6221.
(48) Miskin, M.; Sun, C.; Cohen, I.; Dichtel, W. R.; McEuen, P. Measuring and Manipulating the Adhesion of Graphene. *Nano Lett.* **2018**, *18*, 449.
(49) Bunch, J. S.; van der Zande, A. M.; Verbridge, S. S.; Frank, I. W.; Tanenbaum, D. M.; Parpia, J. M.; Craighead, H. G.; McEuen, P. L. Electromechanical Resonators from Graphene Sheets. *Science* **2007**, *315*, 490.
(50) Smirnova, D.; Mousavi, S. H.; Wang, Z.; Kivshar, Y. S.; Khanikaev, A. B. Trapping and Guiding Surface Plasmons in Curved Graphene Landscapes. *ACS Photonics* **2016**, *3*, 875−880.

DOI: 10.1021/acs.jpclett.8b02461
J. Phys. Chem. Lett. 2018, 9, 6179−6184

Supporting Information

Optically Forged Diffraction-Unlimited Ripples in Graphene

Pekka Koskinen[1], Karoliina Karppinen[2], Pasi Myllyperkiö[2],
Vesa-Matti Hiltunen[1], Andreas Johansson[1,2], and Mika Pettersson[2]

[1]Nanoscience Center, Department of Physics, University of Jyväskylä, 40014 Jyväskylä, Finland
[2]Nanoscience Center, Department of Chemistry, University of Jyväskylä, 40014 Jyväskylä, Finland

Sample fabrication

To prepare the sample, we grew single-layer graphene by chemical vapor deposition (CVD) on a Cu substrate, prepared by Cu evaporation onto a single crystal Sapphire wafer cut in the C plane[1]. The Cu layer crystals preferably align with a (111) surface, which has minimal lattice mismatch for catalysis of graphene. The CVD synthesis was done in a tube furnace at 1070°C with 45 min pregrowth annealing under 450/30 sccm flow of Ar/H_2, under which secondary Cu grain growth takes place, and a 5 min growth time under additional 2 sccm flow of CH_4. The graphene was subsequently transferred onto a p-doped Si wafer with 300 nm thermally grown SiO_2. PMMA was used as support layer and ammonium persulfate as the Cu etchant. The PMMA support layer and graphene stack was cleaned thoroughly in four consecutive baths of distilled water, followed by a 10% HCl bath to remove metal residues. The stack was then washed in another four distilled water baths before placed on the SiO_2 surface. After removal of PMMA in acetone, the graphene sample was annealed at 300°C for two hours under 200/10 sccm flow of Ar/H_2 to clean the graphene surface from residual PMMA contamination.

Characterization of graphene

The graphene was characterized after synthesis using Raman spectroscopy. All the Raman measurements were done using a home-built setup with 532 nm incident laser, laser power of 1 mW and 100 µm slit width. More details of the Raman setup can be found in our previous works[2,3]. Figure S1a shows a typical spectrum that has been acquired using two accumulations with 20 s exposure time per accumulation, a 600 mm^{-1} diffraction grating and center wavelength of 600 nm. Figure S1b shows a spectrum of the 2D band of our graphene, acquired using two accumulations with 60 s exposure time per accumulation, 2400 mm^{-1} grating and center wavelength of 621 nm. The red line in Fig. S1b is a single Lorentzian fit to the data. This shows that the 2D band is defined by a single Lorentzian, which is indicative of single layer graphene. The Raman characterization was done from several areas and it showed continuous single-layer graphene coverage[4].

AFM imaging was made on a Bruker Dimension Icon atomic force microscope, using Peak Force Tapping mode. ScanAsyst Air probes from Bruker were used during imaging with the peak force limited to 2 nN. This ensured the membranes were not compressed, as we have in a recent study shown with nanoindentation measurements that significant compression occurs only at much larger forces [2].

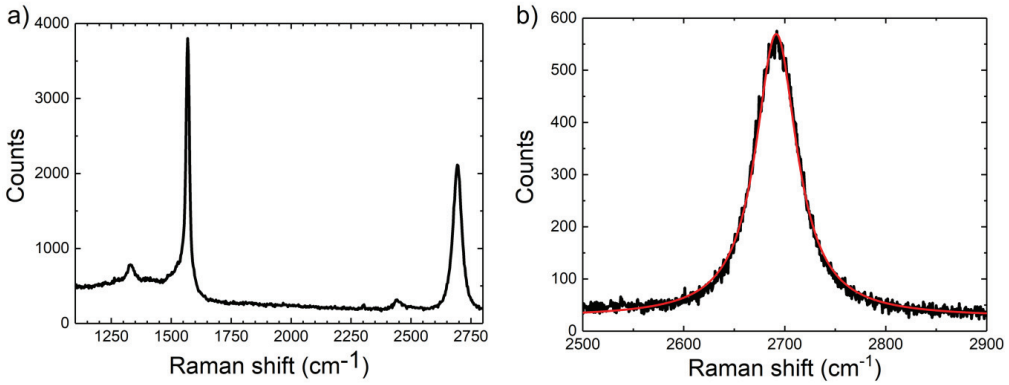

Fig. S1. Raman spectra of graphene after synthesis. a) Spectrum showing all the main Raman bands of graphene. b) A higher resolution spectrum of the 2D band with a single Lorentzian fit (red line).

Individual spectra from the middle points of six blisters with highest exposure time are shown in Fig. S2. The D-band increases in intensity and broadens upon irradiation, indicating increasing number of defects, while the 2D-band loses intensity. Simultaneously a broad background increases. Though it broadens, the G-band is present even after the highest irradiation dose, showing that graphene is still present.

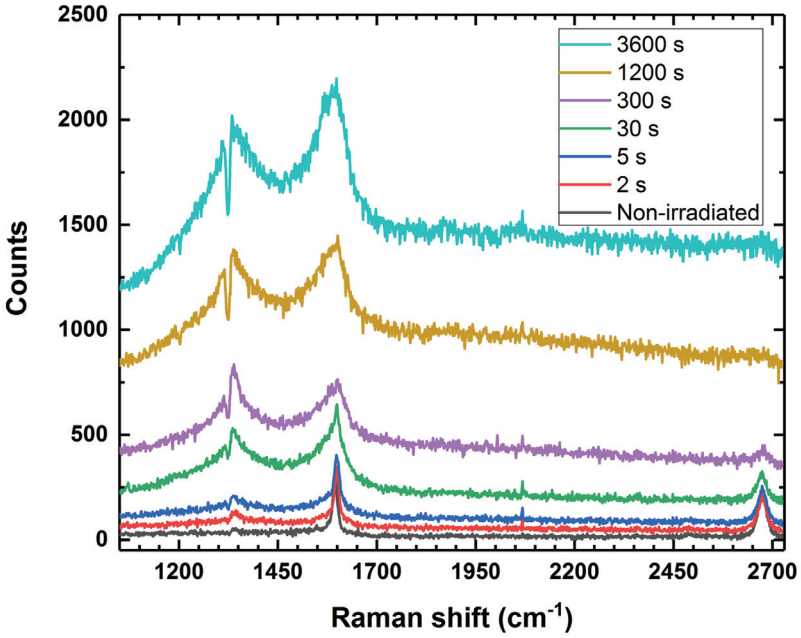

Fig. S2: Raman spectra from the middle points of six blisters on the bottom rows in Fig. S4. Non-irradiated graphene is shown for reference. The systematic changes in the spectra demonstrate the ability to control the defect density, which at 2 s and 5 s irradiations is still modest.

A Raman map of the D-band of graphene blisters is presented in Fig. S3. The map was collected using the same equipment as above, except that each spectrum was measured using two accumulations with 5 s exposure time per accumulation, a 600 mm^{-1} diffraction grating and center wavelength of 585 nm. The map was made by integrating the area under the spectrum between 1300-1400 cm^{-1} in each spot. This takes into account the intensity of the D-band and the broad background. The step size of the scan was 0.325 µm and the data has been interpolated to smoothen the map.

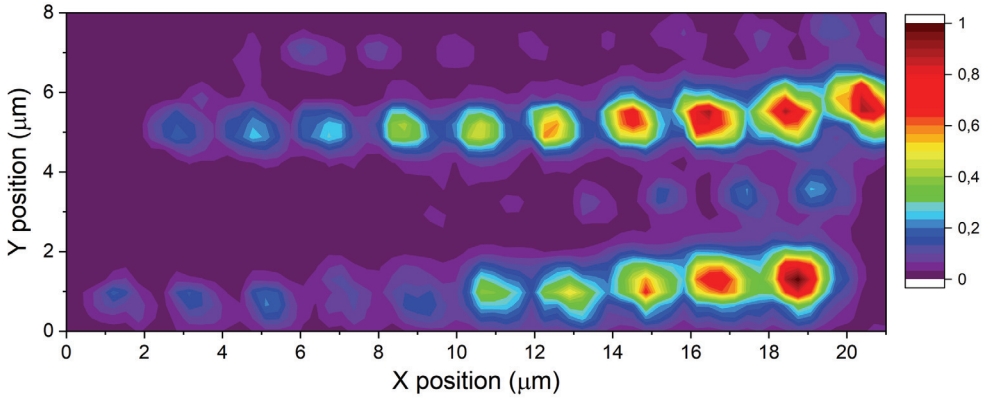

Fig. S3. D-band Raman map of two sets of blisters with irradiation times ranging from 0.1 to 3600 seconds (*cf.* Fig. S4).

The AFM imaging, after the laser irradiation process as described in the main text, was done using Bruker Dimension Icon atomic force microscope with peak force tapping mode. Figure S4 shows an image of the two sets of blisters, of which the upper one is shown in Fig. 1b.

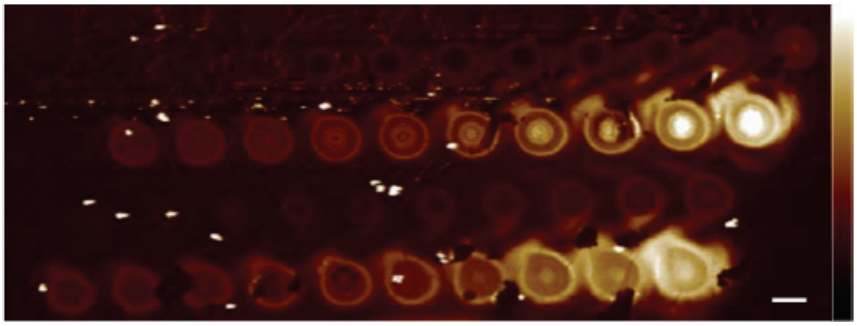

Fig. S4. Atomic Force Microscopy image of two sets of blisters with irradiation times ranging from 0.1 to 3600 seconds. Color scale is linear from 0 to 60 nm; scale bar is 1 μm.

Computer simulations using thin sheet elasticity theory

Graphene blisters were modeled by continuum thin sheet elasticity theory, known to work well in graphene over several length scales[5–7]. Here, the total energy of a sheet with the deformation $\vec{r} = \vec{r}^0 + \vec{a}$ was obtained by the integral $E = \int F dA$ over the total energy density $F = F_s + F_b + F_{ext}$. The first term represents the in-plane strain energy

$$F_s = \frac{k_s}{1-\nu^2}\left[\frac{1}{2}\left(e_{xx}+e_{yy}\right)^2 - (1-\nu)\left(e_{xx}e_{yy} - e_{xy}^2\right)\right],$$

where $k_s = 20$ eV/Å^2 is the in-plane elastic modulus, $\nu = 0.22$ is the Poisson ratio[8], and $e_{\alpha\beta} = \frac{1}{2}\left(\frac{\partial\vec{r}}{\partial\alpha}\cdot\frac{\partial\vec{r}}{\partial\beta} - \delta_{\alpha\beta}\right)$ is the strain tensor. The effect of non-zero, isotropic expansion $\varepsilon(\boldsymbol{r})$ is accounted for by subtracting it from the diagonal of the strain tensor, $e_{\alpha\beta} = e^0_{\alpha\beta} - \delta_{\alpha\beta}\varepsilon(\boldsymbol{r})$, where $e^0_{\alpha\beta}$ is the strain tensor of the unexpanded, pristine graphene. The second term represents the bending energy density

$$F_b = \frac{k_b}{2}\left[\left(C_{xx}+C_{yy}\right)^2 - 2(1-\nu)\left(C_{xx}C_{yy} - C_{xy}^2\right)\right],$$

where $k_b = 1.0$ eV is the bending modulus and $C_{\alpha\beta} = \vec{n}\cdot\frac{\partial^2\vec{r}}{\partial\alpha\cdot\partial\beta}$ is the curvature tensor, with the surface normal $\vec{n}$. The third term represents the energy density due to substrate adhesion, for which we used the Lennard-Jones 6-12 potential,

$$F_{ext} = -\frac{5}{3}\varepsilon_{vdW}\left(\frac{d}{z}\right)^4\left[1 - \frac{2}{5}\left(\frac{d}{z}\right)^6\right],$$

where ε_{vdW} is the adhesion strength (energy per unit area) and d is the bonding distance. The blisters' large heights ($d \ll h$) render the form of the potential irrelevant and make the energy difference ε_{vdW} between adhered and detached membrane the only relevant parameter. Therefore, the results are independent of this particular choice of van der Waals potential.

This theory was discretized using two computer codes. First, to exploit the circular symmetry of the blisters, the membrane was discretized in radial direction using displacement vector $\vec{a}(r) = a_r(r)\hat{r} + a_z(r)\hat{z}$ [*cf.* Eq.(2) in the main text] (with maximum radius of $1.6\ \mu m$ and 1000 radial points). Second, in order to allow for arbitrary deformation after efficient pre-screening using circular symmetry, the theory was discretized and simulated using general two-dimensional deformation field $\vec{a}(x,y) = a_x(x,y)\hat{x} + a_y(x,y)\hat{y} + a_z(x,y)\hat{z}$ (with $2\times 2\ \mu m^2$ area and 200×200 points). The deformation fields were obtained by minimizing the total energy functional $E[\vec{a}]$ with respect to $\vec{a}(r)$ or $\vec{a}(x,y)$ below 10^{-8} eV/Å force tolerance using Broyden-Fletcher-Golfarb-Shanno (BFGS) optimization method.

References:

(1) Miller, D. L.; Keller, M. W.; Shaw, J. M.; Rice, K. P.; Keller, R. R.; Diederichsen, K. M. Giant Secondary Grain Growth in Cu Films on Sapphire. *AIP Adv.* **2013**, *3*, 082105.

(2) Johansson, A.; Myllyperkiö, P.; Koskinen, P.; Aumanen, J.; Koivistoinen, J.; Tsai, H. C.; Chen, C. H.; Chang, L. Y.; Hiltunen, V. M.; Manninen, J. J.; et al. Optical Forging of Graphene into Three-Dimensional Shapes. *Nano Lett.* **2017**, *17*, 6469–6474.

(3) Aumanen, J.; Johansson, A.; Koivistoinen, J.; Myllyperkiö, P.; Pettersson, M.

Patterning and Tuning of Electrical and Optical Properties of Graphene by Laser Induced Two-Photon Oxidation. *Nanoscale* **2015**, *7*, 2851–2855.
(4) Ferrari, A. C. Raman Spectroscopy of Graphene and Graphite: Disorder, Electron-Phonon Coupling, Doping and Nonadiabatic Effects. *Solid State Commun.* **2007**, *143* (1–2), 47–57.
(5) Landau, L. D.; Lifshitz, E. M. *Theory of Elasticity*, 3rd edition; Pergamon, New York, 1986.
(6) Kudin, K.; Scuseria, G.; Yakobson, B. C2F, BN, and C Nanoshell Elasticity from Ab Initio Computations. *Phys. Rev. B* **2001**, *64*, 235406.
(7) Lambin, P. Elastic Properties and Stability of Physisorbed Graphene. *Appl. Sci.* **2014**, *4* (2), 282–304.
(8) Kit, O. O.; Tallinen, T.; Mahadevan, L.; Timonen, J.; Koskinen, P. Twisting Graphene Nanoribbons into Carbon Nanotubes. *Phys. Rev. B* **2012**, *85*, 085428.

AIII

SHAPING GRAPHENE WITH OPTICAL FORGING: FROM SINGLE BLISTER TO COMPLEX 3D STRUCTURES

by

Kamila Mentel, Jyrki Manninen, Vesa-Matti Hiltunen, Pasi Myllyperkiö,Andreas Johansson, Mika Pettersson 2021

Nanoscale Advances, accepted for publication

DOI: 10.1039/d0na00832j

Nanoscale Advances

ROYAL SOCIETY OF CHEMISTRY

PAPER

View Article Online
View Journal

Cite this: DOI: 10.1039/d0na00832j

Shaping graphene with optical forging: from a single blister to complex 3D structures†

Kamila K. Mentel, [a] Jyrki Manninen, [b] Vesa-Matti Hiltunen, [b] Pasi Myllyperkiö, [a] Andreas Johansson [ab] and Mika Pettersson *[a]

Received 8th October 2020
Accepted 31st December 2020

DOI: 10.1039/d0na00832j

rsc.li/nanoscale-advances

Properties of graphene, such as electrical conduction and rigidity can be tuned by introducing local strain or defects into its lattice. We used optical forging, a direct laser writing method, under an inert gas atmosphere, to produce complex 3D patterns of single layer graphene. We observed bulging of graphene out of the plane due to defect induced lattice expansion. By applying low peak fluences, we obtained a 3D-shaped graphene surface without either ablating it or deforming the underlying Si/SiO_2 substrate. We used micromachining theory to estimate the single-pulse modification threshold fluence of graphene, which was 8.3 mJ cm^{-2}, being an order of magnitude lower than the threshold for ablation. The control of exposure parameters allowed the preparation of blisters with various topographies. The optically forged structures were studied with atomic force microscopy and Raman spectroscopy. Optically forged blisters act as building blocks in the formation of more complex structures. We found a simple geometric rule that helps to predict the shape of complex patterns which are created by the overlapping multiple exposures. Optical forging enables writing of extended patterns with diffraction unlimited features, which makes this method promising in the production of nanodevices with locally induced surface modifications.

Introduction

Femtosecond laser micromachining is a well-established method in the fabrication of micrometer-scale patterns and three-dimensional devices, thanks to the beneficial properties of the method, such as sub-micrometer scale precision, mask-free processing and confinement of the induced changes to the laser focal volume.[1,2] Recently, laser micromachining has gained more attention in the alteration of the physical or chemical properties of 2D materials. It was shown to be useful in localized modification and thinning of multilayered graphene,[3] and 2D MoS_2,[4] WS_2,[5] and $PdSe_2$.[6] Direct laser patterning was used for phase transformation of 2D $PdSe_2$.[6] It was used in micro-cutting,[7,8] in ablation of graphene,[9–13] and in producing micro and nano-disks.[14] Direct laser writing was also applied for graphene oxide reduction,[15] for oxidation of graphene in a controlled manner,[16,17] and patterning of the p–n junction in graphene.[18]

Recently, we demonstrated that optical forging, a direct laser writing method with a tightly focused femtosecond laser beam under an inert gas atmosphere, can be used for 3D shaping of graphene.[19–21] Optical forging leads to controllably induced defects, causing lattice expansion and bulging of graphene out of the plane. With a sufficiently large optical forging dose, graphene exhibits strong luminescence.[21]

In this study, we present how optical forging can be used to create spatially precise and well-defined 3D patterns in a single layer of graphene. By careful choice of femtosecond laser exposure parameters, we induce a desired amount of defects over a spatially confined region on the chip surface. Depending on the laser parameters, the shape of the primary laser writing element varies from a Gaussian-shaped dome to a ring structure with sub-diffraction limited ripples.[20] Overlapping basic writing elements leads to extended patterns, the shapes of which depend on the sequence of writing of discrete elements. The overall appearance of the patterns follows a simple geometric rule. These systematic studies on step-by-step optical forging provide basic know-how for complex design and 3D shaping of graphene. The presented method enables writing of extended patterns of 3D objects having feature sizes down to, and even below, 100 nm at the FWHM, while using a far-field laser beam. The introduced out-of-plane deformation in graphene additionally forms a basis for strain engineering of its electronic and photonic properties.[22] This method possibly can be expanded to other 2D materials,

[a]Nanoscience Center, Department of Chemistry, University of Jyväskylä, Finland. E-mail: mika.j.pettersson@jyu.fi

[b]Nanoscience Center, Department of Physics, University of Jyväskylä, Finland

† Electronic supplementary information (ESI) available: Optical forging reproducibility example; cross-sections of blisters and their Raman characterization; AFM nanomechanical data for blisters, tetramers and pentamers; O_2 plasma etching data; and AFM height images of complex patterns prepared under various irradiation conditions. See DOI: 10.1039/d0na00832j

opening an exciting new perspective of modification of atomically thin materials.

Experimental section

Sample fabrication

For both samples used in this study, the graphene was synthesized on Cu(111) thin films evaporated onto single crystal sapphire (0001) substrates. The catalyst film was annealed at 1070 °C under gas flows of 470 sccm argon and 30 sccm hydrogen for 45 minutes. After annealing, the graphene growth was initiated by injecting 2 sccm of 1% methane in argon to the furnace while keeping the temperature at 1070 °C. The growth time was 7 minutes. After the growth, the samples were taken out of the hot zone of the furnace and allowed to cool down.

The graphene films were transferred by a standard PMMA transfer method[23] onto a target substrate, which was a silicon chip with a 300 nm thermal oxide film and a metal marker grid on top. The samples were spin-coated with a PMMA layer and the copper was etched in 1 M ammonium persulfate solution leaving the graphene/PMMA stack floating on the liquid. Then the graphene was rinsed in DI water, placed in 12% HCl to remove possible metal residues, rinsed again in DI water and placed onto the Si/SiO_2 substrate. The samples were baked on a hot plate at 120 °C for 5 minutes to evaporate water between the substrate and the graphene. After this the PMMA film was removed with acetone and IPA. Sample **1** was annealed first at 200 °C in an O_2 atmosphere for 30 minutes, then at 300 °C in an Ar/H_2 atmosphere for two hours and finally at 300 °C in an O_2 atmosphere for two hours. Sample **2** was annealed at 300 °C in an Ar/H_2 atmosphere for two hours to remove PMMA residues.

Optical forging

Direct laser writing of the patterns was performed with a 515 nm femtosecond laser (Pharos-10, Light Conversion Ltd., 600 kHz, 250 fs pulse duration) focused with an objective lens (N.A. = 0.8) to a Gaussian spot. Detailed setup description was presented previously.[19] The laser writing was performed under a nitrogen purge to prevent photo-oxidation of graphene during the writing process. The pulse energies were varied between 20 and 120 pJ. Blisters were irradiated by single spot exposure with irradiation time from 0.1 to 300 s per spot. The complex patterns were prepared by step-by-step irradiation with separation distances between consecutive laser spots of up to 1.5 μm.

All presented data belong to the optical forging studies performed on sample **1**. An exception is etching data which were obtained from sample **2**.

AFM characterization

AFM imaging was made on a Bruker Dimension Icon Atomic Force Microscope (AFM) in the PeakForce Quantitative Nanomechanical Mapping (QNM) mode. ScanAsyst Air probes from Bruker were used during imaging with the peak force limited to 2 nN. The diameter of the blisters was estimated from the collected height image. The Bearing Analysis tool from Nanoscope Analysis 1.9 software was used to estimate the volume expansion of created structures. This tool allows to obtain information about how much surface lies above or below a given height. In the analysis, the AFM height image of each forged blister is sliced at a specified height, ΔZ. A plane drawn at the ΔZ gives an area that is occupied by a region above the indicated background level. By summing areas for each ΔZ between $0 < \Delta Z \leq Z_{max}$, where Z_{max} is the height of the blister, the bearing volume information of the 3D structures is obtained.

Raman characterization

Raman measurements were carried out with a home-built Raman setup in a backscattering geometry using a 532 nm excitation wavelength produced with a continuous wave single frequency laser (Alphalas, Monolas-532-100-SM). Detailed setup description was presented previously.[17] Mapping was conducted using 250 nm steps between measurement points. A laser power of ~0.25 mW was utilized. Two accumulations per each point were collected with 6 s measurement time per accumulation.

Oxygen plasma etching

Oxygen plasma etching was carried out using an Oxford Instruments Plasmalab 80 Plus reactive ion etcher. Plasma was generated using a 30 mT magnetic field at a chamber pressure of 30 mTorr and an oxygen flow of 30 sccm. The etching was performed with a forward power setting of 20 W for 30 s on sample **2**.

Results and discussion

Optical forging experiments were performed in an inert atmosphere to prevent oxidative processes.[19] We used tightly focused pulses with a 515 nm wavelength and 250 fs duration at a 600 kHz repetition rate to modify the graphene surface. In order to determine the influence of the laser dose on the shape of the forged blisters we prepared a series of laser exposures with increasing pulse energies (20–120 pJ) and irradiation times per spot (0.1–300 s), which corresponds to 6×10^4 to 1.8×10^8 applied laser pulses per spot. The laser dose is described as the pulse energy multiplied with irradiation time per spot and divided by the laser spot size, expressed in pJ s cm^{-2}. The blister topography profile was subsequently characterized by atomic force microscopy (Fig. 1a). A single blister is the smallest unit which can be forged. Thanks to the reproducibility of the process, for which an example is presented in Fig. S1,† the blister can be used as a building block to create large and complex structures (presented later). By changing exposure parameters, we gained control over produced blister features such as its height, outer diameter, and complexity (*e.g.* more than one fringe). The cross-sections of blisters are presented in Fig. S2.† Blisters are relatively plastic, and their shape changes upon further irradiation.[20] An increase in dose increases the overall diameter, D, of the formed pattern, which follows logarithmic dependence (Fig. 1b). Blisters with diameters below 1.1 μm exhibit a dome-like structure. Increasing the laser dose introduces a pit in the blister ($D = 1.15$–1.25 μm), until at higher

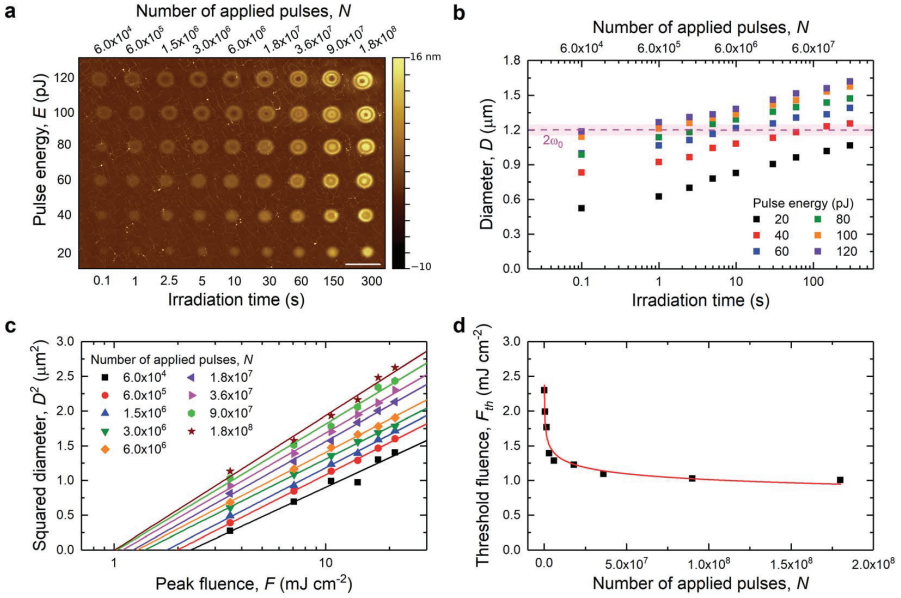

Fig. 1 (a) AFM topography image of blisters formed at different exposure times and laser pulse energies. Scale bar 2.5 μm. (b) Blister diameter as a function of irradiation time (number of applied pulses). Dashed line shows an estimated beam diameter with its uncertainty (pink shade). (c) Squared blister diameter as a function of peak fluence. (d) Calculated laser threshold fluences for *N*-pulses plotted *versus* the number of applied pulses with presented fitting of the power law from eqn (3) (red line).

doses, a single ring-like fringe is formed ($1.25 < D < 1.3$ μm). Further irradiation causes the appearance of a central dome and/or more fringes ($D > 1.3$ μm). The blisters have features that are significantly below the diffraction limit as was observed previously.[20] For example, the ring can have a linewidth of 100 nm. It was suggested that the diffraction-unlimited rippling occurs due to the interplay between surface adhesion and stress induced lattice expansion.[20] Additionally, blisters with diameters equal to or larger than the beam size exhibit an increase in the surface roughness.

We used well-established equations for the ablation threshold in laser micromachining in order to obtain a modification threshold fluence, $F_{th}(N)$, for optical forging.[24] For applied *N*-pulses, the $F_{th}(N)$ can be determined from a plot of the squared diameter of the forged blister, D^2, *versus* the laser peak fluence, F, deposited on the sample related by:[24]

$$D^2 = 2\omega_0^2 \ln\left(\frac{F}{F_{th}(N)}\right) \quad (1)$$

where ω_0 is the $1/e^2$ gaussian laser beam radius. The laser peak fluence is related to the pulse energy, E, by

$$F = \frac{2E}{\pi\omega_0^2} \quad (2)$$

Eqn (2) shows a linear dependence between the laser pulse energy and the peak fluence. Thus, the beam radius can be obtained from plotting D^2 *versus* $\ln(E)$. The average beam radius was estimated to be $\omega_0 = 0.60 \pm 0.02$ μm at $1/e^2$ and was used to calculate the laser peak fluence from eqn (2). The squared diameter as a function of applied laser peak fluence is presented in Fig. 1c. The modification threshold fluence for *N*-pulses was obtained by extrapolation of D^2 to zero. The estimated threshold fluence was 2.3 mJ cm^{-2} for an irradiation time of 0.1 s (6×10^4 pulses), and it decreased with the number of applied laser pulses. The obtained $F_{th}(N)$ values as a function of applied laser pulses are plotted in Fig. 1d. The behavior of lowering threshold fluences can be associated with an incubation effect.[25] This effect can be related *e.g.* to plastic deformation,[26] heat accumulation,[27] and defect formation.[28] It was reported that in a graphene/SiO_2/Si stack, most of the significant absorption occurs in the graphene layer.[29] In addition, due to the use of relatively short laser pulses (250 fs) and very low fluences ($F < 25$ mJ cm^{-2}), we can possibly exclude heat accumulation in our sample. In our system, the incubation effect can be assigned to defect formation due to laser exposure. This is supported by Fig. S3 and S4,† where we show Raman spectra collected for optically forged blisters presented in Fig. 1a. Blisters prepared with short exposures exhibit narrow D bands, which correspond to introduction of point defects into the graphene lattice. An estimated point defect density in non-irradiated graphene is approximately 10^{11} cm^{-2}, and it rapidly increases for the blisters prepared using low laser doses (<2×10^{12} pJ s cm^{-2}) up to 5×10^{11} cm^{-2}. Higher doses increase point defect density at a slower rate up to 10^{12} cm^{-2}. Longer laser exposures and/or increased pulse energies trigger a broadening of D and G bands and increase the intensity of a broad background. Both

changes support an increasing disorder in the graphene lattice. The observed behavior was associated in our previous study with the formation of line defects.[21] Nonetheless, all blisters continue to exhibit spectral features of graphene, confirming that the applied low range of fluences does not lead to ablation. We proposed the Stone–Wales defects[19,21] as plausible point defects created in the graphene lattice, which can gradually develop into extended line defects.[21] We note that in studies by other groups of laser-induced ablation of graphene,[30,31] a blistering effect was not observed. We also stress that the blisters in the present study are smooth and have well-defined shapes, with no signs of missing layer fragments. Moreover, we have shown that pronounced bulging of graphene out of the plane occurs only for optical forging experiments performed under an inert atmosphere, where oxidative processes are excluded.[19] To our knowledge this is the first time when micromachining equations were successfully applied to laser-induced graphene modification studies, when the material is still intact, not partially or fully ablated. This is due to visible blistering which allows us to accurately estimate the diameter of the laser affected area.

To find the relation between single pulse exposure and N-pulse threshold fluence we used the equation:[25]

$$F_{th}(N) = F_{th}(1)N^{S-1} \quad (3)$$

where $F_{th}(1)$ is the threshold fluence for single pulse exposure and S is the incubation coefficient. From the data plot in Fig. 1d and using eqn (3), the incubation coefficient can be estimated to be $S = 0.88$, which is nearly identical to the reported value for graphene, $S = 0.87$, obtained from ablation studies.[11] The estimated single-pulse modification threshold fluence for optically forged graphene is then $F_{th}(1) = 8.3 \pm 1.2$ mJ cm^{-2}. The ablation threshold for graphene for single-pulse exposure was reported to be ~200 mJ cm^{-2} in air ($\lambda_{ex} = 790$ nm, 50 fs to 1.6 ps),[30] and 170 mJ cm^{-2} in an argon atmosphere ($\lambda_{ex} = 800$ nm, 100 fs, 1 kHz).[8] These values are close to the theoretically obtained ablation thresholds for graphitic films (250 mJ cm^{-1}).[32] Our optical forging threshold is significantly lower than these ablation thresholds. Therefore, we have a substantial margin of fluences that can be used before removal of graphene occurs.

For completeness, we will also consider the effect of the laser exposure on the underlying substrate of 300 nm SiO_2 on Si. Rublack *et al.* reported single-pulse ablation and the melting threshold for 100 nm SiO_2 on the Si substrate to be 219 ± 4 mJ cm^{-2} and 137 ± 2 mJ cm^{-2}, respectively ($\lambda_{ex} = 515$ nm, 280 fs).[33] Above the melting threshold, a delamination of the SiO_2 layer may occur. In our experiments we used similar laser parameters (excitation wavelength, pulse duration), and therefore, we can make direct comparison. Our estimated $F_{th}(1)$ value for graphene modification is 25-times lower than the ablation threshold and 16.5 times lower than the melting threshold for single-pulse fluences of a SiO_2 layer. It is worth mentioning that the nature of the delamination and consequent visible bulging of a thin SiO_2 layer is different than in graphene. The bulging of a SiO_2 layer or other thin layer materials is a pressure induced lift off by melting and vaporizing of the silicon layer underneath.[34–36] In graphene, bulging presumably occurs by the expansion of the material lattice due to the presence of laser-induced defects. The obtained modification threshold value is

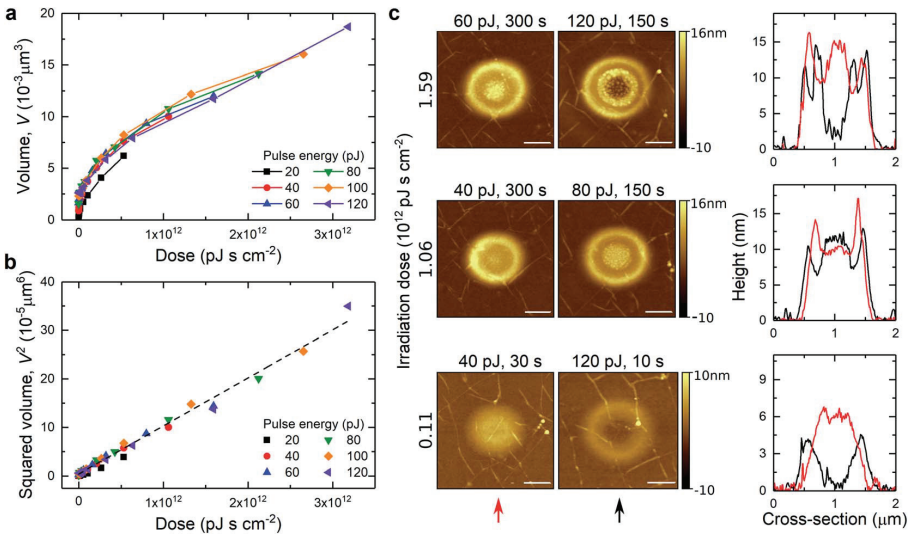

Fig. 2 (a) Estimated volume of blisters and (b) squared volume as a function of applied laser dose. Dashed line represents least square fitting to the points between 40 and 120 pJ. (c) AFM images of pairs of blisters prepared with the same dose: 0.11 × 10^{12}, 1.06 × 10^{12} and 1.59 × 10^{12} pJ s cm^{-2} and their corresponding vertical cross-section (marked by arrows). Above each AFM image, irradiation conditions are presented: pulse energy and irradiation time. Scale bar 0.5 μm.

also ~25 times lower than the reported single-shot ablation threshold fluence for silicon, $F_{th}(1) = 220$ mJ cm^{-2} ($\lambda_{ex} =$ 515 nm, 3 ps).[37] The fluences used in this study ($F < 25$ mJ cm^{-2}) are therefore too low to introduce any changes to the substrate. This was confirmed by removing optically forged graphene squares through O_2 plasma etching. Subsequent AFM imaging revealed an intact surface underneath the removed graphene squares (Fig. S5†).

In laser micromachining, the volume of created holes/craters is frequently studied in order to provide information about the quality of the ablation process. In our studies we do not create holes in the material, but we fabricate blisters which are bulging out of the plane. These structures can also be described with a volume parameter. We estimated the volume of expanded blisters using the bearing analysis tool in Nanoscope Analysis 1.9 software (Fig. 2a). Blisters created with 40 to 120 pJ pulse energies follow the same trend. Blisters formed upon irradiation with 20 pJ seem to have bit smaller volumes, but they also exhibit smaller diameters. From Fig. 2b it is visible that the squared volume expansion, V^2 increases linearly as a function of the applied laser dose. Fig. 2c shows three pairs of blisters formed with the same dose: 0.11×10^{12}, 1.06×10^{12} and 1.59×10^{12} pJ s cm^{-2}. Each pair exhibits similar volume expansion, however, possesses disparate shape/cross sections. This could possibly be explained by different initial irradiation conditions. Higher laser pulse energy produces blisters with

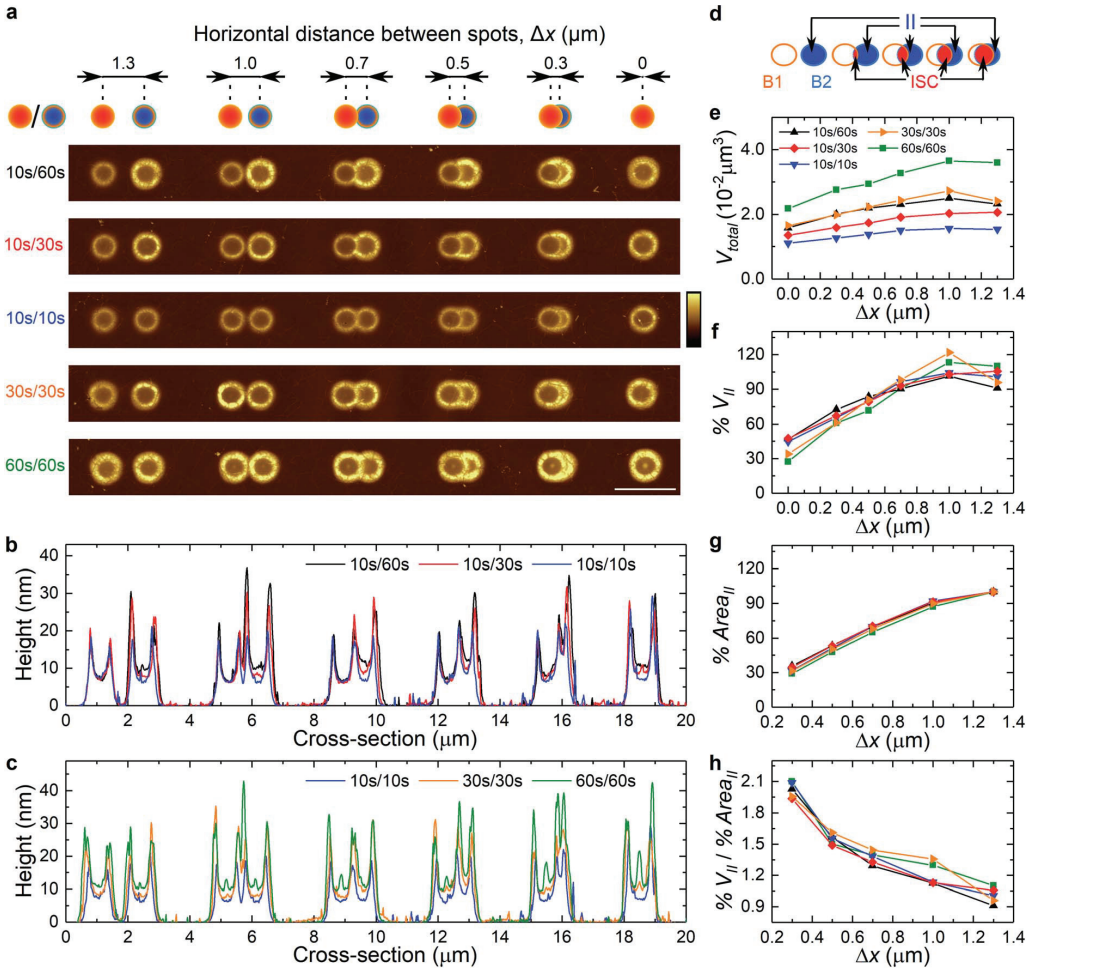

Fig. 3 (a) Illustration of dimer overlap with various separation distances, Δx, and the AFM images of optically forged dimers created with 60 pJ pulse energy and various irradiation times. From the pair of blisters, the one on the left was irradiated first. Scale bar 2 μm. Color bar from −15 to 35 nm. (b and c) Cross-sections of dimers formed under different experimental conditions. (d) Scheme illustrating the nomenclature of the parts of blisters: B1 and B2 correspond to the first and the second irradiated blister, respectively, when they do not intersect, II corresponds to the part of the second blister after subtracting the intersecting part of two overlapping blisters, ISC. (e) Volume of a pair of blisters, V_{total}, as a function of Δx. Percentage of (f) V_{II}, (g) $Area_{II}$ and (h) $V_{II}/Area_{II}$ ratio as a function of Δx. Legend as in (e).

a larger lateral diameter and more pronounced ring structures, whereas lower laser pulse energy and longer exposure produce blisters with a smaller footprint and more dome shaped structures.

We used our AFM's PeakForce Quantitative Nanomechanical Mapping (QNM) mode to characterize the mechanical properties of graphene before and after optical forging. We collected data on qualitative changes in adhesion, elastic modulus (fitted with Derjaguin–Muller–Toporov model, DMT-modulus)[38] and deformation together with the topography measurements. The collected data are presented in Fig. S6.† All types of data show a clear difference between irradiated and non-irradiated areas. The adhesion data provide information about the adhesion between the studied surface and the silicon tip. We noticed that the adhesion is reduced in the area of irradiated spots in comparison to pristine graphene, with the lowest value found on the blister fringes, and on the central domes for blisters larger than the beam size. Essentially, the lowest adhesion corresponds to the highest part of the blisters. This may indicate that graphene is detached from the substrate, and therefore, a smaller area of the sample interacts with the tip leading to the smaller adhesion forces. The reduction of the adhesive forces was associated with the delamination of graphene crumples from the substrate in other studies.[39] The deformation data give information about deformability of the sample upon pressing with the AFM tip. The highest recorded deformation does not correspond to the most elevated region of the blister. It is located on the shoulder of dome-like blisters and outer side of the fringe of ring-like blisters, meaning that this is the softest part. Assuming that blisters are empty inside, they can flex sideways under the load on the outer side of the fringe. This bending would show as increased deformation. Additionally, the outer side of the blister should contain fewer defects, which can be correlated with the shape of the gaussian beam, leading to lower irradiation intensity at the edges. Larger lattice disorder should occur closer to the center of the beam. The relative values of the DMT modulus show that the rigidity of the nanomaterial increases under laser exposure with respect to the pristine graphene. However, used forces are too small to induce material deformation in the in-plane direction, and therefore, it is not certain if we observed just structural flexing, or also real material properties. Blisters with the broad Raman background have higher elastic modulus values. Structures with additional central domes/or extra fringes exhibit mixed stiffness properties, due to high surface roughness. Change in the mechanical properties of graphene is associated with the presence of defects. The rigidity of graphene will depend on the amount and type of introduced defects. It was reported that divacancy always reduces the stiffness of graphene, while it is unclear if a moderate number of sp^3-type defects increase the sample stiffness[40,41] However, experimental studies on the relation between graphene stiffness and defect concentration are still limited. The correlation of high stiffness with the existence of line defects in our studies needs to be verified by further experiments.

After establishing the connection between the irradiation dose and blister shape, we tested forming patterns through multistep irradiation of basic writing elements. The simplest

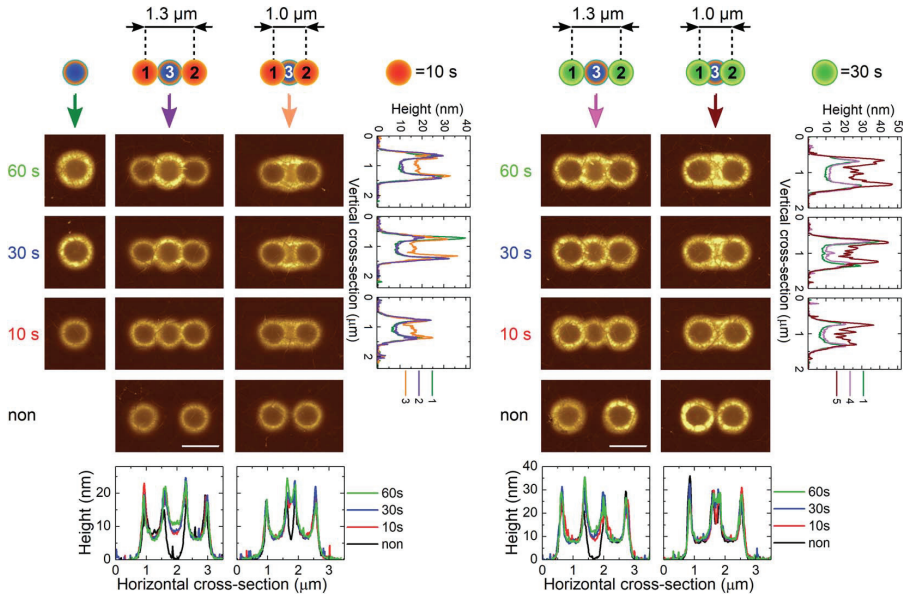

Fig. 4 Illustration of trimer overlap with third exposure in the centre of a dimer. AFM images of an optically forged trimer with images of dimers and single blisters used for comparison. Blisters were prepared with 60 pJ pulse energy. Irradiation times are shown in the figure. Order of irradiation is marked in the schemes. Colour gradient from −15 to 35 nm. Scale bar 1 μm. Cross-sections of patterns formed under different experimental conditions are presented. Vertical cross-sections were collected in the position indicated by a colour coded arrow.

example is a dimer of blisters. In Fig. 3a we show the schematic illustration of dimer formation by two-step irradiation with varying horizontal distance, Δx, between the laser spots. When $\Delta x = 1.3$ μm the blisters do not intersect, while for $\Delta x = 0$ μm they fully overlap. In each pair, the blister on the left was created (optically forged) first. Fig. 3a also contains AFM images of 6 sets of optically forged dimers prepared by varying irradiation times: 10 s/60 s, 10 s/30 s, 10 s/10 s, 30 s/30 s and 60 s/60 s. One of the most striking observations is that the structure of the first blister is always maintained. The second laser exposure cannot deform the overall shape of the previously formed blister but forms a 3D shape under the part of the beam exposing an area of pristine graphene. However, it can subtly expand the first blister by following the volume to dose dependence. This can be seen in the cross-section of the dimers presented in Fig. 3b and c. The profile of the first blister stays virtually the same after the second laser exposure. Small changes can be seen for full overlap and longer exposure such as the 60 s/60 s dimer pair. A full overlap mainly causes lattice expansion on the fringe exterior. In the case of the 60 s/60 s dimer pair, a slight hint of the presence of a central dome starts to be visible. This agrees with the blister growth rule, which stipulates that a dome-like blister evolves into a fringe-like blister and then into a fringe-like blister with a central dome structure with increasing irradiation dose.

To understand better the dimer formation, we estimated the volume expansion of each pair of blisters, V_{total} (Fig. 3e). Firstly, $\Delta x = 1.3$ μm represents a situation when pairs of blisters do not intersect. This provides information about volume expansion of each blister separately, V_{B1} and V_{B2}. The dimer volume decreases with decreasing Δx, showing that two overlapping blisters yield a smaller volume than two individual blisters. The dimer volume reaches its minimal value at full overlap, $\Delta x = 0$ μm. It then corresponds to the volume for a single blister with irradiation time as the sum of both blisters. Full overlap is the case when the highest expansion of the first blister is expected. This gives about 45% volume increase for blisters with the same irradiation time. By increasing Δx, the intersecting area, $Area_{ISC}$, between blisters is reduced. Hence, the effect of consecutive exposures on the first blister decreases in comparison with full overlap. In the case of partial overlap, optical forging does not provide sufficient energy to create further visible changes in an already existing elevated structure. These observations agree with the volume to irradiation dose dependence of an individual blister, where $V^2 \propto$ dose. The increase of volume rate is very fast for low doses and does not change considerably with the additional prolonged exposure.

On the other hand, a second exposure forms a 3D shape mainly over a non-irradiated graphene surface, and on the outer side of the existing blister. It has a fringe-like shape for $\Delta x > 0.7$ μm, and a crescent-like shape for $0 < \Delta x \leq 0.7$ μm. We estimated

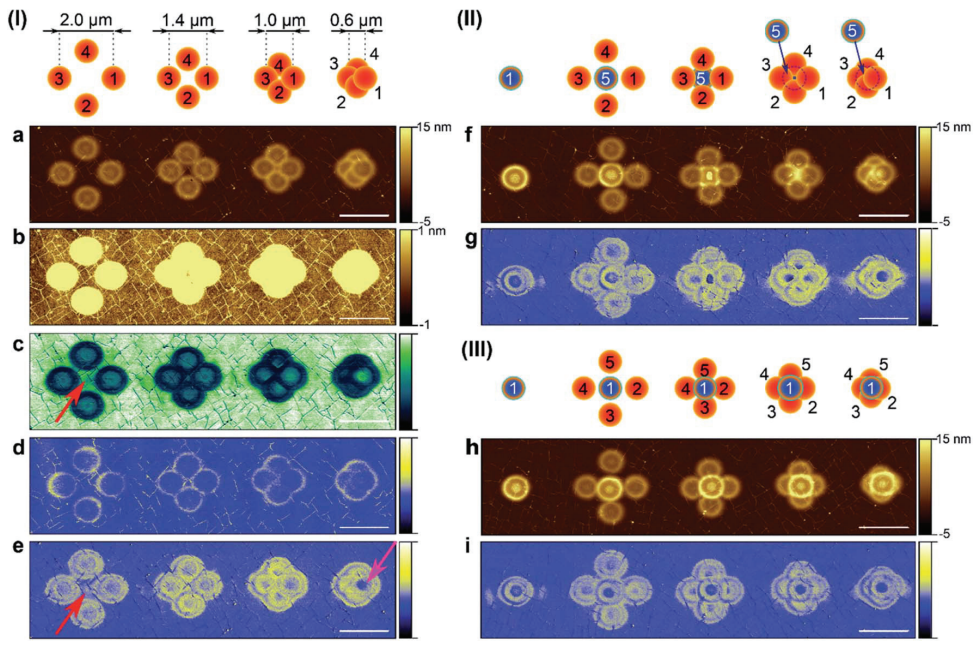

Fig. 5 Schemes I–III present complex patterning with marked order of irradiation. In schemes I and II, blisters with 10 s exposure per spot (orange circles) were prepared first. In scheme III, a blister with longer exposure was irradiated first (60 s, blue circle). All blisters were prepared with 60 pJ pulse energy. Topography AFM images of obtained patterns with (a, f and h) full and (b) reduced colour scale, and corresponding (c) adhesion, (d) deformation and (e, g and i) DMT modulus data. Scale bar 2 μm. Red arrows point at changes in adhesion and DMT modulus channels which occur between irradiated spots. Pink arrow points at reduced rigidity over the firstly created blister.

the volume expansion percentage of the second blister when it overlaps with another one, % V_{II}, compared to the volumes at no overlap, V_{B1} and V_{B2}, using the definition:

$$\%\ V_{II} = \frac{V_{total} - V_{B1}}{V_{B2}} \times 100\% \quad (4)$$

The percentage of area that it occupies, % $Area_{II}$, was calculated from:

$$\%\ Area_{II} = \frac{Area_{B2} - Area_{ISC}}{Area_{B2}} \times 100\% \quad (5)$$

The percentage of V_{II} and $Area_{II}$ as a function of Δx is presented in Fig. 3f and g, respectively. Even though both values decrease with increasing overlap, the ratio between % V_{II} and % $Area_{II}$ increases (Fig. 3h). This indicates that smaller separation leads to a greater height in the second blister, observed as a bulging/squeezing effect. These results suggest that further decrease of Δx would lead to even more pronounced bulging.

The optical forging concept can be further expanded. In Fig. 4, trimer formation is presented. The third laser exposure was located in the center of the previously created dimer. Third laser exposure does not affect formerly created blisters, which can be seen in the horizontal cross-section. The profiles of the exterior blisters are unchanged. The bulging effect of the third blister can be observed in vertical and horizontal cross-sections when $\Delta x = 1.0$ μm.

The schematic illustration of a tetramer created with varying beam separation distances is presented in scheme I in Fig. 5. Each blister was irradiated for 10 s per spot. Topography measurements for experimentally obtained patterns together with collected nanomechanical properties are shown in Fig. 5a to e. The four-step irradiation with 2 μm separation between facing blisters reveals that adhesion and stiffness were modified beyond the blister area (see red arrows in Fig. 5c and e). When the beam separation gets smaller, the forged blisters start to overlap, following the rule of not changing the overall shape of the previously created blister. However, its nanomechanical properties can be changed. For example, when $\Delta x = 0.6$ μm, the central part of the firstly forged blister became less rigid in comparison to the remaining forged shape. This is visible as a blue center on the DMT modulus channel, pointed with a pink arrow in Fig. 5e. This could be related to the different defect concentration over the area exposed to multiple irradiation or increased stress accumulation in the material.

The fifth irradiation for 60 s in the center of the created tetramer is presented in Fig. 5f and schematically presented in scheme II. When the distance between the first and third exposures, Δx_{1-3}, is 2 μm, the fifth blister looks as if it does not overlap with anything. Further decrease in beam separation produces a peculiar pattern. An increasing overlap confines the fifth blister to the remaining small area of pristine graphene

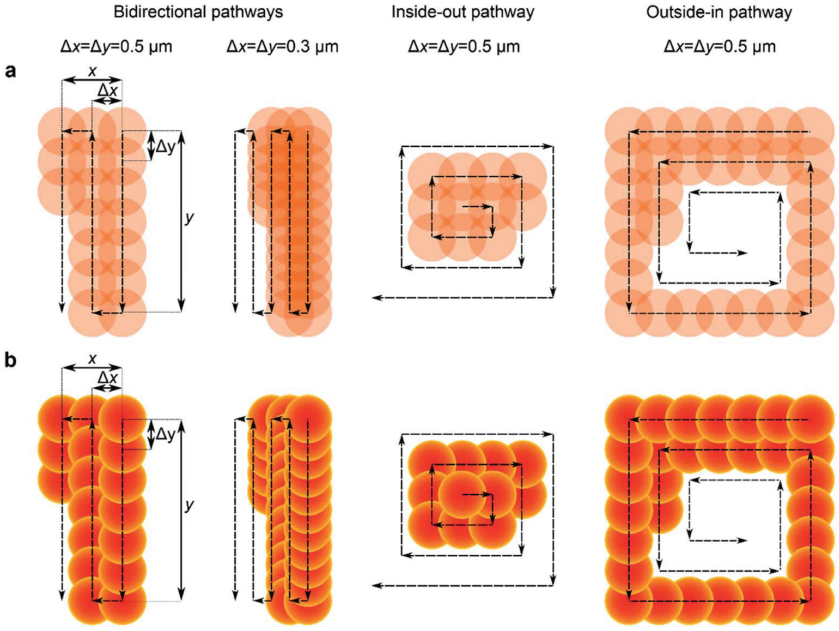

Fig. 6 (a) Illustration of focused laser beam positions during optical forging with the beam following bidirectional, inside-out and outside-in pathways, with equal horizontal (Δx) and vertical (Δy) spacing between laser spots. Arrows indicate the direction of optical forging. The accumulation of dose occurs in the intersecting beam area. (b) Illustration of patterns created with a ring-like blister with $D = 0.8$ μm for pathways and separation distance as in (a). Each new blister is created without changing the profile of the previously created structure. Yellow colour indicates a higher part of the blister.

and the outer side of the earlier forged blisters. This corresponds to the blister part which shows the highest deformation. For Δx_{1-3} of 1.4 and 1.0 μm, the created pattern in the center of the tetramer does not exhibit a ring shape, but it adjusts to the available free space. Further decreasing the distance between the spots leads to forging over the central part of the first blister, which was shown to be less stiff. On the other hand, when the first blister was irradiated for 60 s (scheme III and corresponding pattern in Fig. 5h), the consecutive four laser exposures did not change its volume expansion, even when the overlap between the first and the fifth blister becomes significant. A comparison of all collected AFM data is presented in Fig. S7.† These findings show how crucial the suitable choice of exposure order is, as well as the position of the laser beam in creation of a desired 3D structure.

In Fig. 6a we present optical forging following pre-programmed irradiation pathways along x and y directions. We tested three scanning directions: bidirectional, inside-out and outside-in, for which schematic illustrations are presented in Fig. 6a. Inside-out and outside-in pathways follow the squared spiral shape in the clockwise and counterclockwise direction, respectively. By decreasing the horizontal (Δx) and vertical (Δy) spacing between laser spots, the overlap between them increases in all writing pathways. A higher overlap leads to multiple exposures over the intersecting area.

The gained knowledge of blister formation and dimer overlap allowed us to predict the shape of more complex patterns. The schematic illustrations of the predicted patterns following the pre-programmed laser pathway are presented in Fig. 6b. The patterns were formed by overlapping multiple circles that mimic the shape of a single blister formed by chosen irradiation dose. Blister overlaps were done by considering that consecutive laser exposure does not change the profile of already existing blisters. Hence, in design each new spot 'hides' below the previously forged blisters. Larger blisters will produce larger overlap, causing changes in the outcome of the pattern. The prediction is that the shape of sub-diffraction features closely depends on the laser scan direction and separation between the laser spots.

A proof of principle of creating versatile 3D patterns is presented in Fig. 7. We prepared 3 sets of 4 patterns ($x = y = 3$ μm), each following a different writing path: bidirectional, inside-out or outside-in. Patterns were created using 100 pJ pulse energy and 10 s irradiation time per spot. Each shape was formed with constant laser spot separation $\Delta x = \Delta y$, which was set between 1 μm and 0.1 μm. The optically forged patterns fully resemble the predicted designs. Large step size formed single blisters, which are building blocks for the bigger structure. By decreasing the step size ($\Delta x = \Delta y = 0.3$; 0.5 μm), partial overlap of the blisters was obtained. The idea of a blister not building up over previously formed blisters is beyond doubt visible in experimentally obtained 3D structures. We were also able to write patterns with feature sizes much below the diffraction limit. Patterns created with different irradiation times and

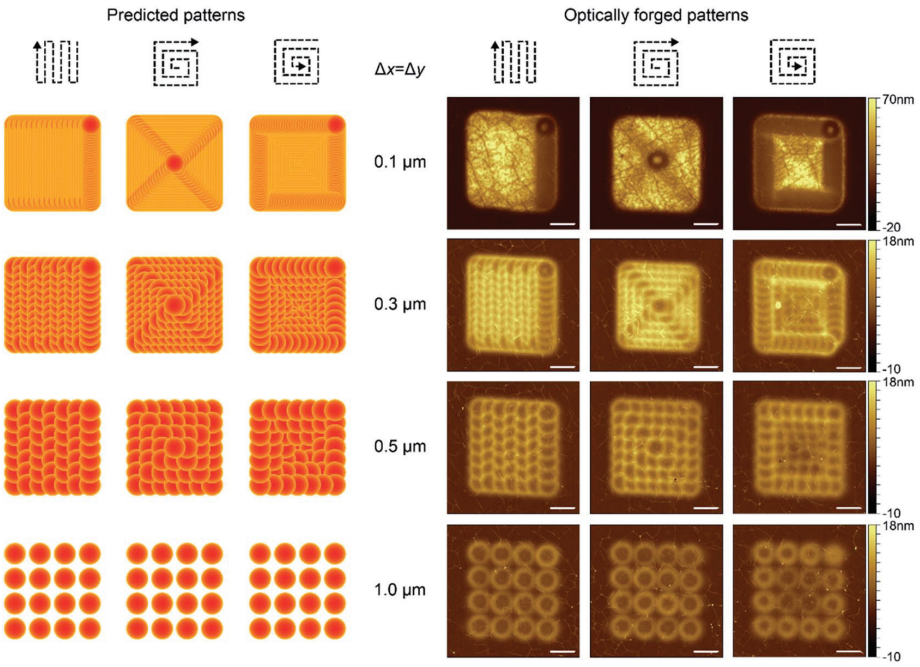

Fig. 7 Predicted shapes (left) and AFM images of optically forged patterns (right) created by following bidirectional, inside-out and outside-in writing pathways. Patterns were prepared with 100 pJ pulse energy and 10 s irradiation time per spot. The horizontal and vertical separations between laser spots were constant, $\Delta x = \Delta y = 0.1$; 0.3; 0.5 and 1 μm. Scale bar 1 μm.

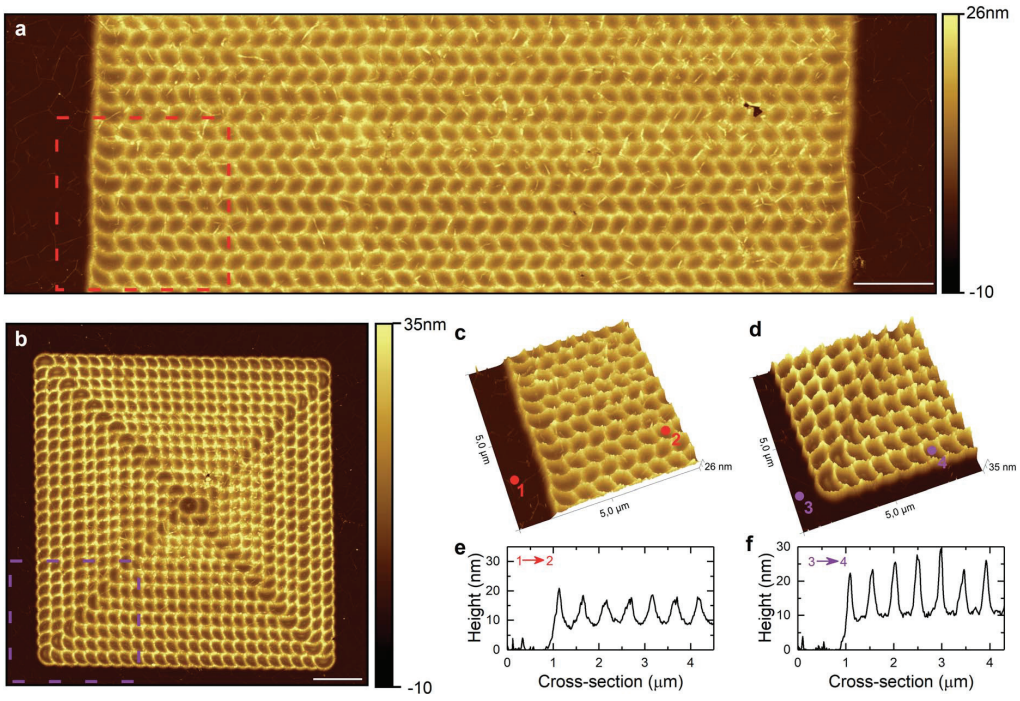

Fig. 8 AFM height images of optically forged graphene prepared with a $\Delta x = \Delta y = 0.5$ μm separation distance between laser spots. Patterns were prepared using 80 pJ pulse energy and (a) the bidirectional pathway with 30 s irradiation time per spot and (b) the inside-out pathway with 60 s irradiation time per spot. Scale bar 2 μm. 3D image of the zoomed area marked by dashed (c) red and (d) purple frames. Cross-section measured between points (e) 1–2 and (f) 3–4.

pulse energies are presented in Fig. S8 and S9,† respectively. Longer irradiation times create taller structures with more pronounced sharp features. The highest used overlap ($\Delta x = \Delta y = 0.1$ μm) exhibits pronounced bulging effects which allowed us to form elevated, flat-top 3D shapes. The height of the structures can be controlled by the laser dose.[21] A square plateau, bulging to the height of 70 nm, was formed with a bidirectional pathway and 0.1 μm separation distance, consisting of 961 highly overlapping laser spots. This shows that low pulse fluences used in optical forging allow a 3D texturing of the irradiated surface instead of removing it, even when a high spatial density of laser exposures is used. This is in contrast to the traditional micromachining, where multiple exposures over the same area usually trigger lowering of the modification threshold. As a consequence, this yields a faster ablation over the intersecting area.[42]

The writing direction plays a crucial role in pattern formation and shaping of sub-micrometer features. Patterns produced by the outside-in pathway follow shape predictions, however, their central parts exhibit lower heights than the patterns created by other routes. Perhaps it is due to the changing strain conditions of the enclosed graphene surface, resulting in a modified optical forging rate.

The geometrical structure for larger Δx may seem similar to the patterns prepared by typical micromachining, however this is misleading. For example, complex two-dimensional patterning could be compared with the production of amorphous micro-structures in crystalline Si wafer.[43] There the structures are formed slightly below the non-irradiated surface. They are created by melting and consecutive solidification with a small fraction of the material evaporating. Most of the traditional micromachining processes are focused on material removal, and therefore holes are produced. In our case we fabricate elevated blisters using low fluences.

Patterning by optical forging can be scaled up. In Fig. 8a and b we present AFM height images of the larger periodic patterns created with spot separation $\Delta x = \Delta y = 0.5$ μm using bidirectional and inside-out irradiation pathways, respectively. The 3D perspective of zoomed regions of optically forged structures is presented in Fig. 8c and d. The repeatable patterns with the same separation of 0.5 μm are observed, with sub-diffraction limited features exhibiting FWHM = 170 nm and FWHM = 110 nm for bidirectional and inside-out pathways, respectively (Fig. 8e and f).

We observed that 3D shaping of bilayer/multilayer graphene is also possible using optical forging (data not shown).

Conclusions

We have demonstrated a reproducible, mask-free method to pattern graphene using femtosecond laser pulses. Using low peak fluences we textured the graphene surface without either ablating it or deforming the underlying Si/SiO_2 substrate. We have shown that the well-established micromachining equations used in ablation studies can be used to calculate the modification threshold and incubation coefficient for 3D shaped graphene, fabricated using optical forging. Single pulse modification threshold fluence was estimated to 8.3 mJ cm^{-2}, which is an order of magnitude smaller than the single-pulse ablation thresholds for graphene and 100 nm SiO_2 on the Si substrate.

Direct laser writing also changes the mechanical properties of the irradiated regions such as adhesion and stiffness. The choice of exposure parameters (*e.g.* pulse energy, irradiation time) controls the level of material modification and shape of created blisters. We showed that knotty patterns can be designed and then experimentally obtained by controlling:

(a) size of the blister created with a specific laser dose,

(b) separation distance between consecutive laser spots,

(c) the irradiation pathway, following the rule of thumb that each new laser exposure will not change the overall shape of previously formed patterns. Our findings indicate that beam shaping would lead to even more complex 3D pattern formations. Optical forging has great potential for strain engineering of graphene, and possibly other atomically-thin materials.[22] It may be a method to shape nanomaterials for applications such as nanoscale scaffolds, novel microelectromechanical systems (MEMS),[44] quantum emitters,[45] trapping of surface plasmons,[46] and use in plasmonic field enhancement.[47,48]

Conflicts of interest

There are no conflicts to declare.

Acknowledgements

V.-M. H. acknowledges funding from the Finnish Cultural Foundation. M. P. acknowledges funding from the Academy of Finland (grant 311330).

Notes and references

1 R. R. Gattass and E. Mazur, *Nat. Photonics*, 2008, **2**, 219–225.
2 Y.-L. Zhang, Q.-D. Chen, H. Xia and H.-B. Sun, *Nano Today*, 2010, **5**, 435–448.
3 G. H. Han, S. J. Chae, E. S. Kim, F. Güneş, I. H. Lee, S. W. Lee, S. Y. Lee, S. C. Lim, H. K. Jeong, M. S. Jeong and Y. H. Lee, *ACS Nano*, 2011, **5**, 263–268.
4 J. Lu, J. H. Lu, H. Liu, B. Liu, K. X. Chan, J. Lin, W. Chen, K. P. Loh and C. H. Sow, *ACS Nano*, 2014, **8**, 6334–6343.
5 A. Venkatakrishnan, H. Chua, P. Tan, Z. Hu, H. Liu, Y. Liu, A. Carvalho, J. Lu and C. H. Sow, *ACS Nano*, 2017, **11**, 713–720.
6 V. Shautsova, S. Sinha, L. Hou, Q. Zhang, M. Tweedie, Y. Lu, Y. Sheng, B. F. Porter, H. Bhaskaran and J. H. Warner, *ACS Nano*, 2019, **13**, 14162–14171.
7 G. Kalita, L. Qi, Y. Namba, K. Wakita and M. Umeno, *Mater. Lett.*, 2011, **65**, 1569–1572.
8 W. Zhang, L. Li, Z. B. Wang, A. A. Pena, D. J. Whitehead, M. L. Zhong, Z. Lin and H. W. Zhu, *Appl. Phys. A*, 2012, **109**, 291–297.
9 R. Sahin, S. Akturk and E. Simsek, *Appl. Phys. A*, 2014, **116**, 555–560.
10 R. Sahin, E. Simsek and S. Akturk, *Appl. Phys. Lett.*, 2014, **104**, 053118.
11 T. Dong, M. Sparkes, C. Durkan and W. O'Neill, *J. Laser Appl.*, 2016, **28**, 022202.
12 A. Gil-Villalba, R. Meyer, R. Giust, L. Rapp, C. Billet and F. Courvoisier, *Sci. Rep.*, 2018, **8**, 14601.
13 E. J. Richman, Y.-T. Chou, Y. Deng, L. Kaelbling, Z. Liang, G. McAlaine, C. Miller, M. Selesnick, C. N. LaFratta and P. Cadden-Zimansky, *Opt. Mater. Express*, 2019, **9**, 3871–3877.
14 B. Wetzel, C. Xie, P.-A. Lacourt, J. M. Dudley and F. Courvoisier, *Appl. Phys. Lett.*, 2013, **103**, 241111.
15 V. Strong, S. Dubin, M. F. El-Kady, A. Lech, Y. Wang, B. H. Weiller and R. B. Kaner, *ACS Nano*, 2012, **6**, 1395–1403.
16 J. Koivistoinen, L. Sládková, J. Aumanen, P. Koskinen, K. Roberts, A. Johansson, P. Myllyperkiö and M. Pettersson, *J. Phys. Chem. C*, 2016, **120**, 22330–22341.
17 A. Johansson, H.-C. Tsai, J. Aumanen, J. Koivistoinen, P. Myllyperkiö, Y.-Z. Hung, M.-C. Chuang, C.-H. Chen, W. Y. Woon and M. Pettersson, *Carbon*, 2017, **115**, 77–82.
18 M. F. El-Kady and R. B. Kaner, *ACS Nano*, 2014, **8**, 8725–8729.
19 A. Johansson, P. Myllyperkiö, P. Koskinen, J. Aumanen, J. Koivistoinen, H.-C. Tsai, C.-H. Chen, L.-Y. Chang, V.-M. Hiltunen, J. J. Manninen, W. Y. Woon and M. Pettersson, *Nano Lett.*, 2017, **17**, 6469–6474.
20 P. Koskinen, K. Karppinen, P. Myllyperkiö, V.-M. Hiltunen, A. Johansson and M. Pettersson, *J. Phys. Chem. Lett.*, 2018, **9**, 6179–6184.
21 V.-M. Hiltunen, P. Koskinen, K. K. Mentel, J. Manninen, P. Myllyperkiö, A. Johansson and M. Pettersson, *J. Phys. Chem. C*, 2020, **124**, 8371–8377.
22 Z. Dai, L. Liu and Z. Zhang, *Adv. Mater.*, 2019, **31**, 1805417.
23 J. W. Suk, A. Kitt, C. W. Magnuson, Y. Hao, S. Ahmed, J. An, A. K. Swan, B. B. Goldberg and R. S. Ruoff, *ACS Nano*, 2011, **5**, 6916–6924.
24 J. M. Liu, *Opt. Lett.*, 1982, **7**, 196–198.
25 Y. Jee, M. F. Becker and R. M. Walser, *J. Opt. Soc. Am. B*, 1988, **5**, 648–659.
26 P. Mannion, J. Magee, E. Coyne, G. O'Connor and T. Glynn, *Appl. Surf. Sci.*, 2004, **233**, 275–287.
27 F. Di Niso, C. Gaudiuso, T. Sibillano, F. P. Mezzapesa, A. Ancona and P. M. Lugarà, *Opt. Express*, 2014, **22**, 12200.
28 A. Rosenfeld, M. Lorenz, R. Stoian and D. Ashkenasi, *Appl. Phys. A*, 1999, **69**, 373–376.
29 D. M. A. Mackenzie, J. D. Buron, P. R. Whelan, B. S. Jessen, A. Silajdźić, A. Pesquera, A. Centeno, A. Zurutuza, P. Bøggild and D. H. Petersen, *2D Mater.*, 2015, **2**, 045003.

30 A. Roberts, D. Cormode, C. Reynolds, T. Newhouse-Illige, B. J. LeRoy and A. S. Sandhu, *Appl. Phys. Lett.*, 2011, **99**, 051912.
31 A. Vasquez, P. Samolis, J. Zeng and M. Y. Sander, *OSA Continuum*, 2019, **2**, 2925–2934.
32 H. O. Jeschke, M. E. Garcia and K. H. Bennemann, *Phys. Rev. Lett.*, 2001, **87**, 015003.
33 T. Rublack and G. Seifert, *Opt. Mater. Express*, 2011, **1**, 543–550.
34 J. Bonse, S. Baudach, J. Krüger, W. Kautek and M. Lenzner, *Appl. Phys. A*, 2002, **74**, 19–25.
35 J. P. McDonald, V. R. Mistry, K. E. Ray, S. M. Yalisove, J. A. Nees and N. R. Moody, *Appl. Phys. Lett.*, 2006, **88**, 153121.
36 J. Sladek and I. M. Mirza, *MM Sci. J.*, 2019, **2019**, 3579–3584.
37 J. Thorstensen and S. Erik Foss, *J. Appl. Phys.*, 2012, **112**, 103514.
38 B. V. Derjaguin, V. M. Muller and Y. P. Toporov, *J. Colloid Interface Sci.*, 1975, **53**, 314–326.
39 W.-K. Lee, J. Kang, K.-S. Chen, C. J. Engel, W.-B. Jung, D. Rhee, M. C. Hersam and T. W. Odom, *Nano Lett.*, 2016, **16**, 7121–7127.
40 D. G. Kvashnin and P. B. Sorokin, *J. Phys. Chem. Lett.*, 2015, **6**, 2384–2387.
41 A. Zandiatashbar, G.-H. Lee, S. J. An, S. Lee, N. Mathew, M. Terrones, T. Hayashi, C. R. Picu, J. Hone and N. Koratkar, *Nat. Commun.*, 2014, **5**, 3186.
42 S. Xiao, E. L. Gurevich and A. Ostendorf, *Appl. Phys. A*, 2012, **107**, 333–338.
43 Y. Fuentes-Edfuf, M. Garcia-Lechuga, D. Puerto, C. Florian, A. Garcia-Leis, S. Sanchez-Cortes, J. Solis and J. Siegel, *Appl. Phys. Lett.*, 2017, **110**, 211602.
44 X. Fan, A. D. Smith, F. Forsberg, S. Wagner, S. Schröder, S. S. A. Akbari, A. C. Fischer, L. G. Villanueva, M. Östling, M. C. Lemme and F. Niklaus, *Microsyst. Nanoeng.*, 2020, **6**, 17.
45 C. Palacios-Berraquero, D. M. Kara, A. R. P. Montblanch, M. Barbone, P. Latawiec, D. Yoon, A. K. Ott, M. Loncar, A. C. Ferrari and M. Atatüre, *Nat. Commun.*, 2017, **8**, 15093.
46 D. Smirnova, S. H. Mousavi, Z. Wang, Y. S. Kivshar and A. B. Khanikaev, *ACS Photonics*, 2016, **3**, 875–880.
47 M. Miscuglio, D. Spirito, R. P. Zaccaria and R. Krahne, *ACS Photonics*, 2016, **3**, 2170–2175.
48 K. Agarwal, C. Dai, D. Joung and J.-H. Cho, *ACS Nano*, 2019, **13**, 1050–1059.

Electronic Supplementary Material (ESI) for Nanoscale Advances.

Shaping graphene with optical forging: from single blister to complex 3D structures

Kamila K. Mentel[a], Jyrki Manninen[b], Vesa-Matti Hiltunen[b], Pasi Myllyperkiö[a], Andreas Johansson[a,b‡], Mika Pettersson[†a]

[a] Nanoscience center, Department of Chemistry, University of Jyväskylä, Finland

[b] Nanoscience center, Department of Physics, University of Jyväskylä, Finland

Reproducibility

Precise control of laser exposure combined with piezo scanning allow us to fabricate reproductible patterns with great precision. In Figure S1 matrices of blisters formed upon irradiation with 80 pJ pulse energy and different irradiation times are presented. Blisters in each matrix resemble each other. These examples show the possibility of scaling up 3D direct writing process. However, one should bear in mind that for high quality patterning steady system is required.

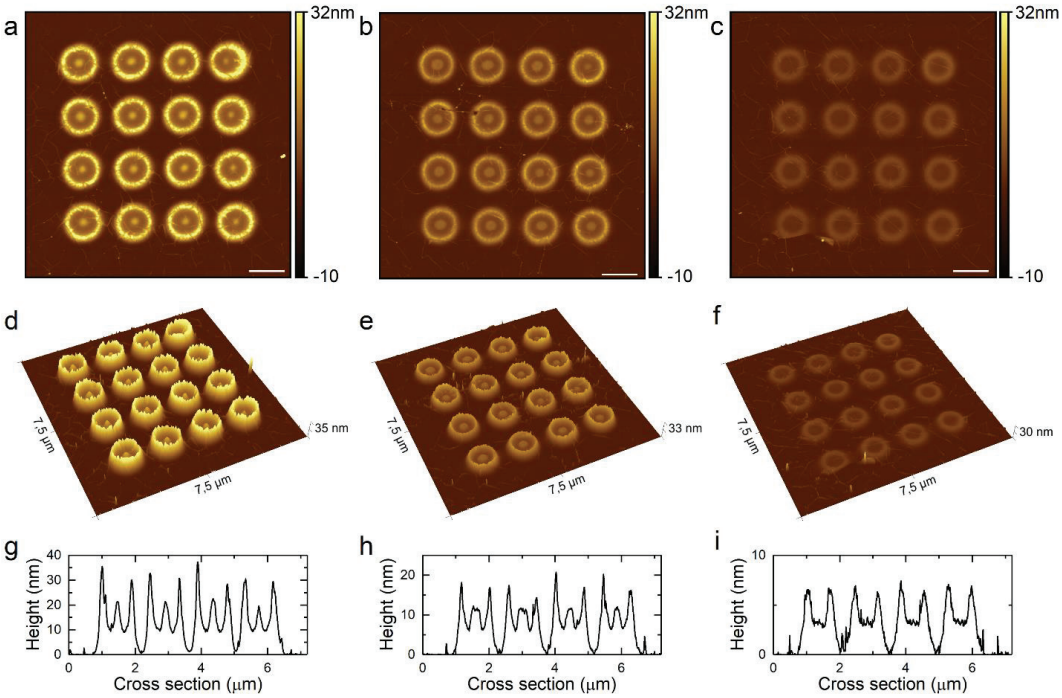

Figure S1. AFM (a, b, c) height images and (d, e, f) 3D view images of matrixes of blisters prepared with 80 pJ pulse energy, 1.5 µm separation between consecutive laser spots, and constant irradiation time: (a, d) 180, (b, e) 60 and (c, f) 10 s per spot. Scale bar 1 µm. Cross section measured through the central part of blisters in third row for dose: (g) 180, (h) 60 and (i) 10 s per spot.

Lateral cross section of forged blisters

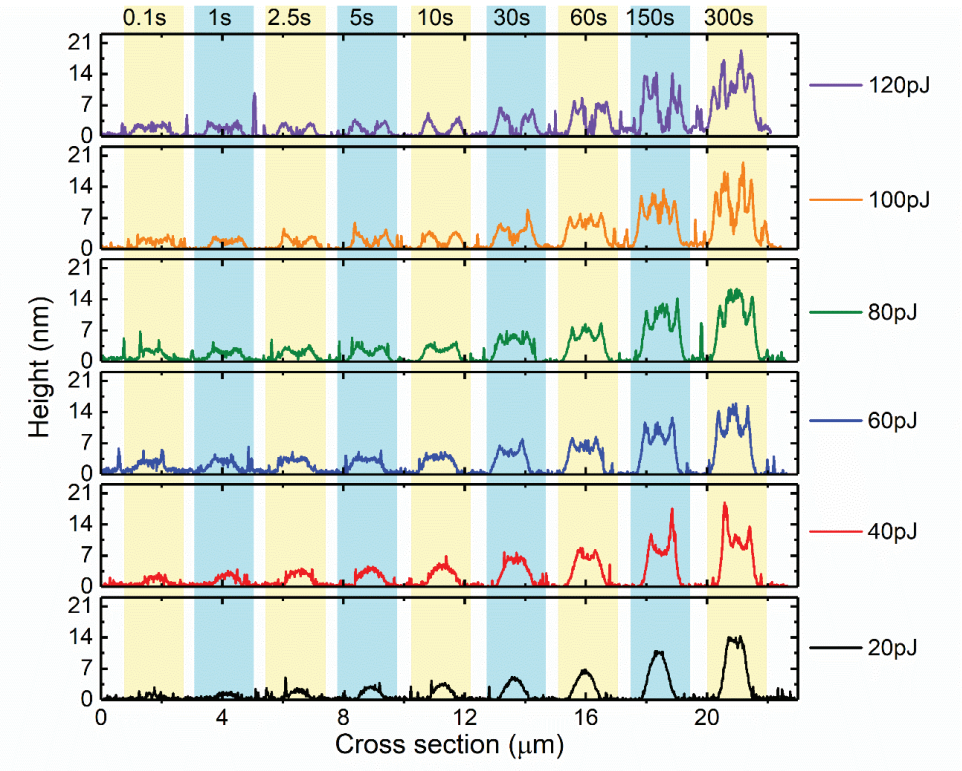

Figure S2. Cross section taken from AFM height image of blisters presented in Figure 1a.

Raman spectroscopy studies

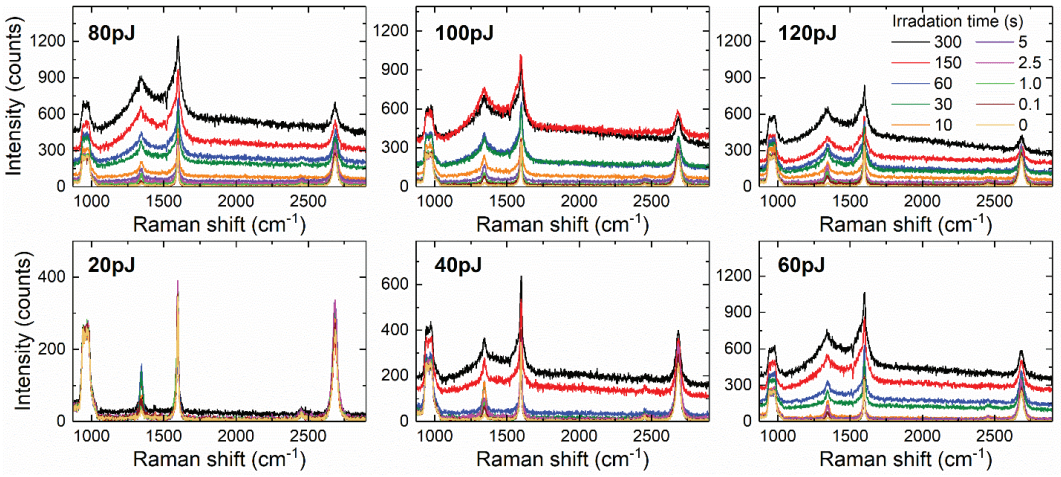

Figure S3. Raman spectra collected for blisters with different irradiation times, grouped by used pulse energies. Excitation wavelength: 515 nm.

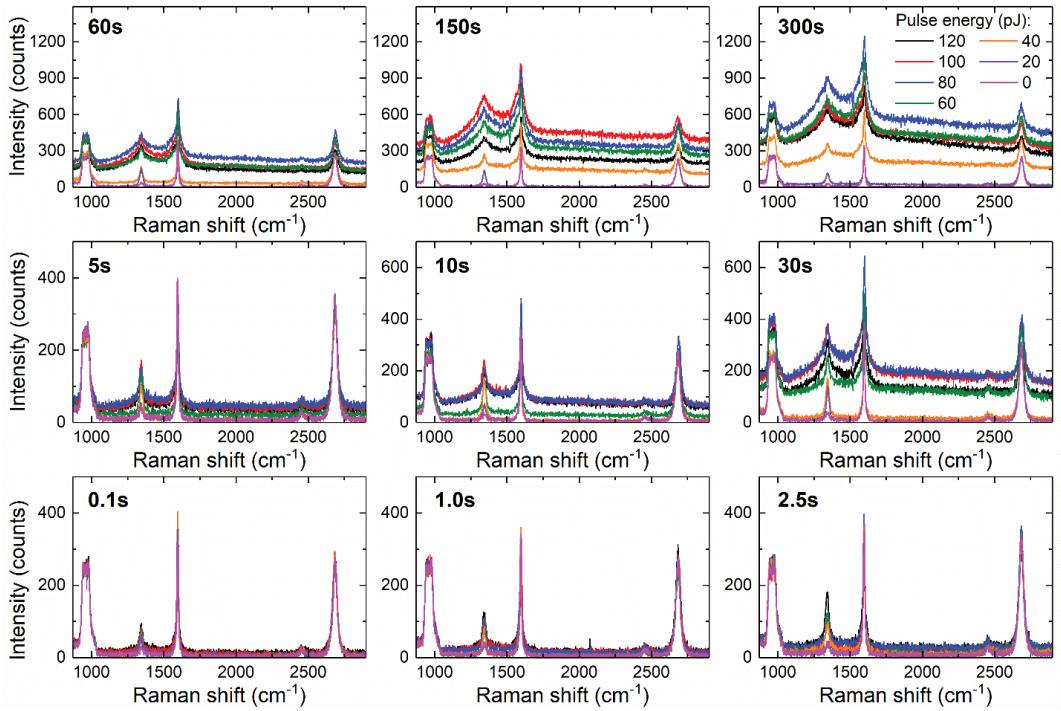

Figure S4. Raman spectra collected for blisters produced with various pulse energies, grouped by used irradiation time. Excitation wavelength: 515 nm.

Oxygen plasma etching

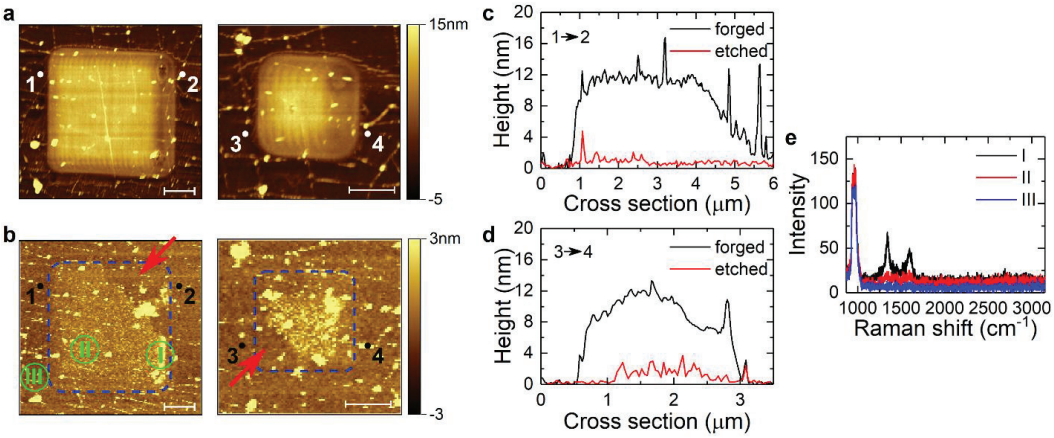

Figure S5. AFM images of optically forged squares (a) before and (b) after O_2 plasma etching. Squares were prepared with 60pJ and 1s irradiation time per spot. Scale bar 1 μm. Red arrows point completely removed optically forged features, and intact substrate surface. Blue dashed frame is added to guide eye to the contour of forged square. Cross section of forged blisters before and after etching taken between points (c) 1-2 and (d) 3-4. (e) Raman spectra collected after O_2 plasma etching in the places indicated at (b), showing a presence of small amount of the amorphous carbon.

AFM channels

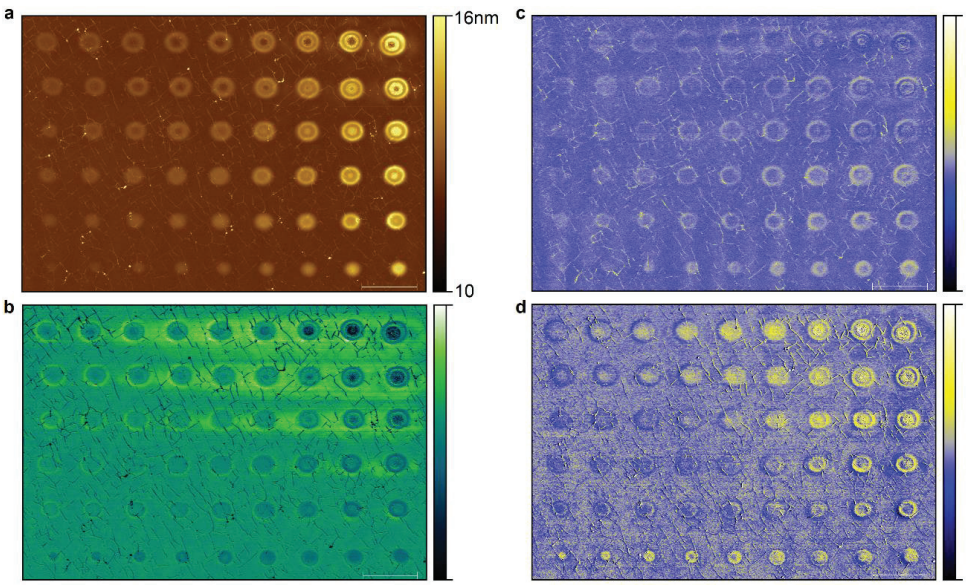

Figure S6. (a) Topography height image of blisters and corresponding (b) adhesion, (c) deformation, and (d) elastic modulus (DMT) channels. Scale bar 3 μm.

Tetramer and pentamer

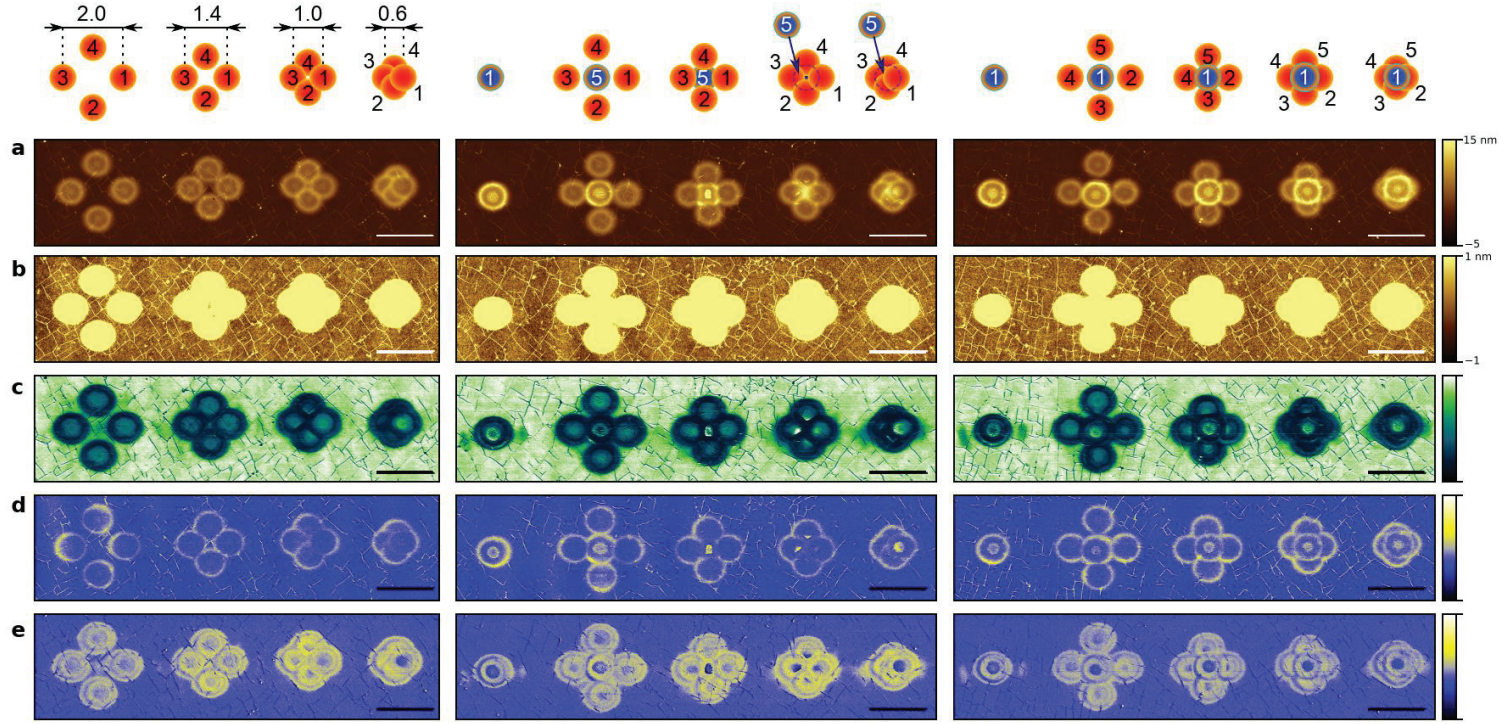

Figure S7. Schemes of complex patterning, with marked order of irradiation. On the left and center, first blisters with 10 s exposure per spot (orange circles) were prepared. On right blister with longer exposure was irradiated first (60 s, blue circle). All blisters were created using 60pJ pulse energy. Topography AFM images of obtained patterns with full (a) and reduced (b) color scale, and corresponding adhesion (c), deformation (d) and DMT modulus (e) channels. Scale bar 2 µm.

Complex structures patterning

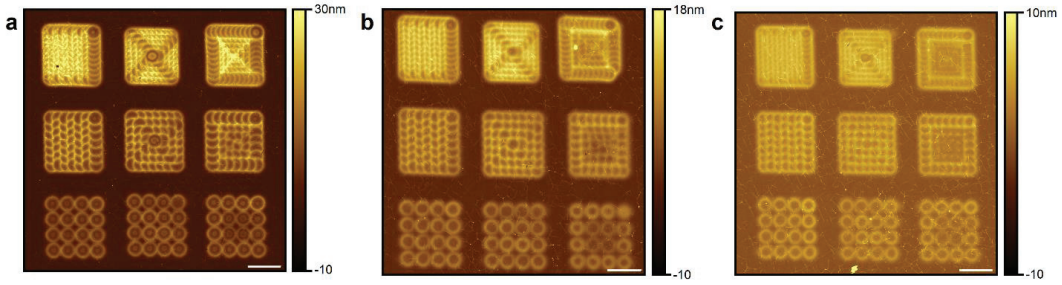

Figure 8. AFM height images of patterns prepared with 100 pJ pulse energy and (a) 30 s, (b) 10 s and (c) 2.5 s irradiation time per spot. Patterns were prepared with 0.3 µm (top row), 0.5 µm (middle row) and 1.0 µm (bottom row) separation distance between the laser spots. Left, central and right columns correspond to the bidirectional, inside-out and outside-in pathways, respectively. Scale bar 1 µm.

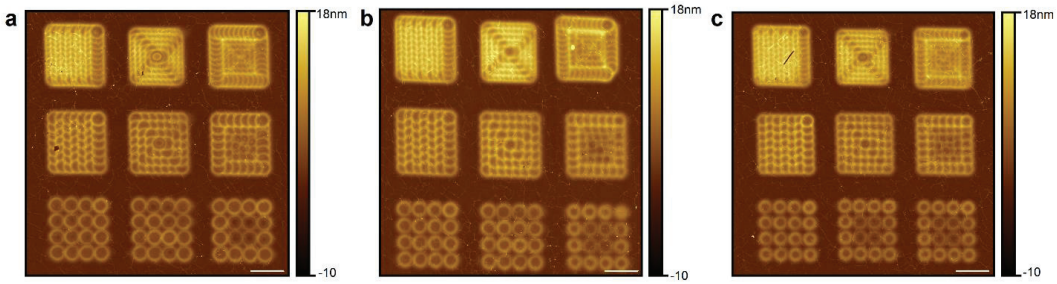

Figure 9. AFM height images of patterns prepared with 10 s irradiation time per spot and (a) 120 pJ, (b) 100 pJ and (c) 80 pJ pulse energy. Patterns were prepared with 0.3 µm (top row), 0.5 µm (middle row) and 1.0 µm (bottom row) separation distance between the laser spots. Left, central and right columns correspond to the bidirectional, inside-out and outside-in pathways, respectively. Scale bar 1 µm.

AIV

MAKING GRAPHENE LUMINESCENT BY DIRECT LASER WRITING

by

Vesa-Matti Hiltunen, Pekka Koskinen, Kamila Mentel, Jyrki Manninen, Pasi Myllyperkiö, Andreas Johansson, Mika Pettersson 2020

The Journal of Physical Chemistry C, 124, 15, 8371-8377

DOI: 10.1021/acs.jpcc.0c00194

THE JOURNAL OF PHYSICAL CHEMISTRY C

pubs.acs.org/JPCC Article

Making Graphene Luminescent by Direct Laser Writing

Vesa-Matti Hiltunen, Pekka Koskinen, Kamila K. Mentel, Jyrki Manninen, Pasi Myllyperkiö, Andreas Johansson,* and Mika Pettersson*

Cite This: J. Phys. Chem. C 2020, 124, 8371−8377 Read Online

ACCESS | Metrics & More | Article Recommendations | Supporting Information

ABSTRACT: Graphene is not intrinsically luminescent due to a lack of band gap, and methods for its creation are tricky for device fabrication. In this study, we create luminescent graphene patterns by a simple direct laser writing method. We analyze the graphene using Raman spectroscopy and find that the laser writing leads to generation of line defects after initial formation of point defects. This Raman data enables us to create a model that explains the luminescence by a formation of small domains due to confinement of graphene by line defects, which is conceptually similar to the mechanism of luminescence in graphene quantum dots.

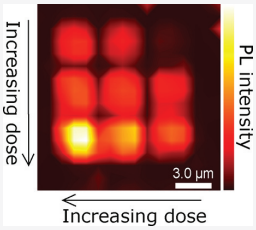

INTRODUCTION

Pristine graphene is not luminescent due to the absence of band gap and the rapid nonradiative relaxation of electrons and holes.[1−4] However, there are methods to obtain broadband luminescence from graphene. For instance, the luminescence can arise from graphene under high doping conditions,[5] from graphene oxide,[6−8] and from graphene quantum dots (GQDs).[9−12] While the luminescence can be obtained by these means, their implementation to devices is not straightforward. Therefore, it would be highly beneficial to find other, more practical means to locally modify graphene to achieve luminescent properties.

Fortunately, the properties of graphene can be modified by laser irradiation.[13−17] Laser modification is simple, it omits chemicals, and it enables writing patterns. For example, femtosecond laser irradiation can be used to oxidize graphene without losing the integrity of the carbon network.[18] When irradiation is carried out under inert gas atmosphere, three-dimensional structures are formed in a process termed "optical forging".[19] The primary process responsible for optical forging is known to be the generation of defects, although the understanding of the process still remains incomplete.

In this work, we report that optically forged graphene exhibits unexpected strong photoluminescence. We study the origin of this irradiation-induced photoluminescence in graphene using Raman spectroscopy. It gives insight into the pulsed laser patterning process since it is sensitive to graphene's lattice defects,[20−24] doping levels,[5,25−32] and strain,[33−36] and with careful analysis, it is possible to differentiate these contributions from each other.[37−41] By combining the Raman measurements with theoretical modeling, we are able to develop a convincing model for the luminescence: it can be explained by formation of small domains due to confinement of graphene by line defects, which is conceptually similar to the mechanism of luminescence of graphene quantum dots.

EXPERIMENTAL SECTION

The graphene was synthesized with chemical vapor deposition (CVD) on a copper thin film and transferred onto a Si/SiO_x substrate using a normal PMMA transfer method.[42] The graphene was then patterned with a tightly focused femtosecond laser in nitrogen atmosphere by raster scanning the sample over the pulsed laser beam with a piezo stage. After the direct laser writing, the processed areas were characterized by atomic force microscope imaging and by Raman mapping. For details of the fabrication process, direct laser writing, and characterizations, see the Supporting Information.

RESULTS AND DISCUSSION

Experimental Observation of Luminescence. The result of the pulsed laser patterning is shown in Figure 1a. Each square pattern in the figure has a different exposure time per spot, and the heights of the patterns increase with increasing exposure time, as reported before.[19] Raman spectra from the middle of each square are shown in Figure 1b. The irradiation dose is an experimental parameter defined by multiplying the pulse energy with irradiation time per spot divided by spot size. This definition helps to compare results obtained with different pulse energies and/or exposure times. There are three notable developments in these Raman spectra

Received: January 8, 2020
Revised: March 13, 2020
Published: March 25, 2020

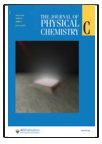

https://dx.doi.org/10.1021/acs.jpcc.0c00194
J. Phys. Chem. C 2020, 124, 8371−8377

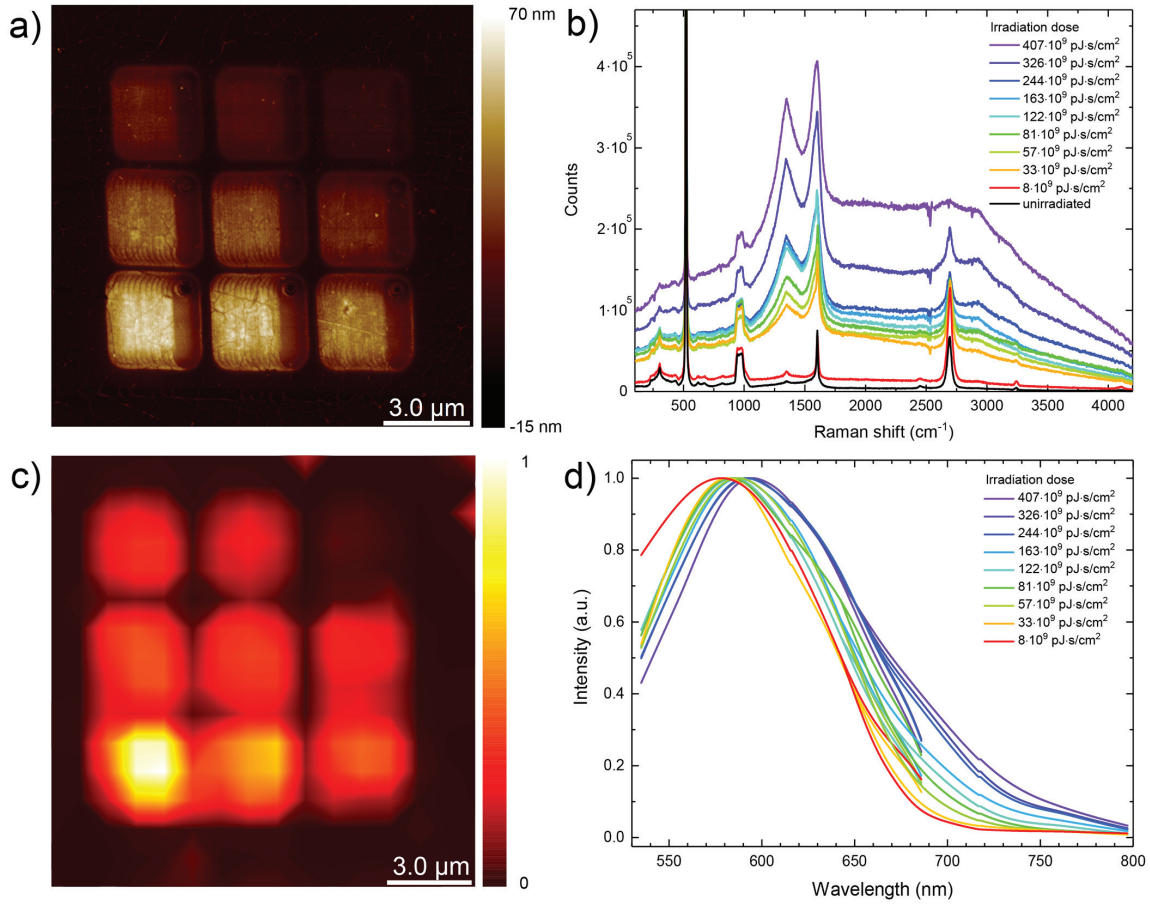

Figure 1. Characterization of the photoluminescent graphene patterns. (a) An atomic force microscopy image of a pattern set made with 160 pJ pulse energy. Exposure dose increases from up to down and right to left. Height of the patterns increase with the exposure dose. (b) Raman spectra from the middle of each pattern measured with a 532 nm excitation wavelength. (c) Photoluminescence map of the same patterns as in panel (a). The intensity is integrated between 1800 and 2500 cm^{-1} (588−614 nm). (d) Normalized PL spectra extracted from the Raman spectra in panel (b) and Figure S1c. The spectra are baselines from the asymmetric least squares smoothing process. The shorter wavelength part is extracted from Raman spectra measured with a 532 nm laser excitation and the long wavelength tail from a 633 nm excitation (Figure S1c).

as the irradiation dose increases. First, the 2D graphene Raman band intensity decreases, diminishing almost completely at the highest dose. Second, the D and G bands both broaden and increase in intensity. Third, there is an appearance of a wide photoluminescence signal. The intensity of the signal increases consistently with the increasing irradiation dose (Figures 1b,c). For example, at the highest dose in Figure 1b, the integrated intensity of the photoluminescence is over 400 times stronger than the G band intensity in unpatterned graphene. We extracted photoluminescence spectra from the Raman data (Figure 1d). These spectra showcase that the emission is very broad, extending nearly the entire visible range.

There are several reports of photoluminescence arising from different graphene-based materials. One of such materials is graphene oxide.[6−8] However, we have previously determined, based on X-ray photoelectron spectroscopy, that our laser written patterns contain only carbon.[19] Chen et al. observed a photoluminescence signal from graphene under high p-type doping, which empties the states in the valence band and enables a broadband emission.[5] Heller et al. assigned this photoluminescence to electronic Raman scattering.[43] We analyzed doping and strain of our samples from the shifts of G and 2D bands in Raman spectra (for details, see the Supporting Information). The analysis revealed that the doping levels in our samples are too low to create emission in the visible region via this mechanism.

Photoluminescence could arise also from graphene quantum dots. The spectral characteristics of some GQDs in the literature are at least qualitatively similar to the spectra in Figure 1d.[9−12] Should the cause of the photoluminescence in our samples be the formation of structures akin to quantum dots, the pulsed laser irradiation would have to form isolated graphene islands. We have determined previously that the pulsed laser irradiation does form lattice defects in graphene,[19] but here, the point- and line-type character of the defects are analyzed for the first time.

From Point to Line Defects. To get a more complete picture about the defect formation during the irradiation, we

https://dx.doi.org/10.1021/acs.jpcc.0c00194
J. Phys. Chem. C 2020, 124, 8371−8377

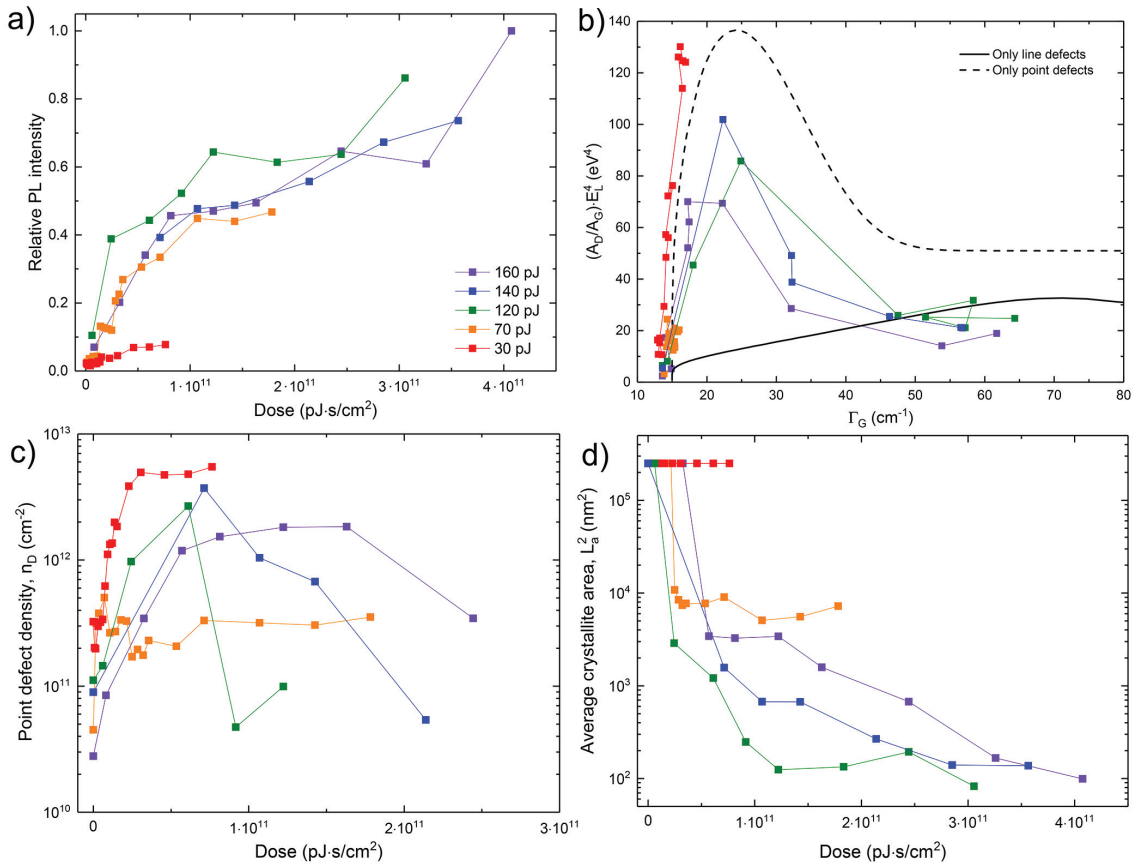

Figure 2. Defect development during pulsed laser irradiation. (a) Integrated photoluminescence intensity between 1800 and 2400 cm^{-1} divided by integrated intensity of the G band versus pulsed irradiation dose. (b) Experimental $(A_D/A_G)\cdot E_L^4$ as a function of Γ_G (lines with markers). The solid black line represents the case where graphene has only line defects and no point defects, and the dashed black line represents the opposite. (c) Point defect density versus irradiation dose. (d) Average crystallite area versus irradiation dose.

prepared four additional sets with pulse energies of 140, 120, 70, and 30 pJ, in addition to the pattern set made with 160 pJ pulse energy. Raman spectra measured from these patterns (presented in the Supporting Information) show that the abovementioned changes in the graphene Raman bands happen with all pulse energies as well as the increase of the broad photoluminescence. The photoluminescence intensities versus irradiation dose is presented in Figure 2a. The trend of intensity increase is similar with all the pulse energies, except with 30 pJ where the increase is more conservative. Also, the Raman peaks from these patterns show that there is a difference between lightly and heavily irradiated patterns. The intensity of the D band increases initially with a low irradiation dose, forming a sharp D peak. The sharpness of the D peak with low irradiation dose suggests that the irradiation initially creates point defects.[24] As the irradiation dose increases and the broad background signal starts to develop, the D band transforms to a wider and less intensive peak compared to the G peak. This indicates that the patterns made with a higher dose have higher amounts of line defects.[23,24]

To better understand the defect character, we estimated the amounts of point and line defects in pulsed laser patterned graphene following a model developed by Cançado et al.[24] (for details, see the Supporting Information). This model is based on point and line defects having different effects on the Raman spectra. The main difference is that, in general, the point defects increase the integrated intensity ratio of the D and G bands (A_D/A_G),[44] while line defects increase the full width at half-maximum of the G band (Γ_G) (Figure 2b).[23] The experimental values for A_D/A_G and Γ_G were acquired from fitting parameters, and the defect densities were calculated from eqs S1 and S2. Details about the fitting and defect calculations are presented in the Supporting Information.

Experimental data shows that the A_D/A_G ratio increases with all pulse energies, while the Γ_G increases further with higher pulse energies. Cançado's model enables calculating point defect densities and the crystallite sizes from the experimental data (Figures 2c,d). In unirradiated graphene, the point defect density is approximately 10^{11} cm^{-2} as is common for CVD graphene. The point defect density increases sharply during the early stages of the irradiation to the $1-5\cdot10^{12}$ cm^{-2} range and starts to decrease with higher doses. An outlier here is the 70 pJ case where the density with low doses saturates to about $2-3\cdot10^{11}$ cm^{-2}. The reason for this behavior is not clear.

https://dx.doi.org/10.1021/acs.jpcc.0c00194
J. Phys. Chem. C 2020, 124, 8371−8377

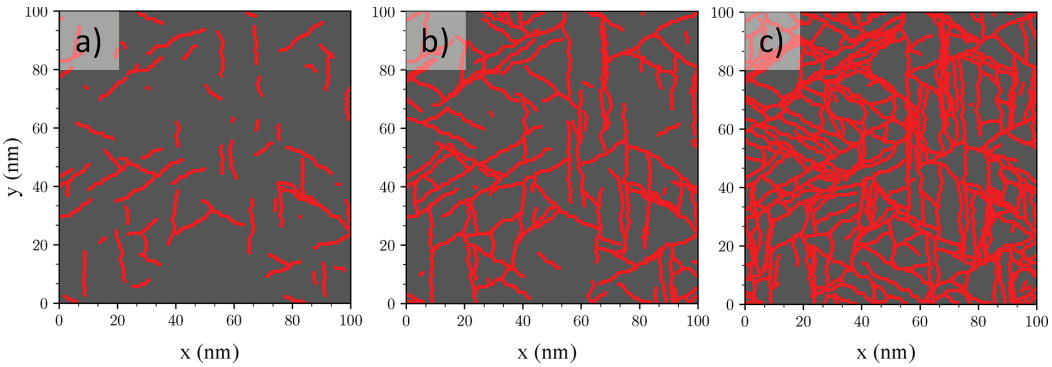

Figure 3. Appearance of line defect-defined crystallites. Panels show the temporal growth of Stone–Wales line defects with $\chi = 10^5$ and (a) $t = 12$, (b) $t = 24$, and (c) $t = 48$. The middle panel corresponds to the percolation time t_{perc} when the line defects reach continuously across the entire irradiated area.

However, since every data point in Figure 2 is from a different individual pattern, it is possible that there could be differences in the initial conditions of the graphene, such as defect or residue amounts, that would affect the defect formation process. For the three highest pulse energies, the points with highest doses are omitted. This omission is because they fall under the black solid line in Figure 2b, which produces unphysical results (point defect density falls below zero).

Yet, the most interesting analysis is the one of crystallite sizes (Figure 2d). Since CVD graphene typically has crystallites with size distribution from tens to hundreds of micrometers, the initial areas are large (Figure 2d). In fact, the crystallites are larger than the spot size of our Raman laser, making it impossible to estimate the crystallite sizes at low irradiation doses. The starting point of the crystallite sizes were therefore set to $2.5{\cdot}10^5$ nm^2, the estimated spot size of our Raman lasers. The crystallite size decreases sharply initially and continues to decrease with higher doses. The exception here is the 30 pJ pattern set where the crystallite size is too large to be measurable in Raman. This pattern set is also the only one where the photoluminescence does not increase significantly during the irradiation. Interestingly, as the crystallite sizes decreases, the point defect densities saturate and even start to decrease with higher doses (Figure 2c), suggesting a gradual conversion of point to line defects.

Insights for Defect Growth from a Mesoscopic Model. The implications from the analysis of Raman spectra trigger several questions. What is the microscopic structure of the defects? How are point and line defects related? What is the origin of the crystallites and their connection to luminescence?

To address these questions, we developed a model that is coherent and builds upon a plausible microscopic origin. We assume that the elementary event in the process is a laser-induced creation of Stone–Wales (SW) defects, as proposed earlier.[19] The SW defect is a 90°C C–C bond rotation that transforms four hexagons into pairs of pentagons and heptagons (Figure S8a). The formation energy of a single SW defect in pristine graphene is around 4.6 eV, given by the density functional theory.[45] This energy coincides well with a two-photon process ($2h\nu$ = 4.8 eV). While not directly indicated by our data, the notion of a two-photon process is plausible as it conforms with observations from similar experimental settings.[46] However, for our interests, the most important feature in SW defects is their strong attractive and highly anisotropic interaction. The interaction of two SW defects depends strongly on their exact orientation and separation. In particular, defects separated precisely by two lattice constants (4.9 Å) are bound almost by 1.5 eV (Supporting Information), which implies that laser irradiation presumably prefers creating new SW defects that conform to this favorable arrangement. This interaction motivated us to develop a kinetic defect growth model involving the formation of new SW defects (for model details, see the Supporting Information).

The only parameter in the model, χ, is the ratio between the probability for forming a new SW defect into any site in pristine graphene and the probability for forming new SW defects in the favorable sites. The energetics of SW interaction imply $\chi \ll 1$, but otherwise, χ is a free parameter; a smaller χ implies small density of long defects, and a larger χ implies high density of short defects.

Using the model, the defect growth kinematics was straightforward to simulate (for details, see the Supporting Information). Based on parameter values from earlier similar models,[18] we used a tentative parameter $\chi = 10^{-5}$ and propagated time onward, observing point defects appearing, then growing into line defects, gradually percolating across the entire area, and ultimately filling the area with an ever thickening network of line defects (Figure 3). These observations align well with the experimental results: (i) defects are initially point-like but gradually turn into line defects. While existing defects keep growing, new defects keep appearing at a constant rate, resulting in a rapid increase in point defect density (Figure 2c). (ii) Consequently, as soon as point defect density increases sufficiently, the Raman spectra becomes governed by line defects. Moreover, once the line defects start to dominate, the area of pristine graphene starts to decrease notably, causing a reduction in the density of point defects (Figures 2c and 3c). (iii) When line defects percolate across the entire area, they define semienclosed regions with electron-scattering boundaries—crystallites that can function as graphene quantum dots. (iv) The crystallites have a broad size distribution, which implies the emission of optical wavelengths over a wide range—the luminescence of white light. In summary, the model provides reasonable explanations to all of the central experimental observations.

https://dx.doi.org/10.1021/acs.jpcc.0c00194
J. Phys. Chem. C 2020, 124, 8371–8377

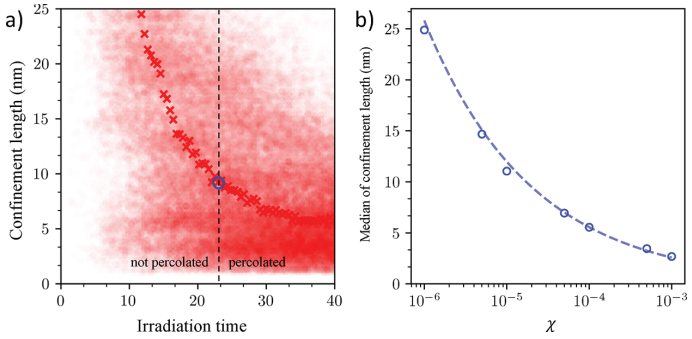

Figure 4. Quantitative analysis of confinement. (a) Sampled 10^3 confinement lengths for each irradiation time ($\chi = 10^{-5}$). The cross is the median over the sampled lengths for a given irradiation time, the vertical dashed line highlights the percolation threshold, and the blue sphere emphasizes the median length upon percolation. (b) The confinement median lengths upon percolation for $\chi = 10^{-6}...10^{-3}$. The dashed line is an analytical estimate from eq S3.

For quantitative comparison between the model and the experiment, we repeated the simulations with χ in the reasonable range $10^{-3}...10^{-6}$ (Figure S10). The crystallite dimensions were characterized by sampling 10^3 random confinement lengths for each time step of the simulation (Figure 4a). At the percolation threshold—manifesting the instant when crystallites supposedly become sufficiently enclosed to define GQDs—the median confinement length for $\chi = 10^{-3}...10^{-6}$ ranges from 3 to 25 nm (Figure 4b). The range agrees well with the experimentally inferred crystallite size of 10 nm. The best agreement with the experiment is obtained by $\chi \approx 10^{-5}$ (Figure 4b), which, in retrospect, motivates our tentative value for χ (Figure 3).

In addition to qualitatively explaining the Raman spectra and to quantitatively implying ~10 nm crystallite areas, the value around $\chi \sim 10^{-5}$ is attractive for two other reasons. First, it suggests a maximum point defect density around $n_D \sim 10^{12}$ cm^{-2}, in reasonable agreement with experiments (Figure 2c). Second, a similar growth model with the same parameter value of 10^{-5} was used in a previous work to explain quantitatively the laser-induced growth of oxidized islands on graphene.[18] This conformity makes a curious connection between optical forging and laser-induced oxidation, hinting toward a similar microscopic origin in the creation of SW defects.

The crystallite area affects strongly on the luminescence if the patterned graphene is considered analogously to the GQDs. This is because the GQD size defines its band gap due to the quantum confinement effect (QCE) of conjugated π-domains.[47−49] In the literature, the GQDs with similar spectra are in the size range of 1−2 nm, while our smallest crystallite size was 10 nm. Yet, it is worth noting that our value is an average value within the spot size of our Raman laser and, based on the modelling, the crystallites within this area have a quite wide size distribution. However, the mechanism of luminescence of GQDs is still under debate and the spectral properties of the GQDs are not explained by the QCE alone.[49] For example, related to the other PL mechanisms, the spectra of GQDs can change depending on the chemical environment,[50−52] functional groups,[53] and defects in the dots.[54,55] We currently lack direct atomic scale information about the graphene in patterned areas, which would reveal important details that affect the luminescence.

The peak positions of luminescence (Figure 1d) shift to longer wavelengths with a higher dose. At first, this might seem contradictory since, during irradiation, the crystallite size decreases and smaller GQDs have a larger band gap. However, this can be explained just with the shifting of the size distribution: if the peak of the distribution shifts toward small crystallite area, then the amount of larger (≥2 nm) crystallites will increase more than the smaller (≥2 nm) crystallites if the peak of the distribution is higher than 2 nm. This is certainly the case in our sample since the smallest average crystallite size measured was about 10 nm.

CONCLUSIONS

To summarize, we demonstrate a method to create photoluminescent patterns from graphene using femtosecond pulsed laser irradiation. Raman analysis revealed that the pulsed laser irradiation generates line defects in addition to point defects. To explain the luminescence, we present a model in which the generation of the line defects confines small graphene islands that behave similarly to graphene quantum dots. The broad white light luminescence from graphene is highly interesting for applications, such as displays. Our process provides an attractive method for achieving luminescence properties from graphene since it is local and does not require lithography or chemical treatments.

ASSOCIATED CONTENT

Supporting Information

The Supporting Information is available free of charge at https://pubs.acs.org/doi/10.1021/acs.jpcc.0c00194.

Experimental details, Raman spectra and AFM images of all pattern sets, description of Raman analyses, and model for defect growth (PDF)

AUTHOR INFORMATION

Corresponding Authors

Andreas Johansson − *Nanoscience Center, Department of Physics and Nanoscience Center, Department of Chemistry, University of Jyväskylä, 40014 Jyväskylä, Finland;* orcid.org/0000-0003-0906-6287; Email: andreas.johansson@jyu.fi

Mika Pettersson − *Nanoscience Center, Department of Chemistry, University of Jyväskylä, 40014 Jyväskylä, Finland;* orcid.org/0000-0002-6880-2283; Email: mika.j.pettersson@jyu.fi

Authors

Vesa-Matti Hiltunen − *Nanoscience Center, Department of Physics, University of Jyväskylä, 40014 Jyväskylä, Finland;* orcid.org/0000-0002-7754-8213

Pekka Koskinen − *Nanoscience Center, Department of Physics, University of Jyväskylä, 40014 Jyväskylä, Finland;* orcid.org/0000-0001-7711-3562

Kamila K. Mentel − *Nanoscience Center, Department of Chemistry, University of Jyväskylä, 40014 Jyväskylä, Finland;* orcid.org/0000-0001-8884-6753

Jyrki Manninen − *Nanoscience Center, Department of Physics, University of Jyväskylä, 40014 Jyväskylä, Finland*

Pasi Myllyperkiö − *Nanoscience Center, Department of Chemistry, University of Jyväskylä, 40014 Jyväskylä, Finland;* orcid.org/0000-0003-1651-1676

Complete contact information is available at: https://pubs.acs.org/10.1021/acs.jpcc.0c00194

Notes

The authors declare no competing financial interest.

■ ACKNOWLEDGMENTS

V.-M.H. acknowledges funding from the Finnish Cultural Foundation. P.K. and M.P. acknowledge funding from the Academy of Finland (grants 297115 and 311330).

■ REFERENCES

(1) Park, C.-H.; Giustino, F.; Cohen, M. L.; Louie, S. G. Velocity Renormalization and Carrier Lifetime in Graphene from the Electron-Phonon Interaction. *Phys. Rev. Lett.* **2007**, *99*, No. 086804.

(2) Dawlaty, J. M.; Shivaraman, S.; Chandrashekhar, M.; Rana, F.; Spencer, M. G. Measurement of Ultrafast Carrier Dynamics in Epitaxial Graphene. *Appl. Phys. Lett.* **2008**, *92*, No. 042116.

(3) Sun, D.; Wu, Z.-K.; Divin, C.; Li, X.; Berger, C.; de Heer, W. A.; First, P. N.; Norris, T. B. Ultrafast Relaxation of Excited Dirac Fermions in Epitaxial Graphene Using Optical Differential Transmission Spectroscopy. *Phys. Rev. Lett.* **2008**, *101*, 157402.

(4) Mak, K. F.; Ju, L.; Wang, F.; Heinz, T. F. Optical Spectroscopy of Graphene: From the Far Infrared to the Ultraviolet. *Solid State Commun.* **2012**, *152*, 1341−1349.

(5) Chen, C.-F.; Park, C.-H.; Boudouris, B. W.; Horng, J.; Geng, B.; Girit, C.; Zettl, A.; Crommie, M. F.; Segalman, R. A.; Louie, S. G.; et al. Controlling Inelastic Light Scattering Quantum Pathways in Graphene. *Nature* **2011**, *471*, 617−620.

(6) Gokus, T.; Nair, R. R.; Bonetti, A.; Böhmler, M.; Lombardo, A.; Novoselov, K. S.; Geim, A. K.; Ferrari, A. C.; Hartschuh, A. Making Graphene Luminescent by Oxygen Plasma Treatment. *ACS Nano* **2009**, *3*, 3963−3968.

(7) Peng, J.; Gao, W.; Gupta, B. K.; Liu, Z.; Romero-Aburto, R.; Ge, L.; Song, L.; Alemany, L. B.; Zhan, X.; Gao, G.; et al. Graphene Quantum Dots Derived from Carbon Fibers. *Nano Lett.* **2012**, *12*, 844−849.

(8) Shang, J.; Ma, L.; Li, J.; Ai, W.; Yu, T.; Gurzadyan, G. G. The Origin of Fluorescence from Graphene Oxide. *Sci. Rep.* **2012**, *2*, 792.

(9) Xu, Q.; Zhou, Q.; Hua, Z.; Xue, Q.; Zhang, C.; Wang, X.; Pan, D.; Xiao, M. Single- Particle Spectroscopic Measurements of Fluorescent Graphene Quantum Dots. *ACS Nano* **2013**, *7*, 10654−10661.

(10) Jiang, F.; Chen, D.; Li, R.; Wang, Y.; Zhang, G.; Li, S.; Zheng, J.; Huang, N.; Gu, Y.; Wang, C.; et al. Eco-Friendly Synthesis of Size-Controllable Amine-Functionalized Graphene Quantum Dots with Antimycoplasma Properties. *Nanoscale* **2013**, *5*, 1137−1142.

(11) Yang, P.; Zhou, L.; Zhang, S.; Wan, N.; Pan, W.; Shen, W. Facile Synthesis and Photoluminescence Mechanism of Graphene Quantum Dots. *J. Appl. Phys.* **2014**, *116*, 244306.

(12) Li, L.; Wu, G.; Yang, G.; Peng, J.; Zhao, J.; Zhu, J.-J. Focusing on Luminescent Graphene Quantum Dots: Current Status and Future Perspectives. *Nanoscale* **2013**, *5*, 4015−4039.

(13) Yoo, J.-H.; Kim, E.; Hwang, D. J. Femtosecond Laser Patterning, Synthesis, Defect Formation, and Structural Modification of Atomic Layered Materials. *MRS Bull.* **2016**, *41*, 1002−1008.

(14) Stöhr, R. J.; Kolesov, R.; Xia, K.; Wrachtrup, J. All-Optical High-Resolution Nanopatterning and 3D Suspending of Graphene. *ACS Nano* **2011**, *5*, 5141−5150.

(15) Zhang, W.; Li, L.; Wang, Z. B.; Pena, A. A.; Whitehead, D. J.; Zhong, M. L.; Lin, Z.; Zhu, H. W. Ti:Sapphire Femtosecond Laser Direct Micro-Cutting and Profiling of Graphene. *Appl. Phys. A* **2012**, *109*, 291−297.

(16) Kiisk, V.; Kahro, T.; Kozlova, J.; Matisen, L.; Alles, H. Nanosecond Laser Treatment of Graphene. *Appl. Surf. Sci.* **2013**, *276*, 133−137.

(17) Yoo, J.-H.; Park, J. B.; Ahn, S.; Grigoropoulos, C. P. Laser-Induced Direct Graphene Patterning and Simultaneous Transferring Method for Graphene Sensor Platform. *Small* **2013**, *9*, 4269−4275.

(18) Aumanen, J.; Johansson, A.; Koivistoinen, J.; Myllyperkiö, P.; Pettersson, M. Patterning and Tuning of Electrical and Optical Properties of Graphene by Laser Induced Two-Photon Oxidation. *Nanoscale* **2015**, *7*, 2851−2855.

(19) Johansson, A.; Myllyperkiö, P.; Koskinen, P.; Aumanen, J.; Koivistoinen, J.; Tsai, H.-C.; Chen, C.-H.; Chang, L.-Y.; Hiltunen, V.-M.; Manninen, J. J.; et al. Optical Forging of Graphene into Three-Dimensional Shapes. *Nano Lett.* **2017**, *17*, 6469−6474.

(20) Pimenta, M. A.; Dresselhaus, G.; Dresselhaus, M. S.; Cançado, L. G.; Jorio, A.; Saito, R. Studying Disorder in Graphite-Based Systems by Raman Spectroscopy. *Phys. Chem. Chem. Phys.* **2007**, *9*, 1276−1290.

(21) Cançado, L. G.; Takai, K.; Enoki, T.; Endo, M.; Kim, Y. A.; Mizusaki, H.; Jorio, A.; Coelho, L. N.; Magalhães-Paniago, R.; Pimenta, M. A. General Equation for the Determination of the Crystallite Size La of Nanographite by Raman Spectroscopy. *Appl. Phys. Lett.* **2006**, *88*, 163106.

(22) Lucchese, M. M.; Stavale, F.; Ferreira, E. H. M.; Vilani, C.; Moutinho, M. V. O.; Capaz, R. B.; Achete, C. A.; Jorio, A. Quantifying Ion-Induced Defects and Raman Relaxation Length in Graphene. *Carbon* **2010**, *48*, 1592−1597.

(23) Ribeiro-Soares, J.; Oliveros, M. E.; Garin, C.; David, M. V.; Martins, L. G. P.; Almeida, C. A.; Martins-Ferreira, E. H.; Takai, K.; Enoki, T.; Magalhães-Paniago, R.; et al. Structural Analysis of Polycrystalline Graphene Systems by Raman Spectroscopy. *Carbon* **2015**, *95*, 646−652.

(24) Cançado, L. G.; da Silva, M. G.; Ferreira, E. H. M.; Hof, F.; Kampioti, K.; Huang, K.; Pénicaud, A.; Achete, C. A.; Capaz, R. B.; Jorio, A. Disentangling Contributions of Point and Line Defects in the Raman Spectra of Graphene-Related Materials. *2D Mater* **2017**, *4*, No. 025039.

(25) Casiraghi, C.; Pisana, S.; Novoselov, K. S.; Geim, A. K.; Ferrari, A. C. Raman Fingerprint of Charged Impurities in Graphene. *Appl. Phys. Lett.* **2007**, *91*, 233108.

(26) Yan, J.; Zhang, Y.; Kim, P.; Pinczuk, A. Electric Field Effect Tuning of Electron- Phonon Coupling in Graphene. *Phys. Rev. Lett.* **2007**, *98*, 166802.

(27) Das, A.; Chakraborty, B.; Piscanec, S.; Pisana, S.; Sood, A. K.; Ferrari, A. C. Phonon Renormalization in Doped Bilayer Graphene. *Phys. Rev. B* **2009**, *79*, 155417.

(28) Pisana, S.; Lazzeri, M.; Casiraghi, C.; Novoselov, K. S.; Geim, A. K.; Ferrari, A. C.; Mauri, F. Breakdown of the Adiabatic Born-Oppenheimer Approximation in Graphene. *Nat. Mater.* **2007**, *6*, 198−201.

(29) Das, A.; Pisana, S.; Chakraborty, B.; Piscanec, S.; Saha, S. K.; Waghmare, U. V.; Novoselov, K. S.; Krishnamurthy, H. R.; Geim, A. K.; Ferrari, A. C.; et al. Monitoring Dopants by Raman Scattering in an Electrochemically Top-Gated Graphene Transistor. *Nat. Nanotechnol.* **2008**, *3*, 210−215.

(30) Basko, D. M.; Piscanec, S.; Ferrari, A. C. Electron-Electron Interactions and Doping Dependence of the Two-Phonon Raman Intensity in Graphene. *Phys. Rev. B* **2009**, *80*, 165413.
(31) Kalbac, M.; Reina-Cecco, A.; Farhat, H.; Kong, J.; Kavan, L.; Dresselhaus, M. S. The Influence of Strong Electron and Hole Doping on the Raman Intensity of Chemical Vapor-Deposition Graphene. *ACS Nano* **2010**, *4*, 6055−6063.
(32) Casiraghi, C. Probing Disorder and Charged Impurities in Graphene by Raman Spectroscopy. *Phys. Status Solidi RRL* **2009**, *3*, 175−177.
(33) Ding, F.; Ji, H.; Chen, Y.; Herklotz, A.; Dörr, K.; Mei, Y.; Rastelli, A.; Schmidt, O. G. Stretchable Graphene: A Close Look at Fundamental Parameters through Biaxial Straining. *Nano Lett.* **2010**, *10*, 3453−3458.
(34) Androulidakis, C.; Tsoukleri, G.; Koutroumanis, N.; Gkikas, G.; Pappas, P.; Parthenios, J.; Papagelis, K.; Galiotis, C. Experimentally Derived Axial Stress-Strain Relations for Two-Dimensional Materials Such as Monolayer Graphene. *Carbon* **2015**, *81*, 322−328.
(35) Tsoukleri, G.; Parthenios, J.; Papagelis, K.; Jalil, R.; Ferrari, A. C.; Geim, A. K.; Novoselov, K. S.; Galiotis, C. Subjecting a Graphene Monolayer to Tension and Compression. *Small* **2009**, *5*, 2397−2402.
(36) Zabel, J.; Nair, R. R.; Ott, A.; Georgiou, T.; Geim, A. K.; Novoselov, K. S.; Casiraghi, C. Raman Spectroscopy of Graphene and Bilayer under Biaxial Strain: Bubbles and Balloons. *Nano Lett.* **2012**, *12*, 617−621.
(37) Liu, J.; Li, Q.; Zou, Y.; Qian, Q.; Jin, Y.; Li, G.; Jiang, K.; Fan, S. The Dependence of Graphene Raman D-band on Carrier Density. *Nano Lett.* **2013**, *13*, 6170−6175.
(38) Beams, R.; Cançado, L. G.; Novotny, L. Raman Characterization of Defects and Dopants in Graphene. *J. Phys.: Condens. Matter* **2015**, *27*, No. 083002.
(39) Mueller, N. S.; Heeg, S.; Alvarez, M. P.; Kusch, P.; Wasserroth, S.; Clark, N.; Schedin, F.; Parthenios, J.; Papagelis, K.; Galiotis, C.; et al. Evaluating Arbitrary Strain Configurations and Doping in Graphene with Raman Spectroscopy. *2D Mater* **2017**, *5*, No. 015016.
(40) Bruna, M.; Ott, A. K.; Ijäs, M.; Yoon, D.; Sassi, U.; Ferrari, A. C. Doping Dependence of the Raman Spectrum of Defected Graphene. *ACS Nano* **2014**, *8*, 7432−7441.
(41) Lee, J. E.; Ahn, G.; Shim, J.; Lee, Y. S.; Ryu, S. Optical Separation of Mechanical Strain from Charge Doping in Graphene. *Nat. Commun.* **2012**, *3*, 1024.
(42) Suk, J. W.; Kitt, A.; Magnuson, C. W.; Hao, Y.; Ahmed, S.; An, J.; Swan, A. K.; Goldberg, B. B.; Ruoff, R. S. Transfer of CVD-Grown Monolayer Graphene onto Arbitrary Substrates. *ACS Nano* **2011**, *5*, 6916−6924.
(43) Heller, E. J.; Yang, Y.; Kocia, L.; Chen, W.; Fang, S.; Borunda, M.; Kaxiras, E. Theory of Graphene Raman Scattering. *ACS Nano* **2016**, *10*, 2803−2818.
(44) Martins Ferreira, E. H.; Moutinho, M. V. O.; Stavale, F.; Lucchese, M. M.; Capaz, R. B.; Achete, C. A.; Jorio, A. Evolution of the Raman Spectra from Single-, Few-, and Many-Layer Graphene with Increasing Disorder. *Phys. Rev. B* **2010**, *82*, 125429.
(45) Ma, J.; Alfè, D.; Michaelides, A.; Wang, E. Stone-Wales Defects in Graphene and Other Planar sp2 -Bonded Materials. *Phys. Rev. B* **2009**, *80*, No. 033407.
(46) Koivistoinen, J.; Sládková, L.; Aumanen, J.; Koskinen, P.; Roberts, K.; Johansson, A.; Myllyperkiö, P.; Pettersson, M. From Seeds to Islands: Growth of Oxidized Graphene by Two-Photon Oxidation. *J. Phys. Chem. C* **2016**, *120*, 22330.
(47) Zhu, S.; Song, Y.; Zhao, X.; Shao, J.; Zhang, J.; Yang, B. The Photoluminescence Mechanism in Carbon Dots (Graphene Quantum Dots, Carbon Nanodots, and Polymer Dots): Current State and Future Perspective. *Nano Res.* **2015**, *8*, 355−381.
(48) Carbonaro, C. M.; Corpino, R.; Salis, M.; Mocci, F.; Thakkar, S. V.; Olla, C.; Ricci, P. C. On the Emission Properties of Carbon Dots: Reviewing Data and Discussing Models. *C* **2019**, *5*, 60.
(49) Zhu, S.; Song, Y.; Wang, J.; Wan, H.; Zhang, Y.; Ning, Y.; Yang, B. Photoluminescence Mechanism in Graphene Quantum Dots: Quantum Confinement Effect and Surface/Edge State. *Nano Today* **2017**, *13*, 10−14.
(50) Zhu, S.; Zhang, J.; Qiao, C.; Tang, S.; Li, Y.; Yuan, W.; Li, B.; Tian, L.; Liu, F.; Hu, R.; et al. Strongly Green-Photoluminescent Graphene Quantum Dots for Bioimaging Applications. *Chem. Commun.* **2011**, *47*, 6858−6860.
(51) Tachi, S.; Morita, H.; Takahashi, M.; Okabayashi, Y.; Hosokai, T.; Sugai, T.; Kuwahara, S. Quantum Yield Enhancement in Graphene Quantum Dots via Esterification with Benzyl Alcohol. *Sci. Rep.* **2019**, *9*, 14115.
(52) Tetsuka, H.; Asahi, R.; Nagoya, A.; Okamoto, K.; Tajima, I.; Ohta, R.; Okamoto, A. Optically Tunable Amino-Functionalized Graphene Quantum Dots. *Adv. Mater.* **2012**, *24*, 5333−5338.
(53) Qu, D.; Zheng, M.; Li, J.; Xie, Z.; Sun, Z. Tailoring Color Emissions From N-Doped Graphene Quantum Dots for Bioimaging Applications. *Light: Sci. Appl.* **2015**, *4*, No. e364.
(54) Zhu, S.; Zhang, J.; Liu, X.; Li, B.; Wang, X.; Tang, S.; Meng, Q.; Li, Y.; Shi, C.; Hu, R.; et al. Graphene Quantum Dots with Controllable Surface Oxidation, Tunable Fluorescence and Up-Conversion Emission. *RSC Adv.* **2012**, *2*, 2717−2720.
(55) Pan, D.; Zhang, J.; Li, Z.; Wu, M. Hydrothermal Route for Cutting Graphene Sheets into Blue-Luminescent Graphene Quantum Dots. *Adv. Mater.* **2010**, *22*, 734−738.

https://dx.doi.org/10.1021/acs.jpcc.0c00194
J. Phys. Chem. C 2020, 124, 8371−8377

Making Graphene Luminescent by Direct Laser Writing - Supporting Information

Vesa-Matti Hiltunen,[†] Pekka Koskinen,[†] Kamila K. Mentel,[‡] Jyrki Manninen,[†] Pasi Myllyperkiö,[‡] Andreas Johansson,[*,†,‡] and Mika Pettersson[*,‡]

†*Nanoscience center, Department of Physics, University of Jyväskylä, 40014 Jyväskylä, Finland*

‡*Nanoscience center, Department of Chemistry, University of Jyväskylä, 40014 Jyväskylä, Finland*

E-mail: andreas.johansson@jyu.fi; mika.j.pettersson@jyu.fi

Experimental Details

Graphene was synthesized on Cu(111) thin films evaporated onto single crystal sapphire(0001) substrate. The catalyst film was annealed at 1070 °C under gas flows of 470 sccm argon and 30 sccm hydrogen for 45 minutes. After annealing the graphene growth was initiated by injecting 2 sccm of 1 % methane in argon to the chamber for 5 minutes at the same temperature, after which the samples were taken out of the hot zone of the furnace and allowed to cool down. The graphene film was transferred with a standard PMMA transfer method[1] onto a target substrate, which was a silicon chip with 300 nm thermal oxide film and a metal marker grid on top. The sample was spin-coated with a PMMA layer and the copper was etched in 1 M ammonium persulfate solution leaving the graphene/PMMA stack floating on the liquid. Then the graphene was rinsed in DI water, placed in 12 % HCl to remove possible metal residues, rinsed again in DI water and placed onto the Si/SiO_x substrate. The sample

was baked on a hot plate at 120 °C for 5 minutes to evaporate water between substrate and graphene. After this the PMMA film was removed with acetone and IPA. The sample was annealed at 300 °C in Ar/H_2 atmosphere for two hours to remove PMMA residues.

Direct laser writing of the patterns was performed with 515 nm femtosecond laser (Pharos-10, Light Conversion Ltd., 600 kHz, 250 fs pulse duration) focused with an objective lens (N.A.= 0.8) to a single Gaussian spot (spot size ~ 500 nm)^2. The laser writing was performed under a nitrogen purge to prevent photo-oxidation of graphene during the writing process. Five pattern sets were fabricated with pulse energies equal to 30, 70, 120, 140 and 160 pJ. Each patterned area ($\sim 2.5 \times 2.5$ μm^2) was prepared by step-by-step irradiation, with 0.1 μm separation between consecutive laser spots and writing speed varying for different squares from 0.05 to 5 s/spot.

Raman measurements were performed with a home-built Raman setup in backscattering geometry. Excitations were done with 532 nm (Alphalas, Monolas-532-100-SM) and 632.8 nm (Melles Griot, 25 LHP 991) CW lasers. The beam was focused to the sample and subsequently collected with a 100x microscope objective (Nikon, L Plan SLWD 100x/0.70). The scattered light was dispersed in a 0.5 m imaging spectrograph (Acton, SpectraPro 2500i) using a 600 g/mm grating (resolution: $\sim 7 - 8$ cm^{-1}). The signal was detected with an EMCCD camera (Andor Newton, EM DU971N-BV) using a 100 μm slit width. A beam splitter was placed between the objective and the spectrometer in order to observe the exact measurement point visually. The Rayleigh scattering for both lasers were attenuated with edge filters (Semrock). The laser powers were 0.5 mW for the 532 nm laser and 1.0 mW for the 632.8 nm laser. The mapping of the graphene patterns was done with a piezo stage (Attocube, ANPxyz101).

AFM imaging was done using Bruker's Dimension Icon microscope with Scanasyst Air probes and PeakForce QNM mode.

AFM images and Raman spectra of all pattern sets

AFM images and Raman spectra of different pattern sets are presented in Figures S1, S2, S3, S4 and S5. In each set the height of the patterns increase with exposure dose, as does the intensity of the broad Raman background signal, i.e. the luminescence.

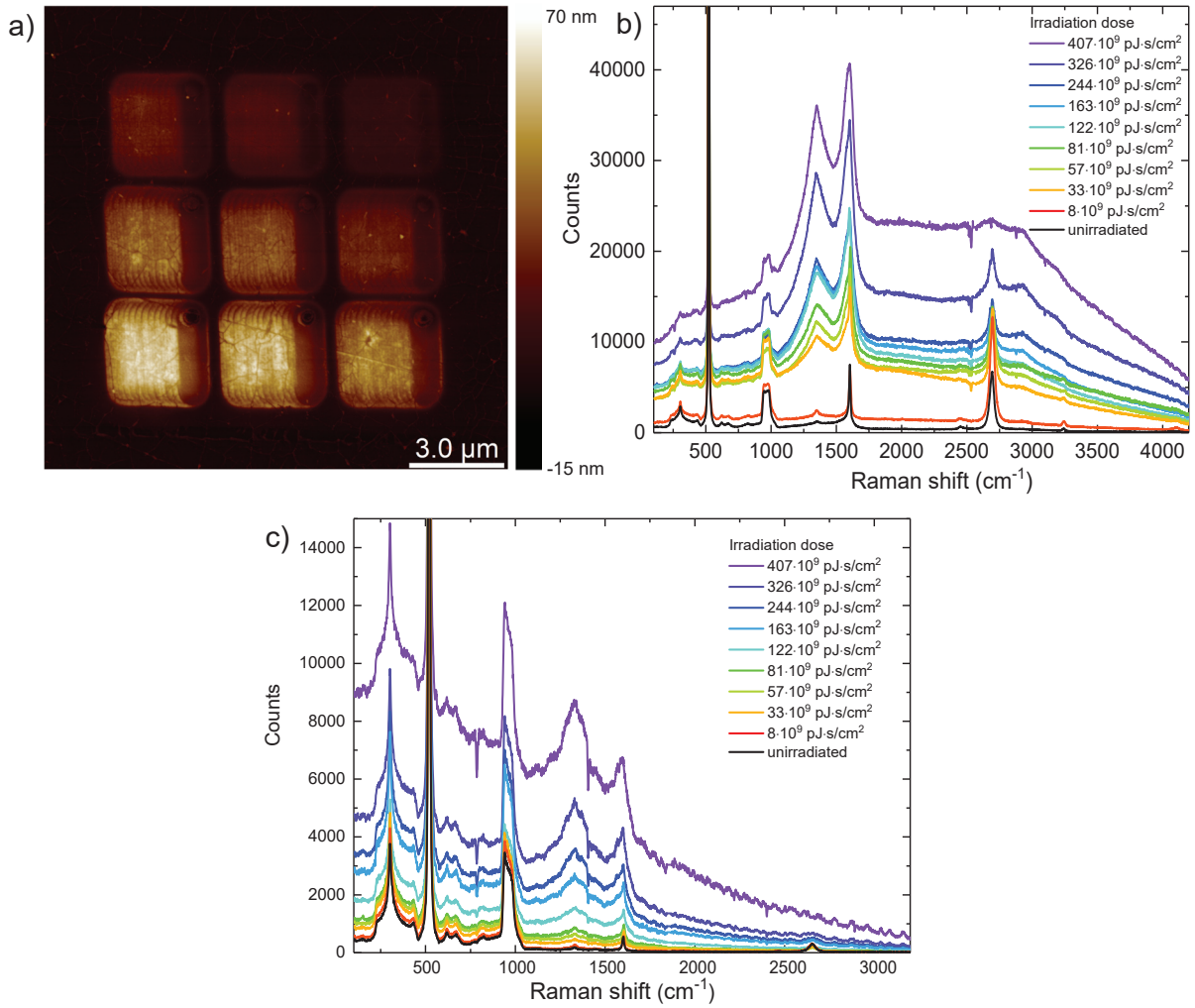

Figure S1: a) AFM image of a pattern set made with 160 pJ pulse energy b) Raman spectra from the middle of each pattern in panel a measured with 532 nm laser. c) Raman spectra from the middle of each pattern in panel a measured with 633 nm laser.

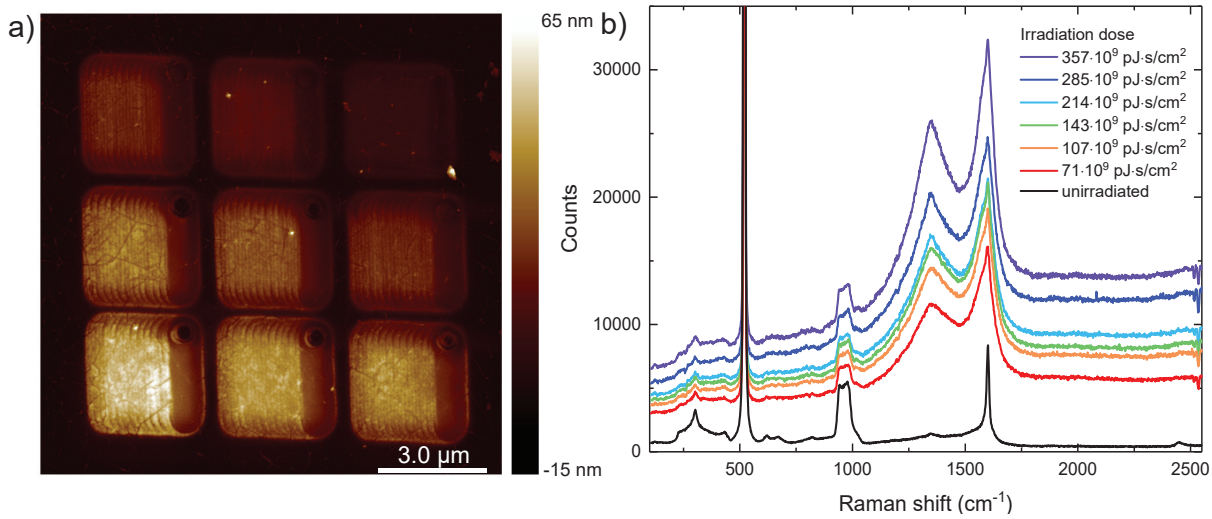

Figure S2: a) AFM image of a pattern set made with 140 pJ pulse energy. b) Raman spectra from the middle of each pattern in panel a measured with 532 nm laser.

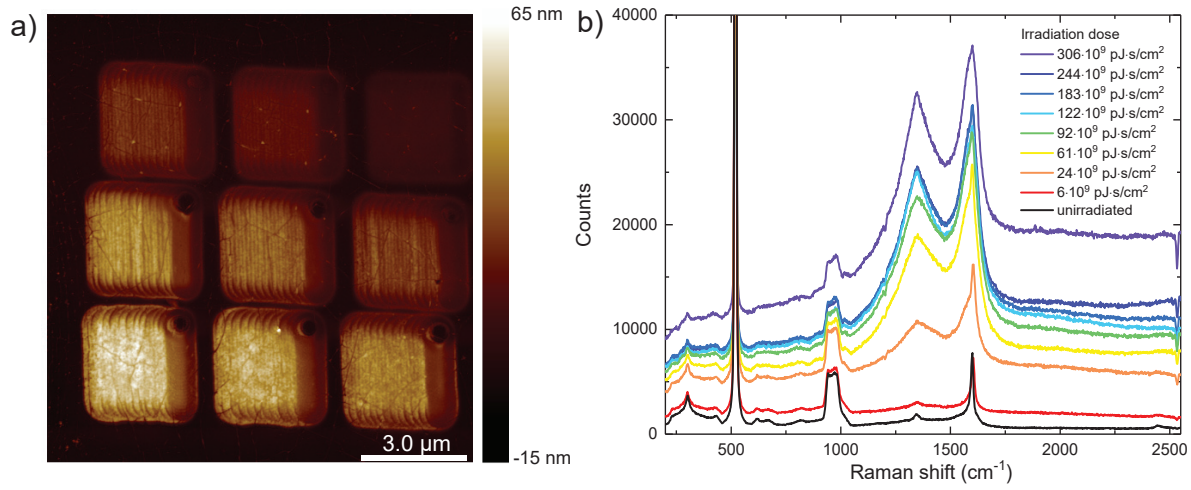

Figure S3: a) AFM image of a pattern set made with 120 pJ pulse energy. b) Raman spectra from the middle of each pattern in panel a measured with 532 nm laser.

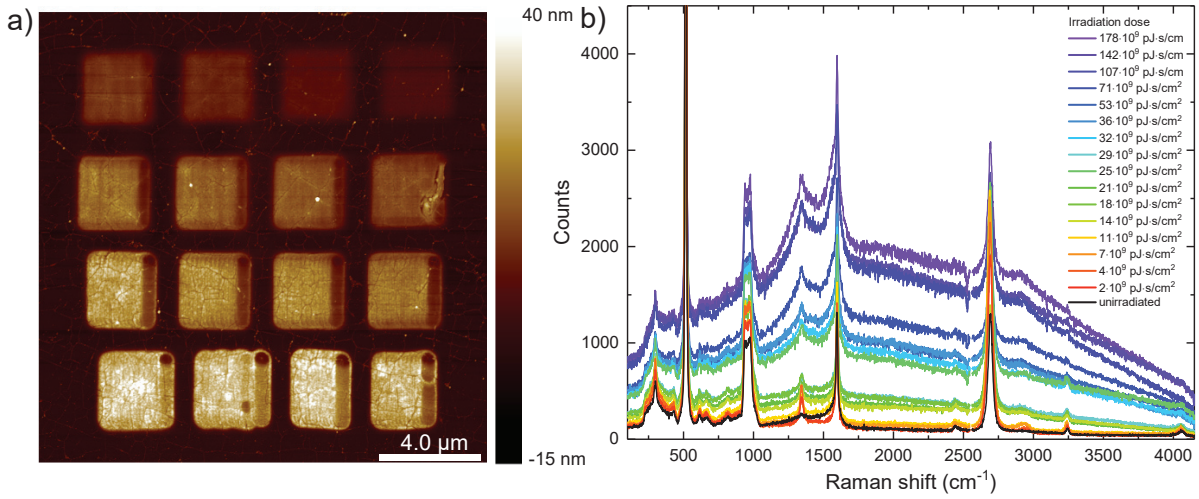

Figure S4: a) AFM image of a pattern set made with 70 pJ pulse energy. b) Raman spectra from the middle of each pattern in panel a measured with 532 nm laser.

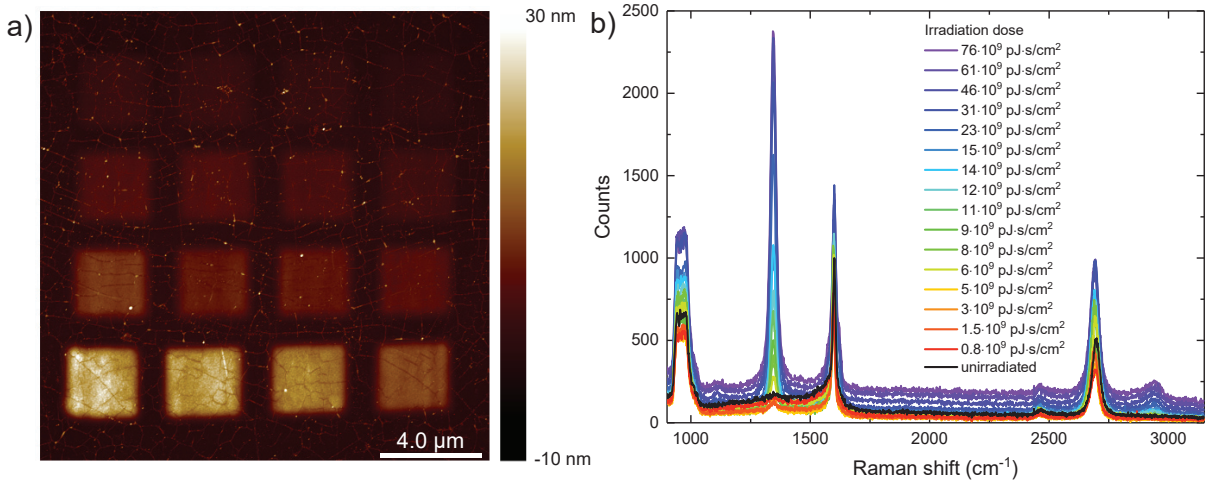

Figure S5: a) AFM image of a pattern set made with 30 pJ pulse energy. b) Raman spectra from the middle of each pattern in panel a measured with 532 nm laser.

Analysis of Raman data

Fitting

For each pattern set a Raman map of the area was acquired and 4-9 spectra per pattern were used for analysis of each individual pattern. The graphene Raman peaks were fitted with two Lorentzians to determine their intensity and FWHM. In order to take into account small amounts of amorphous carbon that the direct laser patterning can deposit, two Gaussians, which represent well the spectrum of amorphous carbon, were added to the fit. An example of fitting of the D and G bands is presented in Figure S6. Only the Lorentzian fit results corresponding to graphene were used in further analyses.

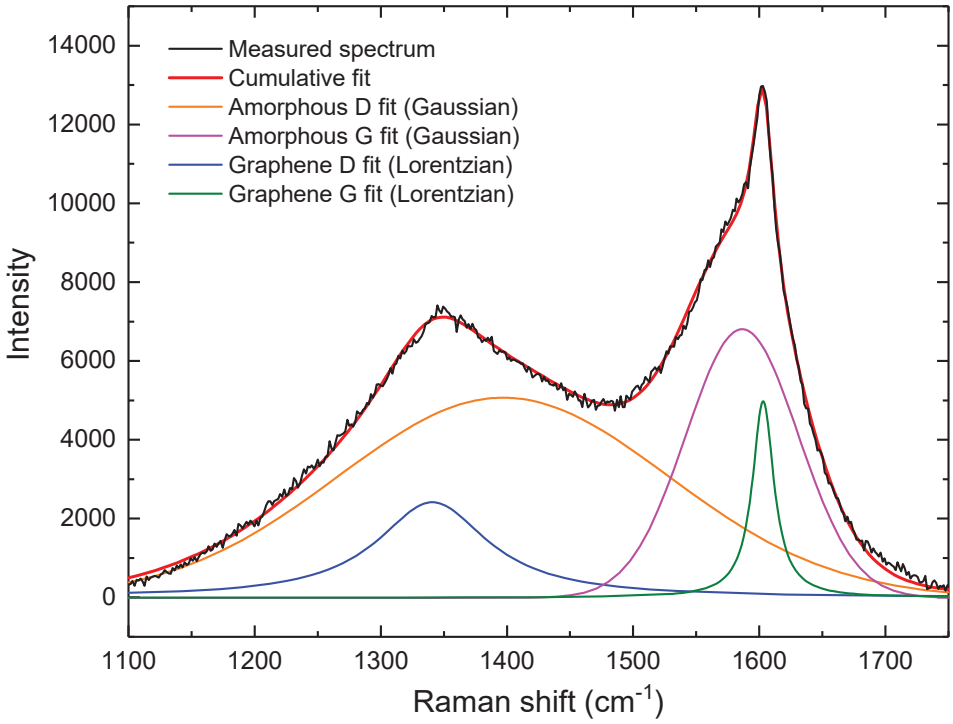

Figure S6: An example of Raman spectrum fitting. Spectrum is from a pattern made with 140 pJ pulse energy and 1.5 s exposure time. Both the D and G bands are fitted with both Lorentzian and Gaussian functions in order to differentiate contributions of graphene and amorphous carbon.

Doping and strain estimations

The peak positions of G and 2D bands can give information about strain and doping of the graphene sample[3–25]. Figure S7 shows how the pulsed laser dose affects these parameters. In Figure S7a the G band frequency upshifts first about $4\,\mathrm{cm}^{-1}$ until $5 \cdot 10^{10}\,\mathrm{pJ \cdot s/cm}^{-2}$ dose and downshifts after that. The trend is consistent with both lasers. Some of this can be seen also in Figure S7b where 2D frequency is plotted, but the trend is not as clear as with G. The 2D frequency is upshifted from zero doping already in unpatterned graphene, for which the 532 nm laser would give a peak position at about $2670\,\mathrm{cm}^{-1}$.[17] This reveals that the graphene is hole-doped, which is to be expected since the graphene is transferred onto a silicon oxide substrate and also might have some residues from the transfer process. In Figure S7c, the G band frequencies are plotted versus the 2D frequency to estimate strain and doping levels with solid lines showing the effect of strain/doping while keeping the other constant[25]. Inset shows a zoom to the measured data with arrows showing how increasing irradiation dose affects the Raman frequencies. This analysis gives a strain of about $-0.047\,\%$ (compressive biaxial) and it changes only by a very small amount during irradiation, while the doping level changes more. The effect of strain on the G band frequency was estimated with a sensitivity factor of $-69.1\,\mathrm{cm}^{-1}/\%$[25], which is an average value from previous studies[17,20,26]. Doping was estimated simply by $n = \left(E_F/\left(\hbar v_F\right)\right)/\pi$, where n is carrier concentration, E_F Fermi energy and v_F Fermi velocity. Shift of the G band frequency is given by $\Delta\Omega_G = E_F \times 42\,\mathrm{cm}^{-1}/\mathrm{eV}$[16]. For the doping and strain calculations, $1581\,\mathrm{cm}^{-1}$ was used as the G band frequency at zero doping and strain[17,25]. Figure S7d shows the effect of the pulsed laser irradiation to Fermi energy in graphene calculated this way. The doping level is quite high, being 0.34 eV even in unpatterned graphene. Reason for this is that the graphene was annealed at 300 °C, which leads to hole doping due to increased graphene-substrate conformity, an effect that has been reported previously[25,27]. The Fermi energy increases with irradiation dose, peaking at 0.44 eV before starting to decrease with even higher doses.

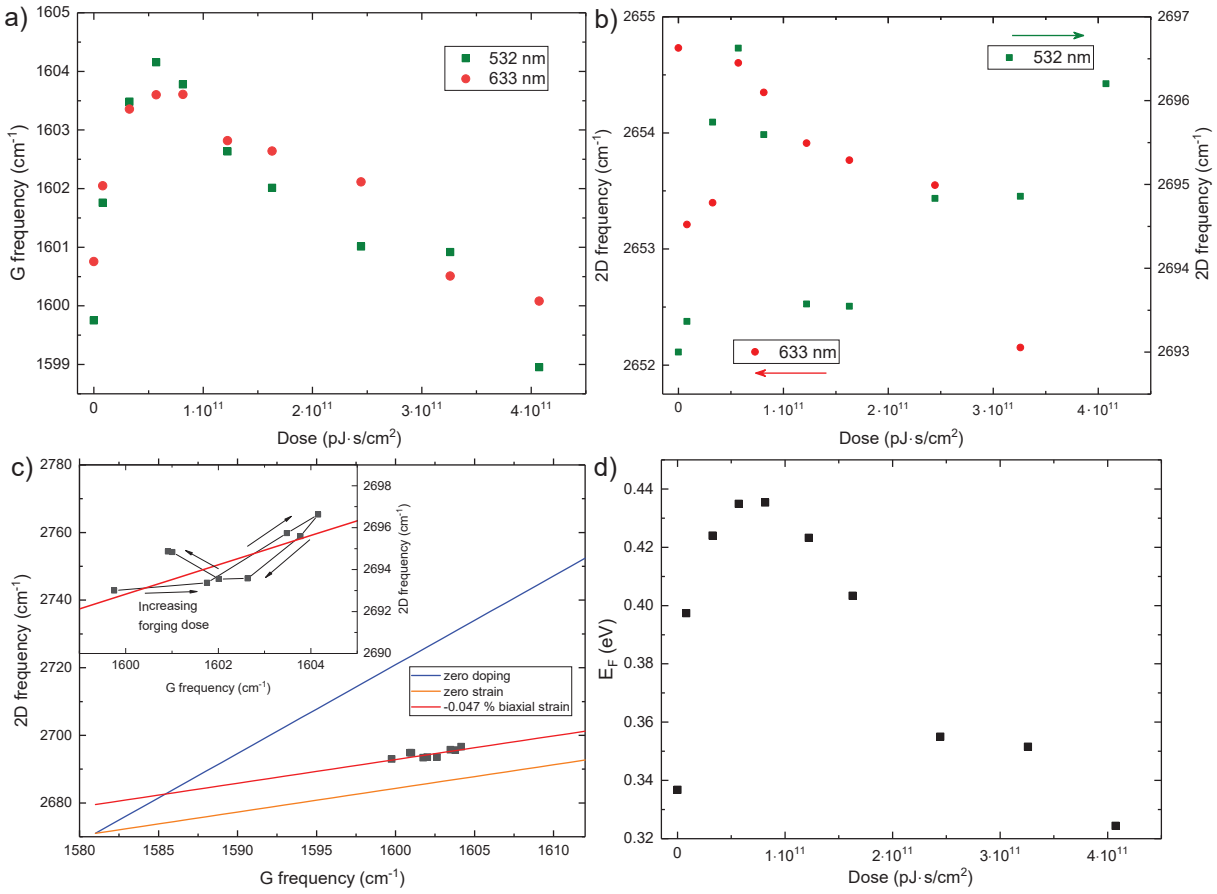

Figure S7: Evaluation of strain and doping of graphene. a) G band frequency and b) 2D band frequency as a function of dose. These are measured from the pattern set made with 160 pJ pulse energy using both the 532 nm and 633 nm lasers. c) 2D vs G frequency plot with examples of the effects of strain and doping. d) Fermi levels calculated from the Raman spectra as a function of dose. The latter two panels show data acquired with the 532 nm laser.

Defect analysis

We analyzed the Raman data in order to estimate point and line defect amounts of our samples. This analysis is following a model by Cançado et al.[7] The model is based on the integrated intensity ratio of the D and G bands (A_D/A_G) and the G band full width at half maximum (Γ_G) having different behaviors for line and point defects. The equation used to calculate A_D/A_G is[7]:

$$\begin{aligned}\left(\frac{A_D}{A_G}\right)E_L^4\left(L_a,L_D\right) = C_S^{0D}\left(1-e^{-\frac{\pi r_S^2}{L_D^2}}\right) + 4C_S^{1D}l_S\frac{(L_a-l_S)}{L_a^2}e^{-\frac{\pi r_S^2}{L_D^2}} \\ + 2\pi C_A^{0D}l_e\frac{(l_e+r_S)}{L_D^2}\left(1-4l_S\frac{(L_a-l_S)}{L_a^2}\right)e^{-\frac{\pi r_S^2}{L_D^2}} \\ + 2C_A^{1D}l_e\frac{(L_a-2l_S)}{L_a^2}\left(1-e^{-\frac{L_a-2l_S}{l_e}}\right)e^{-\frac{\pi r_S^2}{L_D^2}},\end{aligned} \tag{S1}$$

where E_L is the energy of the Raman laser, L_a is the graphene average crystallite size, L_D the average distance between nearest defects, C_S^{0D}, C_S^{1D}, C_A^{0D}, and C_A^{1D} differential Raman cross-section coefficients for either point (0D) or line (1D) defects, r_S the radius of the structurally damaged area of point defects, l_S the width of the structurally damaged lines and l_e the electron coherence length. Letters S and A in Raman coefficients refer respectively to structurally damaged areas or areas activated by the defects. The full-width at half maximum of the G band was[6]:

$$\Gamma_G\left(L_a,L_D\right) = \Gamma(\infty) + C_\Gamma e^{-\xi/l_{ph}}, \tag{S2}$$

where $\Gamma(\infty)$ is the FWHM of the G band with infinitely large L_a, C_Γ is a parameter related to the phonon dispersion relation, ξ the phonon localization length and l_{ph} the phonon coherence length. ξ is the minimum value between L_a and $10\cdot L_D$. Values for all the parameters are presented in Table 1.

Experimental values for A_D, A_G and Γ_G were determined from the measured Raman

Table 1: Parameter values for defect analysis.[7]

Parameter	Value (unit)
C_Γ	87 cm^{-1}
$\Gamma(\infty)$	15 cm^{-1}
l_{ph}	16 nm
C_S^{1D}	30.3 eV^4
C_A^{1D}	30.4 eV^4
l_e	4.1 nm
l_S	2 nm
C_S^{0D}	51 eV^4
C_A^{0D}	26.5 eV^4
r_S	2.2 nm

spectra by fitting Lorentzian functions to the Raman peaks. L_a and L_D were then calculated from equations S1 and S2 using the experimentally determined values for A_D/A_G and Γ_G.

A plot of A_D/A_G as a function of Γ_G is presented in Figure 2b. The A_D/A_G ratio is scaled with the E_L^4 in order to make the results comparable. In order to visualize the contributions of the two defect types, the figure has also theoretical traces that were calculated using equations S1 and S2. The solid black line represents the case where graphene has only line defects and no point defects, and the dashed black line represents the opposite. The point where both defect types are absent is at zero A_D/A_G ratio and 15 cm^{-1} Γ_G. The modelled traces show that the point defects initially only increase the A_D/A_G ratio, while the line defects cause, for the most part, an increase in Γ_G. At low amount of both defect types Cançado's model is inaccurate because of strain and doping affecting the measurement. For this reason all the experimental data in Figure 2 have been corrected to zero doping and strain using the same analysis as for the 160 pJ pattern set above.

Modeling the growth of line defects

Atomistic simulations of defected graphene

To simulate graphene with Stone-Wales (SW) defects at the atomic scale, we used the classical AIREBO interatomic potential, as implemented in the LAMMPS code[28]. The potential overestimates SW formation energy (5.7 eV), but the accuracy suffices for our purposes because the potential describes graphene's elastic properties and the interaction of SW defects well (Figure S8a). We used a cell that was periodic in xy-plane and at least 8 nm long in both lateral directions. This unit cell size gave SW formation energies down to 1 meV accuracy. The structures were fully relaxed using the FIRE method with maximum force tolerance of 0.01 eV/Å.[29]

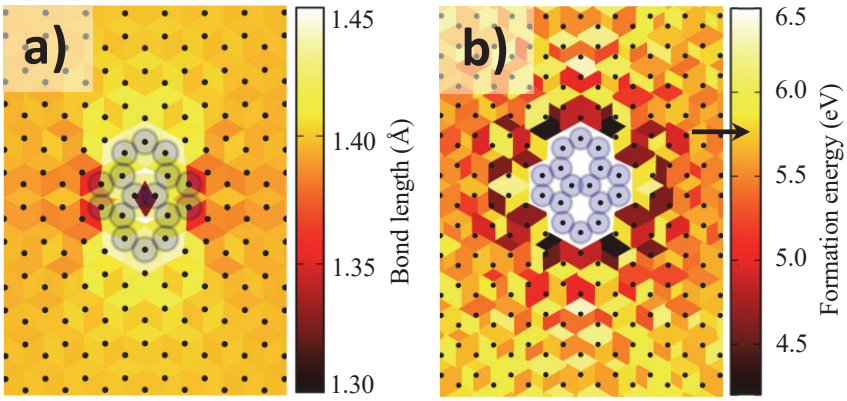

Figure S8: Interaction of SW defects. a) Asymmetric strain field of a single SW defect (blue spheres). Diamonds stand for the bonds between the C atoms (black dots) they join and their colors show the corresponding bond lengths. b) The formation energy of a second SW defect (colored diamonds) next to an existing one (blue spheres). The existing defect remains fixed and the second defect goes through *all* conceivable bond rotations in the neighborhood. Each colored diamond then shows the formation energy for rotating the corresponding bond. The black arrow indicates the formation energy of an isolated SW defect.

Interaction of Stone-Wales defects imply linear defects

The central feature in a SW defect is its asymmetric strain field (Figure S8a). The asymmetry implies that the formation energy of a second SW defect created in the neighborhood depends on the relative distance and orientation of the two SW defects. To prove this assertion, we calculated the formation energy of a second SW defect by rotating *all* C-C bonds within few nm distance from an existing SW defect. The resulting formation energy varied from 4.23 eV to 6.34 eV, the variation being extreme at small distances, in agreement with previous calculations (Figure S8b).[30]

The smallest formation energy of 4.23 eV happens for four specific bonds two lattice constants away from the existing rotated bond. Therefore, with an existing SW defect, the new SW defect is preferentially formed at these specific bonds, which we call α-bonds (Figure S8b). In other words, the SW interaction energy of nearly 1.5 eV for specific geometries makes graphene susceptible for laser-induced creation into SW defects separated by $2a = 4.92$ Å (Figure S9a). The SW defect pair, in turn, creates formation energy pattern similar to Figure S8b (not shown), with four α-bonds for energetically preferred creation of a third SW defect—and so on, recursively. This process leads to staggered lines of SW defects, whose terminals retain the two α-bonds for favourable rotation and concomitant linear growth (Figure S9b).

Kinematic model for the laser-induced creation of defects

Based on the atomistic simulations on the interaction of SW defects, we developed a simple kinematic model for the growth of SW defect arrays, similar to the model used succesfully for oxidized graphene.[31,32]

In the model, we assumed that the irradiation-induced rate (probability per unit time) of forming an SW defect in pristine graphene is p_0 and the rate of forming an SW defect at the α bonds is p_α (Figure S9). The meaningful parameter is the ratio $\chi \equiv p_0/p_\alpha$. This ratio tells the relative probability between creating a new SW defect and extending an existing array

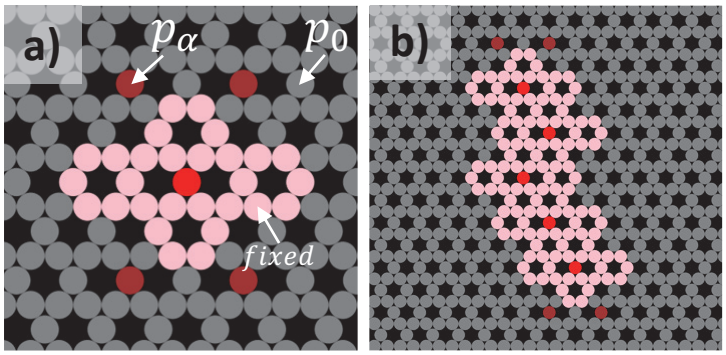

Figure S9: Stone-Wales defects as linearly growing defect patterns. a) Bond rotation rates (probabilities per unit time) around single SW defect. Spheres denote bonds (not atoms!) and colors correspond to rotated bonds (bright red), α-bonds (dark red), pristine bonds (grey), and fixed bonds (pink) with zero rotation rate. b) Illustration of simulated array of five SW defects, forming a staggered line defect.

of SW defects. For example, with $\chi = 10^{-3}$, it is thousand times less probable to create SW defects in pristine graphene than extending an existing array of SW defects. In what follows, we fixed the time scale by choosing $p_\alpha = 1$.

The assumption of singling out α-bonds and ignoring other potentially favourable bond rotation sites in Figure S8b is a daring approximation. However, the approximation was necessary because the precise energy-dependence of the bond rotation rates is unknown and because adding spatial details to bond rotation probabilities would quickly render the model intractable and wobbly. While a more complex model might introduce more branching, we believe that already this plain approximation grasps the essential qualitative features of the interaction between multiple SW defects.

Using a range of values for χ between $10^{-3} \ldots 10^{-6}$, the bond rotation kinematics of a given area was then simulated stochastically using a maximum time step $\delta t = 0.05$. The area had $N_{\text{cells}} = (6l_{\text{perc}}/a)^2$ graphene unit cells, where $a = 2.46$ Å is the graphene lattice constant and $l_{\text{perc}} = 0.26/\chi^{1/3}$, given by Eq.(S3) below, is a characteristic length scale. The length scale is related to the percolation threshold, the instance of the formation of continuous path of line defects across the simulated area.

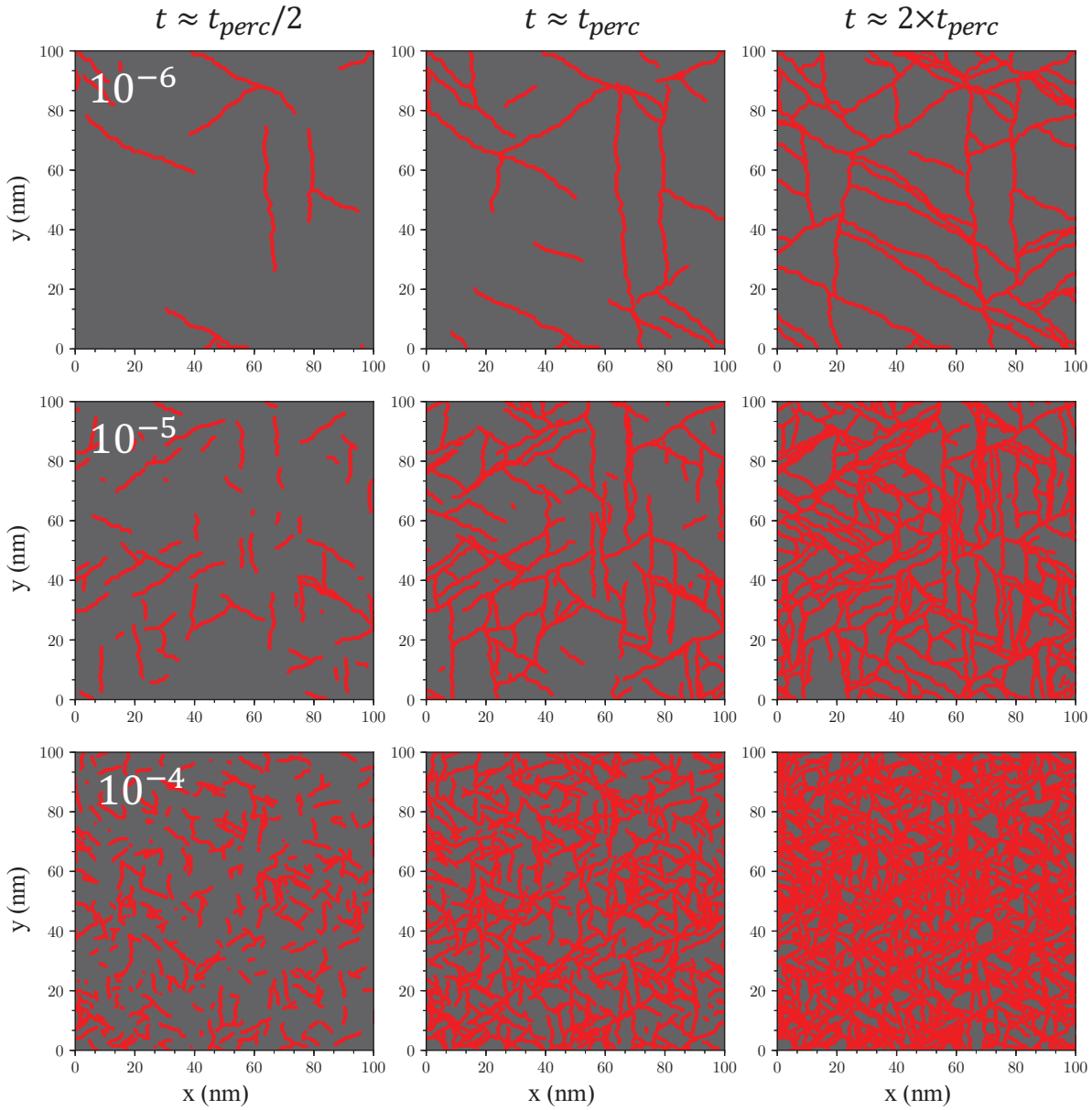

Figure S10: Line defects with different χ at various stages of the growth. The rows correspond to values $\chi = 10^{-6}$, 10^{-5} and 10^{-4} and the columns correspond to different times: the middle column corresponds to the percolation time t_{perc} (line defects reach continously across the entire irradiated area) and the columns on the left and on the right correspond to $t_{perc}/2$ and $2t_{perc}$. The percolation time depends on χ and is roughly $t_{perc} \approx 0.5/\chi^{1/3}$

Analytical results from the kinetic model

The model also lends itself for simple analytical estimates. Before percolation, the line defects are separate and their number is $N(t) \approx 3N_{\text{cells}}p_0 t$. The length of a line defect created at

$t' < t$ is $l \approx \delta l(4p_\alpha)(t - t')$, where $4p_\alpha$ is the total rate of increasing the length of the defect by $\delta l = 2a = 0.49$ nm. Thus, at time t before percolation the mean length of all the defects is $l_{\mathrm{avg}}(t) = \delta l(4p_\alpha)(t/2)$. Percolation can be estimated to occur when the density of line defects matches the density defined by their average length, $N(t_{\mathrm{perc}})/(N_{cells} \times 5.5\ \text{Å}^2) \approx l_{avg}(t_{\mathrm{perc}})^{-2}$. This implies that the length of line defects upon percolation is

$$l_{\mathrm{perc}} \approx l_{avg}(t_{\mathrm{perc}}) = 0.26/\chi^{1/3}\ \mathrm{nm}, \tag{S3}$$

which coincides well with the median of the simulated confinement length (Figure 4b). After percolation, the number of available pristine sites starts to decrease, causing a notable decrease in the creation of new defects and ultimately a marked reduction in the density of point defects.

References

(1) Suk, J. W.; Kitt, A.; Magnuson, C. W.; Hao, Y.; Ahmed, S.; An, J.; Swan, A. K.; Goldberg, B. B.; Ruoff, R. S. Transfer of CVD-Grown Monolayer Graphene onto Arbitrary Substrates. *ACS Nano* **2011**, *5*, 6916–6924.

(2) Johansson, A.; Myllyperkiö, P.; Koskinen, P.; Aumanen, J.; Koivistoinen, J.; Tsai, H.-C.; Chen, C.-H.; Chang, L.-Y.; Hiltunen, V.-M.; Manninen, J. J.; et al., Optical Forging of Graphene into Three-Dimensional Shapes. *Nano Lett.* **2017**, *17*, 6469–6474.

(3) Pimenta, M. A.; Dresselhaus, G.; Dresselhaus, M. S.; Cançado, L. G.; Jorio, A.; Saito, R. Studying Disorder in Graphite-Based Systems by Raman Spectroscopy. *Phys. Chem. Chem. Phys.* **2007**, *9*, 1276–1290.

(4) Cançado, L. G.; Takai, K.; Enoki, T.; Endo, M.; Kim, Y. A.; Mizusaki, H.; Jorio, A.; Coelho, L. N.; Magalhães-Paniago, R.; Pimenta, M. A. General Equation for the De-

termination of the Crystallite Size La of Nanographite by Raman Spectroscopy. *Appl. Phys. Lett.* **2006**, *88*, 163106.

(5) Lucchese, M.; Stavale, F.; Ferreira, E. M.; Vilani, C.; Moutinho, M.; Capaz, R. B.; Achete, C.; Jorio, A. Quantifying Ion-Induced Defects and Raman Relaxation Length in Graphene. *Carbon* **2010**, *48*, 1592–1597.

(6) Ribeiro-Soares, J.; Oliveros, M.; Garin, C.; David, M.; Martins, L.; Almeida, C.; Martins-Ferreira, E.; Takai, K.; Enoki, T.; Magalhães-Paniago, R.; et al., Structural Analysis of Polycrystalline Graphene Systems by Raman Spectroscopy. *Carbon* **2015**, *95*, 646–652.

(7) Cançado, L. G.; da Silva, M. G.; Ferreira, E. H. M.; Hof, F.; Kampioti, K.; Huang, K.; Pénicaud, A.; Achete, C. A.; Capaz, R. B.; Jorio, A. Disentangling Contributions of Point and Line Defects in the Raman Spectra of Graphene-Related Materials. *2D Mater.* **2017**, *4*, 025039.

(8) Casiraghi, C.; Pisana, S.; Novoselov, K. S.; Geim, A. K.; Ferrari, A. C. Raman Fingerprint of Charged Impurities in Graphene. *Appl. Phys. Lett.* **2007**, *91*, 233108.

(9) Yan, J.; Zhang, Y.; Kim, P.; Pinczuk, A. Electric Field Effect Tuning of Electron-Phonon Coupling in Graphene. *Phys. Rev. Lett.* **2007**, *98*, 166802.

(10) Das, A.; Chakraborty, B.; Piscanec, S.; Pisana, S.; Sood, A. K.; Ferrari, A. C. Phonon Renormalization in Doped Bilayer Graphene. *Phys. Rev. B* **2009**, *79*, 155417.

(11) Pisana, S.; Lazzeri, M.; Casiraghi, C.; Novoselov, K. S.; Geim, A. K.; Ferrari, A. C.; Mauri, F. Breakdown of the Adiabatic Born-Oppenheimer Approximation in Graphene. *Nat. Mater.* **2007**, *6*, 198–201.

(12) Das, A.; Pisana, S.; Chakraborty, B.; Piscanec, S.; K Saha, S.; Waghmare, U.; S Novoselov, K.; Krishnamurthy, H.; Geim, A.; Ferrari, A.; et al., Monitoring Dopants

by Raman Scattering in an Electrochemically Top-Gated Graphene Transistor. *Nat. Nanotechnol.* **2008**, *3*, 210–215.

(13) Basko, D. M.; Piscanec, S.; Ferrari, A. C. Electron-Electron Interactions and Doping Dependence of the Two-Phonon Raman Intensity in Graphene. *Phys. Rev. B* **2009**, *80*, 165413.

(14) Kalbáč, M.; Reina-Cecco, A.; Farhat, H.; Kong, J.; Kavan, L.; Dresselhaus, M. S. The Influence of Strong Electron and Hole Doping on the Raman Intensity of Chemical Vapor-Deposition Graphene. *ACS Nano* **2010**, *4*, 6055–6063.

(15) Casiraghi, C. Probing Disorder and Charged Impurities in Graphene by Raman Spectroscopy. *Phys. Status Solidi RRL* **2009**, *3*, 175–177.

(16) Chen, C.-F.; Park, C.-H.; Boudouris, B. W.; Horng, J.; Geng, B.; Girit, C.; Zettl, A.; Crommie, M. F.; Segalman, R. A.; Louie, S. G.; et al., Controlling Inelastic Light Scattering Quantum Pathways in Graphene. *Nature* **2011**, *471*, 617–620.

(17) Ding, F.; Ji, H.; Chen, Y.; Herklotz, A.; Dörr, K.; Mei, Y.; Rastelli, A.; Schmidt, O. G. Stretchable Graphene: A Close Look at Fundamental Parameters through Biaxial Straining. *Nano Lett.* **2010**, *10*, 3453–3458.

(18) Androulidakis, C.; Tsoukleri, G.; Koutroumanis, N.; Gkikas, G.; Pappas, P.; Parthenios, J.; Papagelis, K.; Galiotis, C. Experimentally Derived Axial Stress-Strain Relations for Two-Dimensional Materials Such as Monolayer Graphene. *Carbon* **2015**, *81*, 322–328.

(19) Tsoukleri, G.; Parthenios, J.; Papagelis, K.; Jalil, R.; Ferrari, A. C.; Geim, A. K.; Novoselov, K. S.; Galiotis, C. Subjecting a Graphene Monolayer to Tension and Compression. *Small* **2009**, *5*, 2397–2402.

(20) Zabel, J.; Nair, R. R.; Ott, A.; Georgiou, T.; Geim, A. K.; Novoselov, K. S.; Casiraghi, C. Raman Spectroscopy of Graphene and Bilayer under Biaxial Strain: Bubbles and Balloons. *Nano Lett.* **2012**, *12*, 617–621.

(21) Liu, J.; Li, Q.; Zou, Y.; Qian, Q.; Jin, Y.; Li, G.; Jiang, K.; Fan, S. The Dependence of Graphene Raman D-band on Carrier Density. *Nano Lett.* **2013**, *13*, 6170–6175.

(22) Beams, R.; Cançado, L. G.; Novotny, L. Raman Characterization of Defects and Dopants in Graphene. *J. Phys.: Condens. Matter* **2015**, *27*, 083002.

(23) Mueller, N. S.; Heeg, S.; Alvarez, M. P.; Kusch, P.; Wasserroth, S.; Clark, N.; Schedin, F.; Parthenios, J.; Papagelis, K.; Galiotis, C.; et al., Evaluating Arbitrary Strain Configurations and Doping in Graphene with Raman Spectroscopy. *2D Mater.* **2017**, *5*, 015016.

(24) Bruna, M.; Ott, A. K.; Ijäs, M.; Yoon, D.; Sassi, U.; Ferrari, A. C. Doping Dependence of the Raman Spectrum of Defected Graphene. *ACS Nano* **2014**, *8*, 7432–7441.

(25) Lee, J. E.; Ahn, G.; Shim, J.; Lee, Y. S.; Ryu, S. Optical Separation of Mechanical Strain from Charge Doping in Graphene. *Nat. Commun.* **2012**, *3*, 1024.

(26) Mohiuddin, T. M. G.; Lombardo, A.; Nair, R. R.; Bonetti, A.; Savini, G.; Jalil, R.; Bonini, N.; Basko, D. M.; Galiotis, C.; Marzari, N.; et al., Uniaxial Strain in Graphene by Raman Spectroscopy: *G* Peak Splitting, Grüneisen Parameters, and Sample Orientation. *Phys. Rev. B* **2009**, *79*, 205433.

(27) Kim, H. G.; Kihm, K. D.; Lee, W.; Lim, G.; Cheon, S.; Lee, W.; Pyun, K. R.; Ko, S. H.; Shin, S. Effect of Graphene-Substrate Conformity on the In-Plane Thermal Conductivity of Supported Graphene. *Carbon* **2017**, *125*, 39 – 48.

(28) Plimpton, S. Fast Parallel Algorithms for Short-Range Molecular Dynamics. *J. Comp. Phys.* **1995**, *117*.

(29) Bitzek, E.; Koskinen, P.; Gähler, F.; Moseler, M.; Gumbsch, P. Structural Relaxation Made Simple. *Phys. Rev. Lett.* **2006**, *97*, 170201.

(30) Openov, L. A.; Podlivaev, A. I. Interaction of the Stone-Wales Defects in Graphene. *Phys. Solid State* **2015**, *57*, 1477–1481.

(31) Eden, M. *A two-dimensional growth process.* Proceedings of the Fourth Berkeley Symposium on Mathematical Statistics and Probability, Statistical Laboratory of the University of California, Berkeley, USA, June 20-July 30, 1960; Neyman J.; Berkeley, Calif.: University of California Press, **1961**, *4*, 223–239.

(32) Koivistoinen, J.; Sladkova, L.; Aumanen, J.; Koskinen, P. J.; Roberts, K.; Johansson, A.; Myllyperkiö, P.; Pettersson, M. From Seeds to Islands: Growth of Oxidized Graphene by Two-Photon Oxidation. *J. Phys. Chem. C* **2016**, *120*, 22330.

AV

ULTRASTIFF GRAPHENE

by

Vesa-Matti Hiltunen, Pekka Koskinen, Kamila Mentel, Jyrki Manninen, Pasi Myllyperkiö, Mika Pettersson, Andreas Johansson 2021

npj 2D Materials and Applications, accepted for publication

Request a copy from the author.